Title
Artificial Melanin: From Synthesis to Chemical Properties and Applications

Author
Wang, Zhao

Publication Date
2018

UNIVERSITY OF CALIFORNIA, SAN DIEGO

Artificial Melanin: From Synthesis to Chemical Properties and Applications

A Dissertation Submitted in Partial Satisfaction of The
Requirement for The Degree of Doctor of Philosophy

in

Chemistry

by

Zhao Wang

Committee in charge:

Professor Nathan C. Gianneschi, Chair
Professor Michael Burkart, Co-Chair
Professor Karen Christman
Professor Kamil Godula
Professor Michael J. Sailor

2018

The dissertation of Zhao Wang is approved, and it is acceptable in quality and form for publication on microfilm and electronically:

Co-Chair

Chair

University of California, San Diego

2018

DEDICATION

I dedicate this thesis to my dear families,

Jianping Wang (Father),

Xiaohong Jiang (Mother),

Fang Zhou (Wife).

for introducing me the love and strength.

EPIGRAPH

Opportunities favor the prepared minds.

TABLE OF CONTENTS

SIGNATURE PAGE iii

DEDICATION iv

EPIGRAPH v

TABLE OF CONTENTS vi

LIST OF ABBREVIATIONS ix

LIST OF FIGURES xiv

LIST OF TABLES xx

ACKNOWLEDGEMENTS xxi

VITA xxiii

ABSTRACT OF THE DISSERTATION xxiv

Chapter 1 Introduction and History 1

1.1 Introduction 1

1.2 Synthesis of Melanin 1

1.2.1 Structure and Biosynthesis of Melanin 1

1.2.2 Base-Catalyzed Oxidative Self-Polymerization Of Dopamine 4

1.2.3 Other Methods of Synthesis of Artifical Melanins 8

1.2.4 Characterize Chemistry and Structure of Melanin 10

1.3 Metal Chelation in Melanins 13

1.3.1 Metal ions in Natural Melanin 13

1.3.2 Preparation of Metal-Loaded Synthetic Melanins 13

1.3.3 Characterize Melanin Metal Chelation 16

1.4 Magnetic Resonance Imaging (MRI) Contrast Agents 20

1.4.1 The Fundamentals of MRI 21

1.4.2 The Development of MRI Contrast Agents 22

1.5 References 25

Chapter 2 Structure and Function of Iron-Loaded Synthetic Melanin 32

2.1 Introduction 32

2.2 Synthetic Routes for the Preparation of Iron-Loaded Synthetic Melanin 34

2.2.1 Synthesis of SMNP-1 34

2.2.2 Synthesis of SMNP-2, 3, 4 and 5 35

2.3 Characterization of SMNPs 37

2.3.1 Analysis the Metal Loading via ICP-OES 37

2.3.2 Characterization of SMNPs by Electron Microscopy 37

2.3.3 Characterization of SMNPs NMRD and MR Imaging Analysis 40

2.3.4 MR Imaging of SMNP Contrast Agents 43

2.3.5 Magnetochemical Analysis of SMNPs 45

2.4 Conclusion 53

2.5 Acknowledge 53

2.6 References 54

Chapter 3 Tunable, Metal-Loaded Synthetic Melanin Nanoparticles Analyzed by Magnetometry 59

3.1 Introduction 59

3.2 Synthesis of Metal Loaded Synthetic Melanin Nanoparticles 61

3.2.1 Spectral Characterization of Fe(III)-dopamine complex 61

3.2.2 Post and Pre-Doping to Synthesize Metal-Loaded Synthetic Melanin Nanoparticles 63

3.2.3 Synthetic Control Over Metal-Loaded Synthetic Melanin Nanoparticles 64

3.3 Characterization of Metal-Loaded Synthetic Melanin Nanoparticles 71

3.3.1 Analysis the Morphology and Metal Content of Nanoparticles 71

3.3.2 Magnetochemical Analysis & MR Imaging Analysis 77

3.4 Conclusion 84

3.5 Acknowledge 85

3.6 References ... 85
Chapter 4 High Relaxivity Gadolinium-Polydopamine Nanoparticles ... 88
4.1 Introduction ... 88
4.2 Preparation of Gd(III)-Loaded Synthetic Melanin Nanoparticles ... 90
4.3 Characterization of Metal-Loaded Synthetic Melanin Nanoparticles ... 93
4.3.1 Analysis the Metal Loading via ICP-OES and XPS ... 93
4.3.2 Characterization via NMRD and MR Imaging Analysis ... 96
4.3.3 Cell Viability Assay and Stability of Nanoparticles in Different Mediums ... 103
4.3.4 Magnetochemical Analysis ... 106
4.4 Conclusion ... 108
4.5 Acknowledge ... 108
4.6 References ... 109
Chapter 5 Enzyme-Regulated Topology of a Cyclic Peptide Brush Polymer for Tuning Assembly ... 113
5.1 Introduction ... 113
5.2 Synthetic Route for Preparation of Cyclic ELP-Based Brush Polymer ... 114
5.2.1 Synthesis of Cyclic ELP-Based Norbornene Monomer ... 114
5.2.2 Synthesis of Gd-Based Termination Agent ... 117
5.2.3 Synthesis ELP-Based Homopolymer ... 120
5.2.4 Synthesis ELP-Based Copolymer ... 124
5.3 Self-assembly of ELP-Based Homopolymer and Copolymer ... 125
5.4 Conclusion ... 138
5.5 Acknowledge ... 138
5.6 References ... 139

LIST OF ABBREVIATIONS

AHP = aminohydroxyphenylalanine

Ac = acetate

BF-STEM = bright field scanning transmission electron microscopy

Boc = tert-butyloxycarbonyl

CCK-8 = cell counting kit-8

Cr = Chromium

Co = Cobalt

Cu = Copper

Cryo-TEM = Cryo- transmission electron microscopy

D = axial anisotropy parameter

DHI = 5,6-dihydroxyindole

DHICA = 5,6-dihydroxyindole-2-carboxylic acid

DIPEA = N,N-Diisopropylethylamine

DLS = dynamic light scattering

DMF = dimethylformamide

DMSO = dimethylsulfoxide

DMEM = Dulbecco's Modified Eagle Medium

DOPA = 3,4-dihydroxyl-L-phenylalanine

DOTA = diethylene triamine pentaacetic acid

DPTA = diethylene triamine pentaacetic acid

EDS = energy dispersive X-ray spectroscopy

EDTA = ethylenediaminetetraacetic acid

ELP = Elastin-like polypeptides

EPR = enhanced permeation and retention effect

equiv = equivalents

ESI = electrospray ionization

eV = electron volts

FBS = fetal bovine serum

Fe= iron

FTIR = Fourier Transform Infrared Spectroscopy

Fmoc = Fluorenylmethyloxycarbonyl

g = grams

Ga = gallium

Gd= gadolinium

G = Gauss

h = hours

HAADF-STEM = high angle annular dark field scanning transmission electron microscopy

HBTU = N,N,N’,N’-Tetramethyl-O-(1H-benzotriazol-1-yl)uronium hexafluorophosphate

HCl = Hydrogen Chloride

HEKa = human epidermal keratinocytes

HEPES = 4-(2-hydroxyethyl)-1-piperazineethanesulfonic acid

HPLC = high performance liquid chromatography

HRMS = high-resolution mass spectra

ICP-OES = inductively coupled plasma-optical emission spectrometry

IR = Infrared Spectroscopy

K = degrees Kelvin, thousand

L = liters

LCST = lower critical solution temperature

L-DOPA = 3-(3,4-dihydroxyphenyl)-L-alanine

LS = light scattering

Lys = Lysine

MALDI-TOF = matrix-assisted laser desorption ionization-time of flight

MALS = multi-angle light scattering

Mn = Manganese

MeOH = methanol (CH3OH)

min = minutes

Mn = number average molecular weight

Nor- Gly = N-(Glycine)-cis-5-norbornene-exo dicarboximide

mol = moles

MRI = magnetic resonance imaging

MS = mass spectrometry

Mw = weight average molecular weight

NaOH = Sodium hydroxide

Ni = Nickel

NMR= Nuclear magnetic resonance

NMRD = nuclear magnetic relaxation dispersion

NSF = nephrogenic systemic fibrosis

NP = nanoparticle

OEG = oligo(ethylene glycol)

Oe = oersted

PBS = Phosphate-buffered saline

PDI = polydispersity

PDA = polydopamine

PDCA = pyrrole-2,3-dicarboxylic acid (PDCA)

PEG = polyethylene glycol

PET = positron emission tomography

PTCA = pyrrole 2-3-5-tricarboxylic acid

ppm = parts per million

R = organic group, alkyl group

R_1 = the longitudinal proton relaxation rates

RAFT = reversible addition-fragmentation chain-transfer

RP-HPLC = reversed-phase high performance liquid chromatography

RI = refractive index

ROI = regions of interest

ROMP = ring-opening methathesis polymerization

ROP = ring-opening polymerization

ROI = regions of interest

RT = room temperature

SBM = the Solomon-Bloembergen-Morgan theory

SEC = size-exclusion chromatoraphy

SEC-MALS = multiangle light scattering detector

SEM = Scanning electron microscope

SMN = spherical micellar nanoparticles

SPPS = solid phase peptide synthesis

SQUID = superconducting quantum interference device

STEM = scanning transmission electron microscopy

T = temperature

T_1 = longitudinal relaxation time

T_2= transverse relaxation time

TA = termination agent

TEM = transmission electron microscopy

TFA = Trifluoroacetic acid

THF = Tetrahydrofuran

Ti = titanium

TIPS = Triisopropylsilane

Tris, TRIS, = tris(hydroxymethyl)aminomethane

UA = uranyl acetate

UV = Ultraviolet

V = Vanadium

XPS = X-ray photoelectron spectroscopy

ZFS = zero-field splitting

Zn = Zinc

LIST OF FIGURES

Figure 1.1. Biosynthetic pathng to eumelanin and pheomelanin production. 2

Figure 1.2. Casing model of mixed melanogenesis. In the process of mixed melanogenesis, pheomelanic pigment is produced first, followed by deposit of eumelanic pigment. In the granule with the eumelanin surface, the side is intentionally cut away to reveal the inner pheomelanin core. Copyright 2006 National Academy of Sciences of the United States of America. 3

Figure 1.3. Scheme illustrating the possible effect of Tris as a covalent modifier of dopamine and polydopamine structural components. Copyright 2014 American Chemical Society. 5

Figure 1.4. SEM images of PDA obtained in various ethanol/water mixtures. The volume fractions of ethanol are (a) 0%, (b) 20%, (c) 25, (d) 30%, (e) 35%, (f) 40%, (g) 50%, (h) 70%, and (i) 100%, respectively. The scale bars are 500 nm. Copyright 2014 Springer Nature. 6

Figure 1.5. SEM images of polydopamine in various experimental conditions: (a) pH 1, 160 °C, and 0.5 mg/mL, (b) pH 1, 160 °C, and 4.5 mg/mL, (c) pH 5, 120 °C, and 0.5 mg/mL, and (d) pH 5, 160 °C, and 0.5 mg/mL. Copyright 2015 American Chemical Society. 7

Figure 1.6. Photopatterning of polydopamine. a) Schematic representation of the polydopamine UV patterning. b) ToF-SIMS characterization of a pattern produced by photopatterning on a silicon wafer surface (CN− intensity map). c) Bright-field microscopy image of a silver nanoparticle pattern produced on a polydopamine patterned surface. d) Red fluorescence pattern. 9

Figure 1.7. HRTEM images of carbonized PDA nanoparticles. (a) TEM image of carbonized PDA nanoparticles. There are some dark domains. (b) Magnified image of dark domains in (a), which shows well-organized graphite-like nanostructure. The size of one typical domain is about 14 × 20 nm2. (c, d) Distance between stacking layers can be obtained from enlarged images. 11

Figure 1.8. Polydopamine synthesis occurs via two pathways: A) a pathway of covalent bond-forming oxidative polymerization and B) a newly proposed pathway of physical self-assembly of dopamine and DHI. Copyright 2012 John Wiley & Sons, Inc. 12

Figure 1.9. (a) Schematic illustration of the development of efficient T1-weighted MRI contrast agents using polydopamine nanoparticles. (b) TEM images of polydopamine nanoparticles and (c) EPR spectra of polydopamine nanoparticles before and after complexation with Fe3+ ions. Copyright 2013 American Chemical Society. 15

Figure 1.10. The weight of the solid product obtained in dopamine polymerization as a function of reaction time for the solutions with and without Ni2+ ions, shown by ▪ and • with solid lines, respectively. The feed molar ratio of DOPA to Ni2+ ions was 2:1. The ▲ dashed line shows the weight of neat polydopamine in the polydopamine/Ni2+ solid product as a function of reaction time. 16

Figure 1.11. EPR spectra of the free radicals generated by PDA-NPs, Cu-PDA-NPs, and Ag-PDA-NPs. EPR spectra of (a) Cu-PDA-NPs (red) showing a broad Cu-related signal at g = 2.13 and of (b) Ag-PDA-NPs (blue) displaying a narrow peak at g = 2.004. (c) Effect of EDTA (20 mM) on the EPR spectrum of Cu-PDA-NPs. 20

Figure 1.12. The spin and charge of a proton (a) causes it to have a magnetic field that tends to align with an applied magnetic field Bo analogous to a gyroscope hanging from a vertical pivot in the earth's gravitational field (b). When the gyroscope is tilted away from vertical it undergoes precession (d). Similarly, the proton also has angular momentum in the form of spin. 21

Figure 1.13.   T1. T1 is defined as the time that it takes the longitudinal magnetization to grow back to 63% of its final value. T2. T2 is defined as the time that it takes the transverse magnetization to decrease to 37% of its starting value. Copyright 2005 RSNA. 22

Figure 1.14. Chemical structure of gadopentetate dimeglumine. 23

Figure 1.15. Relaxivities of different generations of Gd−DTPA-based dendrimers 5n: ionic relaxivities versus molecular weight (left) and molecular relaxivities versus the generation of the dendrimer (right). The maximum molecular relaxivity is defined as the ionic relaxivity multiplied by the theoretical number of gadolinium moieties attached to a single dendrimer. 25

Figure 2.1. Scheme for the preparation of SMNP-i samples: (a) Post-doping strategy for SMNP-1, and (b) Pre-doping strategy for SMNP-2, SMNP-3, SMNP-4, and SMNP-5. Copyright 2016 American Chemical Society. 34

Figure 2.2. Representative electron microscopy characterization of SMNP-4: (a) TEM; (b) cryo-TEM; (c) SEM; and (d) HAADF-STEM (insert is the selected area EDS Fe elemental mapping image). Copyright 2016 American Chemical Society. . 38

Figure 2.3. Representative TEM images of SMNP-0 (a), SMNP-1 (b), SMNP-2 (c), SMNP-3 (d), SMNP-4 (e), and SMNP-5 (f). Copyright 2016 American Chemical Society. 39

Figure 2.4. Representative SEM images of SMNP-0 (a), SMNP-1 (b), SMNP-2 (c), SMNP-3 (d), SMNP-4 (e), and SMNP-5 (f). Copyright 2016 American Chemical Society. 39

Figure 2.5. (a) BF-STEM and (b) HAADF-STEM images of SMNP-4. Copyright 2016 American Chemical Society. . 40

Figure 2.6. (a) HAADF-STEM image of SMNP-4 with the selected area chosen for EDS spectral mapping outlined with a yellow box. Insert in lower right is the EDS Fe elemental mapping image of the selected area; (b) EDS spectra of SMNP-4 from the testing area (red) and background (blue) in (a). Copyright 2016 American Chemical Society. 40

Figure 2.7. (a) ^{1}H NMRD profiles for SMNP-i (i=1-5). The x-axis is proton Larmor frequency, y-axis is r1 value per Fe(III) ion for each SMNP. (b)1H NMRD profiles for SMNP-i (i=1-5). The x-axis is proton Larmor frequency, y-axis is r1 value per particle for each SMNP. Copyright 2016 American Chemical Society. 42

Figure 2.8. Stability study of Fe(III)-chelated SMNP-i (i=2-5) in PBS. Copyright 2016 American Chemical Society. 43

Figure 2.9. T1-weighted MR images captured on a Bruker 7.0 T magnet from SMNP-0, SMNP-1, and SMNP-4 in different media (particle concentration is 1.3 mg/mL in each tube). T1 results for each phantom are shown below in milliseconds, respectively. Copyright 2016 American Chemical Society. 44

Figure 2.10. MRI characterization of SMNP-i (i=1-5) nanoparticles on a Bruker 7.0 T magnet. Plots of 1/T1 versus FeIII concentration for SMNP-i in different medium with calculated r1 (green plot: SMN-i in water, blue plot: SMNP-i in freshly prepared complete DMEM medium (10% FBS), red plot: SMNP-i in complete DMEM medium (10% FBS) for 5 d). 45

Figure 2.11. (a) Experimental EPR spectra of SMNP-i (i = 0–5). (b) Temperature-dependent EPR analysis of SMNP-5. Copyright 2016 American Chemical Society. 46

Figure 2.12. Line width of g=4.3 EPR spectrum as a function of iron. Black circles, line width from data acquired at 125 K. Red line is first order fit of data showing that line width increases linearly with iron content. Copyright 2016 American Chemical Society. 47

Figure 2.13. Temperature dependence of the product of magnetic susceptibility and temperature (χMT) for SMNP-i (i = 1–5). The dotted line describes the behavior of an isolated, isotropic Fe(III) ion. Solid lines represent a global fit of the data between 25 and 300 K as described in the text. Copyright 2016 American Chemical Society. 49

Figure 2.14. (a) Plot of the product of temperature and magnetic susceptibility vs. temperature (χMT) for SMNP-0. (b) Low-temperature magnetization data under different applied fields for SMNP-1. The black lines represent fits to data. Copyright 2016 American Chemical Society. 50

Figure 2.15. (a) Plot of variable-temperature variable-field magnetization data for SMNP-1. The color bar represents the difference between experimental data and fitting results. A standard 2D M vs H/T plot is shown in Figure 2.14b. (b) UV–vis spectra of 0.1 mg/mL SMNP showing the transition from a featureless absorption for SMNP-0 to a well-defined yet broad structure in SMNP-5. 52

Figure 3.1. Time-dependent UV-visible absorption spectra of reaction solutions at different dopamine/Fe molar ratios. (a) dopamine/Fe = 3:1; (b) dopamine/Fe = 10:1; (c) dopamine/Fe = 50:1; (d) dopamine/Fe = 100:1. Copyright 2017 American Chemical Society. 62

Figure 3.2. Representative TEM images of Fe(III)-loaded synthetic melanin nanoparticles quenched at different time points (a)15 min, (b)30 min, (c)45 min, (d) 60 min, (e) 120 min, (f) 240 min, (g) 360 min, (h) 480 min, (i) reaction time versus particle diameter, (j) reaction time versus particle yield. Copyright 2017 American Chemical Society. 65

Figure 3.3. (a) Fitting curve of particle volume versus yield. (b) Reaction time versus Fe(III) weight percent. Copyright 2017 American Chemical Society. 67

Figure 3.4. Representative TEM images of Fe(III)-loaded synthetic melanin nanoparticles synthesized at different dopamine concentrations (a) 0.7 mM, (b) 1.1 mM, (c) 1.6 mM, (d) 2.2 mM, (e) 2.8 mM, (f) 3.5 mM. Copyright 2017 American Chemical Society. 68

Figure 3.5. (a) Dopamine concentration versus particle diameter. (b) Dopamine concentration versus particle diameter. Copyright 2017 American Chemical Society. 69

Figure 3.6. Representative TEM images of Fe(III)-loaded synthetic melanin nanoparticles synthesized at different pH: (a) 8.7, (b) 9.1, (c) 9.3, (d) 9.5, (e) 9.6. Copyright 2017 American Chemical Society. 70

Figure 3.7. (a) pH versus particle diameter. (b) pH versus Fe(III) loading. Copyright 2017 American Chemical Society. 71

Figure 3.8. TEM images of metal-loaded synthetic melanin nanoparticles (a) Mn(III)-1, (b) Co(II)-1, (c) Ni(II)-1, (d) Cu(II)-1, (e) Zn(II)-1, (f) Ga(III)-1.Copyright 2017 American Chemical Society. 72

Figure 3.9. STEM-EDS analysis of Mn(III)-loaded PDA -NPs. (a) Dark Field STEM image of particles prior to EDS elemental mapping. (b) Bright field STEM image of the region of interest used for mapping. (c-e) EDS elemental maps of the ROI for the characteristic X-ray emission peaks for (c) Al, (d) Mn, and (e) Cu.. 75

Figure 3.10. STEM -EDS analysis of Co(II)-loaded PDA NPs. (a) Dark Field STEM image of particles prior to EDS elemental mapping. (b-e) EDS elemental maps of the region of interest (as indicated in f) for the characteristic X-ray emission peaks for (b) Aluminum, (c) Silicon, (d) Cobalt, and (e) Copper. Al, Si, and Cu signal is background signal from the microscope column. 76

Figure 3.11. STEM-EDS analysis of Ni(II)-loaded PDA NPs. (a) Dark Field STEM image of particles prior to EDS elemental mapping. (b-e) EDS elemental maps of the region of interest (as indicated in f) for the characteristic X-ray emission peaks for (b) Al, (c) Si, (d) Ni, and (e) Cu. Al, Si, and Cu signal is background signal from the microscope column or sample holder/grid. 77

Figure 3.12. Temperature dependence of the product of magnetic susceptibility and temperature (χMT) for (a) Ni(II)-, (b) Co(II)-, and (c) Mn(III)-loaded synthetic melanin nanoparticles. Susceptibility data for Mn(III)-loaded particles are globally fit using 79

Figure 3.13. Representative TEM images of (a) Mn(III)-1, (b) Mn(III)-2, (c) Mn(III)-3, (d) Mn(III)-4. Copyright 2017 American Chemical Society. 80

Figure 3.14. T1-weighted MR images of (a) Mn(III)-1, (b) Mn(III)-2, (c) Mn(III)-3, (4) Mn(III)-4 in aqueous solution at different particle concentrations. Copyright 2017 American Chemical Society. 82

Figure 3.15. T1 MRI relaxivity plots of (a) Mn(III)-1, (b) Mn(III)-2, (c) Mn(III)-3, (4) Mn(III)-4 at at 7 T to determine r1. Copyright 2017 American Chemical Society........ 83

Figure 3.16. The r1 relaxation rates (a) per metal ion, (b) per spin as a function of weight percent of metal ion (%). Copyright 2017 American Chemical Society. 84

Figure 4.1. TEM image of Gd-polydopamine nano-aggregates synthesized via pre-doping strategy. Copyright 2017 John Wiley & Sons, Inc. 91

Figure 4.2 Synthesis of Gd(III)-loaded synthetic melanin nanoparticle (SMNP) via pre-doping strategy generate particles. White and red dots represent Gd(III) and Mn(III) ions respectively (c) TEM micrograph of Mn-4 and (d) corresponding Gd-4. Copyright 2017 John Wiley & Sons, Inc. 92

Figure 4.3. XPS spectrum of (a) Mn(III)-loaded synthetic melanin nanoparticles and (b) Gd(III)-loaded synthetic melanin nanoparticles. Copyright 2017 John Wiley & Sons, Inc. 94

Figure 4.4. Representative TEM images: (a) Mn-1; (b) Gd-1; (c) Mn-2 ; (d) Gd-2; (e) Mn-3; (f) Gd-3; (g) Mn-5 and (h)Gd-5. Copyright 2017 John Wiley & Sons, Inc. 95

Figure 4.5. Dynamic light scattering of: (a) Mn-1 and Gd-1; (b) Mn-2 and Gd-2; (c) Mn-3; and Gd-3; (d) Mn-4 and Gd-4; (e) Mn-5 and Gd-5. Copyright 2017 John Wiley & Sons, Inc. 96

Figure 4.6. 1H NMRD profiles for Gd-i (i=1-5). The x-axis is proton Larmor frequency, y-axis is r1 value per Gd(III) ion for each sample. Copyright 2017 John Wiley & Sons, Inc. 97

Figure 4.7. The r2/ r1 value at various field strengths (20-70MHz) of Gd-i (i=1-5). Copyright 2017 John Wiley & Sons, Inc. 100

Figure 4.8. ^{1}H NMRD profiles for Gd-i (i=1-5). The x-axis is proton Larmor frequency, y-axis is r1 value per nanoparticle for each sample. Copyright 2017 John Wiley & Sons, Inc. 101

Figure 4.9. MRI characterization of Gd-i (i=1-5) on a Bruker 7T magnet. Plots of 1/T1 versus Gd(III) concentration and its corresponding image of (a) Gd-1; (b) Gd-2; (c) Gd-3; (d) Gd-4; (e) Gd-5.(f) In vitro T1-weighted MR images of HeLa cells incubated with Gd-3 and PD- NP at diffferent concentrations for 24h. Copyright 2017 John Wiley & Sons, Inc........ 103

Figure 4.10. Cell viability of HeLa cells exposed to different concentrations of Gd-1, Gd-3, Gd-4, Gd-5 and control (PD-NP) at 24 and 48 hours. Copyright 2017 John Wiley & Sons, Inc........ 105

Figure 4.11. Gd-polydopamine complex stability over Ca2+ and Zn2+ cations. Copyright 2017 John Wiley & Sons, Inc........ 105

Figure 4.12. Stability of Gd-3 sample over different media. Copyright 2017 John Wiley & Sons, Inc. .. 106

Figure 4.13. Temperature dependence of the product of magnetic susceptibility and temperature (χMT) for Gd-1, Gd-3 and Gd-4 samples. The solid line describes the behavior of an isolated, isotropic Gd (III) ion. Copyright 2017 John Wiley & Sons, Inc. 107

Figure 5.1. Cyclization reaction of linear peptide monomer (L1). Range I is the elastin-based sequence VPGGGVPGLG (red color). Copyright 2015 Royal Society of Chemistry. 115

Figure 5.2. ^{1}H NMR spectrum of 1 in DMF-d7. Copyright 2015 Royal Society of Chemistry................ 116

Figure 5.3. ESI-MS data and HPLC traces of linear peptide monomer (L1) and cyclic peptide monomer (1). HPLC gradient: 20%-60% ACN over 30mins. Copyright 2015 Royal Society of Chemistry......... 116

Figure 5.4. Synthesis of 2. Copyright 2015 Royal Society of Chemistry. 117

Figure 5.5 ^{1}H NMR and 13C NMR of 2 in DMF-d7. Copyright 2015 Royal Society of Chemistry........ 118

Figure 5.6 (a) HPLC trace of 2 (10%-50% ACN over 30 mins) and (b) ESI-MS of 2. Copyright 2015 Royal Society of Chemistry. 118

Figure 5.7. Synthesis of Gd-TA. Copyright 2015 Royal Society of Chemistry. 119

Figure 5.8. (a) HPLC trace of Gd-TA (10%-50% ACN over 30 mins) and (b) ESI-MS of GD-TA. Copyright 2015 Royal Society of Chemistry. 119

Figure 5.9 Synthetic scheme of homopolymer P1 using ROMP initiator (IMesH2)(C5H5N)2(Cl)2Ru=CHPh (“Ru”) and Gd-containing termination agent (Gd-TA). For P1, m = 5. The structure post-enzyme treatment is drawn to represent the ideal result of 100% peptide cleavage. Enzyme cleavage site is shown in red color. 121

Figure 5.10. HPLC trace of (a) Gd-TA and (b) P1 after dialysis. HPLC gradient: 20%-100% ACN over 30 min. Copyright 2015 Royal Society of Chemistry. 122

Figure 5.11. (a): MALDI-TOF mass spectrum, and (b) SEC trace of P1. Copyright 2015 Royal Society of Chemistry. 122

Figure 5.12 ^{1}H NMR spectra of (a) P0 and (b) 1 in DMF-d7. Copyright 2015 Royal Society of Chemistry. 123

Figure 5.13 General synthetic scheme of copolymer P2 using ROMP initiator “Ru”, and Gd-TA. For P2, m = 5, n = 10. The structure post enzyme treatment is drawn to represent an ideal 100% peptide cleavage. Enzyme cleavage site is shown in red color. Copyright 2015 Royal Society of Chemistry. 124

Figure 5.14. SEC trace of P2. Copyright 2015 Royal Society of Chemistry. 125

Figure 5.15. Thermolysin cleavage of 1 at position 1 (red color). Position 2 and 3 (blue color) are not the cleavage sites as Proline residues besides the cleavage sites block the thermolysin cleavage. After the cleavage, one carboxylic acid and amine group were released (pink color). Copyright 2015 Royal Society of Chemistry. 126

Figure 5.16. HPLC trace of (a) 1; (b) 1 treated with denatured thermolysin at 55 °C for 1 h; (c) 1 treated with thermolysin at 55 °C for 1 h. HPLC gradient: 20%-60% ACN over 30mins. Copyright 2015 Royal Society of Chemistry. 126

Figure 5.17. ESI-MS of (a) 1 treated with thermolysin for 1 h, and (b) 1 treated with denatured thermolysin for 1 h. Copyright 2015 Royal Society of Chemistry. 127

Fig. 5.18. (a) LCST behavior of P1 measured by UV-Vis spectroscopy at 550 nm; (b) TEM image of cylindrical structure formed by P1 (0.6mg/ml) at 40°C. (c) LCST behavior of P1 treated with thermolysin at 55 °C for 1 h. (d) LCST behavior of P1 treated with denatured thermolysin at 55 °C for 1 h. Copyright 2015 Royal Society of Chemistry. 128

Figure 5.19. LCST versus concentrations of P1 in PBS at pH = 6. LCST was taken as the midpoint on the UV-Vis spectrum. Copyright 2015 Royal Society of Chemistry. 129

Figure 5.20. HPLC trace of (a) P1, (b) P1 with denatured enzyme at 55 °C for 1 h, (c) P1 treated with thermolysin at 55 °C for 1h. HPLC gradient: 20%-100% ACN over 30 min. Copyright 2015 Royal Society of Chemistry. 130

Figure 5.21. Digital photographs showing the cloudy solution become clear after enzyme treatment. Copyright 2015 Royal Society of Chemistry. 130

Figure 5.22. (a) UV-Vis spectroscopy of the enzyme-driven disassembly process at 550 nm and (b) Scattering intensity of the polymers during the enzyme-driven disassembly process as measured by DLS. All solutions were pre-heat to 55 °C and equilibrant for 5 min before starting. P1 (black), P1 with an enzyme (red) and P1 with a denatured enzyme (blue).. 131

Figure 5.23. TEM image of the cylindrical structure formed by P1 with denatured enzyme above the LCST. Copyright 2015 Royal Society of Chemistry. 132

Figure 5.24. TEM images of P2 micelles (a) at room temperature, (b) at 55 °C for 6 h, and (c) with enzyme at 55 °C for 6 h. (d) DLS data of P2 micelles: at room temperature (black curve), at 55 °C for 6 h (red curve), with enzyme at 55 °C for 6 h (blue curve). Copyright 2015 Royal Society of Chemistry.... 134

Figure 5.25. LCST behavior of P2 micelle solution (0.6 mg/mL) at 550 nm. Copyright 2015 Royal Society of Chemistry. 135

Figure 5.26. TEM image of P2 micelles treated with denatured enzyme. Copyright 2015 Royal Society of Chemistry. 135

Figure 5.27. TEM image of P2 micelles treated at 55°C for 6 h followed by cooling at room temperature for 3days. Copyright 2015 Royal Society of Chemistry. 136

Figure 5.28. Zeta potential of P2-1: P2 micelle at r.t., P2-2: P2 micelle at 55 °C, E2-1: Enzyme treated P2 micelle at rt, E2-2: Enzyme treated P1 at 55 °C, C2-1: Denatured enzyme treated P2 micelle at rt, C2-2: Denatured enzyme treated P2 micelle above 55 °C. Copyright 2015 Royal Society of Chemistry. 136

Figure 5.29. Relaxivity of P1 and P2 micelles: (a) P1: untreated P1, E1: enzyme treated P1, C1: denatured enzyme treated P1. (b) P2: untreated P2 micelle, E2: enzyme treated P2 micelle, C2: denatured enzyme treated P2 micelle. Copyright 2015 Royal Society of Chemistry. 137

LIST OF TABLES

Table 1.1. Spectral data for metal–catecholate.......... 17

Table 2.1. Reactants and their formulations for the preparation of SMNP-*i* (*i* = 2, 3, 4, 5).......... 36

Table 2.2. Physical parameters of SMNP-i (i=0-5).......... 36

Table 2.3. r_1 result for each sample shown in Figure 2.10.......... 45

Table 3.1. Reactants and their formulations for the particle preparation via pre-doping strategy. 64

Table 3.2. Reactants and their formulations for the dopamine concentration dependent experiments.......... 68

Table 3.3. Reactants and their formulations for the pH dependent experiments.......... 70

Table 3.4. Physical parameters of metal-loaded synthetic melanin nanoparticles.......... 73

Table 3.5. Diameter and zeta potential of metal-loaded synthetic melanin nanoparticle.......... 73

Table 3.6. Reactants and their formulations for the preparation of metal-loaded synthetic nanoparticle.......... 78

Table 3.7. MR relaxivity results for Mn(III)-loaded synthetic melanin nanoparticles.......... 83

Table 4.1. Metal loading of Mn(III) and Gd(III)-loaded synthetic melanin nanoparticles. 94

Table 4.2. Selected relaxation parameters obtained from the analysis of NMRD profiles (298 K).$^{a)}$.......... 99

Table 4.3. r_1 and r_2 values at 1.4T (60 MHz). 100

Table 4.4. r_1 result for each sample shown in Figure 4.9.......... 103

ACKNOWLEDGEMENTS

I'd like to thank my advisor Professor Nathan C. Gianneschi for his guidance and support over the past five years for my research work. He gave me so much freedom to choose my research topics and suggestions on problems as well as support for collaborations. I would like to thank all my committees, Prof. Michael Burkart, Prof. Michael J. Sailor, Prof. Kamil Godula and Prof. Karen Christman for their support and suggestions on my research and dissertation. I also appreciate all my colleagues in the lab, especially Dr. Mathew Thompson and Dr. Yiwen Li for helping me with everything through life to science. In addition, I want to thank all my collaborators: Yijun Xie, Prof. Jeffrey Rinehart's lab, Jeanne Lemaster from Prof. Jesse Jokerst's lab, Fabio Carniato from Prof Mauro Botta's lab. Dr. Ming Xiao and Weiyao Li from Ali Dhinojwala's lab.

I also want to thank my father and mother for their understanding and support for chasing my dream. They are always there when I need them, though they never said it out loud how much they love you, they are like a shelter when the storm is coming. I also want to thank my wife Fang Zhou especially. Though people always say that "It is very likely that love at a distance will end up with failure", We have gone through all of the grieves at separation and joys in the union in the past ten years and this can't be made without her greatness.

Chapter 2 is adapted in full print from Yiwen Li,[a] Yijun Xie,[a] Zhao Wang,[a] Nanzhi Zang, Fabio Carniato, Yuran Huang, Christopher M. Andolina, Lucas R. Parent, Treffly B. Ditri, Eric D. Walter, Mauro Botta, Jeffrey D. Rinehart,* Nathan C. Gianneschi,* "Structure and Function of Iron-Loaded Synthetic Melanin" ACS Nano, 2016, 10, 10186-10194.; Copyright 2016 American Chemical Society. The dissertation author is the co-first author of this chapter. For the Chapter 2, I would like to thank Dr. Yiwen Li for initiate this project. I also appreciate my colleague Yuran Huang, Nanzhi Zang, Dr. Lucas R. Parent and Dr. Treffly B. Ditri to provide help of synthesis and characterization of nanoparticles used in this project. Thanks to our collaborators, Fabio Carniato, Christopher M. Andolina, Eric D. Walter and Dr. Mauro Botta for providing their contributions to the characterization of our nanoparticles. Moreover, I appreciate the help from Yijun Xie and Prof. Jeffrey D. Rinehart about the discussion and analysis of magnetic properties of our nanoparticles and Prof. Nathan Gianneschi for the design and guidance of the entire project.

Chapter 3 is adapted in full print from Zhao Wang,[a] Yijun Xie,[a] Yiwen Li, Huang Y., Lucas R Parent, Treffly B. Ditri, Nanzhi Zang., Jeffery D. Rinehart,* and Nathan C. Gianneschi,* Tunable, Metal-Loaded Polydopamine Nanoparticles Analyzed by Magnetometry, Chemistry of Materials 2017, 29, 8195-8201. Copyright 2017 American Chemical Society. The dissertation author is the first author of this paper. For Chapter 3, I would like to thank our collaborators Yijun Xie and Prof. Jeffrey D. Rinehart for analysis of magnetic properties of the nanoparticles. I appreciate my colleague Dr. Lucas R Parent and Yuran Huang for helping to character the nanoparticles. I also thank the helpful discussion from Dr. Treffly B. Ditri Dr. Yiwen Li and Nanzhi Zang.

Chapter 4 is adapted in full print from Zhao Wang, Fabio Carniato, Yijun Xie, Yuran Huang, Yiwen Li, Sha He, Nanzhi Zang., Jeffery D. Rinehart,* Mauro Botta,* and Nathan C. Gianneschi,* High Relaxivity Gadolinium-Polydopamine Nanoparticles, Small 2017, DOI: 10.1002/smll.201701830. Copyright 2017 Wiley-VCH. The dissertation author is the first author of this paper. For Chapter 4, I would like to thank our collaborators: Fabio Carniato, Prof. Mauro Botta, Yijun Xie, Prof. Jeffery D. Rinehart. I also appreciate the help from my colleague Yuran Huang, Yiwen Li and Nanzhi Zang. In addition, I want to thank Dr. Sha He for support with the measurement of relaxivities.

Chapter 5 is adapted in full print from Zhao Wang, [a] Yiwen Li, [a] Yuran Huang, Matthew P. Thompson, Clare L. M. LeGuyader, Swaget Sahu, Nathan Gianneschi, “Enzyme-regulated Topology of a Cyclic Peptide Brush Polymer for Tuning Assembly” Chemical Communications, 2015, 51, 17108-17111. Copyright 2015 Royal Society of Chemistry. The dissertation author is the first author of this paper. For Chapter 5, I would like to thank Dr. Yiwen Li and Prof. Nathan C. Gianneschi for designing this project. I also appreciate Yuran Huang and Dr. Matthew P. Thompson for helping with synthesis and characterization of the materials. Dr. Clare L. M. LeGuyader and Dr. Swaget Sahu give valuable suggestions and discussion.

VITA

2011 Bachelor of Science, East China University of Science and Technology, Shanghai, China

2013 Master of Science, University of Akron, Akron, USA

2018 Doctor of Philosophy, University of California, San Diego, USA

PUBLICATIONS

Zhao Wang, Fabio Carniato, Yijun Xie, Yuran Huang, Yiwen Li, Sha He, Nanzhi Zang., Jeffery D. Rinehart,* Mauro Botta,* and Nathan C. Gianneschi,* High Relaxivity Gadolinium-Polydopamine Nanoparticles, Small 2017, DOI: 10.1002/smll.201701830.

Zhao Wang, [a] Yijun Xie, [a] Yiwen Li, Huang Y., Lucas R Parent, Treffly B. Ditri, Nanzhi Zang., Jeffery D. Rinehart,* and Nathan C. Gianneschi,* Tunable, Metal-Loaded Polydopamine Nanoparticles Analyzed by Magnetometry, Chemistry of Materials 2017, 29, 8195-8201.

Ming Xiao, [a] Ziying Hu, [a] **Zhao Wang**, Yiwen Li, Alejandro Diaz Tormo, Nicolas Le Thomas, Boxiang Wang, Nathan C. Gianneschi,* Matthew D. Shawkey,* and Ali Dhinojwala,* Bioinspired bright noniridescent photonic melanin supraballs, Science Advance 2017, 3, e1701151.

Yuran Huang, Alexander M. Vezeridis, James Wang, **Zhao Wang**, Matthew P. Thompson, Robert F. Mattrey, Nathan C. Gianneschi,* "Polymer-Stabilized Perfluorobutane Nanodroplets for Ultrasound Imaging Agents" Journal of the American Chemical Society, 2016, 166, 2049-2054.

Yiwen Li,[a] Yuran Huang,[a] **Zhao Wang**, Fabio Carniato, Yijun Xie, Joseph P. Patterson, Matthew P. Thompson, Christopher M. Andolina, Treffly B. Ditri, Jill E. Millstone, Joshua S. Figueroa, Jefferey D. Rinehart, Miriam Scadeng, Mauro Botta, Nathan C. Gianneschi,* "Polycatechol Nanoparticle MRI Contrast Agents" Small, 2016, 12, 668-677.

Yiwen Li,[a] Yijun Xie,[a] **Zhao Wang**,[a] Nanzhi Zang, Fabio Carniato, Yuran Huang, Christopher M. Andolina, Lucas R. Parent, Treffly B. Ditri, Eric D. Walter, Mauro Botta, Jeffrey D. Rinehart,* Nathan C. Gianneschi,* "Structure and Function of Iron-Loaded Synthetic Melanin" ACS Nano, 2016, 10, 10186-10194.

Ming Xiao, [a] Yiwen Li, [a] Jiuzhou Zhao, **Zhao Wang**, Min Gao, Nathan C. Gianneschi,* Ali Dhinojwala,* and Matthew D. Shawkey,* Stimuli-Responsive Structurally Colored Films from Bioinspired Synthetic Melanin Nanoparticles, *Chemistry of Materials* 2016, 28, 5516-5521.

Zhao Wang, [a] Yiwen Li, [a] Yuran Huang, Matthew P. Thompson, Clare L. M. LeGuyader, Swaget Sahu, Nathan Gianneschi, titled "Enzyme-regulated Topology of a Cyclic Peptide Brush Polymer for Tuning Assembly" Chemical Communications, 2015, 51, 17108-17111.

[a] co-first author

ABSTRACT OF THE DISSERTATION

Artificial Melanin: From Synthesis to Chemical Properties and Applications

by

Zhao Wang

Doctor of Philosophy in Chemsitry

University of California, San Diego, 2018

Professor Nathan C. Gianneschi, Chair

Professor Michael Burkart, Co-Chair

Melanins are a class of naturally occurring pigments found throughout nature. They have gained great attention because it has a unique combination of properties functions from metal ion chelation, photoprotection, free radical quenching, and coloration. We apply the synthetic chemistry combined with our increasing understanding of the natural systems to target, control, combine, and enhance the functionality of natural melanin, far beyond their natural capabilities. We term these nanostructures “Artificial Melanin”. Polydopamine (PDA), one type of synthetic melanin, reproduces essential properties of natural melanin. For example, PDA displays a keen ability to chelate various metal ions, making it a promising material for a wide range of applications, including in bioimaging, surface modification, electrocatalysis, batteries, and biosensing. We demonstrate that the introduction of metal to PDA can allow us to understand the effect of the spin centers towards the magnetic relaxation properties of a surrounding medium. These findings offer a guide to design more efficient contrast agents.

For Chapter 2, we employ a synthetic method for drastically increasing and controlling the iron loading of artificial melanin particles to perform a quantitative investigation on the structure-property relationship by using a family of Fe(III)-chelated polydopamine nanoparticles doped with a tunable concentration of Fe(III) ions. A comprehensive analysis by magnetometry, electron paramagnetic resonance (EPR), and nuclear magnetic resonance dispersion (NMRD) demonstrates that the population of isolated Fe(III) centers dictates the degree of MRI contrast. These analyses allow prediction of the optimal Fe(III) loading via a quantitative modeling of antiferromagnetic coupling. These conclusions not only offer an intuitive understanding of the atomic origins of MRI contrast in complex polycatechol nanoparticles but also suggest future directions for the development of new enhanced MRI contrast agents.

For Chapter 3, we synthesize metal-loaded polydopamine nanoparticles via autoxidation polymerization of dopamine in the presence of metal-dopamine complexes. Various metal ions including Mn(III), Fe(III), Co(II), Ni(II), Cu(II), Zn(II), and Ga(III) ions could be incorporated into these artificial melanin nanoparticles with this strategy. We perform analysis on the doping range and parameters that affect the particles' morphology. An investigation by magnetometry reveals general electronic structure and interactions for artificial melanin nanoparticles doped with Mn(III), Ni(II) and Co(II) ions. In addition, we compare the magnetic properties of high Mn(III)-loaded nanoparticles with Fe(III)-loaded nanoparticles to assess their potential as MRI contrast agents.

For Chapter 4, we report the preparation artificial melanin nanoparticles with tunable Gadolinium loadings. These nanoparticles are analyzed by NMRD and with a 7 T magnetic resonance imaging (MRI) scanner. We observed a relaxivity of 75 mM^{-1} s^{-1} and 10.3 mM^{-1} s^{-1} at 1.4 T and 7 T, respectively. Furthermore, we examined intraparticle magnetic interactions using Superconducting Quantum Interference Device (SQUID) magnetometry and determine these nanoparticles consist of isolated Gd ions even at the maximum metal loadings. This study shows the potential of this scaffold as a basis for developing T_1- weighted, high relaxivity MRI contrast agents.

For Chapter 5, we report the preparation of norborenyl cyclic elastin-like polypeptides based homopolymers and amphiphilic block copolymers via ring opening metathesis polymerization. The resulting materials contain side chains that can undergo conformational and topological changes upon heating and treatment with a proteolytic enzyme. This work demonstrates that by incorporating a cyclic form of a peptide into a polymer as a functional sidechain, one can access a new mode of action regarding the enzymatic stimulus.

Chapter 1

Introduction and History

1.1 Introduction

Chapter one is intended to provide insight into the biosynthetic pathway of natural melanin and synthetic method to prepare artificial melanin as well as strategies to introduce metal ions to the melanin nanoparticles. Magnetometry analysis is also discussed to reveal the electronic structure and interactions of the metal loaded nanoparticles. Also, the history and development of magnetic resonance imaging (MRI) are covered. These research not only reveals the fundamentals of melanin chemistry but also suggest future directions for the development of new enhanced MRI contrast agents.

1.2 Synthesis of Melanin

1.2.1 Structure and Biosynthesis of Melanin

Natural melanin has three forms, eumelanin, pheomelanin, and neuromelanin. Eumelanin is a brown to black chemically inert and poorly-soluble pigment polymer that is derived from tyrosine; pheomelanin is a cysteine-containing reddish polymer, and neuromelanin is found in the brain.[1] The regulation of these melanin pigments in mammals is central to skin, neural and oncogenic pigmentation pathways.[2-3] In skin, melanin production serves in part as a natural shield to protect against DNA damage from UV radiation.[4]

The biosynthesis of eumelanin has been studied for more than 100 years. In the 1920's, the Mason-Raper pathway was reported, which describe the chemical reactions starting from tyrosine to dihydroxyphenylalanine (dopa), then to dopaquinone, catalyzed by enzyme tyrosinase.[5] Raper was able to isolate two indoles derivatives: 5,6-dihydroxyindole (DHI) and 5,6-dihydroxyindole-2-carboxylic acid (DHICA); which are now accepted as the building blocks of eumelanin. In the late 1940's, a polymerization model was proposed by Mason. 6 He believed that the indole-5,6-quinone could undergo self-coupling to form a polymer. Though tons of work has been done afterward, the details of eumelanin structure and its associated biosynthesis remain elusive.

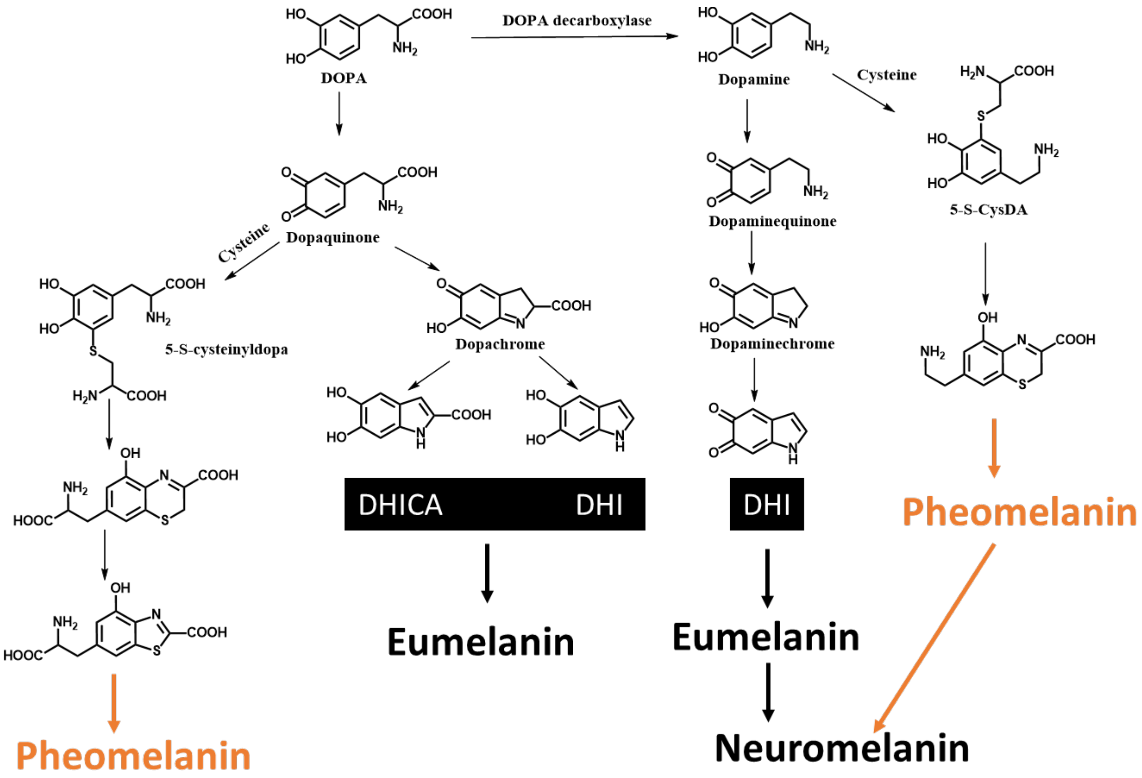

Figure 1.1. Biosynthetic pathways leading to eumelanin and pheomelanin production**.**

Most of the present work relies on the analysis and identification of chemical degradation products of the melanin, which in turn can be related to the existence of specific chemical component present in the original sample. For example, pyrrole 2-3-5-tricarboxylic acid (PTCA) was identified as one of the major fragment from the degradation of Sepia melanin. Nicolaus proposed the model for the biosynthetic pathway of pheomelanin in the late 1960s. 5-S-cysteinyldopa, produced by the reaction of cysteine with the quinones, was identified as the precursor for the pheomelanin synthesis.[7] Till now, the best approaches available for analysis molecular information of eumelanin and pheomelanin are summarized by ITO et al.[8] The method involves degradation of melanin samples, followed by HPLC analysis of the formation of marker molecules. Pyrrole-2,3,5-tricarboxylic acid (PTCA) is the oxidative degradation product of eumelanin and aminohydroxyphenylalanine (AHP) is the acid hydrolysis product of pheomelanin. In a more recent paper, the same group develops a similar method to identify the DHICA and DHI unit in the melanin. They find that the DHICA-rich polymer has higher yields of PTCA compared with DHI polymer. Meanwhile, DHI-polymer yields pyrrole-2,3-dicarboxylic acid (PDCA) after H_2O_2 oxidation, which can be used as the indicator of DHI unit.[9]

Neuromelanin is dark pigment made of a mixture of eumelanin and pheomelanin. Figure 1.2 shows the casting model of neuromelanin consisting of a pheomelanin core covered by a eumelanin shell. In 2006, Simon and co-authors used photoelectron emission microscopy integrated with a free electron laser as the light source to measure the ionization threshold of the human neuromelanin's surface isolated from the substantia nigra region of human brain. This surface technique can only penetrate several nanometers into the nanoparticles, which allows the detection of only surface oxidation potential. Human hair melanosome is used as a standard to measure the threshold potentials of eumelanin (-0.2 ± 0.2 V) and pheomelanin (-0.5 ± 0.2 V). Therefore, the composition of eumelanin and pheomelanin can be distinguished in neuromelanin samples.[10]

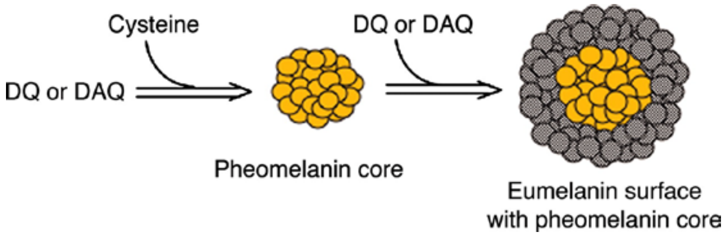

Figure 1.2. Casing model of mixed melanogenesis. In the process of mixed melanogenesis, pheomelanic pigment is produced first, followed by deposit of eumelanic pigment. In the granule with the eumelanin surface, the side is intentionally cut away to reveal the inner pheomelanin core. Copyright 2006 National Academy of Sciences of the United States of America.[11]

1.2.2 Base-Catalyzed Oxidative Self-Polymerization Of Dopamine

Polydopamine is the most widely used artificial melanin material. They can be synthesized to mimic the eumelanin from Sepia officinalis. The synthesis of polydopamine nanoparticles not only provide a model to investigate the chemistry and structure of its natural counterpart,[12-15] but also reproduce the functions of eumelanin.[16-18] In another valuable aspect, the enriched surface functional group (catechol, amine, and imine) can serve as the reactive site for further chemical modification and anchor for metal ions, allowing its broad application from substrate modification to biomedical imaging.[19-23]

The self-oxidation polymerization in Tris(hydroxymethyl)aminomethane (Tris) buffer solution is the most widely used synthetic strategy. This method originates from a work published in Science in 2007. In that paper, a universe multifunctional coating method for various substrates including metal oxides, noble metals, polymers, and ceramics is described via using dopamine as a building block.[24] This solution oxidation method takes advantage of the fact that dopamine can be oxidized and spontaneously self-polymerize under alkaline tris buffer solution, with O_2 as the oxidant. This technique is so easy that no complicated setup and instruments are needed. However, a recent study reveals that Tris can participate in the polydopamine formation via nucleophilic addition to the dopamine quinone (Figure 1.3).[25] Apparently, the incorporation of tris into the polydopamine is irreversible. Therefore, the final polydopamine structure is even more complicated and this covalent adducts can affect the properties as a mimic of natural eumelanin.

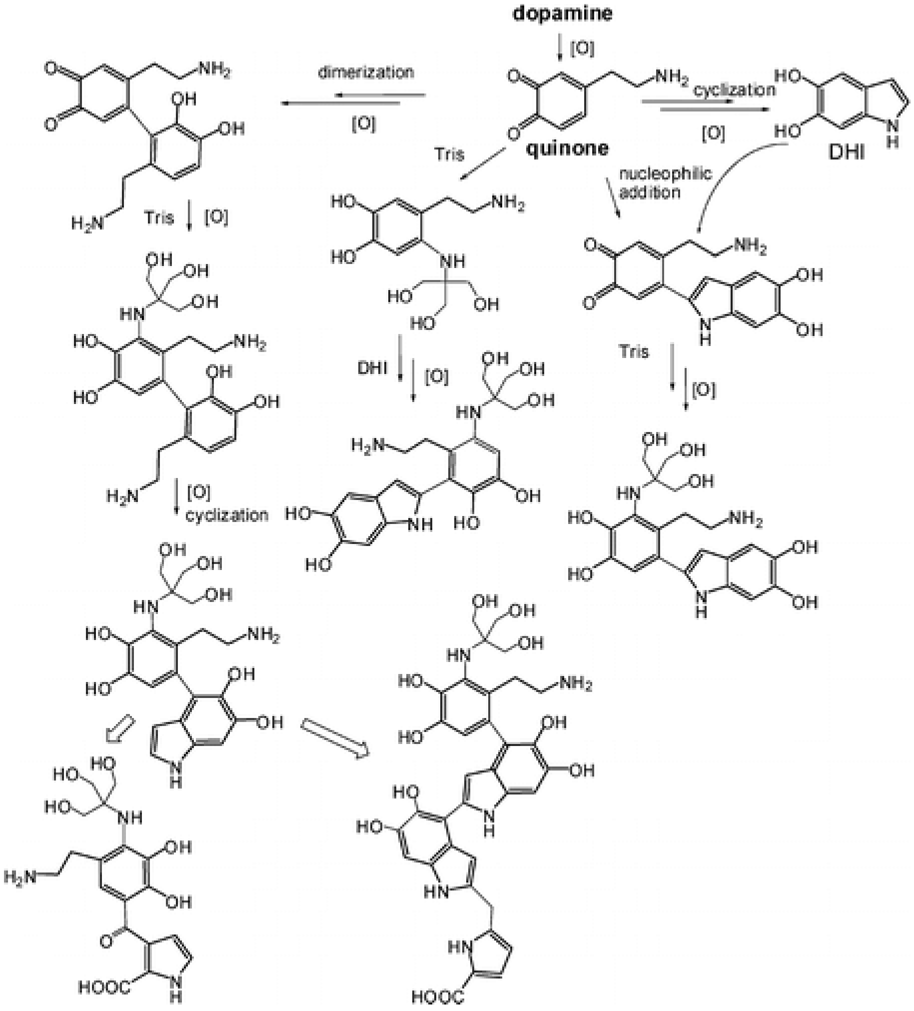

Figure 1.3. Scheme illustrating the possible effect of Tris as a covalent modifier of dopamine and polydopamine structural components. Copyright 2014 American Chemical Society.[25]

In another example, the polydopamine nanoparticles have been prepared in a water-alcohol solvent system. Ammonia solution is used to give alkaline environment while ethanol is employed to control the polymerization process of dopamine.[26] This method avoids the potential problem that Tris can bring into the system. A later paper performs a comprehensive study on the alcohol effect toward the synthesis of the polydopamine nanoparticles.[27] Figure 1.4 shows that the size and morphology of polydopamine nanoparticle are strongly dependent on the volume fraction of ethanol in water. As shown in Figure 1.4, the monodispersed spherical nanoparticles are obtained with the volume fractions of ethanol from 25% to 35%. Smaller volume fractions of ethanol (0-

20%) result in a more dispersity in size distribution (Figure 1.4a and b). It is difficult to obtain special shape nanoparticle at very high volume fractions of ethanol (above 70%). It is also worthwhile to mention that Lee and co-authors report the first successful example of preparing melanin-like polydopamine nanoparticles with controllable size.[28] They use NaOH solution to oxidize dopamine monomers. The resulting nanoparticles have a good dispersibility in water and biological media compared with the ones using the enzymatic reaction of tyrosine. In addition, they demonstrate that, under the N_2 protection, the polymerization of dopamine is stopped in the presence of NaOH. This experiment suggests that oxygen is a necessary component for the self-oxidation polymerization of dopamine.

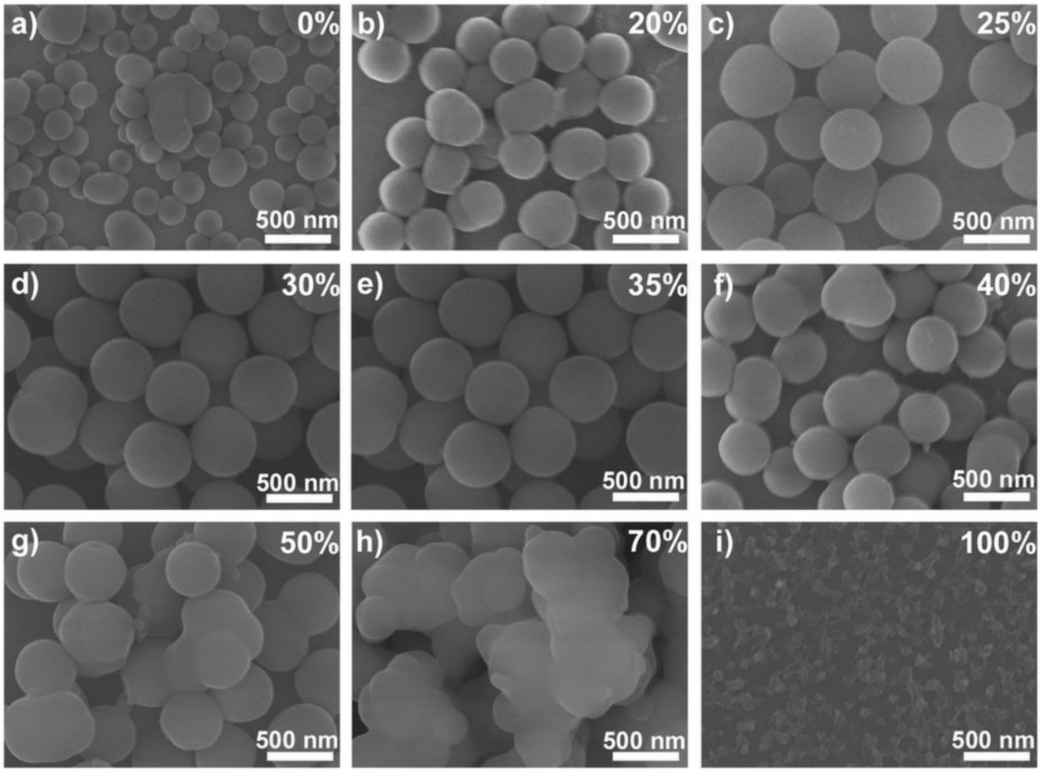

Figure 1.4. SEM images of PDA obtained in various ethanol/water mixtures. The volume fractions of ethanol are (a) 0%, (b) 20%, (c) 25, (d) 30%, (e) 35%, (f) 40%, (g) 50%, (h) 70%, and (i) 100%, respectively. The scale bars are 500 nm. Copyright 2014 Springer Nature.[27]

In general, the alkaline condition is a necessary condition for the synthesis of polydopamine since dopamine is unable to oxidize in acidic solution. However, the presence of metal ions, such as Fe(III), Cu(II) or VO(II) can initiate the dopamine reaction in weak acid environment.[29] Jin and co-authors report that synthesis of polydopamine via oxidative self-polymerization of dopamine in a strongly acidic condition (pH =1) through the hydrothermal process.[30] Figure 1.5c shows the microspheres polydopamine (about 700nm in diameter) can be obtained in weak acid condition. In contrast, the strong acid condition yields polydopamine with the morphology of aggregated of nanoparticles (Figure 1.5a and b). The authors claim that the formation of polydopamine is attributed to high pressure and temperature that gives a more pronounced auto-ionization of water.

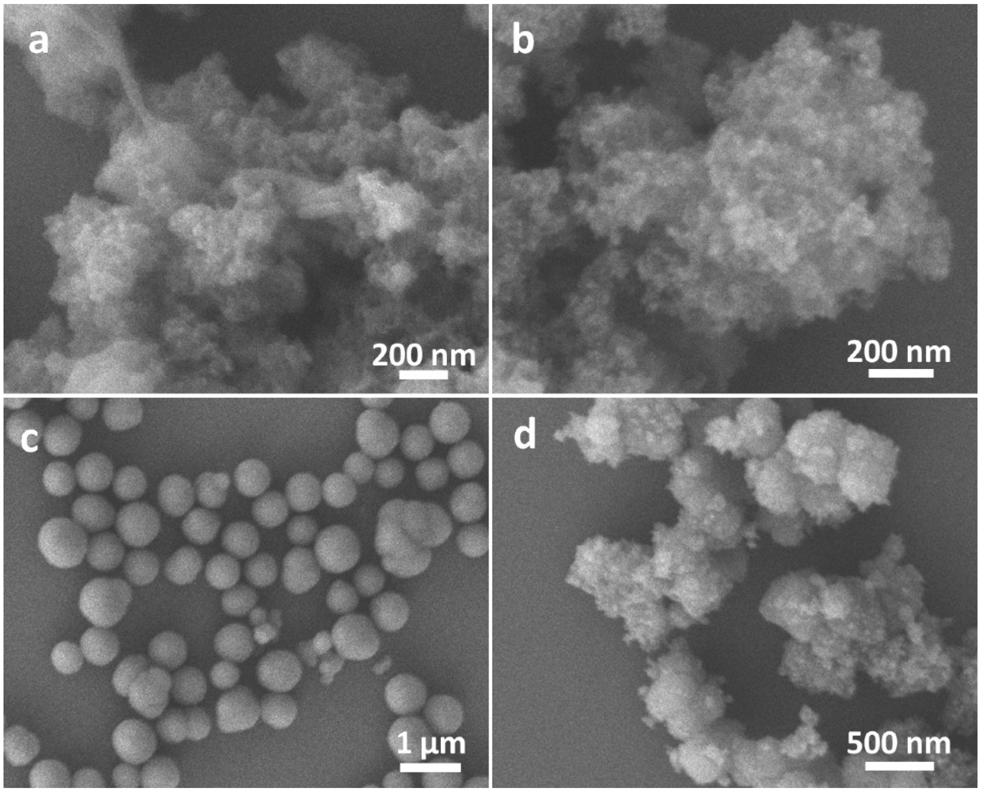

Figure 1.5. SEM images of polydopamine in various experimental conditions: (a) pH 1, 160 °C, and 0.5 mg/mL, (b) pH 1, 160 °C, and 4.5 mg/mL, (c) pH 5, 120 °C, and 0.5 mg/mL, and (d) pH 5, 160 °C, and 0.5 mg/mL. Copyright 2015 American Chemical Society.[30]

1.2.3 Other Methods of Synthesis of Artifical Melanins

Until now, the most popular strategy to prepare synthetic melanin is through the oxidative polymerization of dopamine under alkaline conditions as mentioned in the above section. Besides this approach, several examples of using an enzyme,[31] strong oxidants, an electrochemical method,[32-33] and plasma have been proposed. It is noted that these strategies generate nanoaggregates or deposition into films. The uniform spherical shape nanoparticle is hard to achieve via these methods.

In cell, eumelanin is synthesized via oxidation of L-tyrosine by tyrosinase to form 3-(3,4-dihydroxyphenyl)-L-alanine (L-DOPA), followed by further reaction of L-DOPA to form eumelanin. Inspired by this natural biosynthetic pathway, in vitro incubation of L-DOPA with tyrosinase has been employed to prepare the Poly(L-DOPA) materials. Xie and co-authors report that the Poly(L-DOPA) can be used to immobilize enzymes. This Poly(L-DOPA) -based enzyme electrode shows excellent biosensing performance.[31]

In general, oxidization of dopamine to dopamine-quinone is considered to be the critical step in the polydopamine synthesis. This step is a redox reaction that can be easily achieved by an electrochemical method. The advantage of the electrochemical method that can precise control over the redox reactions, researchers report the electrochemical polymerization of dopamine without the addition of oxidants. The formation of electropolymerized polydopamine is characterized by cyclic voltammograms and electrochemical impedance spectroscopy. The results indicate a compact coating of polydopamine after electropolymerization. Also, they find that the coating thickness is much higher than the traditional one.[32]

The spatial and temporal control of the dopamine polymerization is tough due to the poor control of the initiation and termination of the polymerization. To solve this problem, Levkin and co-workers use UV irradiation to generate reactive oxygen species that can initiate dopamine polymerization under various pH condition.[34] Figure 1.6 shows that the UV-induced dopamine polymerization is compatible with photopatterning. Since catechols can react with thiols via Michael addition or Schiff base reactions,[24] immersion of polydopamine pattern surfaces into a thiol-containing solution provided a convenient route to organic ad-layer deposition through thiol- and amine-catechol adduct formation A fluorescence image of Rhodamine is shown by immersing the pattern with the Rhodamine-SH solution for 24 h (Figure 1.6d). It shows that only the positions where polydopamine are located have a red color.

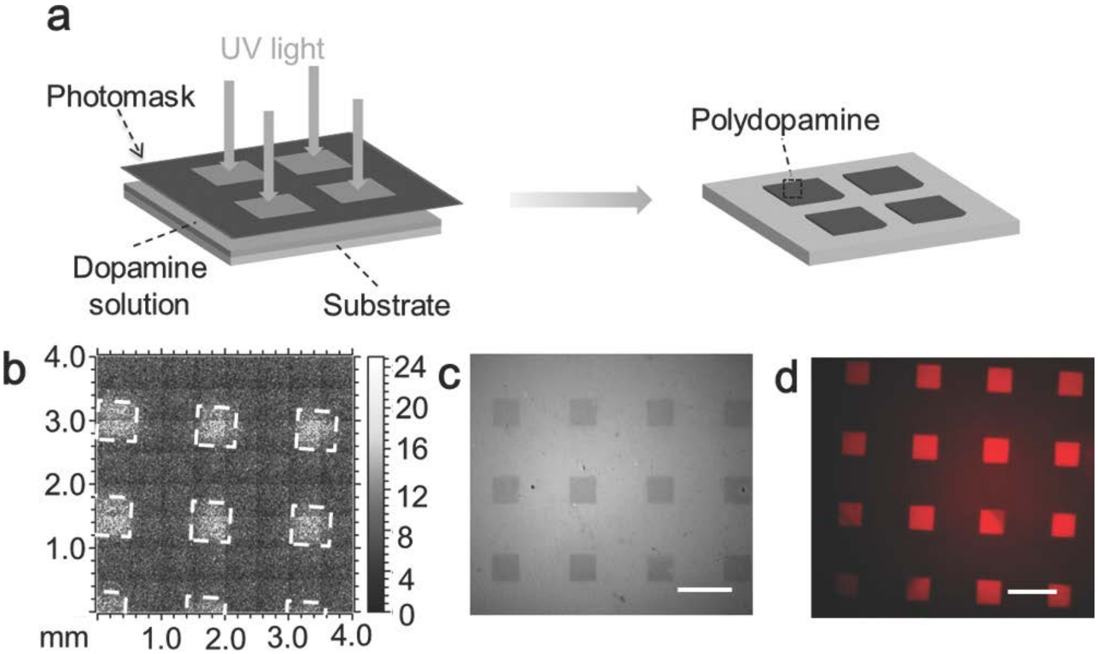

Figure 1.6. Photopatterning of polydopamine. a) Schematic representation of the polydopamine UV patterning. b) ToF-SIMS characterization of a pattern produced by photopatterning on a silicon wafer surface (CN− intensity map). c) Bright-field microscopy image of a silver nanoparticle pattern produced on a polydopamine patterned surface. d) Red fluorescence pattern formed by a treatment of the PD pattern with a Rhodamine-thiol solution. The scale bars are 1 mm. Copyright 2014 John Wiley & Sons, Inc.[34]

In another study, dopamine polymerization is reported to happen in plasma-activated water under acidic pH without the assistance of oxygen.[35] Similar to the idea of using UV-irradiation, nonthermal plasmas treatment of water can also generate reactive oxygen species. They find that polydopamine formed through this method possess same chemistry as those made by base-catalyzed solution method.

1.2.4 Characterize Chemistry and Structure of Melanin

The structure of eumelanin has long been a debate till today. The term eumelanin cannot be used to describe a single well-defined structure. The definition of eumelanin structure relies on the statistical description of main units and functional groups. This is primarily due to the amorphous feature of the material that can't obtain crystalline structures via x-ray diffraction techniques. In addition, eumelanin isn't a true polymer or macromolecule that have defined repeat units or structures, attributing to the hierarchy in multi-length scales: from monomer disorder to supramolecular disorder.[14]

Despite these difficulties in characterization the chemistry and structure of melanin, a recent study suggests that the polydopamine is a combination of a covalently crosslinked 5,6-dihydroxyindole (DHI) unit plus the noncovalent components including a physically assembled trimer of $(dopamine)_2/DHI$ (Figure 1.7).[36] In contrast, another study using solid-state NMR technique proposes the supramolecular aggregate of monomers, like DHI and its indole derivatives, is dominated by the polydopamine structures. By carbonization of polydopamine, a study of its structure provides a different point of view: they report a graphite-like nanostructure of carbonized polydopamine visualized by high-resolution transmission electron microscopy (TEM) (Figure 1.8).[37]

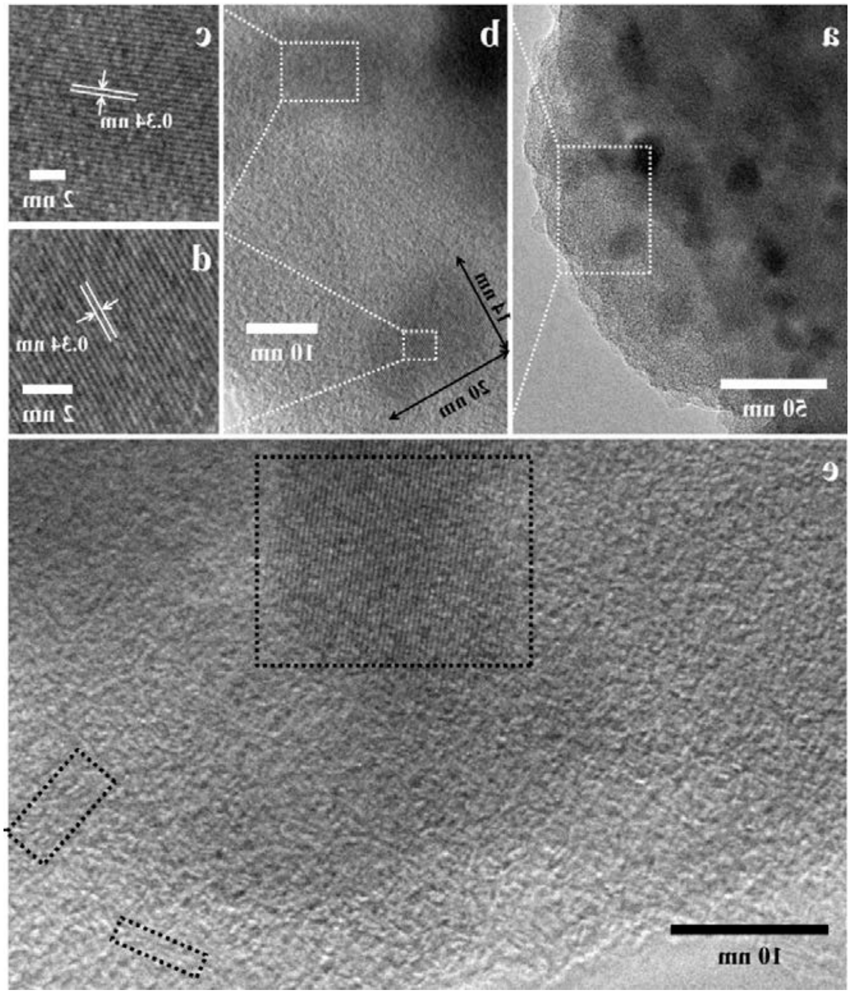

Figure 1.7. HRTEM images of carbonized PDA nanoparticles. (a) TEM image of carbonized PDA nanoparticles. There are some dark domains. (b) Magnified image of dark domains in (a), which shows well-organized graphite-like nanostructure. The size of one typical domain is about 14 × 20 nm2. (c, d) Distance between stacking layers can be obtained from enlarged images. (e) HRTEM image shows that there are some parts containing only two or three stacking layers, except large domains with 40–50 stacking layers. Copyright 2015 American Chemical Society.[37]

Spectroscopic methods, such as ^{1}H NMR, ^{13}C solid-state NMR, high-resolution mass spectra (HRMS), X-ray photoelectron spectroscopy (XPS) and IR spectroscopy has been employed to support the structural assignment of polydopamine. Beck et al. find the presence of C–C connections between the DHI monomers. In addition, the HR-MS shows the existence of mixtures of different oligomers in polydopamine. Fourier Transform Infrared (FTIR) is used to characterize the functional group on the polydopamine surface. For example, an FTIR study of the polydopamine film shows a feature peak at 1723 cm^{-1} that can be assigned to ν(C=O) groups, indicating the quinone group. Another two feature peaks at 1596 and 1510 cm^{-1} from the broad peak at 1580 cm^{-1} and are assigned to νring(C=C) and νring(C=N) stretching, respectively. These two peaks confirm the presence of aromatic amine species (DHI derivatives) in the polydopamine film.[38] XPS has been used to provide the elemental composition and functional group of polydopamine films. It can detect different elements, such as carbon, nitrogen, and oxygen, and their state information.[38]

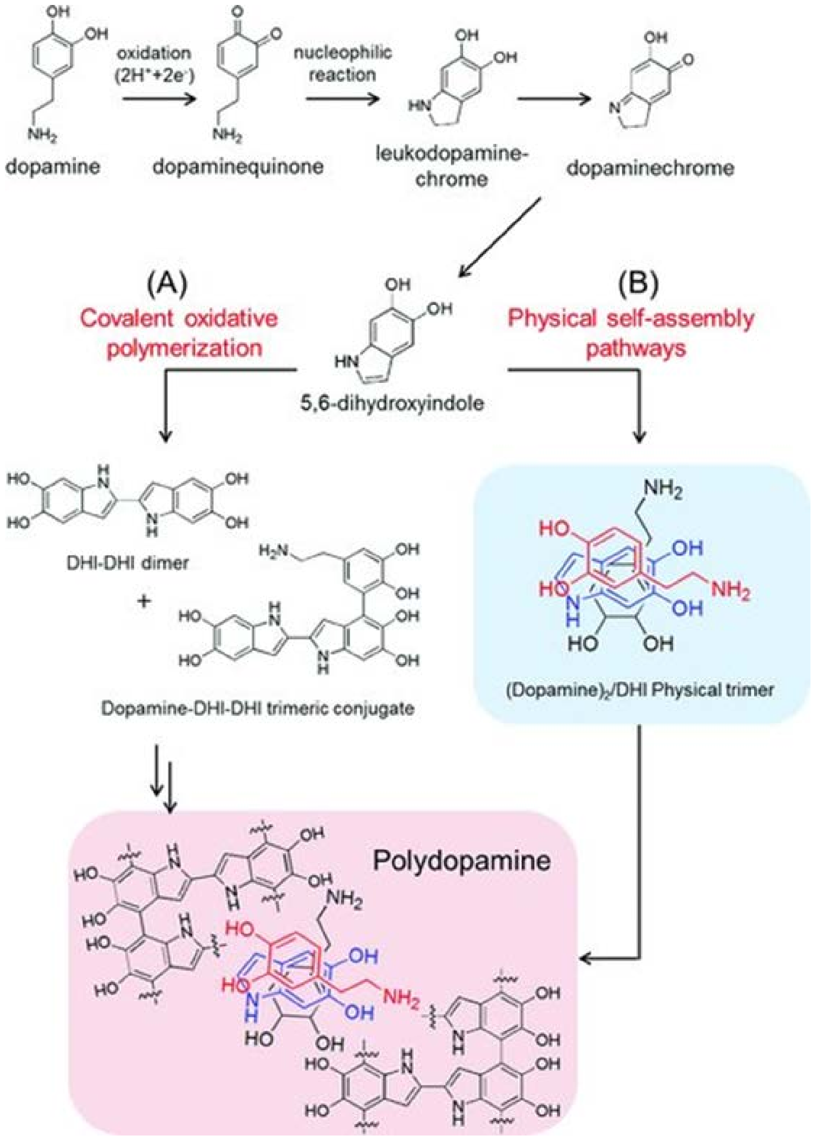

Figure 1.8. Polydopamine synthesis occurs via two pathways: A) a pathway of covalent bond-forming oxidative polymerization and B) a newly proposed pathway of physical self-assembly of dopamine and DHI. Copyright 2012 John Wiley & Sons, Inc.[36]

1.3 Metal Chelation in Melanins

1.3.1 Metal ions in Natural Melanin

Melanin pigment is known to bind metal ions. It is found that the melanosomes-containing tissues have a much higher level of metal ions, such as including Fe^{2+}, Fe^{3+}, Cu^{2+} and Zn^{2+}.[39-40] Since metal ions are highly involved in the biological process, the study of melanin in the regulation of metals has gained much attention.[41] In 1978, Larsson studied the melanin (from beef eyes and synthesized from L-DOPA with tyrosinase) affinity to various alkali and alkaline earth metals. In that paper, the authors attribute the metal ion binding of melanin is to the free carboxyl groups.[42] Later researchers on the eumelanin structures reveal that carboxyl, amine, hydroxyl, quinone and semiquinone groups can be the potential metal binding sites. Though alkali and alkaline earth metals binds mainly to the carboxylate group,[43] another work from the same research group (John D. Simon) demonstrate that Cu^{2+} binds to hydroxyl group and Fe^{3+} binds to amine or hydroxyl.[44]

The beauty of nature is that melanin-metal binding behavior highly depends on the specific metal. The analysis of tissue samples shows a high concentration of Ca^{2+} and Zn^{2+}, indicating the high binding capacity of these two metal ions. In contrast, the binding affinity of this two metal ions towards melanin isn't high.[45] This allows the accumulated Ca^{2+} and Zn^{2+} ions to release upon the stimulus. Fe^{2+} and Cu^{+} are toxic to a biological system, and melanin shows high affinity to iron and copper that helps to sequester these metals and protect cells from damage.[46] More toxic metal, such as Hg, Pb, Cr, and Mn, can also be sequestered via this pathway.

1.3.2 Preparation of Metal-Loaded Synthetic Melanins

Although the natural melanins have had extensive analysis for metal content, the metal coordination chemistry and the effect of metals ions are poorly understood. To explore new coordination chemistry and functionality of in melanins, synthetic melanin (polydopamine) loaded with designed metal ions has been prepared via both post-polymerization doping and pre-polymerization doping strategy. The post-polymerization doping strategy contains two steps: polydopamine nanoparticles are prepared and purified through a centrifuge. Then the excess amount of metal salts that are soluble and stable in water are added to the polydopamine nanoparticles solution for further complexation. Pre-polymerization doping strategy is a one-pot synthesis: the stoichiometric amount of metal salts are added to the dopamine solution before polymerization. The formation of the dopamine-metal complex can further polymerize to form nanoparticles.

Inspired by the phenomenon that malacotic melanomas are much brighter on T_1-weighted magnetic resonance (MR) images,[47] Gadolinium (Gd) ion is incubated with melanin (extract from tea). It is found that Gd–melanin complexes possess high relaxivity which can reduce the overall toxicity to the patient during MRI examination.[48] A more recent paper use the similar synthetic strategy- incubation of Iron (III) salt with polydopamine nanoparticle (Figure 1.8). Figure 1.8c shows a decrease in EPR signal after complexation with Fe^{3+}, due to magnetic dipolar interactions between free radicals of polydopamine and Fe^{3+}. The highest Fe loading achieved in this work is 0.72%.[49] It is speculated that the Fe^{3+}-polydopamine complexation occurs mostly on the surface of the nanoparticle. Therefore, the majority of the hydroxyl and amine groups remains unchelated. In another example, Mn^{2+}-chelated polydopamine nanoparticles are reported as contrast agents. These Mn^{2+}-chelated nanoparticles show very high relaxivity in high field. (6.55 mM^{-1} s^{-1} at 9.4 T).[50] Besides the above examples, Cu^{2+} can also be incorporated into polydopamine nanoparticles via the same strategy. Interestingly, they find that the molar extinction coefficient of polydopamine nanoparticles is enhanced by 4 times, thus providing better photothermal performance.[51]

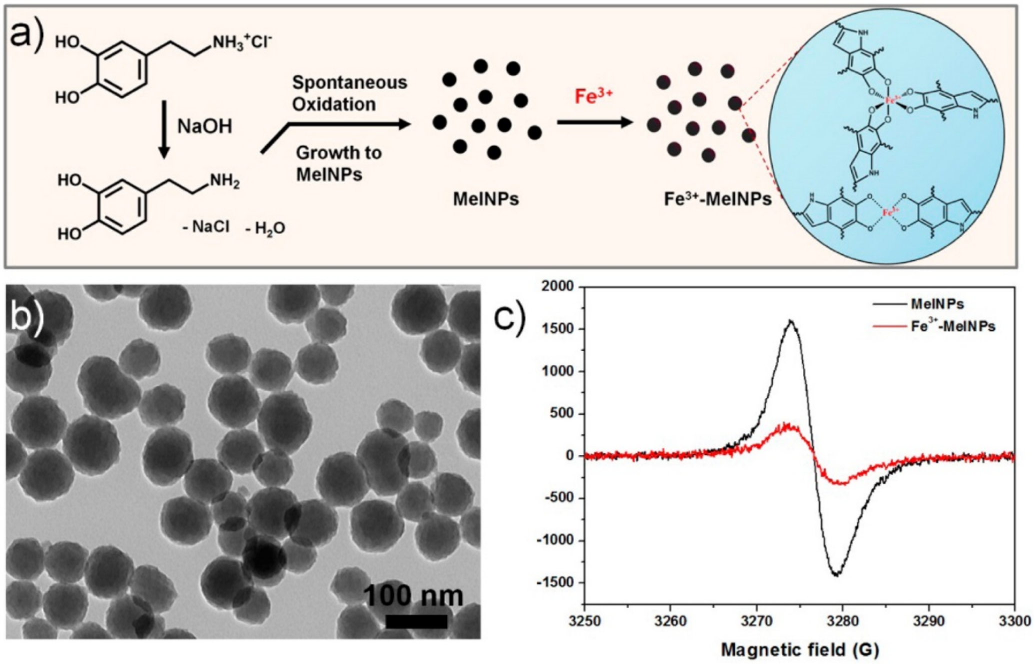

Figure 1.9. (a) Schematic illustration of the development of efficient T1-weighted MRI contrast agents using polydopamine nanoparticles. (b) TEM images of polydopamine nanoparticles and (c) EPR spectra of polydopamine nanoparticles before and after complexation with Fe3+ ions. Copyright 2013 American Chemical Society.[49]

As mentioned above, the post-polymerization doping strategy- incubation of metal salt with polydopamine nanoparticles- has been successfully applied to construct metal-loaded synthetic melanin nanoparticles. However, the precise control over the metal loading is still a problem by this method. Inspired by nature, Fe^{3+} found to involve in the formation of mussel adhesive plaques. Therefore, metal ions are designed to add during the dopamine polymerization. The pioneer work using this method is reported by Lee et al. During the dopamine polymerization medium, Ag^{+} ions are added into the reaction and then reduce to metallic silver, forming a silver-polydopamine hybrid coating.[52] Lu and co-authors study the role of Ni^{2+} in the polymerization of dopamine. They suggest that the Ni^{2+} can accelerate the polymerization of dopamine via monitoring the yield of solid product over time (Figure 1.9).[53] However, the authors claim that “The Ni^{2+} ions do not form complexes with dopamine itself in the solutions.” This is in contrast with ours and other results, showing several characteristic absorbance peaks of metal- catecholate.[22, 54] This is because the authors only measure the UV-vis spectrum below the wavelength of 400 nm. The same group explores the dopamine polymerization in the presence two metal ions: Fe^{2+} and Zn^{2+}. The resulting nanoparticles are carbonized for use as anodes in lithium-ion batteries due to their great electrochemical performances.[55]

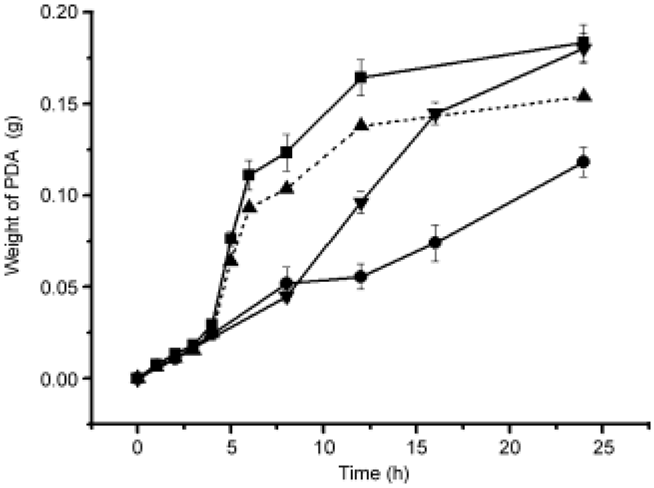

Figure 1.10. The weight of the solid product obtained in dopamine polymerization as a function of reaction time for the solutions with and without Ni2+ ions, shown by ▪ and • with solid lines, respectively. The feed molar ratio of DOPA to Ni2+ ions was 2:1. The □ dashed line shows the weight of neat polydopamine in the polydopamine/Ni2+ solid product as a function of reaction time, estimated based on the assumption that the molar ratio of polydopamine units to Ni2+ ions in the solid product is still 2:1. □ with a solid line shows the weight of the solid product as a function of reaction time when the Ni2+ ions were added in the solution after dopamine polymerization had proceeded for 8 h. Copyright 2014 John Wiley & Sons, Inc.[53]

1.3.3 Characterize Melanin Metal Chelation

Identification of characteristic UV-Vis absorbance signals associated with the metal–catechol complexes has been established. Table 1.1 shows a summary of studies on the UV–vis spectroscopy of metal–catecholate complexes, including Cu^{2+}, Co^{2+}, Zn^{2+}, Ni^{2+}, Cr^{2+}, Mn^{2+}, Fe^{3+}, Ti^{4+}, V^{3+}, V^{4+}, Cr^{3+}, and Mn^{3+}). Among them, divalent metal ions can form mono and bis complex with catechol, while higher valent ion can form mono, bis and tris complex with catechol.[54] Although this library is built based on the metal-catechol small molecules, it is useful in the characterization of the catechol-based polymer system, since the metal-catecholate complex in the polymer systems remains the similar behavior.[56]

Table 1.1. Spectral data for metal–catecholate.[54]

Metal	Species	Catechol $\lambda_{\max}$/nm (ε/M^{-1}cm^{-1})	Catechol literature $\lambda_{\max}$/nm (ε/M^{-1} cm^{-1})	
Ti^{4+}	Tris	378 (3300)	389 (9300); 385 (5600); 270 (12600), 375 (12300)	
V^{3+}	Mon	~425 (790), 467 (710)	–	
	Bis	402 (1600), ~635 (140)	–	
	Tris	361 (1900), ~600 (220), ~650 (220)	–	
VO^{2+}	Mon	553 (17), 736 (23)	550 (28), 750 (33)	
	Bis	605 (270), 645 (270)	540 (38), 656 (69)	
	Tris	582 (3200), 670 (3000)	552 (9200), 650 (8200, sh)	
Cr^{2+}	Mon	415 (35), 606 (38)	–	
	Bis	428 (40), ~560 (35)	–	
Cr^{3+}	Mon	~425 (57), 539 (36)	–	
	Tris	430 (110), 594 (94)	425 (100), 592 (78); 429 (209), 599 (166)	
Mn^{2+}	Mon	Precipitate	–	–
	Bis	–	–	–
Mn^{3+}	Mon	399 (630)	–	
	Bis	~625 (230)	–	
	Tris	~590 (110)	~575 (~190); 580 (78)	
Fe^{3+}	Mon	~429 (880), ~700 (1000)	714 (~2100)	

Table 1.1. Spectral data for metal–catecholate, Continued

	Bis	374 (1950), 576 (2900)	570 (3300); 573 (3530)
	Tris	483 (3700)	490 (4190); 473 (4320)
Co^{2+}	Mon	Precipitate	–
	Bis	469 (49), 562 (52), ~615 (34, sh)	~460, ~550
Ni^{2+}	Mon	Precipitate	–
	Bis	~490 (48, sh), 722 (~13)	400 (85), 704 (5.62); 402 (200), 740 (20, sh), 766 (25), 853 (275); 465, 662, 740
Cu^{2+}	Mon	449 (53), 743 (36)	–
	Bis	401 (220), 655 (28)	403 (210), 671 (70); 403 (447), 690 (75.9)
Zn^{2+}	Mon	Precipitate	–
	Bis	–	–

Inductively coupled plasma optical emission spectrometry (ICP-OES) is an optical emission spectrometry technique to determine the metal type and concentration in the sample. It has very high sensitivity and can precisely measure the amount of metal. However, this technique only provides the global information of the metal. The local position and distribution of the metal ion are hardly got through this measurement. Therefore, Energy-dispersive X-ray spectroscopy (EDS) elemental mapping can be complementary to provide the metal ion distribution of the samples. In addition to this two techniques, X-ray photoelectron spectroscopy (XPS) analyses are used to determine the chemical states of the elements. It is noted that XPS is a surface characterization method, which shows a penetration limits of several nanometers. Therefore, other techniques complementary to XPS should be performed to reveal the global information of these elements.

The first paragraph of this section describe the methods to characterization the metal amount, location and oxidation state. Methods that are used for evaluation of the magnetic properties will be discussed in this paragraph. Electron paramagnetic resonance spectroscopy (EPR) is a technique used to study the chemical species with unpaired electrons. Since polydopamine material is found bear free radical in the structure and paramagnetic ions in the polydopamine can interact with these radicals. In one example, EPR spectroscopy is used to characterize the paramagnetic species involved in Ag-polydopamine nanoparticles and Cu-polydopamine nanoparticles. Figure 1.10 shows Cu-polydopamine nanoparticles have a characteristic peak of Cu^{2+} at $g = 2.13$. The suppressing of the signal from free radical in the Cu-polydopamine sample can be attributed to dipole-dipole interactions between the Cu^{2+} ions and the free radical. However, EPR is less effective for analyzing magnetically concentrated systems. We find that magnetometry is good at the analysis of polydopamine samples with high metal concentrations.[23] In addition, this technique allows the analysis of local anisotropy and coupling interactions that helps to understand the magnetic nature of highly metal-loaded materials. Therefore, the combination of magnetometry with electron paramagnetic resonance (EPR), provides high-sensitivity information on metal oxidation state, coordination mode, content, and magnetic interaction between metals within the polydopamine structure.

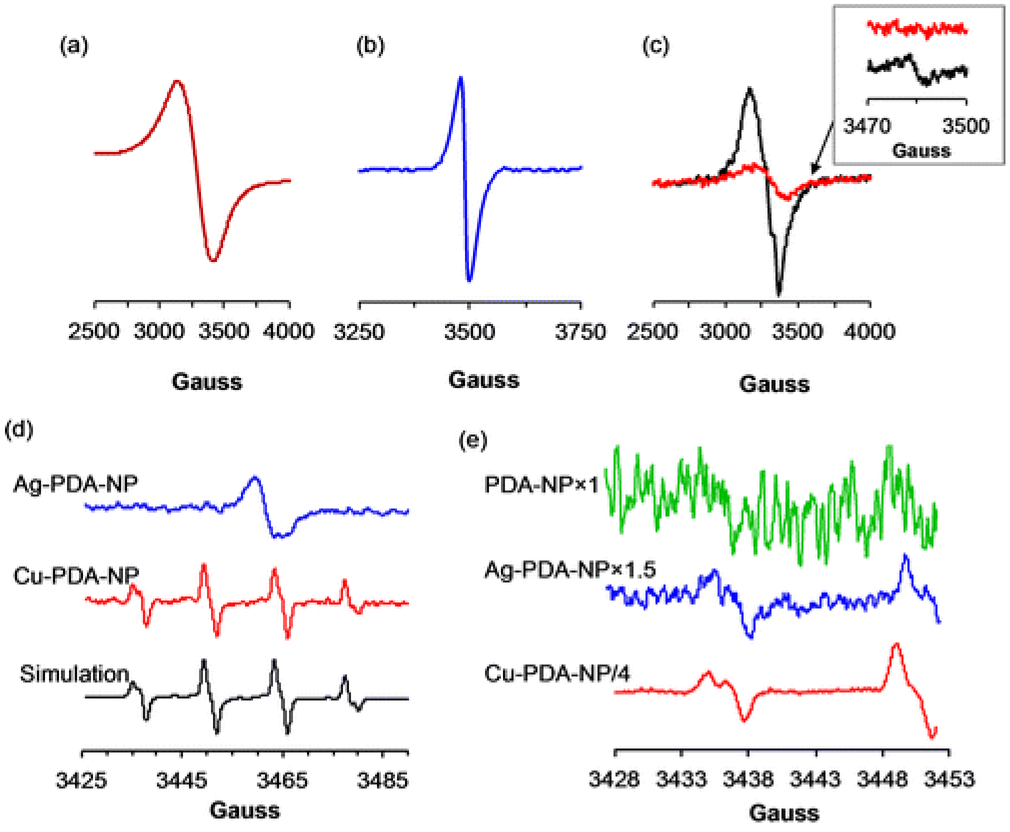

Figure 1.11. EPR spectra of the free radicals generated by PDA-NPs, Cu-PDA-NPs, and Ag-PDA-NPs. EPR spectra of (a) Cu-PDA-NPs (red) showing a broad Cu-related signal at g = 2.13 and of (b) Ag-PDA-NPs (blue) displaying a narrow peak at g = 2.004. (c) Effect of EDTA (20 mM) on the EPR spectrum of Cu-PDA-NPs (with EDTA, black; without EDTA, red; inset, magnified region of SQR signal in both spectra). (d) Spin trapping studies of Ag- and Cu-PDA-NPs in the presence of BMPO (top and middle panels, respectively) and a simulation of the BMPO-OH/BMPO-OOH signal (bottom panel; EPR coupling constants are given in Table S2). (e) Low field EPR spectra (3428–3452 G) of PDA-NPs, Cu-PDA-NPs, and Ag-PDA-NPs in the presence of BMPO (the graphs have been scaled as indicated for comparative purposes). Copyright 2016 American Chemical Society. [57]

1.4 Magnetic Resonance Imaging (MRI) Contrast Agents

Magnetic resonance imaging (MRI) is one of the most widely used non-invasive and non-ionizing diagnostic technique in the clinic. It is initially named as Nuclear Magnetic Resonance (NMR) imaging when developed in 1973 since it is based on the NMR phenomenon. In 2003, Nobel Prize in medicine was award to jointly with Peter Mansfield and Paul Lauterbur “for their discoveries concerning magnetic resonance imaging.” The development of this technique is so fast in the past 40 years: from single standard ^{1}H MRI techniques to the "second color" ^{19}F MRI. The resolution of MRI technique is also greatly enhanced via increasing the operating field strength.

1.4.1 The Fundamentals of MRI

MRI is developed based on the principle of NMR.The spin of nuclei is the key to exhibit the phenomenon of magnetic resonance. A Proton can be regarded as a spinning sphere with charges. This spinning charged sphere can produce a magnetic field, like a small magnet. Without applying an external magnetic field, protons are oriented in all directions. Therefore, the net magnetic field is zero. However, if an external magnetic field B_0 is presented, these protons will be aligned parallel or antiparallel to the external magnetic field. The excess of spins in one direction will generate a net magnetic moment. Figure 1.11c shows that proton also wobbles around the external magnetic field beside spinning about its own axis, which is called precession behavior. This precession frequency ω as shown in Figure 1.11c is called the Larmor frequency.

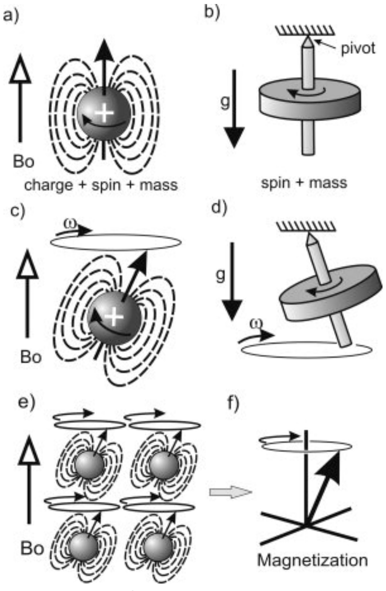

Figure 1.12. The spin and charge of a proton (a) causes it to have a magnetic field that tends to align with an applied magnetic field Bo analogous to a gyroscope hanging from a vertical pivot in the earth's gravitational field (b). When the gyroscope is tilted away from vertical it undergoes precession (d). Similarly, the proton also has angular momentum in the form of spin, which will cause it to precession at a frequency ω when it is tipped out of alignment with the Bo field (c). A group of spins precess in synchrony when exposed to a uniform magnetic field (e), which forms a bulk magnetization (f) represented by a vector that precess at the same frequency. Copyright 2012 John Wiley & Sons, Inc. [58]

The magnetic field in the MR system is generated by a giant magnet. The homogeneity of the generated magnetic field can be controlled via a shim coil. It is noted that the system is in its equilibrium state while only external magnetic field B_0 is applied. Then a radiofrequency coil is equipped to transfer a radio signal into the body. Therefore, the application of this radiofrequency can induce the perturbation of the net magnetic moment, allowing it to be observed. The perturbed system will recover back to its equilibrium state. T_1 relaxation is defined as the net magnetic moment goes back to its original state (parallel to B_0). T_2 relaxation is described as "the transverse components of magnetization decay."[58] Based on the equation shown in the Figure 1.12, T_2 is the time required for this transverse magnetization to recover to 37% of its original value.

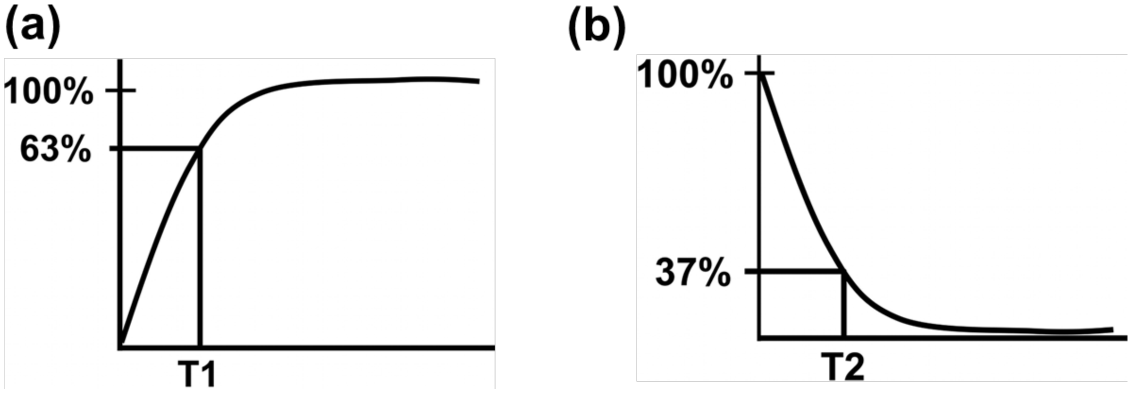

Figure 1.13. T1. T1 is defined as the time that it takes the longitudinal magnetization to grow back to 63% of its final value. T2. T2 is defined as the time that it takes the transverse magnetization to decrease to 37% of its starting value. Copyright 2005 RSNA. [59]

1.4.2 The Development of MRI Contrast Agents

The primary challenge of the MRI is the low image contrast, resulting from the long relaxation nature of water. To provide additional contrast, MRI contrast agent is used to shorten the relaxation of water protons. The relaxivity (r_1) is a measure of contrast agent efficacy, with high relaxivity agents, lending better signal-to-noise ratios and reducing the required contrast agent dose. Paramagnetic ions, such as Gd, Fe, and Mn can strongly increase the longitudinal and transverse relaxation of protons, thus increasing the contrast of the image. However, the free Gd^{3+} ion is toxic in the body, the Gadolinium ion must first be chelated to a chelate ligand before injection.

Typical contrast agents used in MRI diagnostics include ferromagnetic inorganic nanoparticles[60-61] and stable paramagnetic chelates.[62] Among them, Gadolinium (Gd)-based chelates are of particular interest in the clinic due to their high magnetic moment and asymmetric electronic ground states, offering excellent performance in efficiently enhancing signal contrast by increasing the relaxation rates of surrounding water protons.[63-64] The first clinic used MRI contrast agent was developed in 1988, called Magnevist®. It is the brand name of gadopentetate dimeglumine. In Figure 1.13, the gadolinium ion is coordinated by the three nitrogen and five oxygen atoms, leaving one coordination site for a water molecule. After the discovery of Magnevist®, a lot of other Gd-based contrast agents have been synthesized and used in clinic, including Gadodiamide, Gadoversetamide, Gadoxetate disodium and Gadofosveset trisodium.[65]

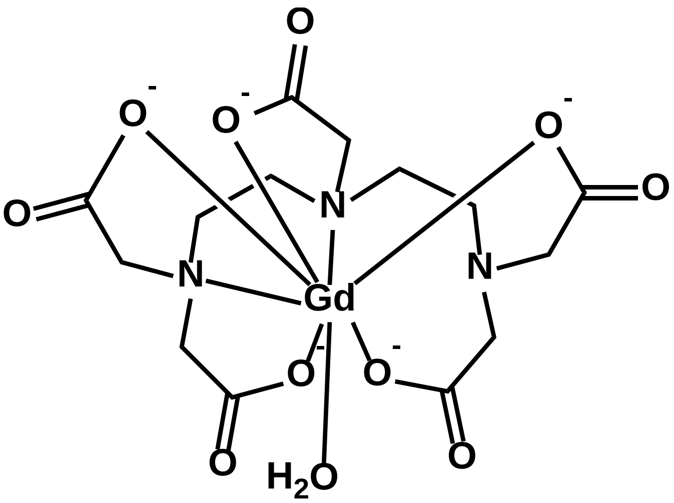

Figure 1.14. Chemical structure of gadopentetate dimeglumine.

An important goal in the design of Gd-based MRI contrast agents is to reduce the accumulation Gd ions *in vivo*, as Gd has been shown to cause a range of long-term health issues including nephrogenic systemic fibrosis (NSF).[66-67] This can be achieved by designing high relaxivity contrast agent to lower the dose. To date, current commercial contrast agents have low relaxivity (<10 $mM^{-1}s^{-1}$) due to their fast rotational correlation (τ_R=100 ps) and a low coordinate water molecule (q=1).[64] Moreover, these small molecular contrast agents have short blood half-life and tissue retention time that limit its application to long-time imaging collection.

The relaxivity of contrast agent can be affected by a few parameters: (1) the electronic properties of the gadolinium, (2) water exchange rate, (3) the ion to water proton distance, (4) the number of coordinated water molecules (q), (5) rotational correlation time (τ_R). Since the electronic properties of the gadolinium are hard to change, researchers have been dedicated to optimizing other four parameters to get higher relaxivity. For example, the correlation time, τ_R, of small molecular contrast agents can be significantly increased by covalently or non- covalently bound to macromolecules, such as polymers,[68-70] nanoparticles,[71-73] proteins[74-76] and liposomes.[77-78] The rigidity of the polymer greatly affects the enhancement of the relaxivity for the macromolecular contrast agents. The rigid polymers can effectively slow the rotational correlation time of the complex and therefore give a higher number of relaxivity than the ones with the flexible chain. For example, A rigid poly (propylene imine) dendrimers based contrast agent has been reported by Meijer and co-authors. The results show that r_1 increase with the increase of the dendrimer's generations (Figure 1.14).[79] By contrast, Raymond et al. found that flexible PEG chain has an insufficient effect on the relaxivity.[80] More recently, the development of protein engineering enables the design of Gd-specific binding proteins that showed excellent metal selectivity and stability. The relaxivity of this protein-based MRI contrast can be as high as 48 $mM^{-1}s^{-1}$ at 3 T. In contrast, the protein with the flexible binding site has very low relaxivity (3.5 $mM^{-1}s^{-1}$ at 3 T).[74] The number of coordinated water molecules can also be increased via design new class of chelate ligands other than polyamine carboxylate. Raymond group developed hexadentate oxygen donor chelators with higher relaxivity due to the increased coordinated water molecules.[81-82]

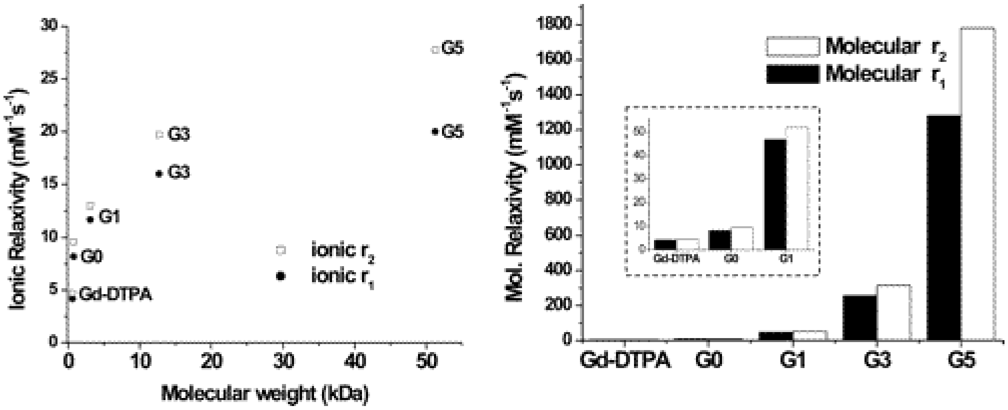

Figure 1.15. Relaxivities of different generations of Gd−DTPA-based dendrimers 5n: ionic relaxivities versus molecular weight (left) and molecular relaxivities versus the generation of the dendrimer (right). The maximum molecular relaxivity is defined as the ionic relaxivity multiplied by the theoretical number of gadolinium moieties attached to a single dendrimer. Copyright 2016 American Chemical Society.[79]

1.5 References

1. d'Ischia, M.; Wakamatsu, K.; Cicoira, F.; Di Mauro, E.; Garcia-Borron, J. C.; Commo, S.; Galván, I.; Ghanem, G.; Kenzo, K.; Meredith, P.; Pezzella, A.; Santato, C.; Sarna, T.; Simon, J. D.; Zecca, L.; Zucca, F. A.; Napolitano, A.; Ito, S., Melanins and melanogenesis: from pigment cells to human health and technological applications. *Pigment Cell & Melanoma Research* **2015,** *28* (5), 520-544.

2. Rass, K.; Reichrath, J., UV Damage and DNA Repair in Malignant Melanoma and Nonmelanoma Skin Cancer. In *Sunlight, Vitamin D and Skin Cancer*, Reichrath, J., Ed. Springer New York: New York, NY, 2008; pp 162-178.

3. Sebaratnam, D. F.; Venugopal, S. S.; Frew, J. W.; McMillan, J. R.; Finkelstein, E. R.; Martin, L. K.; Murrell, D. F., Diffuse melanosis cutis: A systematic review of the literature. *Journal of the American Academy of Dermatology* **2013,** *68* (3), 482-488.

4. Natarajan, V. T.; Ganju, P.; Ramkumar, A.; Grover, R.; Gokhale, R. S., Multifaceted pathways protect human skin from UV radiation. *Nature Chemical Biology* **2014,** *10*, 542.

5. Raper, H. S., THE AEROBIC OXIDASES. *Physiological Reviews* **1928,** *8* (2), 245-282.

6. Mason, H. S., THE CHEMISTRY OF MELANIN: III. MECHANISM OF THE OXIDATION OF DIHYDROXYPHENYLALANINE BY TYROSINASE. *Journal of Biological Chemistry* **1948,** *172* (1), 83-99.

7. Prota, G. P., Mario; Nicolaus, Rodolfo A, Preliminary results in the study of pheomelanins *Rendiconto dell'Accademia delle Scienze Fisiche e Matematiche* **1966,** *33*, 146-150.

8. Ito, S.; Wakamatsu, K.; Ozeki, H., Chemical Analysis of Melanins and its Application to the Study of the Regulation of Melanogenesis. *Pigment Cell Research* **2000,** *13*, 103-109.

9. Wakamatsu, K.; Ito, S., Advanced Chemical Methods in Melanin Determination. *Pigment Cell Research* **2002,** *15* (3), 174-183.

10. Bush, W. D.; Garguilo, J.; Zucca, F. A.; Albertini, A.; Zecca, L.; Edwards, G. S.; Nemanich, R. J.; Simon, J. D., The surface oxidation potential of human neuromelanin reveals a spherical architecture with a pheomelanin core and a eumelanin surface. *Proceedings of the National Academy of Sciences* **2006,** *103* (40), 14785-14789.

11. Ito, S., Encapsulation of a reactive core in neuromelanin. *Proceedings of the National Academy of Sciences* **2006,** *103* (40), 14647-14648.

12. Chen, C.-T.; Martin-Martinez, F. J.; Jung, G. S.; Buehler, M. J., Polydopamine and eumelanin molecular structures investigated with ab initio calculations. *Chemical Science* **2017,** *8* (2), 1631-1641.

13. Costa, T. G.; Younger, R.; Poe, C.; Farmer, P. J.; Szpoganicz, B., Studies on Synthetic and Natural Melanin and Its Affinity for Fe(III) Ion. *Bioinorganic Chemistry and Applications* **2012,** *2012*, 9.

14. d'Ischia, M.; Napolitano, A.; Ball, V.; Chen, C.-T.; Buehler, M. J., Polydopamine and Eumelanin: From Structure–Property Relationships to a Unified Tailoring Strategy. *Accounts of Chemical Research* **2014,** *47* (12), 3541-3550.

15. Liebscher, J.; Mrówczyński, R.; Scheidt, H. A.; Filip, C.; Hădade, N. D.; Turcu, R.; Bende, A.; Beck, S., Structure of Polydopamine: A Never-Ending Story? *Langmuir* **2013,** *29* (33), 10539-10548.

16. Haywood, R. M.; Lee, M.; Linge, C., Synthetic melanin is a model for soluble natural eumelanin in UVA-photosensitised superoxide production. *Journal of Photochemistry and Photobiology B: Biology* **2006,** *82* (3), 224-235.

17. Huang, Y.; Li, Y.; Hu, Z.; Yue, X.; Proetto, M. T.; Jones, Y.; Gianneschi, N. C., Mimicking Melanosomes: Polydopamine Nanoparticles as Artificial Microparasols. *ACS Central Science* **2017,** *3* (6), 564-569.

18. Xiao, M.; Hu, Z.; Wang, Z.; Li, Y.; Tormo, A. D.; Le Thomas, N.; Wang, B.; Gianneschi, N. C.; Shawkey, M. D.; Dhinojwala, A., Bioinspired bright noniridescent photonic melanin supraballs. *Science Advances* **2017,** *3* (9).

19. Iqbal, Z.; Lai, E. P. C.; Avis, T. J., Antimicrobial effect of polydopamine coating on Escherichia coli. *Journal of Materials Chemistry* **2012,** *22* (40), 21608-21612.

20. Ryu, J.; Ku, S. H.; Lee, H.; Park, C. B., Mussel-Inspired Polydopamine Coating as a Universal Route to Hydroxyapatite Crystallization. *Advanced Functional Materials* **2010,** *20* (13), 2132-2139.

21. Wang, Z.; Carniato, F.; Xie, Y.; Huang, Y.; Li, Y.; He, S.; Zang, N.; Rinehart, J. D.; Botta, M.; Gianneschi, N. C., High Relaxivity Gadolinium-Polydopamine Nanoparticles. *Small*, 1701830-n/a.

22. Wang, Z.; Xie, Y.; Li, Y.; Huang, Y.; Parent, L. R.; Ditri, T.; Zang, N.; Rinehart, J. D.; Gianneschi, N. C., Tunable, Metal-Loaded Polydopamine Nanoparticles Analyzed by Magnetometry. *Chemistry of Materials* **2017,** *29* (19), 8195-8201.

23. Li, Y.; Xie, Y.; Wang, Z.; Zang, N.; Carniato, F.; Huang, Y.; Andolina, C. M.; Parent, L. R.; Ditri, T. B.; Walter, E. D.; Botta, M.; Rinehart, J. D.; Gianneschi, N. C., Structure and Function of Iron-Loaded Synthetic Melanin. *ACS Nano* **2016,** *10* (11), 10186-10194.

24. Lee, H.; Dellatore, S. M.; Miller, W. M.; Messersmith, P. B., Mussel-Inspired Surface Chemistry for Multifunctional Coatings. *Science* **2007,** *318* (5849), 426-430.

25. Della Vecchia, N. F.; Luchini, A.; Napolitano, A.; D'Errico, G.; Vitiello, G.; Szekely, N.; d'Ischia, M.; Paduano, L., Tris Buffer Modulates Polydopamine Growth, Aggregation, and Paramagnetic Properties. *Langmuir* **2014,** *30* (32), 9811-9818.

26. Ai, K.; Liu, Y.; Ruan, C.; Lu, L.; Lu, G., Sp2 C-Dominant N-Doped Carbon Sub-micrometer Spheres with a Tunable Size: A Versatile Platform for Highly Efficient Oxygen-Reduction Catalysts. *Advanced Materials* **2013,** *25* (7), 998-1003.

27. Jiang, X.; Wang, Y.; Li, M., Selecting water-alcohol mixed solvent for synthesis of polydopamine nano-spheres using solubility parameter. *Scientific Reports* **2014,** *4*, 6070.

28. Ju, K.-Y.; Lee, Y.; Lee, S.; Park, S. B.; Lee, J.-K., Bioinspired Polymerization of Dopamine to Generate Melanin-Like Nanoparticles Having an Excellent Free-Radical-Scavenging Property. *Biomacromolecules* **2011,** *12* (3), 625-632.

29. Herlinger, E.; Jameson, R. F.; Linert, W., Spontaneous autoxidation of dopamine. *Journal of the Chemical Society, Perkin Transactions 2* **1995,** (2), 259-263.

30. Zheng, W.; Fan, H.; Wang, L.; Jin, Z., Oxidative Self-Polymerization of Dopamine in an Acidic Environment. *Langmuir* **2015,** *31* (42), 11671-11677.

31. Dai, M.; Huang, T.; Chao, L.; Tan, Y.; Chen, C.; Meng, W.; Xie, Q., Tyrosinase-catalyzed polymerization of l-DOPA (versus l-tyrosine and dopamine) to generate melanin-like biomaterials for immobilization of enzymes and amperometric biosensing. *RSC Advances* **2016,** *6* (21), 17016-17022.

32. Wang, J.-l.; Li, B.-c.; Li, Z.-j.; Ren, K.-f.; Jin, L.-j.; Zhang, S.-m.; Chang, H.; Sun, Y.-x.; Ji, J., Electropolymerization of dopamine for surface modification of complex-shaped cardiovascular stents. *Biomaterials* **2014,** *35* (27), 7679-7689.

33. Bernsmann, F.; Voegel, J.-C.; Ball, V., Different synthesis methods allow to tune the permeability and permselectivity of dopamine–melanin films to electrochemical probes. *Electrochimica Acta* **2011,** *56* (11), 3914-3919.

34. Du, X.; Li, L.; Li, J.; Yang, C.; Frenkel, N.; Welle, A.; Heissler, S.; Nefedov, A.; Grunze, M.; Levkin, P. A., UV-Triggered Dopamine Polymerization: Control of Polymerization, Surface Coating, and Photopatterning. *Advanced Materials* **2014,** *26* (47), 8029-8033.

35. Chen, T.-P.; Liu, T.; Su, T.-L.; Liang, J., Self-Polymerization of Dopamine in Acidic Environments without Oxygen. *Langmuir* **2017,** *33* (23), 5863-5871.

36. Hong, S.; Na, Y. S.; Choi, S.; Song, I. T.; Kim, W. Y.; Lee, H., Non-Covalent Self-Assembly and Covalent Polymerization Co-Contribute to Polydopamine Formation. *Advanced Functional Materials* **2012,** *22* (22), 4711-4717.

37. Yu, X.; Fan, H.; Liu, Y.; Shi, Z.; Jin, Z., Characterization of Carbonized Polydopamine Nanoparticles Suggests Ordered Supramolecular Structure of Polydopamine. *Langmuir* **2014,** *30* (19), 5497-5505.

38. Zangmeister, R. A.; Morris, T. A.; Tarlov, M. J., Characterization of Polydopamine Thin Films Deposited at Short Times by Autoxidation of Dopamine. *Langmuir* **2013,** *29* (27), 8619-8628.

39. Hong, L.; Simon, J. D., Physical and Chemical Characterization of Iris and Choroid Melanosomes Isolated from Newborn and Mature Cows. *Photochemistry and Photobiology* **2005,** *81* (3), 517-523.

40. Liu, Y.; Hong, L.; Wakamatsu, K.; Ito, S.; Adhyaru, B.; Cheng, C.-Y.; Bowers, C. R.; Simon, J. D., Comparison of Structural and Chemical Properties of Black and Red Human Hair Melanosomes. *Photochemistry and Photobiology* **2005,** *81* (1), 135-144.

41. Hong, L.; Simon, J. D., Current Understanding of the Binding Sites, Capacity, Affinity, and Biological Significance of Metals in Melanin. *The Journal of Physical Chemistry B* **2007,** *111* (28), 7938-7947.

42. Larsson, B.; Tjälve, H., Studies on the melanin-affinity of metal ions. *Acta Physiologica Scandinavica* **1978,** *104* (4), 479-484.

43. Hong, L.; Simon, J. D., Insight into the Binding of Divalent Cations to Sepia Eumelanin from IR Absorption Spectroscopy. *Photochemistry and Photobiology* **2006,** *82* (5), 1265-1269.

44. Hong, L.; Liu, Y.; Simon, J. D., Binding of Metal Ions to Melanin and Their Effects on the Aerobic Reactivity¶. *Photochemistry and Photobiology* **2004,** *80* (3), 477-481.

45. Salceda, R.; Sánchez-Chávez, G., Calcium uptake, release and ryanodine binding in melanosomes from retinal pigment epithelium. *Cell Calcium* **2000,** *27* (4), 223-229.

46. Zecca, L.; Shima, T.; Stroppolo, A.; Goj, C.; Battiston, G. A.; Gerbasi, R.; Sarna, T.; Swartz, H. M., Interaction of neuromelanin and iron in substantia nigra and other areas of human brain. *Neuroscience* **1996,** *73* (2), 407-415.

47. Enochs, W. S.; Petherick, P.; Bogdanova, A.; Mohr, U.; Weissleder, R., Paramagnetic metal scavenging by melanin: MR imaging. *Radiology* **1997,** *204* (2), 417-423.

48. Hung, Y.-C.; Sava, V. M.; Juang, C.-L.; Yeh, T.-c.; Shen, W.-C.; Huang, G. S., Gastrointestinal enhancement of MRI with melanin derived from tea leaves (Thea sinensis Linn.). *Journal of Ethnopharmacology* **2002,** *79* (1), 75-79.

49. Ju, K.-Y.; Lee, J. W.; Im, G. H.; Lee, S.; Pyo, J.; Park, S. B.; Lee, J. H.; Lee, J.-K., Bio-Inspired, Melanin-Like Nanoparticles as a Highly Efficient Contrast Agent for T1-Weighted Magnetic Resonance Imaging. *Biomacromolecules* **2013,** *14* (10), 3491-3497.

50. Miao, Z.-H.; Wang, H.; Yang, H.; Li, Z.-L.; Zhen, L.; Xu, C.-Y., Intrinsically Mn2+-Chelated Polydopamine Nanoparticles for Simultaneous Magnetic Resonance Imaging and Photothermal Ablation of Cancer Cells. *ACS Applied Materials & Interfaces* **2015,** *7* (31), 16946-16952.

51. Ge, R.; Lin, M.; Li, X.; Liu, S.; Wang, W.; Li, S.; Zhang, X.; Liu, Y.; Liu, L.; Shi, F.; Sun, H.; Zhang, H.; Yang, B., Cu2+-Loaded Polydopamine Nanoparticles for Magnetic Resonance Imaging-Guided pH- and Near-Infrared-Light-Stimulated Thermochemotherapy. *ACS Applied Materials & Interfaces* **2017,** *9* (23), 19706-19716.

52. Son, H. Y.; Ryu, J. H.; Lee, H.; Nam, Y. S., Silver-Polydopamine Hybrid Coatings of Electrospun Poly(vinyl alcohol) Nanofibers. *Macromolecular Materials and Engineering* **2013,** *298* (5), 547-554.

53. Yang, L.; Kong, J.; Zhou, D.; Ang, J. M.; Phua, S. L.; Yee, W. A.; Liu, H.; Huang, Y.; Lu, X., Transition-Metal-Ion-Mediated Polymerization of Dopamine: Mussel-Inspired Approach for the Facile Synthesis of Robust Transition-Metal Nanoparticle–Graphene Hybrids. *Chemistry – A European Journal* **2014,** *20* (25), 7776-7783.

54. Sever, M. J.; Wilker, J. J., Visible absorption spectra of metal-catecholate and metal-tironate complexes. *Dalton Transactions* **2004,** (7), 1061-1072.

55. Yao, X.; Zhao, C.; Kong, J.; Wu, H.; Zhou, D.; Lu, X., Dopamine-assisted one-pot synthesis of zinc ferrite-embedded porous carbon nanospheres for ultrafast and stable lithium ion batteries. *Chemical Communications* **2014,** *50* (93), 14597-14600.

56. Holten-Andersen, N.; Harrington, M. J.; Birkedal, H.; Lee, B. P.; Messersmith, P. B.; Lee, K. Y. C.; Waite, J. H., pH-induced metal-ligand cross-links inspired by mussel yield self-healing polymer networks with near-covalent elastic moduli. *Proceedings of the National Academy of Sciences* **2011,** *108* (7), 2651-2655.

57. Yeroslavsky, G.; Lavi, R.; Alishaev, A.; Rahimipour, S., Sonochemically-Produced Metal-Containing Polydopamine Nanoparticles and Their Antibacterial and Antibiofilm Activity. *Langmuir* **2016,** *32* (20), 5201-5212.

58. Plewes, D. B.; Kucharczyk, W., Physics of MRI: A primer. *Journal of Magnetic Resonance Imaging* **2012,** *35* (5), 1038-1054.

59. Pooley, R. A., Fundamental Physics of MR Imaging. *RadioGraphics* **2005,** *25* (4), 1087-1099.

60. Na, H. B.; Song, I. C.; Hyeon, T., Inorganic nanoparticles for MRI contrast agents. *Advanced Materials* **2009,** *21* (21), 2133-2148.

61. Laurent, S.; Forge, D.; Port, M.; Roch, A.; Robic, C.; Vander Elst, L.; Muller, R. N., Magnetic iron oxide nanoparticles: Synthesis, stabilization, vectorization, physicochemical characterizations and biological applications. *Chemical Reviews* **2008,** *108* (6), 2064-2110.

62. Lauffer, R. B., Paramagnetic metal complexes as water proton relaxation agents for NMR imaging: Theory and design. *Chemical Reviews* **1987,** *87* (5), 901-927.

63. Caravan, P.; Ellison, J. J.; McMurry, T. J.; Lauffer, R. B., Gadolinium(III) chelates as MRI contrast agents: Structure, dynamics, and applications. *Chemical Reviews* **1999,** *99* (9), 2293-2352.

64. Caravan, P., Strategies for increasing the sensitivity of gadolinium based MRI contrast agents. *Chemical Society Reviews* **2006,** *35* (6), 512-523.

65. Lohrke, J.; Frenzel, T.; Endrikat, J.; Alves, F. C.; Grist, T. M.; Law, M.; Lee, J. M.; Leiner, T.; Li, K.-C.; Nikolaou, K.; Prince, M. R.; Schild, H. H.; Weinreb, J. C.; Yoshikawa, K.; Pietsch, H., 25 Years of Contrast-Enhanced MRI: Developments, Current Challenges and Future Perspectives. *Advances in Therapy* **2016,** *33* (1), 1-28.

66. Aime, S.; Caravan, P., Biodistribution of gadolinium-based contrast agents, including gadolinium deposition. *Journal of Magnetic Resonance Imaging* **2009,** *30* (6), 1259-1267.

67. Kribben, A.; Witzke, O.; Hillen, U.; Barkhausen, J.; Daul, A. E.; Erbel, R., Nephrogenic Systemic Fibrosis. Pathogenesis, Diagnosis, and Therapy. *Journal of the American College of Cardiology* **2009,** *53* (18), 1621-1628.

68. Wen, X.; Jackson, E. F.; Price, R. E.; Kim, E. E.; Wu, Q.; Wallace, S.; Charnsangavej, C.; Gelovani, J. G.; Li, C., Synthesis and Characterization of Poly(l-glutamic acid) Gadolinium Chelate: A New Biodegradable MRI Contrast Agent. *Bioconjugate Chemistry* **2004,** *15* (6), 1408-1415.

69. Huang, C.-H.; Tsourkas, A., Gd-based macromolecules and nanoparticles as magnetic resonance contrast agents for molecular imaging. *Current topics in medicinal chemistry* **2013,** *13* (4), 411-421.

70. Bogdanov, A. A.; Weissleder, R.; Frank, H. W.; Bogdanova, A. V.; Nossif, N.; Schaffer, B. K.; Tsai, E.; Papisov, M. I.; Brady, T. J., A new macromolecule as a contrast agent for MR angiography: preparation, properties, and animal studies. *Radiology* **1993,** *187* (3), 701-706.

71. Randolph, L. M.; LeGuyader, C. L. M.; Hahn, M. E.; Andolina, C. M.; Patterson, J. P.; Mattrey, R. F.; Millstone, J. E.; Botta, M.; Scadeng, M.; Gianneschi, N. C., Polymeric Gd-DOTA amphiphiles form spherical and fibril-shaped nanoparticle MRI contrast agents. *Chemical Science* **2016**.

72. Taylor, K. M. L.; Kim, J. S.; Rieter, W. J.; An, H.; Lin, W.; Lin, W., Mesoporous Silica Nanospheres as Highly Efficient MRI Contrast Agents. *Journal of the American Chemical Society* **2008,** *130* (7), 2154-2155.

73. Chen, K.-J.; Wolahan, S. M.; Wang, H.; Hsu, C.-H.; Chang, H.-W.; Durazo, A.; Hwang, L.-P.; Garcia, M. A.; Jiang, Z. K.; Wu, L.; Lin, Y.-Y.; Tseng, H.-R., A small MRI contrast agent library of gadolinium(III)-encapsulated supramolecular nanoparticles for improved relaxivity and sensitivity. *Biomaterials* **2011,** *32* (8), 2160-2165.

74. Yang, J. J.; Yang, J.; Wei, L.; Zurkiya, O.; Yang, W.; Li, S.; Zou, J.; Zhou, Y.; Maniccia, A. L. W.; Mao, H.; Zhao, F.; Malchow, R.; Zhao, S.; Johnson, J.; Hu, X.; Krogstad, E.; Liu, Z.-R., Rational Design of Protein-Based MRI Contrast Agents. *Journal of the American Chemical Society* **2008,** *130* (29), 9260-9267.

75. Song, Y.; Kang, Y. J.; Jung, H.; Kim, H.; Kang, S.; Cho, H., Lumazine Synthase Protein Nanoparticle-Gd(III)-DOTA Conjugate as a T1 contrast agent for high-field MRI. *Scientific Reports* **2015,** *5*, 15656.

76. Caravan, P., Protein-Targeted Gadolinium-Based Magnetic Resonance Imaging (MRI) Contrast Agents: Design and Mechanism of Action. *Accounts of Chemical Research* **2009,** *42* (7), 851-862.

77. Kabalka, G. W.; Buonocore, E.; Hubner, K.; Davis, M.; Huang, L., Gadolinium-labeled liposomes containing paramagnetic amphipathic agents: Targeted MRI contrast agents for the liver. *Magnetic Resonance in Medicine* **1988,** *8* (1), 89-95.

78. Cheng, Z.; Thorek, D. L. J.; Tsourkas, A., Porous Polymersomes with Encapsulated Gd-Labeled Dendrimers as Highly Efficient MRI Contrast Agents. *Advanced Functional Materials* **2009,** *19* (23), 3753-3759.

79. Langereis, S.; de Lussanet, Q. G.; van Genderen, M. H. P.; Backes, W. H.; Meijer, E. W., Multivalent Contrast Agents Based on Gadolinium−Diethylenetriaminepentaacetic Acid-Terminated Poly(propylene imine) Dendrimers for Magnetic Resonance Imaging. *Macromolecules* **2004,** *37* (9), 3084-3091.

80. Doble, D. M. J.; Botta, M.; Wang, J.; Aime, S.; Barge, A.; Raymond, K. N., Optimization of the Relaxivity of MRI Contrast Agents: Effect of Poly(ethylene glycol) Chains on the Water-Exchange Rates of GdIII Complexes. *Journal of the American Chemical Society* **2001,** *123* (43), 10758-10759.

81. Werner, E. J.; Datta, A.; Jocher, C. J.; Raymond, K. N., High-Relaxivity MRI Contrast Agents: Where Coordination Chemistry Meets Medical Imaging. *Angewandte Chemie International Edition* **2008,** *47* (45), 8568-8580.

82. Thompson, M. K.; Misselwitz, B.; Tso, L. S.; Doble, D. M. J.; Schmitt-Willich, H.; Raymond, K. N., In Vivo Evaluation of Gadolinium Hydroxypyridonate Chelates: Initial Experience as Contrast Media in Magnetic Resonance Imaging. *Journal of Medicinal Chemistry* **2005,** *48* (11), 3874-3877.

Chapter 2

Structure and Function of Iron-Loaded Synthetic Melanin

2.1 Introduction

Melanins are a type of pigments found throughout nature. They have gained considerable attention because it has a unique combination of properties functions.[1-4] Very recently, self-oxidation polymerization of dopamine monomer under alkaline condition enables the successful synthesis of natural melanin mimics with the similar chemical structure as well as physical and biological properties, which indeed have opened up a new area of synthetic melanin particles. For example, polydopamine (PDA)-based materials retain many of the desirable properties of natural melanin and have been employed in a growing number of studies probing their utility for bioadhesion,[5-8] metal ion chelation,[9-10] free radical quenching,[11-12] environmental remediation,[13-15] photothermal therapy,[16-17] and structural coloration.[18-20] Many of these applications take advantage of the strong binding affinity between the catecholate compound and various metal ions.[21-23]

One of the most promising advancements in this field was the invention of synthetic melanin-based magnetic resonance imaging (MRI) contrast agents with high efficiency and excellent biocompatibility. After complexation with paramagnetic metal ions like Fe(III), the PDA nanoparticles are capable of exhibiting hyperintense contrast enhancing ability in T_1-weighted MR imaging. This allows people to design various kinds of non-gadolinium multimodal imaging models further. Facile aqueous dispersion and notable structural regularity make PDA-based materials especially desirable for fully understanding the magnetic factors that influence MRI contrast in a broad range of synthetic melanin nanoparticles. Two important issues hinder the advancement of such particles as effective contrast agents: their inability to support high metal loadings and the difficulty in characterizing the magnetic interactions that lead to the MRI contrast enhancement. The conventional method to prepare SMNP MRI contrast agents exploits the high binding affinity of catechol for metal ions to post-synthetically complex pristine PDA nanoparticles with Fe(III) salts (post-synthetic strategy; see Figure 2.1a). This methodology is convenient and allows for the complexation of a variety of cations; [24] however, the majority of Fe(III) centers are localized on or nearby the surface of the PDA nanoparticles. This surface-binding mode severely limits the metal loading efficiency of Fe(III) to less than 1% in SMNP by mass.[24] Although this situation can be improved somewhat by decreasing the surface-to-volume ratio of the PDA nanoparticles,[24] achieving ultrahigh Fe(III) loading (i.e. > 5%) for enhanced SMNP MRI contrast agents is still not possible. Improving these metal-loading levels is of key importance because T_1-weighted MRI contrast should scale with the number of paramagnetic centers per particle.

Additionally, considerable insight into the magnetic properties of catechol-based materials has been obtained through electron paramagnetic resonance (EPR) and Mössbauer spectroscopies.[25-29] EPR is particularly useful in detecting the radicals as well as trace metal ions but is less effective for analyzing magnetically concentrated systems. Magnetometry is superior to the magnetically concentrated system. It tells the local anisotropy information and coupling interactions between metal centers, which helps to understand the magnetic nature of high metal-loaded polydopamine system for MRI contrast. Notably, although kinds of analytical methods have been individually used to characterize natural melanins, the combined methodology we use herein has never been systematically applied to synthetic melanin systems. Herein we address both of these issues: the need for higher Fe(III) ion loadings and a more thorough characterization of the product. We outline a new synthetic method that employs pre-chelated metal ions to enhance Fe(III) incorporation and develop a quantitative model that ties the atomic-level magnetic interactions to the particles' ability to enhance MRI contrast.

2.2 Synthetic Routes for the Preparation of Iron-Loaded Synthetic Melanin

2.2.1 Synthesis of SMNP-1

The SMNP-0 was synthesized through the oxidation and self-polymerization of dopamine in a basic solution mixture of water, ethanol, and ammonia at room temperature.[30] In a typical reaction, 50 mL of deionized water and 20 mL of ethanol were the first mixtures together, followed by addition of 1.1 mL of ammonium hydroxide solution (28–30%) under vigorous stir for about 30 mins. Then, five mL of 4mg/mL dopamine hydrochloride stock solution was quickly injected into this reaction mixture. The solution turned to yellow immediately after adding the dopamine hydrochloride and then slowly turn to black after one hour. The SMNPs were purified by centrifugation and washing with deionized water three times after overnight reaction.

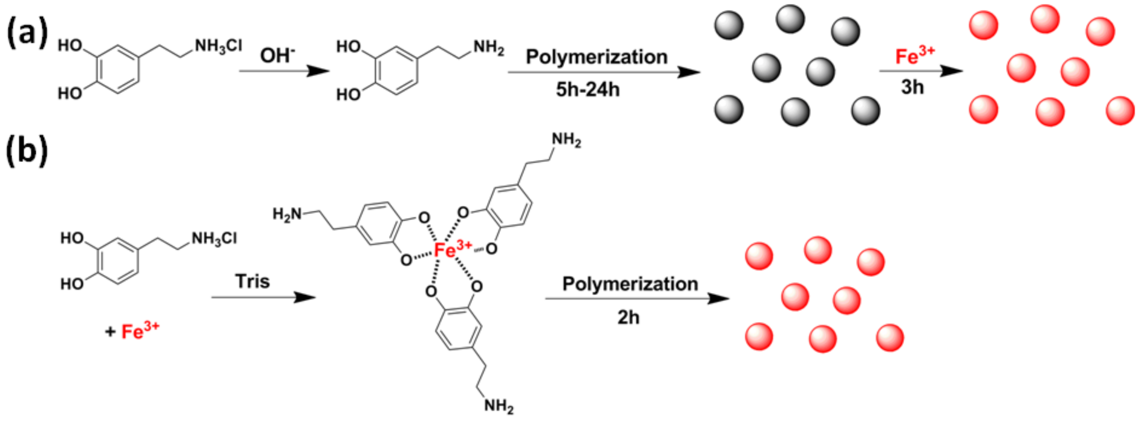

Figure 2.1. Scheme for the preparation of SMNP-i samples: (a) Post-doping strategy for SMNP-1, and (b) Pre-doping strategy for SMNP-2, SMNP-3, SMNP-4, and SMNP-5. Copyright 2016 American Chemical Society.[31]

2.2.2 Synthesis of SMNP-2, 3, 4 and 5

We propose a pre-doping strategy, which employs Fe(III)(dopamine)$_3$ as the supramolecular monomer to fully/partially instead of dopamine monomer to in-situ form the Fe(III)-chelated PDA nanoparticles (Figure 2.1b). During the polymerization process under alkaline condition (Table 2.1), Fe(III) can be distributed at everywhere of the formed SMNP, directly achieving tunable, high doping levels of metal ions inside the particle. We use this pre-doping strategy to synthesize SMNP-i (i=2-5) (Table 2.2) to combine with SMNP-1 obtained from a conventional post-doping strategy for systematic magnetometry investigation. In the example of synthesizing SMNP-5, 45 mg dopamine hydrochloride and 20.4 mg of Fe(III) chloride hexahydrate were fully dissolved in 130 mL deionized water under stirring at room temperature for 1 h. Subsequently, 20 mL of 75mg/mL Tris buffer was quickly injected into the established solution. It was observed that the solution color immediately turned red, gradually turning black after 0.5 h. After another 1.5 h, the sample was separated by centrifugation and washed three times with deionized water. Additionally, our pre-doping strategy has some advantages from the one-pot reaction compared with the conventional post-doping approach, including less purification work, more time efficient and usually higher yielding. Therefore, this new pre-doping approach may be ideal to achieve SMNP MRI contrast agent with a tunable range of Fe(III) ions, especially in the high metal loading level.

Table 2.1. Reactants and their formulations for the preparation of SMNP-*i* (*i* = 2, 3, 4, 5).

Sample	Dopamine Hydrochloride (mg)	$FeCl_3 \cdot 6H_2O$ (mg)	Tris (mg)	Total Water (mL)	PH
SMNP-2	45	0.6	45	150	8.90
SMNP-3	45	1.3	90	150	8.91
SMNP-4	45	16.4	450	150	9.36
SMNP-5	45	21.4	1500	150	9.80

Table 2.2. Physical parameters of SMNP-i (i=0-5).

Sample	Fe(III)%	Size (nm)	Coupled Ion (%)	Synthetic Method
SMNP-0	0	150±25	0	-
SMNP-1	0.46	150±25	10	Post-Doping
SMNP-2	1.89	190±20	18	Pre-Doping
SMNP-3	2.88	170±25	22	Pre-Doping
SMNP-4	5.86	140±20	38	Pre-Doping
SMNP-5	10.26	250±30	61	Pre-Doping

2.3 Characterization of SMNPs

2.3.1 Analysis the Metal Loading via ICP-OES

To analyze the Fe(III) loading in the SMNPs, we used ICP-OES to measure the concentration of Fe in a digested solution. The procedure is described as follows: the concentration of the SMNP-0 solution was determined by taking 1mL of the sample in a pre-weighed plastic tube. Then the solution was lyophilized and measure the weight. 100 µL of SMNP-0 (known concentration) solution was added to a 1.9 mL of 1% HNO_3.The mixture was heated to 60 degrees for 12 h. The digestion solution was sent to the ICP-OES analysis using a Perkin Elmer Optima 3000DV spectrometer. The Fe (III) loading of other SMNPs is determined via the same method. Table 2.2 shows the weight percent of Fe (III) in the SMNPs. The Fe(III) loading in SMNP-5 is up to 10.26%, which almost reach the maximum theoretical loading of 10.7% calculated from the assumption that three dopamine molecule can coordinate with one Fe(III).

2.3.2 Characterization of SMNPs by Electron Microscopy

SMNP-4 was firstly characterized by TEM, Cryo-TEM and SEM (Figure 2.2 a, b and c). The working voltage was set at 200 keV on an FEI Sphera microscope. TEM grids were purchased from Ted Pella Inc. with formvar stabilized with carbon on 400 copper mesh. 3.5 µL of solution was deposited onto grids and let it dry at room temperature. Cryo-TEM image of SMNP-4 was also obtained from FEI Sphera microscope operating at 200 keV. 3.5 µL of solution was deposited onto Cryo-TEM grids (Quantifoil R2/2 holey carbon) at a cold room (4 ^{o}C). Then the solution was blotted with a small piece of filter paper to generate a thin film. The grid was suddenly plunged into liquid ethane and transferred into a Gatan 626 cryo-transfer holder in liquid N_2. SEM image of SMNP-4 was obtained on an FEI XL ESEM-FEG (FEI Company) with mica substrate. A 5uL sample solution was deposited on the substrate and thoroughly dried under vacuum for 12 h before the imaging. TEM, cryo-TEM and SEM (Figure 2.2) show the SMNP-4 nanoparticle with spherical morphology. The diameter of this nanoparticle is determined to be 140±20 nm (average size from TEM images). The morphology of other SMNPs is characterized by TEM and SEM. Figure 2.3 and Figure 2.4 shows all the nanoparticles have uniform spherical shape. Interestingly, we find that Fe loading can affect the size –lower loading nanoparticle present smaller size. Actually, the size of nanoparticles can be affected by several factors. The systematic investigation will be discussed in the next chapter.

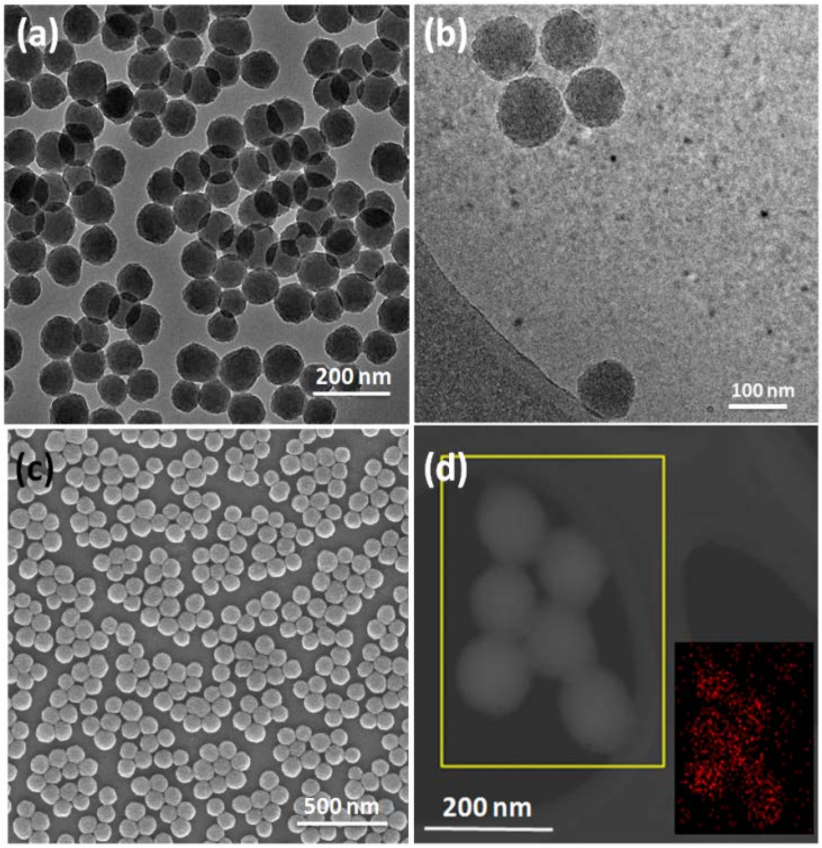

Figure 2.2. Representative electron microscopy characterization of SMNP-4: (a) TEM; (b) cryo-TEM; (c) SEM; and (d) HAADF-STEM (insert is the selected area EDS Fe elemental mapping image). Copyright 2016 American Chemical Society.[31]

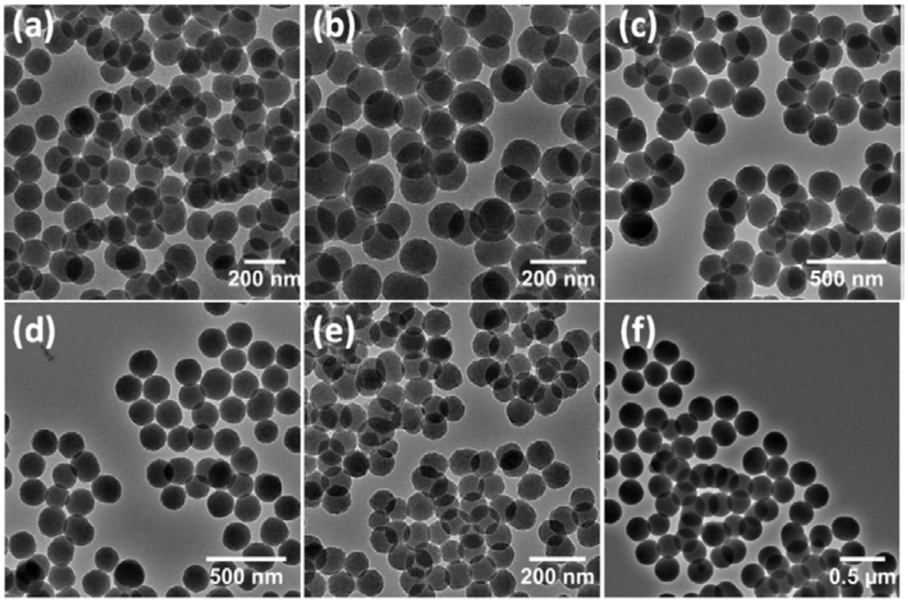

Figure 2.3. Representative TEM images of SMNP-0 (a), SMNP-1 (b), SMNP-2 (c), SMNP-3 (d), SMNP-4 (e), and SMNP-5 (f). Copyright 2016 American Chemical Society.[31]

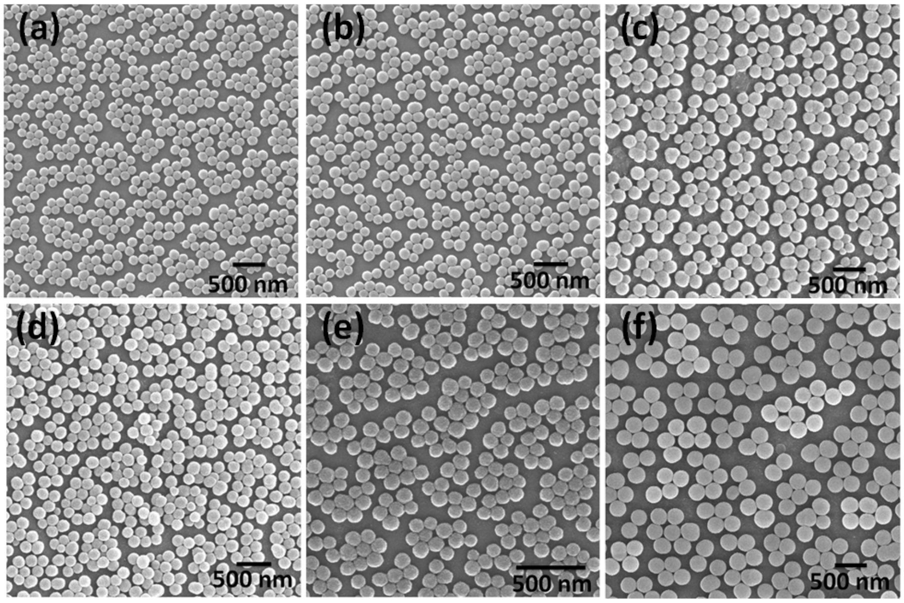

Figure 2.4. Representative SEM images of SMNP-0 (a), SMNP-1 (b), SMNP-2 (c), SMNP-3 (d), SMNP-4 (e), and SMNP-5 (f). Copyright 2016 American Chemical Society.[31]

The presence of high contrast metal elements inside the SMNP-4 was evident in high angle annular dark field (HAADF)-STEM and the bright field scanning transmission electron microscopy (BF-STEM) (Figure 2.5). Additionally, Figures 2.6 shows the selected area image of HAADF-

STEM and EDX, confirming the presence of iron (III) ions localized in the SMNP-4. Note that the EDX profiles indicated that the amount of Fe(III) in the testing area was much higher than that on the background, which is in good agreement with the mapping results (Figure 2.6). The Cu signal peak in the EDX profile is from the grid substrate.

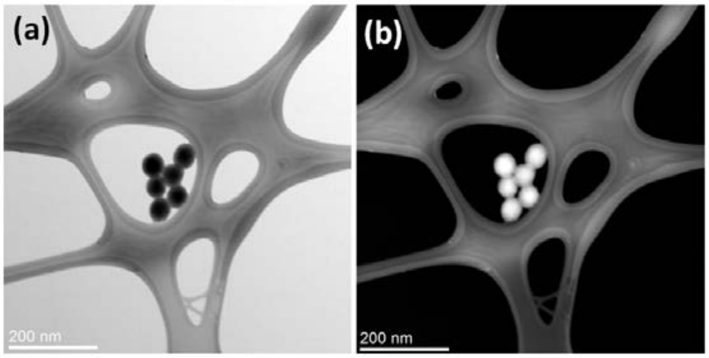

Figure 2.5. (a) BF-STEM and (b) HAADF-STEM images of SMNP-4. Copyright 2016 American Chemical Society.[31]

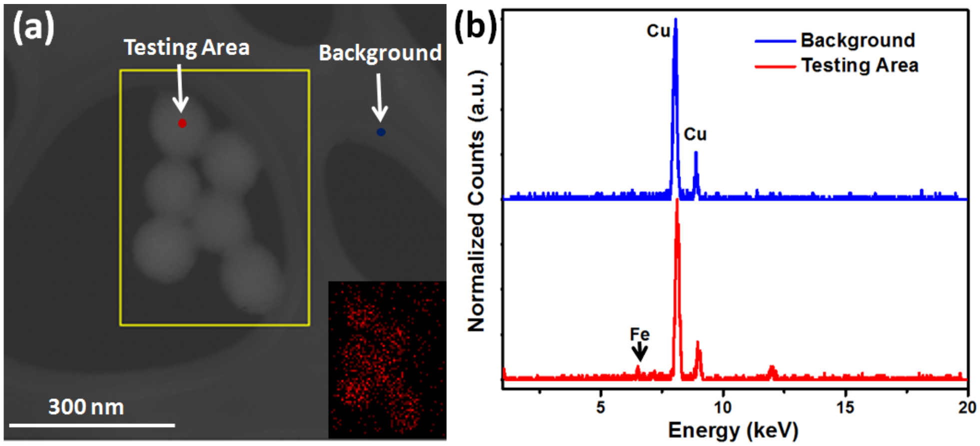

Figure 2.6. (a) HAADF-STEM image of SMNP-4 with the selected area chosen for EDS spectral mapping outlined with a yellow box. Insert in lower right is the EDS Fe elemental mapping image of the selected area; (b) EDS spectra of SMNP-4 from the testing area (red) and background (blue) in (a). Copyright 2016 American Chemical Society.[31]

2.3.3 Characterization of SMNPs NMRD and MR Imaging Analysis

The measurement of the longitudinal water proton relaxation rates (R_1) as a function of the applied magnetic field for the SMNP samples was then undertaken to assess their T_1 contrast enhancing ability. This experimental technique, known as Nuclear Magnetic Relaxation Dispersion (NMRD), allows accurate determination of the field dependence of R_1 from the dipolar interactions between water solvent and metal center.[32-33] Two types of paramagnetic relaxation are taken place: Inner sphere relaxation, which describes the exchange of bulk water and water molecule bound to the metal center. And outer sphere relaxation that represents the chemical exchange of second shell water molecules with the bulk water.

In Figure 2.7a, the ^{1}H NMRD profiles of SMNP-*i* (*i*=1-5) are measured at 298 K in the range 2.3 mT to 1.6 T. The y-axis is the relaxation rate enhancement induced by 1 mmol per liter of Fe(III), defined as r_{1p}. The NMRD profiles of the SMNP-2, 3, 4 and 5 show a similar trend. Below 1 MHz, the r_{1p} remains unchanged. The r_{1p} has a small decrease above 1MHz followed by an increase at above 30 MHz. The single dispersion at around 3 MHz corresponds to a correlation time $\tau_C \approx 9\times10^{-11}$ s. Because of the large τ_R values (slow rotational) of paramagnetic centers in these nanoparticles, we can safely attribute this correlation time to the τ_S (electronic relaxation time), which is in the range 10^{-11} s to 10^{-9} s.[34] The increase of r_{1p} at frequencies above 30 MHz indicates that τ_S is dependent on the field strength. Also, the electronic relaxation time is a predominant factor in determining the correlation time. Bertini et al reported the similar behavior in the example of different glycerol-water mixtures with Fe (III) ion. [35] The NMRD profile of SMNP-1 shows a more significant drop of r_{1p} value with the increase of frequency. This behavior resembles the general trend in iron-binding glycoprotein transferrin system.[36] These data indicate that for a certain population of the Fe(III), the water coordinate number of the Fe(III) center can be larger than 1 ($q\geq1$), However, an inspection of the shape and amplitude of the NMRD profiles suggests the occurrence of different contributions to the relaxivity. The outer sphere contribution is the predominant factor in the tris-dopamine-Fe(III) complex (water coordination number q=0). But this effect is relatively small based on the literature(about 1-2 $mM^{-1}\,s^{-1}$).[37] Although the second sphere contribution is often a limited factor in the polymer system, we have previously found that the presence of dynamic hydrogen bonding of water molecules to hydroxide ligands on or next to iron(III) center can significantly enhance the overall relaxivity of the polycatechol nanoparticles system.[38] Inner, second and outer sphere contributions are all the considerable parameters in determining SMNP nanoparticles' relaxation behavior, suggesting the presence of iron ions with different binding modes. The decrease of r_1 with the increase of the Fe-loading could reflect the increasing amount of coupled Fe(III) ions, which will be further discussed via the results from magnetometry.

Furthermore, we believe it is also interesting to consider the "per particle-relaxivity" of SMNPs to describe the local concentration of particles needed for achieving the desirable T_1 MR imaging under different magnetic fields,[39] which can be directly obtained via multiplying the concentration of Fe(III) per particle by the per-Fe(III) relaxivity value. Figure 2.7b shows the calculated per particle-relaxivity value of each SMNPs. It is observed that a continuous increase in relaxivity with increasing Fe (III) loading from 0.46% (SMNP-1) to 5.86%(SMNP-4) and a decrease from SMNP-4 to SMNP-5. From this result, it is suggested that the optimal sample is SMNP-4 with 5.86 % Fe(III) loading. We will discuss the origin of this effect in the next section.

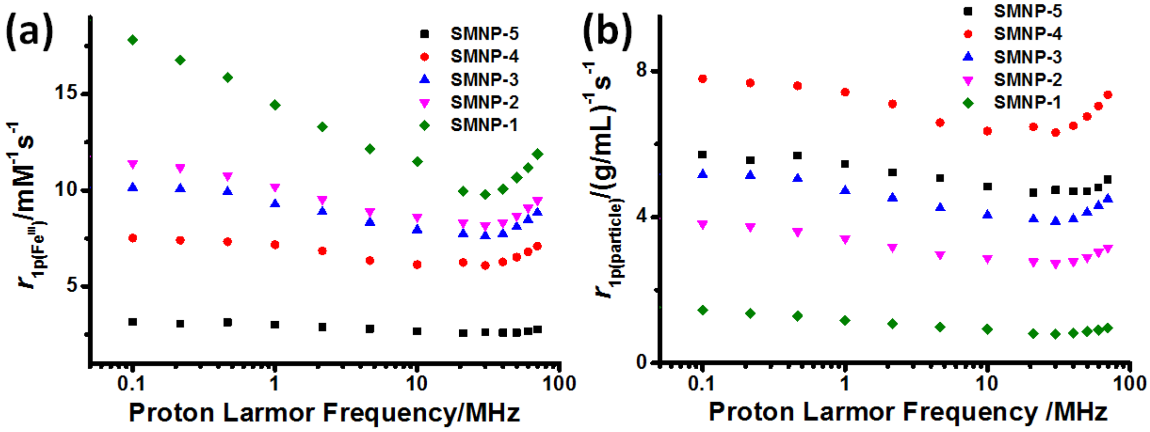

Figure 2.7. (a) ^{1}H NMRD profiles for SMNP-i (i=1-5). The x-axis is proton Larmor frequency, y-axis is r1 value per Fe(III) ion for each SMNP. (b)1H NMRD profiles for SMNP-i (i=1-5). The x-axis is proton Larmor frequency, y-axis is r1 value per particle for each SMNP. Copyright 2016 American Chemical Society.[31]

2.3.4 MR Imaging of SMNP Contrast Agents

The long-term stability of those SMNP MRI contrast agents in bio-fluid is vital to ensure their MR imaging performance *in vitro* and *in vivo*. To determine the stability of Fe(III) complex in SMNP-2, 3, 4 and 5, the nanoparticles were added in PBS solution. 300ul of the solution (three replicates) were added in a dialysis tubes respectively. The tubes were left for dialysis again PBS water for certain period. At each time, 20 ul of the sample solution was from the dialysis tube and sent for ICP-OES analysis. Figure 2.8 shows the stability result of each nanoparticle in PBS buffer. Notably, there is a negligible amount of Fe (III) releasing from the nanoparticles even after seven days. This result indicates the viability of *in vivo* use without the release of Fe.

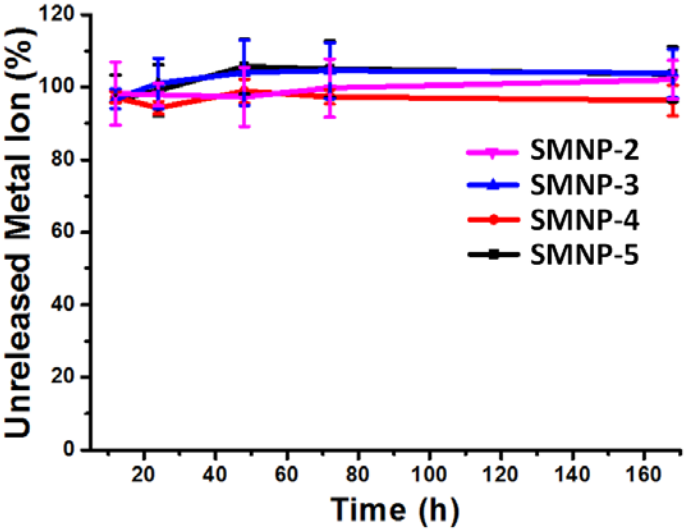

Figure 2.8. Stability study of Fe(III)-chelated SMNP-i (i=2-5) in PBS. Copyright 2016 American Chemical Society.[31]

The *in vitro* MRI enhancement ability of SMNPs was tested under a Bruker 7.0T magnet with Avance II hardware equipped with a 72 mm quadrature transmit/receive coil. The images were obtained in different media, such as water, PBS buffer, fetal bovine serum (FBS), and Dulbecco's Modified Eagle Medium (DMEM). SMNP-1 and SMNP-4 (optimal MRI particle as discussed above) were chosen as representative samples in this experiment and SMNP-0 was employed as the control. It was observed that both of SMNP-1 and SMNP-4 indeed show signal enhancement on the T_1-weighted MR images in different medium (Figure 2.9). Even after five days incubation with serum and DMEM, the bright MR images for both SMNP-1 and SMNP-4 samples maintain their intensity, suggesting the promising long-term stability of SMNPs in biological medium. In addition, images from the SMNP-4 are brighter (shorter T_1 relaxation) than the SMNP-1's under the same particle concentration (Figure 2.9). Moreover, a more systematic study was employed to investigate long-term MRI enhancement of SMNPs in water and cell culture medium (i.e. 90% DMEM with 10% FBS). Figure 2.10 shows that the freshly prepared SMNPs indeed show enhanced relaxivity in cell culture medium compared to the water. Even after five days incubation with cell culture medium, the relaxivity of the SMNPs doesn't decrease, confirming the promising long-term stability of SMNPs in cell culture medium. The slight increase in relaxivity values of SMNP nanoparticles might due to the interactions between nanoparticles and proteins in FBS.[40] Considering the data at the same nanoparticle concentration, SMNP-4 possess the best MRI performance *in vitro*.

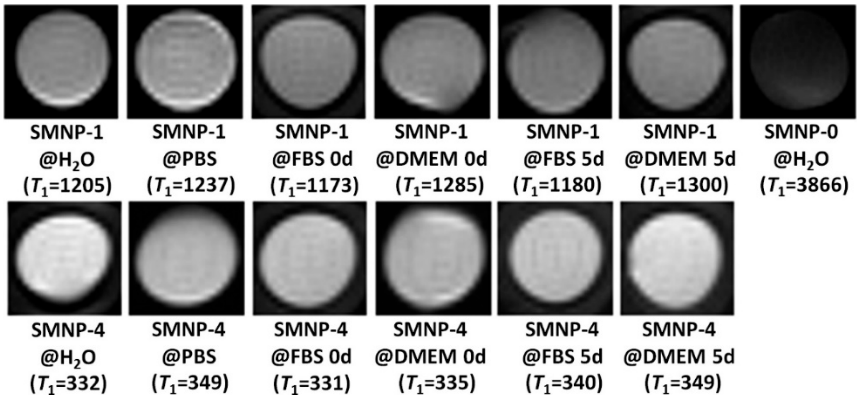

Figure 2.9. T1-weighted MR images captured on a Bruker 7.0 T magnet from SMNP-0, SMNP-1, and SMNP-4 in different media (particle concentration is 1.3 mg/mL in each tube). T1 results for each phantom are shown below in milliseconds, respectively. Copyright 2016 American Chemical Society.[31]

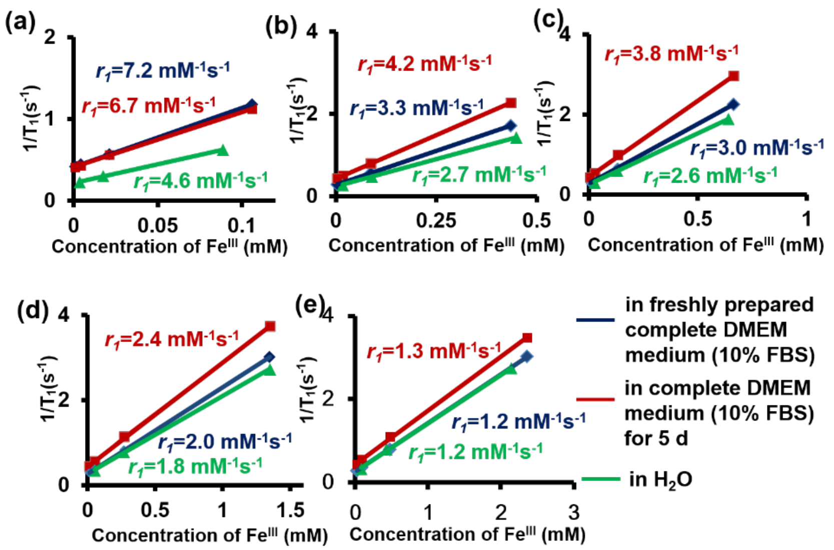

Figure 2.10. MRI characterization of SMNP-i (i=1-5) nanoparticles on a Bruker 7.0 T magnet. Plots of 1/T1 versus FeIII concentration for SMNP-i in different medium with calculated r1 (green plot: SMN-i in water, blue plot: SMNP-i in freshly prepared complete DMEM medium (10% FBS), red plot: SMNP-i in complete DMEM medium (10% FBS) for 5 d). (a) SMNP-1, (b) SMNP-2, (c) SMNP-3 , (d)SMNP-4, and (e) SMNP-5. Copyright 2016 American Chemical Society.[31]

Table 2.3. r_1 result for each sample shown in Figure 2.10.

Sample	r_1 (mM^{-1}s^{-1})	Sample	r_1 (mM^{-1}s^{-1})	Sample	r_1 (mM^{-1}s^{-1})
SMNP-1@H_2O	4.6	SMNP-1@DMEM 0d	7.2	SMNP-1@DMEM 5d	6.7
SMNP-2@H_2O	2.7	SMNP-2@DMEM 0d	3.3	SMNP-2@DMEM 5d	4.2
SMNP-3@H_2O	2.6	SMNP-3@DMEM 0d	3.0	SMNP-3@DMEM 5d	3.8
SMNP-4@H_2O	1.8	SMNP-4@DMEM 0d	2.0	SMNP-4@DMEM 5d	2.4
SMNP-5@H_2O	1.2	SMNP-5@DMEM 0d	1.2	SMNP-5@DMEM 5d	1.3

2.3.5 Magnetochemical Analysis of SMNPs

The magnetic properties of SMNP were first investigated by EPR technique. Figure 2.11 shows the EPR spectra of SMNPs collected from frozen solutions at 125 K. As is known to all, Fe(III) will reduce the amplitude of the free radical peak,[41] that is consistent with the profile of Figure 2.11a. The peak at 1600 G (g= 4.3) from spectra of SMNP-1, 2, 3, 4 and 5 is attributed to high spin Fe(III) in sites of low symmetry of tetrahedral or octahedral coordination.[42] The width of this peak increases with increased iron loading due to spin-spin dipolar coupling.[43] Figure 2.12 shows the change in the full width at half maximum as a function of total iron. The linear progression suggests that the iron loading is evenly distributed in a 3-D matrix of sites, as opposed to either lower dimensional arrangements or clusters. For a random distribution of sites, the broadening is proportional to the concentration raised to $4 - D$, with D being the effective dimensionality.[44] Thus for $D = 3$, a linear dependence is produced, while for $D = 2$ (a plane or the surface of a sphere) the function displays the downward curvature of a parabola. For clusters, the function is bowed in the upward direction. This is because the bulk of the broadening occurs as soon as a cluster is formed; additional concentration mainly adds to the amplitude but has a limited effect on spectral width.

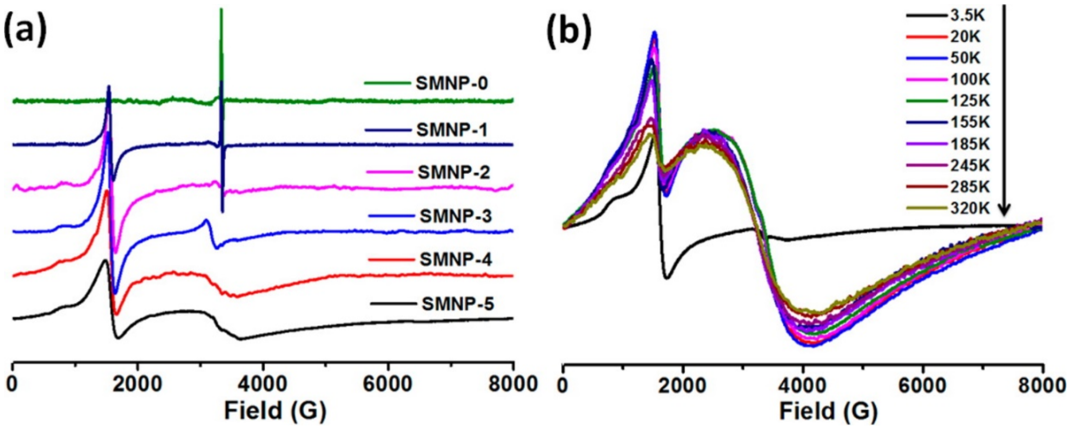

Figure 2.11. (a) Experimental EPR spectra of SMNP-i (i = 0–5). (b) Temperature-dependent EPR analysis of SMNP-5. Copyright 2016 American Chemical Society.[31]

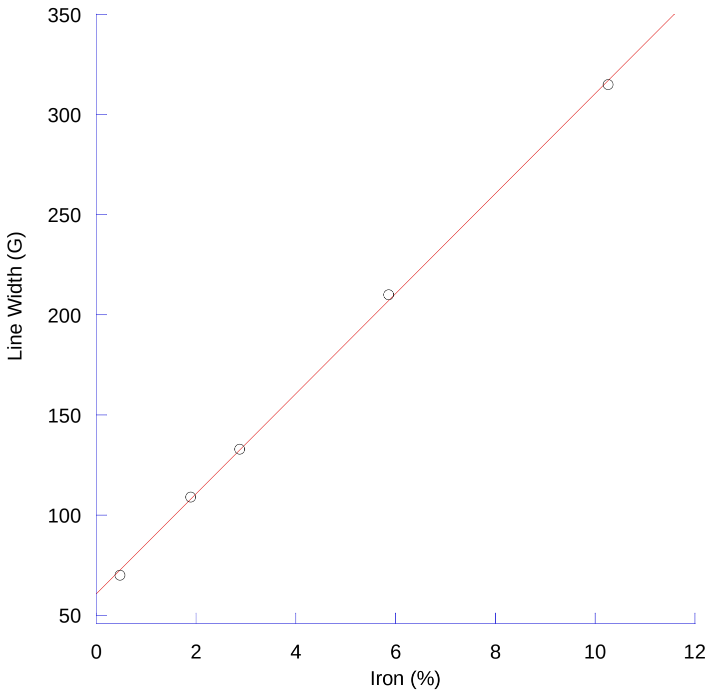

Figure 2.12. Line width of g=4.3 EPR spectrum as a function of iron. Black circles, line width from data acquired at 125 K. Red line is first order fit of data showing that line width increases linearly with iron content. Copyright 2016 American Chemical Society.[31]

The spectrum of SMNP-5 shows a broad peak centered around 3400G, indicating the formation of superparamagnetic or ferromagnetic iron oxide nanoparticles. To exclude the formation of superparamagnetic or ferromagnetic nanoparticles, a variable-temperature experiment was done on the SMNP-5.[45] Figure 2.11b shows that this peak increases in amplitude from 320K to 20 K, but then suddenly decreased at 3.5 K. This phenomenon is consistent with the existence of a weak antiferromagnetic coupling between iron centers in SMNP-5. By contrast, the ferromagnetic material would have a constant intensity of this peak whereas the peak of superparamagnetic material would shift to the lower field when the temperature is lowered. Together these results yield a structural model of SMNP with a capacity for 2-5% iron in isolated sites, with higher amounts of iron going to species that experience antiferromagnetic coupling. Both species are spatially distributed throughout the synthetic melanin.

The magnetic properties of SMNP were then investigated by variable-temperature magnetic susceptibility measurements from 2 to 300 K under a 5000 Oe magnetic field (Figure 2.13). SMNP-1 which has the lowest Fe(III) loading was expected to largely exhibit feature of isolated octahedral high-spin d^5 of Fe (III) (g=2, S=5/2). The value of magnetic susceptibility times temperature per mole Fe ($\chi_M T$) at a temperature of 300 K approaches the expected value of spin-only Fe(III) sample (4.375 emu K cm^{-3} mol^{-1}). This close agreement indicates that there is a negligible amount of Fe(II) and low-spin Fe(III) populations since these species have significantly different $\chi_M T$ value. When temperature decreased from 300 K, antiferromagnetic coupling interaction between Fe(III) center starts to manifest the $\chi_M T$ value. For example, SMNP-1 has a 0.46% (by weight percentage) iron loading, therefore most of the iron(III) centers are sufficiently isolated so that they display an entirely uncoupled moment. However, when Fe(III) loading starts to increase, the Fe(III) centers are so close to each other that the antiferromagnetic interactions manifest the $\chi_M T$ data. For example, SMNP-5 has a Fe(III) loading as high as 10.26% thus the system exists strong antiferromagnetic interactions that lead to a decrease of more than 20% of the $\chi_M T$ value at room temperature. This data is consistent with the conclusion from the EPR data.

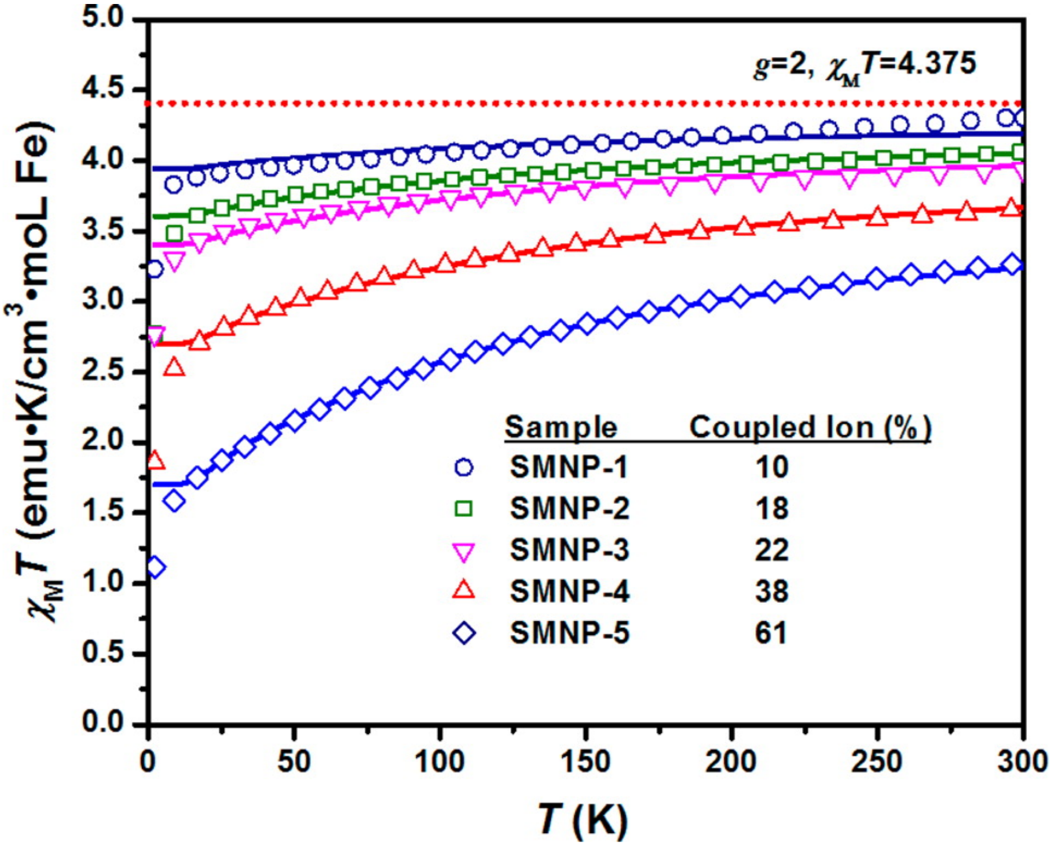

Figure 2.13. Temperature dependence of the product of magnetic susceptibility and temperature (χMT) for SMNP-i (i = 1–5). The dotted line describes the behavior of an isolated, isotropic Fe(III) ion. Solid lines represent a global fit of the data between 25 and 300 K as described in the text. Copyright 2016 American Chemical Society.[31]

It might be expected that modeling the magnetic properties and calculating the amount of coupled Fe(III) in this complex system would be prone to overparameterization. However, we use a simplified model, that is, introducing anisotropic *g* value as well as magnetic coupling constant ($J_{\mathrm{Fe-Fe}}$) to describe the coupling behavior of Fe(III). In this model, we only take consideration of magnetically isolated and magnetically coupled Fe(III) centers, based on the assumptions that catechol groups on the polydopamine surface provide weak superexchange. In general, small molecular Fe(III) catecholates have a coupling constants of less than 30 cm^{-1}.[46-48] The ratio between the magnetically isolated Fe(III) and magnetically coupled Fe(III) is fitted along with an isotropic g and $J_{\mathrm{Fe-Fe}}$ value by simultaneous global fitting of magnetic susceptibility. In the fitting, isolated Fe(III) is regarded as the ideal paramagnetic Fe(III) (*S*=5/2). By contrast, magnetically coupled

Fe(III) is calculated via an HDVV Hamiltonian (Eq. 1) where $\hat{\boldsymbol{S}}_{\boldsymbol{1}}$ and $\hat{\boldsymbol{S}}_{\boldsymbol{2}}$ are spin operators for equivalent interacting spins. It is noted that we don't consider radical electrons contribution from the polydopamine in our model, since the control sample (SMNP-0) shows no paramagnetic moment from 0 to 300K (Figure 2.14).

$$\hat{\boldsymbol{H}} = -2J_{\mathrm{Fe-Fe}}\,\hat{\boldsymbol{S}}_{\boldsymbol{1}} \cdot \hat{\boldsymbol{S}}_{\boldsymbol{2}} \qquad \text{(Eq 1)}$$

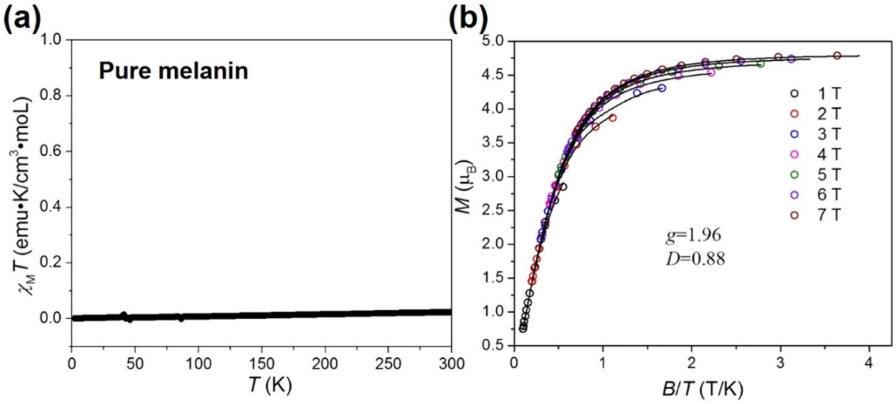

Figure 2.14. (a) Plot of the product of temperature and magnetic susceptibility vs. temperature (χMT) for SMNP-0. (b) Low-temperature magnetization data under different applied fields for SMNP-1. The black lines represent fits to data. Copyright 2016 American Chemical Society.[31]

The global fit data of g value (2.05±0.04) and magnetic coupling constant $J_{\mathrm{Fe-Fe}}$ (−24.8±2.7 cm^{-1}) fits well to the small molecular Fe-catecholate systems.[46, 49-50] It is noted that for SMNP-5 sample, there is very high level (61%) of coupled ion (Figure 2.13). Compared this data with the MRI result, the low relaxivity value of high loading sample is attribute to the strong antiferromagnetic coupling effect that lower the magnetic moment compared with less concentrated samples. The strong antiferromagnetic coupling also indicates that short Fe-Fe bridges can exist within the polydopamine structure, consistent with our synthetic conditions (pH ~9) at which the bis- and tris-Fe(III)-dopamine complexes exist.[51]

Since a high dopamine coordination number to Fe(III) (e.g. tris-Fe-dopamine complex) can hinder the formation of super-exchange bridges, we investigate the dopamine coordination number to Fe(III) via scrutinizing the deviations from ideal Fe(III) behavior obtained at low temperature. A set of low-temperature and variable- field experiments were designed on the SMNP-1 to isolate the effects of magnetic anisotropy (Figure 2.15), since SMNP-1 has the minimized antiferromagnetic coupling. We use an axially anisotropic Hamiltonian (Eq. 2) in the MagProp module of DAVE 2.3 to fit the data.[52] Interestingly, we find a small axial anisotropy (*D* = 0.88±0.29) that agree with the mono- Fe(III)-catechol value in acidic solution (*D* = 0.82). In contrast, bis- and tris-Fe-catechol complexes have much lower values (*D* = 0.42 and *D* = 0.32, respectively).[27] We also measure SMNP-2, 3, 4 and 5. Figure 2.16 shows that all of these samples have much higher axial anisotropy than bis- and tris-Fe-catechol complexes. The less agreement with the mono-Fe(III)-catechol value is due to the strong antiferromagnetic coupling in these high Fe(III) loading samples.

$$\hat{\boldsymbol{H}} = g\mu_{\mathrm{B}}\hat{\boldsymbol{S}} \cdot \boldsymbol{B} + D[\hat{\boldsymbol{S}}_{\boldsymbol{z}}^{\boldsymbol{2}} - \frac{\boldsymbol{S(S+1)}}{\boldsymbol{3}}] \qquad \text{(Eq 2)}$$

The above magnetic evidence strongly suggests that despite the high concentration of catechol in SMNP materials and pH values during synthesis that should initially favor a tris-catechol binding mode, Fe(III) is largely coordinated as the mono-catechol in the final product. UV-vis spectroscopy is employed to support the magnetic fitting data. Figure 2.15b confirms that SMNP-3 and 5 exhibit a characteristic mono-Fe(III)-catechol peak at 710 nm (green dot line).[26, 51, 53] From all the data discussed above, we can summarize that the Fe(III) tends to form antiferromagnetic coupling interactions at high iron concentration. Additionally, we found the evidence of existence for the low coordination number of dopamine to Fe(III) species (mono-Fe(III) -dopamine) that enables the water exchange through an “inner-sphere” mechanism.

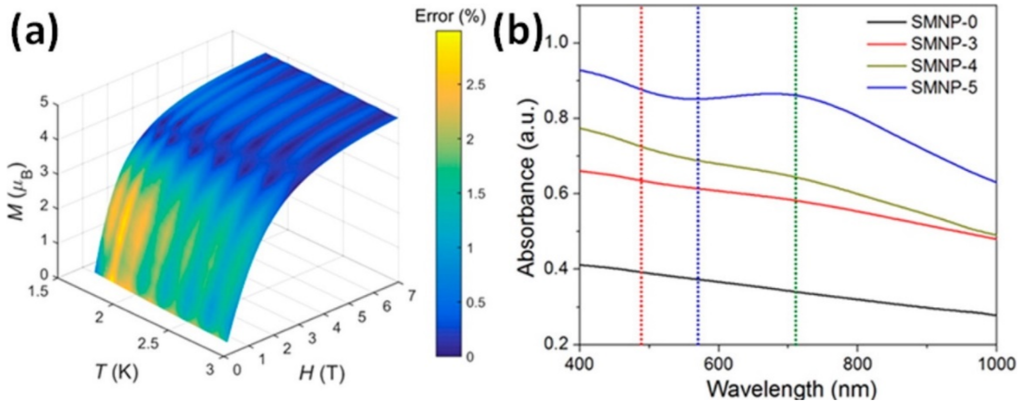

Figure 2.15. (a) Plot of variable-temperature variable-field magnetization data for SMNP-1. The color bar represents the difference between experimental data and fitting results. A standard 2D M vs H/T plot is shown in Figure 2.14b. (b) UV–vis spectra of 0.1 mg/mL SMNP showing the transition from a featureless absorption for SMNP-0 to a well-defined yet broad structure in SMNP-5. Absorption peaks for mono- (~710 nm), bis- (~570 nm), and tris-catechol (~490 nm) are identified by dashed green, blue, and red lines, respectively. Copyright 2016 American Chemical Society.[31]

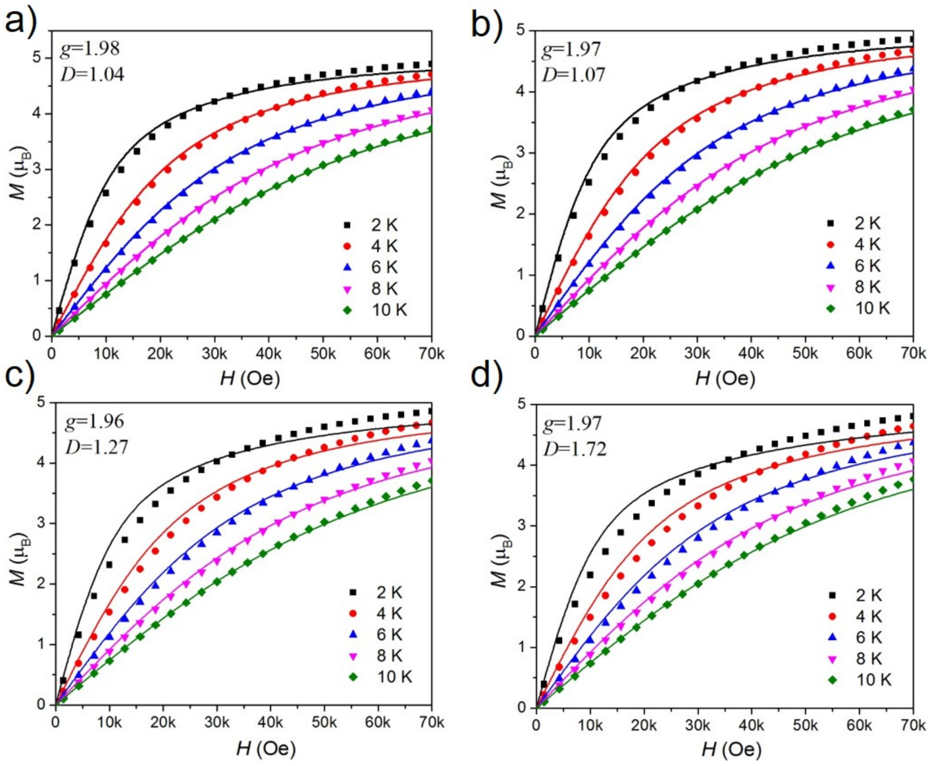

Figure 2.16. Low-temperature magnetization data under different applied fields for (a) SMNP-2; (b) SMNP-3; (c) SMNP-4; (d) SMNP-5. The black lines represent fits to data. Copyright 2016 American Chemical Society.[31]

2.4 Conclusion

In summary, a new technique for accessing SMNPs with tunable iron loadings has opened the door for their magneto-structural analysis through the combined utilization of SQUID magnetometry, EPR and ^{1}H NMRD. These analyses provide the opportunity for a fundamental understanding of the electronic and magnetic structure. The results give some suggestions on optimizing MRI performance of Fe(III)-loaded synthetic melanin nanoparticles: (1) It was demonstrated that high Fe(III) loading leads to a lowering of the moment per Fe(III) center due to antiferromagnetic coupling. Thus, lower coupling effect between paramagnetic centers would necessarily increase the magnetic moment at higher loadings. In the following chapters, we will demonstrate the synthesis of highly effective contrast agents via incorporating higher-spin, weaker-coupling ions such as manganese and gadolinium.

2.5 Acknowledge

Chapter 2 is adapted in full print from Yiwen Li,[a] Yijun Xie,[a] Zhao Wang,[a] Nanzhi Zang, Fabio Carniato, Yuran Huang, Christopher M. Andolina, Lucas R. Parent, Treffly B. Ditri, Eric D. Walter, Mauro Botta, Jeffrey D. Rinehart,* Nathan C. Gianneschi,* "Structure and Function of Iron-Loaded Synthetic Melanin" ACS Nano, 2016, 10, 10186-10194.; Copyright 2016 American Chemical Society. The dissertation author is the co-first author of this chapter. For the Chapter 2, I would like to thank Dr. Yiwen Li for initiate this project. I also appreciate my colleague Yuran Huang, Nanzhi Zang, Dr. Lucas R. Parent and Dr. Treffly B. Ditri to provide help of synthesis and characterization of nanoparticles used in this project. Thanks to our collaborators, Fabio Carniato, Christopher M. Andolina, Eric D. Walter and Dr. Mauro Botta for providing their contributions to the characterization of our nanoparticles. Moreover, I appreciate the help from Yijun Xie and Prof.

Jeffrey D. Rinehart about the discussion and analysis of magnetic properties of our nanoparticles and Prof. Nathan Gianneschi for the design and guidance of the entire project.

2.6 References

1. d’Ischia, M.; Napolitano, A.; Ball, V.; Chen, C.-T.; Buehler, M. J., Polydopamine and Eumelanin: From Structure–Property Relationships to a Unified Tailoring Strategy. *Accounts of Chemical Research* **2014,** *47* (12), 3541-3550.

2. Dadachova, E.; Casadevall, A., Ionizing radiation: how fungi cope, adapt, and exploit with the help of melanin. *Current Opinion in Microbiology* **2008,** *11* (6), 525-531.

3. Burtt, E. H.; Schroeder, M. R.; Smith, L. A.; Sroka, J. E.; McGraw, K. J., Colourful parrot feathers resist bacterial degradation. *Biology Letters* **2011,** *7* (2), 214-216.

4. Hung, Y.-C.; Sava, V. M.; Juang, C.-L.; Yeh, T.-c.; Shen, W.-C.; Huang, G. S., Gastrointestinal enhancement of MRI with melanin derived from tea leaves (Thea sinensis Linn.). *Journal of Ethnopharmacology* **2002,** *79* (1), 75-79.

5. Wang, Z.; Li, C.; Xu, J.; Wang, K.; Lu, X.; Zhang, H.; Qu, S.; Zhen, G.; Ren, F., Bioadhesive Microporous Architectures by Self-Assembling Polydopamine Microcapsules for Biomedical Applications. *Chemistry of Materials* **2015,** *27* (3), 848-856.

6. Liu, A.; Zhao, L.; Bai, H.; Zhao, H.; Xing, X.; Shi, G., Polypyrrole Actuator with a Bioadhesive Surface for Accumulating Bacteria from Physiological Media. *ACS Applied Materials & Interfaces* **2009,** *1* (4), 951-955.

7. Lee, H.; Dellatore, S. M.; Miller, W. M.; Messersmith, P. B., Mussel-Inspired Surface Chemistry for Multifunctional Coatings. *Science* **2007,** *318* (5849), 426-430.

8. Waite, J. H., Surface chemistry: Mussel power. *Nature Materials* **2008,** *7* (1), 8-9.

9. Zeng, H.; Hwang, D. S.; Israelachvili, J. N.; Waite, J. H., Strong reversible Fe3+-mediated bridging between dopa-containing protein films in water. *Proceedings of the National Academy of Sciences of the United States of America* **2010,** *107* (29), 12850-12853.

10. d'Ischia, M.; Napolitano, A.; Pezzella, A.; Meredith, P.; Sarna, T., Chemical and Structural Diversity in Eumelanins: Unexplored Bio-Optoelectronic Materials. *Angewandte Chemie International Edition* **2009,** *48* (22), 3914-3921.

11. Ju, K.-Y.; Lee, Y.; Lee, S.; Park, S. B.; Lee, J.-K., Bioinspired Polymerization of Dopamine to Generate Melanin-Like Nanoparticles Having an Excellent Free-Radical-Scavenging Property. *Biomacromolecules* **2011,** *12* (3), 625-632.

12. Liu, Y.; Ai, K.; Lu, L., Polydopamine and Its Derivative Materials: Synthesis and Promising Applications in Energy, Environmental, and Biomedical Fields. *Chemical Reviews* **2014,** *114* (9), 5057-5115.

13. Gao, H.; Sun, Y.; Zhou, J.; Xu, R.; Duan, H., Mussel-Inspired Synthesis of Polydopamine-Functionalized Graphene Hydrogel as Reusable Adsorbents for Water Purification. *ACS Applied Materials & Interfaces* **2012,** *5* (2), 425-432.

14. Xie, Y.; Yan, B.; Xu, H.; Chen, J.; Liu, Q.; Deng, Y.; Zeng, H., Highly Regenerable Mussel-Inspired Fe3O4@Polydopamine-Ag Core–Shell Microspheres as Catalyst and Adsorbent for Methylene Blue Removal. *ACS Applied Materials & Interfaces* **2014,** *6* (11), 8845-8852.

15. Huang, S.; Yang, L.; Liu, M.; Phua, S. L.; Yee, W. A.; Liu, W.; Zhou, R.; Lu, X., Complexes of Polydopamine-Modified Clay and Ferric Ions as the Framework for Pollutant-Absorbing Supramolecular Hydrogels. *Langmuir* **2013,** *29* (4), 1238-1244.

16. Liu, Y.; Ai, K.; Liu, J.; Deng, M.; He, Y.; Lu, L., Dopamine-Melanin Colloidal Nanospheres: An Efficient Near-Infrared Photothermal Therapeutic Agent for In Vivo Cancer Therapy. *Advanced Materials* **2013,** *25* (9), 1353-1359.

17. Stritzker, J.; Kirscher, L.; Scadeng, M.; Deliolanis, N. C.; Morscher, S.; Symvoulidis, P.; Schaefer, K.; Zhang, Q.; Buckel, L.; Hess, M.; Donat, U.; Bradley, W. G.; Ntziachristos, V.; Szalay, A. A., Vaccinia virus-mediated melanin production allows MR and optoacoustic deep tissue imaging and laser-induced thermotherapy of cancer. *Proceedings of the National Academy of Sciences of the United States of America* **2013,** *110* (9), 3316-3320.

18. Xiao, M.; Li, Y.; Allen, M. C.; Deheyn, D. D.; Yue, X.; Zhao, J.; Gianneschi, N. C.; Shawkey, M. D.; Dhinojwala, A., Bio-Inspired Structural Colors Produced via Self-Assembly of Synthetic Melanin Nanoparticles. *ACS Nano* **2015,** *9* (5), 5454-5460.

19. Wu, T.-F.; Hong, J.-D., Dopamine-Melanin Nanofilms for Biomimetic Structural Coloration. *Biomacromolecules* **2015,** *16* (2), 660-666.

20. Kohri, M.; Nannichi, Y.; Taniguchi, T.; Kishikawa, K., Biomimetic non-iridescent structural color materials from polydopamine black particles that mimic melanin granules. *Journal of Materials Chemistry C* **2015,** *3* (4), 720-724.

21. Krogsgaard, M.; Behrens, M. A.; Pedersen, J. S.; Birkedal, H., Self-Healing Mussel-Inspired Multi-pH-Responsive Hydrogels. *Biomacromolecules* **2013,** *14* (2), 297-301.

22. Li, L.; Smitthipong, W.; Zeng, H., Mussel-inspired hydrogels for biomedical and environmental applications. *Polymer Chemistry* **2015,** *6* (3), 353-358.

23. Guo, L.; Liu, Q.; Li, G.; Shi, J.; Liu, J.; Wang, T.; Jiang, G., A mussel-inspired polydopamine coating as a versatile platform for the in situ synthesis of graphene-based nanocomposites. *Nanoscale* **2012,** *4* (19), 5864-5867.

24. Ju, K.-Y.; Lee, J. W.; Im, G. H.; Lee, S.; Pyo, J.; Park, S. B.; Lee, J. H.; Lee, J.-K., Bio-Inspired, Melanin-Like Nanoparticles as a Highly Efficient Contrast Agent for T1-Weighted Magnetic Resonance Imaging. *Biomacromolecules* **2013,** *14* (10), 3491-3497.

25. Borg, D. C., TRANSIENT FREE RADICAL FORMS OF HORMONES: EPR SPECTRA FROM CATECHOLAMINES AND ADRENOCHROME. *Proceedings of the National Academy of Sciences of the United States of America* **1965,** *53* (3), 633-639.

26. Sever, M. J.; Weisser, J. T.; Monahan, J.; Srinivasan, S.; Wilker, J. J., Metal-Mediated Cross-Linking in the Generation of a Marine-Mussel Adhesive. *Angewandte Chemie International Edition* **2004,** *43* (4), 448-450.

27. Weisser, J. T.; Nilges, M. J.; Sever, M. J.; Wilker, J. J., EPR Investigation and Spectral Simulations of Iron−Catecholate Complexes and Iron−Peptide Models of Marine Adhesive Cross-Links. *Inorganic Chemistry* **2006,** *45* (19), 7736-7747.

28. Burlamacchi, L.; Lai, A.; Monduzzi, M.; Saba, G., NMR, EPR, and INDO Studies on the complexes of dopamine with Cu2+, Mn2+, and Fe3+ in aqueous solution. *Journal of Magnetic Resonance (1969-1992)* **1983,** *55* (1), 39-50.

29. Lucarini, M.; Pedulli, G. F.; Guerra, M., A Critical Evaluation of the Factors Determining the Effect of Intramolecular Hydrogen Bonding on the O□H Bond Dissociation Enthalpy of Catechol and of Flavonoid Antioxidants. *Chemistry – A European Journal* **2004,** *10* (4), 933-939.

30. Ai, K.; Liu, Y.; Ruan, C.; Lu, L.; Lu, G., Sp2 C-Dominant N-Doped Carbon Sub-micrometer Spheres with a Tunable Size: A Versatile Platform for Highly Efficient Oxygen-Reduction Catalysts. *Advanced Materials* **2013,** *25* (7), 998-1003.

31. Li, Y.; Xie, Y.; Wang, Z.; Zang, N.; Carniato, F.; Huang, Y.; Andolina, C. M.; Parent, L. R.; Ditri, T. B.; Walter, E. D.; Botta, M.; Rinehart, J. D.; Gianneschi, N. C., Structure and Function of Iron-Loaded Synthetic Melanin. *ACS Nano* **2016,** *10* (11), 10186-10194.

32. Koenig, S. H.; Brown 3rd, R. D.; Spiller, M.; Chakrabarti, B.; Pande, A., Intermolecular protein interactions in solutions of calf lens alpha-crystallin. Results from 1/T1 nuclear magnetic relaxation dispersion profiles. *Biophysical Journal* **1992,** *61* (3), 776-785.

33. Aime, S.; Botta, M.; Terreno, E., Gd(III)-BASED CONTRAST AGENTS FOR MRI. In *Advances in Inorganic Chemistry*, Academic Press: 2005; Vol. Volume 57, pp 173-237.

34. Bertini, I., C. Luchinat, and G. Parigi., Chapter 5 Transition metal ions: Shift and relaxation. In *Current Methods in Inorganic Chemistry*, Ivono Bertini, C. L.; Giacomo, P., Eds. Elsevier: 2001; Vol. Volume 2, pp 143-203.

35. Bertini, I.; Capozzi, F.; Luchinat, C.; Xia, Z., Nuclear and electron relaxation of hexaaquairon(3+). *The Journal of Physical Chemistry* **1993,** *97* (6), 1134-1137.

36. Bertini, I.; Galas, O.; Luchinat, C.; Messori, L.; Parigi, G., A theoretical analysis of the 1H nuclear magnetic relaxation dispersion profiles of diferric transferrin. *The Journal of Physical Chemistry* **1995,** *99* (39), 14217-14222.

37. Bertini, I.; Luchinat, C.; Nerinovski, K.; Parigi, G.; Cross, M.; Xiao, Z.; Wedd, A. G., Application of NMRD to Hydration of Rubredoxin and a Variant Containing a (Cys-S)3FeIII(OH) Site. *Biophysical Journal* **2003,** *84* (1), 545-551.

38. Li, Y.; Huang, Y.; Wang, Z.; Carniato, F.; Xie, Y.; Patterson, J. P.; Thompson, M. P.; Andolina, C. M.; Ditri, T. B.; Millstone, J. E.; Figueroa, J. S.; Rinehart, J. D.; Scadeng, M.; Botta, M.; Gianneschi, N. C., Polycatechol Nanoparticle MRI Contrast Agents. *Small* **2016,** *12* (5), 668-677.

39. Sitbon, G.; Bouccara, S.; Tasso, M.; Francois, A.; Bezdetnaya, L.; Marchal, F.; Beaumont, M.; Pons, T., Multimodal Mn-doped I-III-VI quantum dots for near infrared fluorescence and magnetic resonance imaging: from synthesis to in vivo application. *Nanoscale* **2014,** *6* (15), 9264-9272.

40. Caravan, P., Protein-Targeted Gadolinium-Based Magnetic Resonance Imaging (MRI) Contrast Agents: Design and Mechanism of Action. *Accounts of Chemical Research* **2009,** *42* (7), 851-862.

41. Sarna, T.; Hyde, J. S.; Swartz, H. M., Ion exchange in melanin: an electron spin resonance study with lanthanide probes. *Science* **1976,** *192*, 1132-1134.

42. Aime, S.; Bergamasco, B.; Biglino, D.; Digilio, G.; Fasano, M.; Giamello, E.; Lopiano, L., EPR investigations of the iron domain in neuromelanin. *Biochim. Biophys. Acta, Mol. Basis Dis.* **1997,** *1361*, 49-58.
43. Rabenstein, M. D.; Shin, Y.-K., Determination of the distance between two spin labels attached to a macromolecule. *Proc. Natl. Acad. Sci. U. S. A.* **1995,** *92*, 8239-8243.

44. Sebby, K. B.; Walter, E. D.; Usselman, R. J.; Cloninger, M. J.; Singel, D. J., End-group distributions of multiple generations of spin-labeled PAMAM dendrimers. *J. Phys. Chem. B* **2011,** *115*, 4613-4620.

45. Usselman, R. J.; Russek, S. E.; Klem, M. T.; Allen, M. A.; Douglas, T.; Young, M.; Idzerda, Y. U.; Singel, D. J., Temperature dependence of electron magnetic resonance spectra of iron oxide nanoparticles mineralized in Listeria innocua protein cages. *J. Appl. Phys.* **2012,** *112*, 084701.

46. Grillo, V. A.; Hanson, G. R.; Wang, D.; Hambley, T. W.; Gahan, L. R.; Murray, K. S.; Moubaraki, B.; Hawkins, C. J., Synthesis, X-ray Structural Determination, and Magnetic Susceptibility, Mössbauer, and EPR Studies of (Ph4P)2[Fe2(Cat)4(H2O)2]·6H2O, a Catecholato-Bridged Dimer of Iron(III). *Inorganic Chemistry* **1996,** *35* (12), 3568-3576.

47. Anderson, B. F.; Web, J.; Buckingham, D. A.; Robertson, G. B., Crystal and molecular structure of piperidinium μ-acetato-di-μ-1,2-benzenediolato-bis-1,2-benzenediolatoferrate(III), (C5H12N)3 [(CH3COO){Fe(C6H4O2)2}2]: a compound of relevance to the 2Fe-active site of the respiratory protein hemerythrin. *Bioinorganic Chemistry* **1982,** *16* (1), 21-32.

48. Ainscough, E. W.; Brodie, A. M.; McLachlan, S. J.; Brown, K. L., The reaction of 1,1[prime or minute]-biphenyl-2,2[prime or minute]-dial with iron(III) and the crystal structure of piperidinium bis[[small micro]-(1,1[prime or minute]-biphenyl-2,2[prime or minute]-diolato-O,[small micro]-O[prime or minute])(1,1[prime or minute]-biphenyl-2,2[prime or minute]-diolato-O,O[prime or minute])ferrate(III)]-ethanol(1/2). *Journal of the Chemical Society Dalton Transactions* **1983,** (7), 1385-1389.

49. Gorun, S. M.; Lippard, S. J., Magnetostructural correlations in magnetically coupled (.mu.-oxo)diiron(III) complexes. *Inorganic Chemistry* **1991,** *30* (7), 1625–1630.

50. Taylor, S. W.; Chase, D. B.; Emptage, M. H.; Nelson, M. J.; Waite, J. H., Ferric Ion Complexes of a DOPA-Containing Adhesive Protein from Mytilus edulis. *Inorganic Chemistry* **1996,** *35* (26), 7572-7577.

51. Holten-Andersen, N.; Harrington, M. J.; Birkedal, H.; Lee, B. P.; Messersmith, P. B.; Lee, K. Y. C.; Waite, J. H., pH-induced metal-ligand cross-links inspired by mussel yield self-healing polymer networks with near-covalent elastic moduli. *Proceedings of the National Academy of Sciences of the United States of America* **2011,** *108* (7), 2651-2655.

52. Azuah, R. T.; Kneller, L. R.; Qiu, Y., DAVE: A Comprehensive Software Suite for the Reduction, Visualization, and Analysis of Low Energy Neutron Spectroscopic Data. *Journal of Research of the National Institute of Standards & Technology* **2009,** *114* (6), 341-358.

53. Sever, M. J.; Wilker, J. J., Visible absorption spectra of metal-catecholate and metal-tironate complexes. *Dalton Transactions* **2004,** (7), 1061-1072.

Chapter 3

Tunable, Metal-Loaded Synthetic Melanin Nanoparticles Analyzed by Magnetometry

3.1Introduction

We have introduced the concept of melanin and their synthetic mimics in the past charters. A general approach to produce this kind of metal-polydopamine hybrid material involves the synthesis of colloidal polydopamine nanoparticles followed by post-synthetic chelation with aqueous solutions of the metal ion of interest. A variety of applications for metal-polydopamine hybrid materials have been identified because of the marked effect the identity of the metal ion has on the properties of the PDA. For example, Fe(III) and Mn(II)-doped polydopamine have been used for magnetic resonance imaging (MRI) contrast agents and photothermal therapy,[1-2] while Cu(II)-doped polydopamine has been utilized for positron emission tomography (PET).[3]

To date, the post-doping strategy has been routinely employed for the preparation of metal-doped polydopamine nanoparticles with metal ions possessing a strong affinity for the catechol binding sites in polydopamine.[4-6] However, this strategy requires that metal ion precursors are both stable and highly soluble in water, precluding the use of insoluble metal complexes such as Manganese(III) acetylacetonate in the synthesis metal-doped polydopamine nanoparticles. In addition, we mentioned in the last chapter that this post-doing strategy yields polydopamine with less than 1% by mass metal loading and requires multiple steps. [1, 7] In chapter 2, we discuss the solution of these problems by developing a one-pot synthesis (pre-doping strategy) of high Fe(III)-loaded synthetic melanin nanoparticles through molecular chelation of Fe(III) ions to the monomeric precursors to dopamine polymerization (Figure 2.1). In general, the post-doping synthesis of polydopamine nanoparticle requires overnight reaction to achieve maximal Fe(III) incorporation and has limited Fe(III) loading (1% by weight), while the pre-doping strategy is complete within 2 hours and can produce polydopamine nanoparticles with up to 10% iron loading. It was found that these Fe(III)-loaded synthetic melanin nanoparticles show improved MRI contrast and low cytotoxicity when compared to those produced by post- doping strategy. Despite these advantages, it is still challenging to prepare this kind of materials for controllable metal loadings of a variety of different metal ions other than Fe(III). Therefore, we will discuss the preparation of synthetic melanin nanoparticles with six different metal ions: Mn(III), Co(II), Ni(II), Cu(II), Zn(II), and Ga(III) in this chapter. An essential aspect of natural melanin is its ability to extract metals from the environment and chelate them to coordination sites within the polymer framework.[8-9] The depth and breadth of this study will uncover a wide variety of the metal environment in synthetic melanin that has not been studied before, exposing new bioinorganic coordination chemistry and functionality.

Critical to the desired application of nanoparticles is the precise manipulation of the nanoparticle (size, morphology, and functionalities), thus a detailed understanding of the parameters governing particle growth, aggregation, and morphology is particularly vital for guiding the development of metal-loaded synthetic melanin nanoparticles. Recently, Lee *et al.* reported that the size of polydopamine nanoparticles can be controlled by tailoring experimental parameters, such as pH, and dopamine concentration.[10] However, the addition of metal ions pre-polymerization serves as a new influencing factor on particle growth, and it is important to establish how the addition of this new variable changes the dynamics of particle formation. Therefore, we choose the Fe(III)-loaded synthetic melanin nanoparticles as a model to investigate the parameters (reaction time, dopamine concentration, pH,) that affect the particle size, yield and percent metal loading. In addition, in our previous studies on Fe(III)-loaded synthetic melanin nanoparticles, magnetometry was used as an effective tool to study magnetic interactions between adjacent Fe(III) metal centers, and in turn help elucidate the MRI contrast ability of these materials. As follows, we synthesize Mn(III)-loaded synthetic melanin nanoparticles and demonstrate how the reduced antiferromagnetic coupling leads to a linear relationship between Mn(III) concentration and T_1 relaxivity.[1] Furthermore, we prepare Ni(II)-loaded synthetic melanin nanoparticles and observe a weak coupling and ground state (S = 1) from octahedrally-coordinated Ni(II). Additionally, we find that Co(II)-loaded synthetic melanin nanoparticles has a strong single-ion anisotropy. In summary, these chemical and magnetic data demonstrate the vast potential of magnetometry analysis in the application of study complicated metal- containing biomaterial systems.

3.2Synthesis of Metal Loaded Synthetic Melanin Nanoparticles

3.2.1 Spectral Characterization of Fe(III)-dopamine complex

The coordination chemistry between metal ions and catecholates is well established.[11] The observed mono-, bis-, and tris- metal-catecholate complex are highly dependent on the solution's pH environment. In general, the higher coordination number of catecholate comes with higher pH.[12] The idea of the pre-doping strategy relies on the formation of metal-dopamine complexes and then used as monomers for the preparation of metal-loaded synthetic melanin nanoparticles. Therefore, we survey different metals that are known to form stable complexes with catecholate: Ti(IV), V(III), Cr(III), Mn(III), Fe(III), Co(II), Ni(II), Cu(II), Zn(II), Ga(III) and Gd(III).[11, 13-14] UV-Vis spectroscopy has been used to identify these metal-catecholate species. For example, dopamine is known to forms tris-complexes with Fe(III) at basic pH, indicated by a strong absorption peak at 493 nm.[15-16] We can easily tune the amount of the tris- complex by controlling the feed ratio of the Fe(III) salt to the dopamine. Figure 3.1 shows the amount of tris-Fe(III)-dopamine complex decreases as the amount of Fe(III) salt decreases. Therefore, a large amount of dopamine (without complex with Fe(III)) can participate in the auto-oxidation polymerization. Additionally, we observed a strong increase of a broad absorption peak between 500-700 nm after initiating the polymerization, indicating the formation of mono- and bis–Fe(III)-dopamine complexes. We attribute the conversion from saturated tris-Fe(III)-dopamine complex to unsaturated mono and bis-Fe(III)-dopamine complexes in the polymerized network to the steric constraints in the highly crosslinked structure.

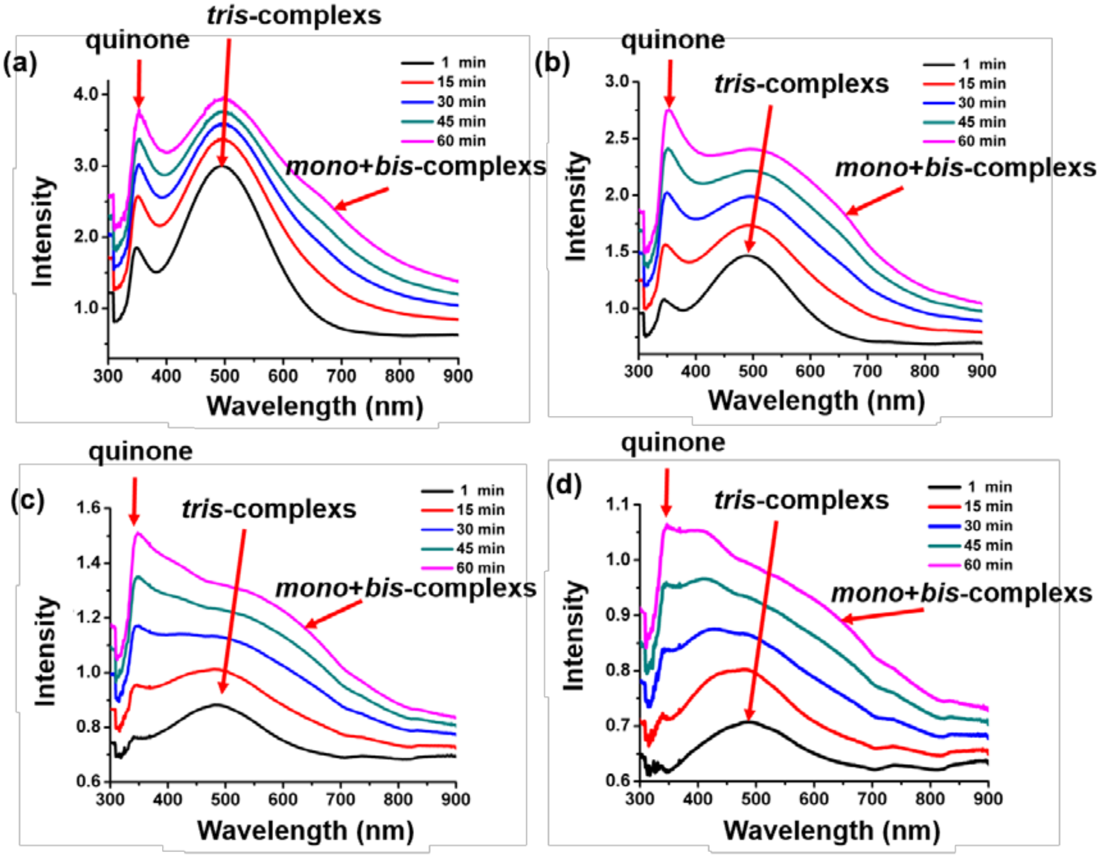

Figure 3.1. Time-dependent UV-visible absorption spectra of reaction solutions at different dopamine/Fe molar ratios. (a) dopamine/Fe = 3:1; (b) dopamine/Fe = 10:1; (c) dopamine/Fe = 50:1; (d) dopamine/Fe = 100:1. Copyright 2017 American Chemical Society.[17]

3.2.2 Post and Pre-Doping to Synthesize Metal-Loaded Synthetic Melanin Nanoparticles

All chemicals were obtained from Sigma-Aldrich and used without further purification. Samples using post-doping strategy, including Mn(III)-2, Co(II)-1, Ni(II)-2, Cu(II)-2, Zn(II)-2, Ga(III)-2 were prepared according to the literature methods[7, 18] The first step is to synthesize polydopamine nanoparticles through auto-oxidation polymerization of dopamine. In a typical reaction, 50 mL of deionized water and 20 mL of ethanol were the first mixtures together, followed by addition of 1.1 mL of ammonium hydroxide solution (28–30%) under vigorous stir for about 30 mins. Then, 5 mL of 4mg/mL dopamine hydrochloride stock solution was quickly injected into this reaction mixture. The solution turned to yellow immediately after adding the dopamine hydrochloride and then slowly turn to black after 1 h. The polydopamine nanoparticles were purified by centrifugation and washing with deionized water three times after overnight reaction. The nanoparticle concentration was then determined by lyophilizing 1mL of solution and measure the weight. In the second step, 20mL of polydopamine nanoparticle solution was incubated with a large excess of metal salts, including $Mn(Ac)_3•2H_2O$, $Co(NO_3)_2•6H_2O$, $Ni(Ac)_2•4H_2O$, $CuCl_2•2H_2O$, $ZnCl_2$ and $Ga(NO_3)_3•xH_2O$. Since $Mn(Ac)_3•2H_2O$ isn't dissolved in water, we removed the precipitate after reaction by filtration. Other excess of water-soluble metal salts can be removed via repeated wash with water and centrifuge.

Mn(III)-1, Co(II)-1, Ni(II)-1, Cu(II)-1, Zn(II)-1and Ga(III)-1 were prepared via pre-doping strategy. A certain concentration of metal salts (from 0.37 to 1.1 mM) and dopamine hydrochloride (1.1 to 4.4 mM) were mixed in a 250mL flask and keep stirring at room temperature for 1 h. Subsequently, a certain concentration of Tris buffer solution (from 55 to 124 mM) was quickly injected into the reaction mixture. It was observed that the reaction gradually turned black within 30 mins of stirring. The formulations of the reagents are summarized in Table 3.1. After further reaction for 1.5h, the metal-loaded synthetic melanin nanoparticles were separated by centrifugation and washed three times with deionized water.

Table 3.1. Reactants and their formulations for the particle preparation via pre-doping strategy.

pH	Dopamine Hydrochloride (mM)	Metal Salt	Metal Salt (mM)	Tris (mM)
9.7	**1.1**	$Mn(Ac)_3•2H_2O$	0.37	55
10	**1.6**	$Co(NO_3)_2•6H_2O$	0.53	83
10.1	**1.1**	$Ni(Ac)_2•4H_2O$	0.37	83
9.7	**4.4**	$CuCl_2•2H_2O$	1.1	83
9.9	**2.2**	$ZnCl_2$	1.1	124
9.8	**2.2**	$Ga(NO_3)_3•xH_2O$	0.73	83

3.2.3 Synthetic Control Over Metal-Loaded Synthetic Melanin Nanoparticles

In this section, I will discuss the synthetic parameters, including reaction time, dopamine concentration and pH that can affect the size, yield and percent metal loading. This study can help us to optimize reaction conditions so that the designed particle size and metal loading can be achieved for future applications.

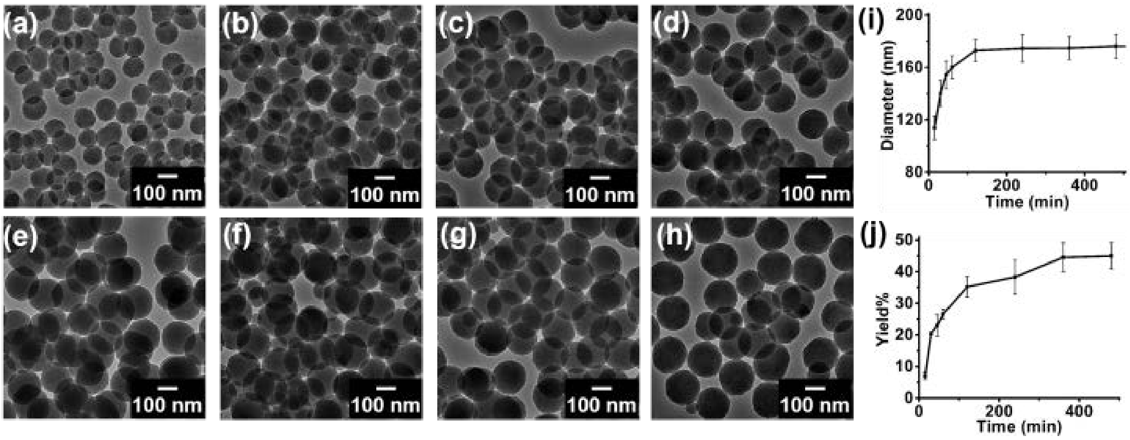

Figure 3.2. Representative TEM images of Fe(III)-loaded synthetic melanin nanoparticles quenched at different time points (a)15 min, (b)30 min, (c)45 min, (d) 60 min, (e) 120 min, (f) 240 min, (g) 360 min, (h) 480 min, (i) reaction time versus particle diameter, (j) reaction time versus particle yield. Copyright 2017 American Chemical Society.[17]

We first investigate the reaction kinetics of dopamine polymerization in the presence $FeCl_3(H_2O)_6$. 50 mL Tris Base (9 mg/mL) was added to a 100 mL solution containing 45 mg dopamine hydrochloride and 6.4 mg $FeCl_3(H_2O)_6$ at a final pH of 9.25. The reactions were quenched at a series of time points by addition of 1M HCl to neutralize the solution. Samples were centrifuged at 12000 rpm, then the precipitated nanoparticles were washed with deionized water and this procedure was repeated two times. The morphology of these synthesized nanoparticles was analyzed by TEM (Figure 3.2 a to h) Figure 3.2i summarizes the particle diameter as a function of reaction time and shows that the size of the particle increases dramatically at the onset of polymerization and reaches a plateau within 2 hours. After two hours, the decreased dopamine/Fe^{3+}concentration, as well as the solution pH efficiently stops the polymerization, and particle size remains unchanged after this time.[19] The particle yield is calculated by the mass of Fe(III)-loaded synthetic melanin nanoparticle versus mass of dopamine hydrochloride plus Fe(II) salts. Figure 3.2j showed the particle yield as a function of the polymerization time. It is noted that the plots of the particle size and yield as a function of time are roughly similar in shape. These two plots both have plateau around two-hour mark (Figure 3.2i and j), indicating that the number of metal-loaded nanoparticles remains relatively same shortly after the initiation of the polymerization. Previous works have demonstrated that the oxidation of dopamine to 5,6-dihydroxyindole is quite fast and the following polymerization step is relative slow, suggesting it is the rate-determining step.[10] In comparison to the iron-free synthesis of the polydopamine nanoparticle, which typically requires 12 h to reach completion, the presence of Fe(III) ions significantly accelerates the speed of the reaction. To investigate the role of Fe(III) in the determination of polymerization rate, we use a simple spherical model: the radius of the particle (r) is assumed to be the same, M is the total mass of the spherical particles and n is the number of particles. If oxidation step is quite fast, the number of particles (n) is constant during the polymerization, and the yield of spherical particles shows a linear relationship to the volume of the nanoparticle. As depicted in Figure 3.3a, an excellent direct correlation is observed in the plot of particle volume versus the particle yield, thus confirming the assumption that the number of particles remains fixed during the polymerization. Thus, the polymerization of dopamine/Fe(III) is the rate-determining step consistent with the result of the polydopamine system. Additionally, it is also interesting to further understand the mechanistic role of the Fe(III) ion in the nanoparticle formation. So, we monitored the content of Fe(III) in the nanoparticles at a different time of the polymerization. The content of Fe(III) in the nanoparticle was determined by ICP-OES. We set the molar ratio of dopamine to the Fe(III) to be 10:1 in the reaction mixture, equivalent to weight percent of 3.5% Fe(III). Under basic pH, it is well known that Fe(III) ions tend to chelate three dopamine molecules,[11] and therefore, under the conditions probed, a large excess of unchelated dopamine would be present in solution (3:1 versus 10:1). As is shown in Figure 3.3b, the weight percent of Fe(III) continuously decreased from 7.9% to 5.0% in the isolated nanoparticles. Considering this decrease in the percent weight of Fe(III) in the polydopamine overtime, we suggest that dopamine chelated to Fe(III) may polymerize faster than the unchelated form of the molecule.

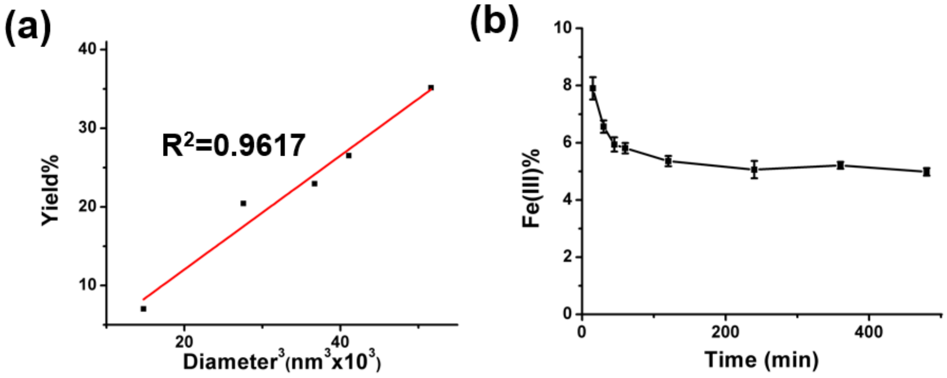

Figure 3.3. (a) Fitting curve of particle volume versus yield. (b) Reaction time versus Fe(III) weight percent. Copyright 2017 American Chemical Society.[17]

Secondly, we study the effect of monomer concentration has on particle size and metal content of the Fe(III)-loaded synthetic melanin nanoparticles, since the size and Fe(III) loading will directly affect the MRI performance in vivo.[20] The pH of the reaction was kept consistent between each experiment to exclude the interference of the pH(Table 3.2). Figure 3.4 shows the particles size and morphology of nanoparticles synthesized at different dopamine concentration (reactions were all quenched after 6 hours). We summary the size and dopamine concentration information in Figure 3.5 that reveals a relationship between the initial dopamine concentrations and particle size. When the initial dopamine concentration was low (1.1 mM), the diameter of the particle was as small as 112 nm. Notably, Figure 3.4a shows no visible particle was obtained with dopamine concentrations of 0.7 mM. When the dopamine concentration was increased from 1.1 mM to 3.5 mM a significant increase in size was observed: from 112 nm to 473 nm, which is in agreement with polydopamine nanoparticle synthesis.[10] Importantly, Figure 3.4a demonstrated that the polymerization speed of dopamine/Fe(III) is directly proportional to their concentrations as reflected by the larger particle diameter at higher monomer concentrations. In addition, Figure 3.4b reveals that the Fe(III) content is independent on the monomer concentration, indicating that monomer concentrations have similar accelerate effect on the polymerization of Fe(III)-dopamine complex and free dopamine.

Table 3.2. Reactants and their formulations for the dopamine concentration dependent experiments.

pH	Dopamine Hydrochloride (mM)	$FeCl_3 \cdot 6H_2O$ (mM)	Yield%
9.3	1.1	0.11	25.9
9.3	1.6	0.16	44.5
9.3	2.2	0.22	47.6
9.3	2.8	0.28	56.1
9.3	3.5	0.35	57.0

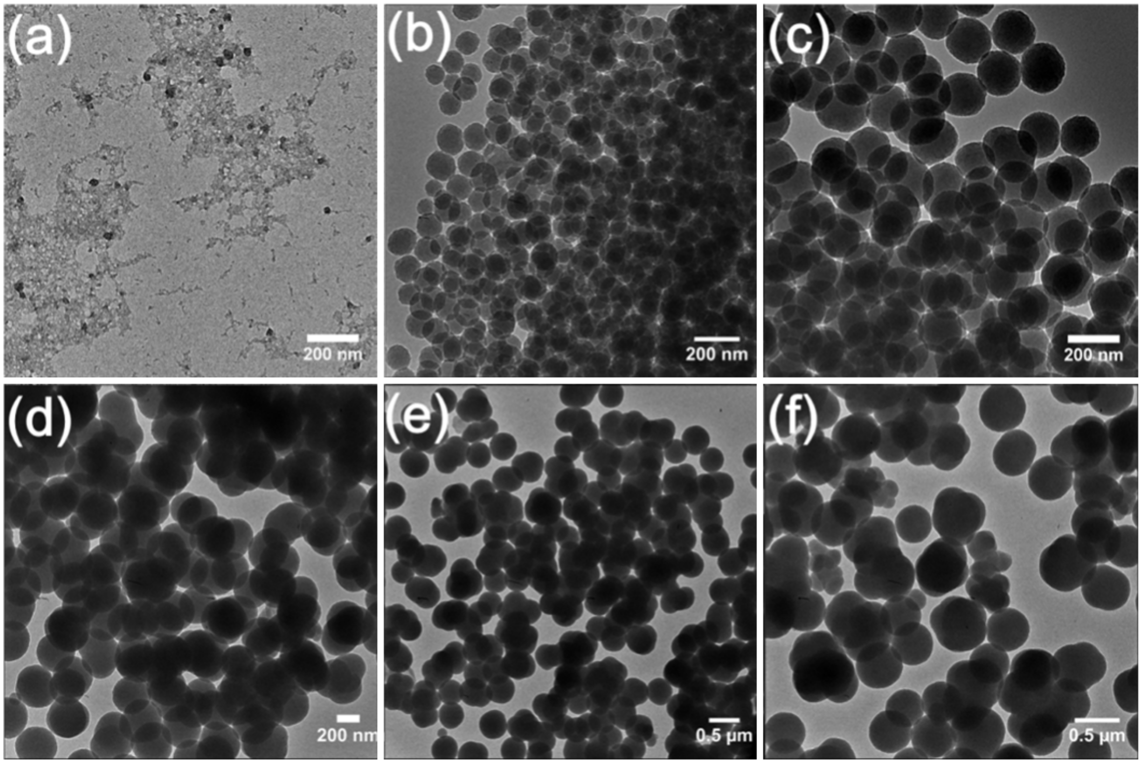

Figure 3.4. Representative TEM images of Fe(III)-loaded synthetic melanin nanoparticles synthesized at different dopamine concentrations (a) 0.7 mM, (b) 1.1 mM, (c) 1.6 mM, (d) 2.2 mM, (e) 2.8 mM, (f) 3.5 mM. Copyright 2017 American Chemical Society.[17]

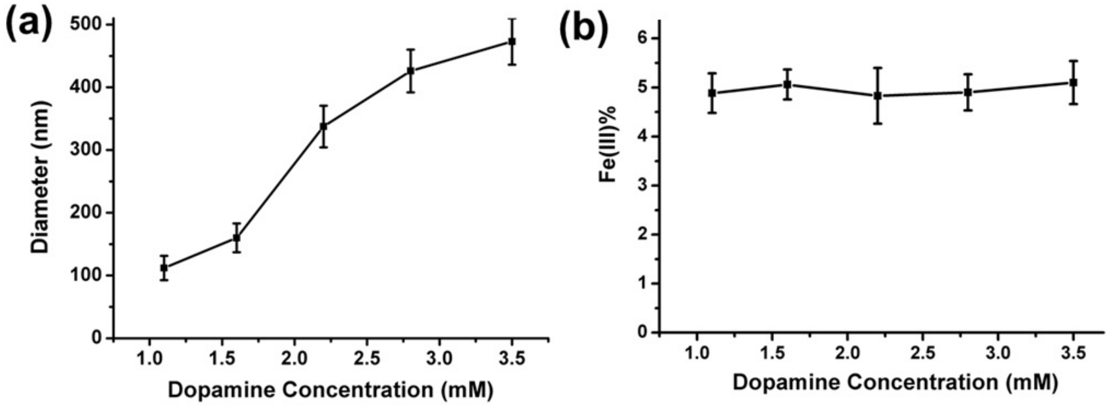

Figure 3.5. (a) Dopamine concentration versus particle diameter. (b) Dopamine concentration versus particle diameter. Copyright 2017 American Chemical Society.[17]

It has been reported that higher pH value will result in a smaller polydopamine nanoparticle as higher pH can enhance the nucleation step.[19] To examine the pH effect on the particle formation in the presence of Fe(III) salts, we perfumed the studies in the same monomer concentration (1.6mM) and reactions time 6 hours between runs (Table 3.3). Figure 3.6 shows the morphology of the polydopamine nanoparticles synthesized at different pH value. As summarized in Figure 3.7a, the diameter of Fe(III)-loaded synthetic melanin nanoparticle decreases from 350nm to 70nm as the initial pH raises from 8.7 to 9.6, and this trend is similar to what is observed in polydopamine synthesis in the absence of $FeCl_3(H_2O)_6$. Seemingly, the spontaneous autoxidation of dopamine is not affected by the presence of $FeCl_3(H_2O)_6$.[19] In contrast to the monomer effect, the iron contents in the nanoparticles were found to decrease with the increase of pH, suggesting that free dopamine polymerization is more sensitive to the pH variation than that of Fe(III)-dopamine complex (Figure 3.7b).

Table 3.3. Reactants and their formulations for the pH dependent experiments.

pH	Dopamine Hydrochloride (mM)	$FeCl_3$•$6H_2O$ (mM)	Yield%
8.7	1.6	0.16	24.7
9.1	1.6	0.16	44.1
9.4	1.6	0.16	46.6
9.5	1.6	0.16	53.1
9.6	1.6	0.16	56.5

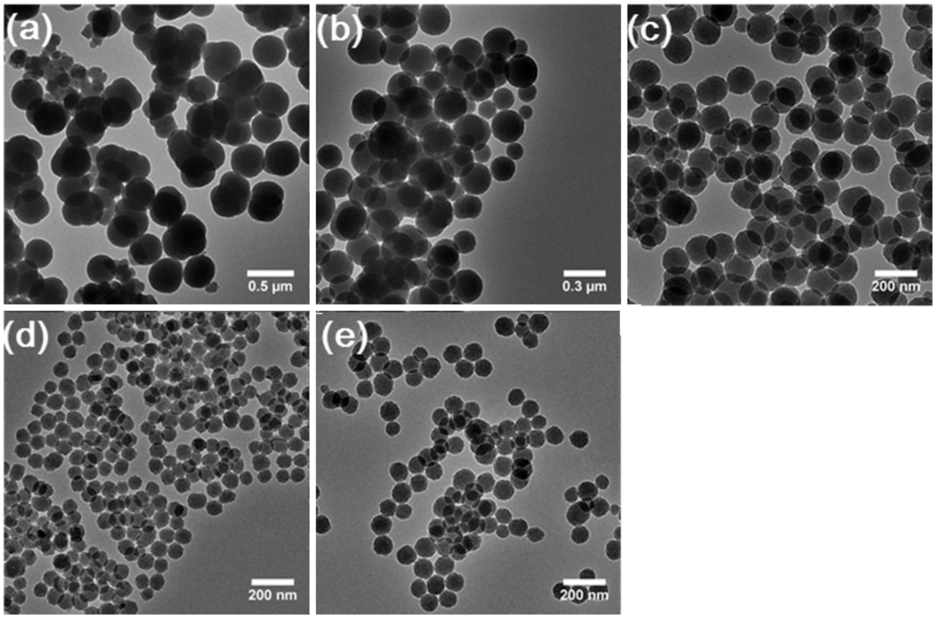

Figure 3.6. Representative TEM images of Fe(III)-loaded synthetic melanin nanoparticles synthesized at different pH: (a) 8.7, (b) 9.1, (c) 9.3, (d) 9.5, (e) 9.6. Copyright 2017 American Chemical Society.[17]

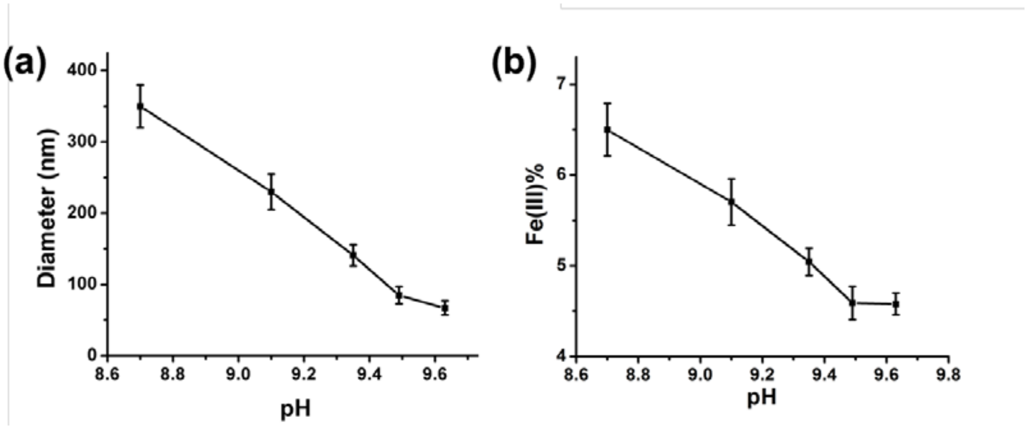

Figure 3.7. (a) pH versus particle diameter. (b) pH versus Fe(III) loading. Copyright 2017 American Chemical Society.[17]

3.3 Characterization of Metal-Loaded Synthetic Melanin Nanoparticles

3.3.1 Analysis the Morphology and Metal Content of Nanoparticles

Beside the Fe(III)-loaded nanoparticles, the morphology of other metal-loaded synthetic melanin nanoparticles was examined by to TEM (Figure 3.8). From data shown in Figure 3.8, we can conclude that different kinds of metal ions have a significant effect on the nanoparticle morphology. For instance, among these samples, Zn(II)-loaded synthetic melanin nanoparticle (Figure 3.8e) has the largest diameter and highest weight percentage of metal loading. By contrast the Cu(II)-loaded nanoparticle shows the smallest diameter and lowest metal loading. The TEM images show Cu(II)-loaded synthetic melanin nanoparticle has much less contrast compared with Zn(II)-loaded synthetic melanin nanoparticles, which may be attributed to the difference in the metal content. Additionally, Ga(III)-loaded nanoparticles has the most uniform morphology, while the Ni-(II) loaded nanoparticle has the highest dispersity in size. We attribute this to the different polymerization kinetics of these metal–dopamine complexes. We also found that this pre-doping strategy can’t generate uniform particles morphology when using Ti(IV), V(III), Cr(III) and Gd(III) salts during the reaction. It is anticipated that the different affinities and coordination geometries for dopamine and Ti(IV), V(III), Cr(III) and Gd(III) ions can be the reason.[21] The stability of these nanoparticles in solution was investigated by testing the zeta potential. Table 3.5 list the zeta potential values of all the sample solution. The very negative values suggest high stability of these nanoparticles in solution.

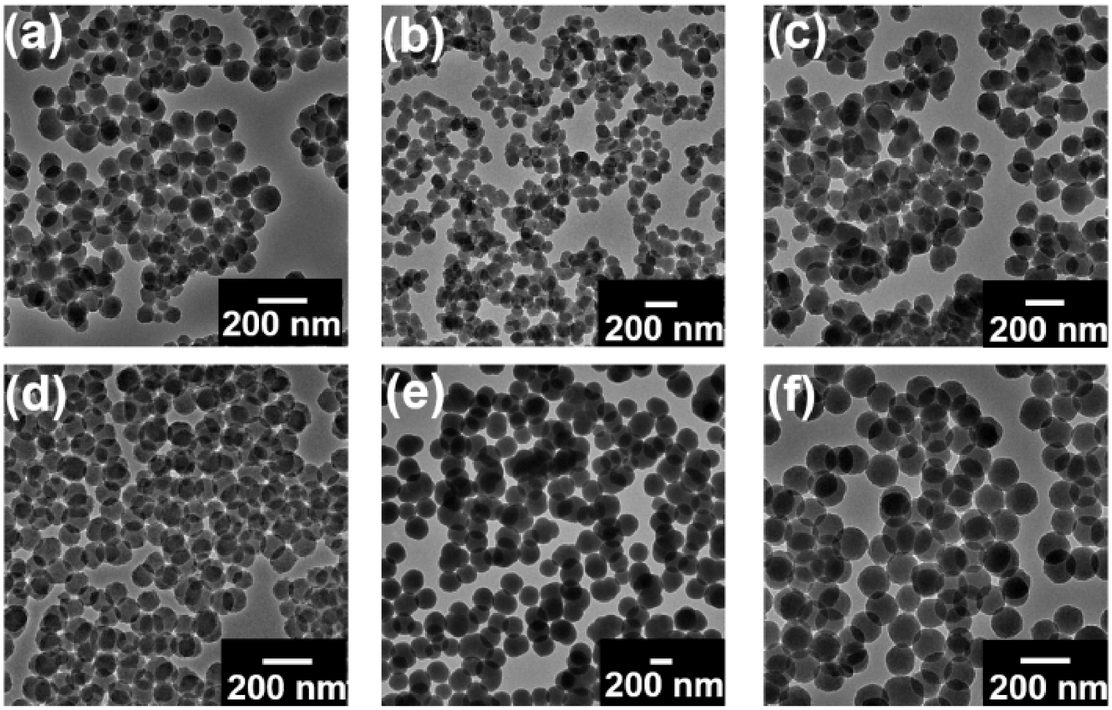

Figure 3.8. TEM images of metal-loaded synthetic melanin nanoparticles (a) Mn(III)-1, (b) Co(II)-1, (c) Ni(II)-1, (d) Cu(II)-1, (e) Zn(II)-1, (f) Ga(III)-1.Copyright 2017 American Chemical Society.[17]

Table 3.4. Physical parameters of metal-loaded synthetic melanin nanoparticles.

Sample Name	Metal Loading (%)[a]	Synthetic Method
Mn(III)-1	9.6	Pre-Doping
Co(II)-1	9.6	Pre-Doping
Ni(II)-1	13.4	Pre-Doping
Cu(II)-1	8.0	Pre-Doping
Zn(II)-1	17.2	Pre-Doping
Ga(III)-1	13.2	Pre-Doping
Mn(III)-2	0.1	Post-Doping
Co(II)-2	0.4	Post-Doping
Ni(II)-2	0.7	Post-Doping
Cu(II)-2	0.4	Post-Doping
Zn(II)-2	0.8	Post-Doping
Ga(III)-2	2.4	Post-Doping

[a] Weight percentage of metal in nanoparticles.

Table 3.5. Diameter and zeta potential of metal-loaded synthetic melanin nanoparticle.

Sample Name	Diameter (nm)	Zeta Potential (mV)
Mn(III)-1	99 ± 14	-18.1
Co(II)-1	94 ± 16	-17.5
Ni(II)-1	114 ± 24	-35.4
Cu(II)-1	71 ± 12	-27.7
Zn(II)-1	208 ± 30	-31.8
Ga(III)-1	131 ± 12	-29.2

The advance of pre-doping strategy is to control the metal loading in the nanoparticle via adding different amounts of metal salt during the polymerization. In theory, bis- and/or tris- (depend on the type of metal) metal -dopamine complexes are formed in basic solution. Thus, the highest achievable feed ratio for the metal versus dopamine is between 1:2 and 1:3. Table 3.1 list the highest molar ratio of the dopamine versus metal that can form spherical nanoparticles. It is noted that higher amount of metal salt would result in the formation of inter-nanoparticle crosslinking and lower amounts of metal salt would result in the structure of nanoparticle with less metal loading. To characterize the metal in the nanoparticles, we first used ICP-OES to measure the concentration of metal in a digested solution. The procedure is described in chapter 2. The metal loading in Table 3.4 was calculated based on the ICP results. Additionally, dark field and bright field scanning transmission electron microscopy were used to image the Mn(III), Co(II) and Ni(II)-loaded synthetic melanin nanoparticles. Figure 3.9a and b show the dark field and bright field image of Mn(III)-loaded nanoparticles. The higher contrast at the nanoparticles' location in these two images suggests the presence of metal inside the nanoparticles. Figure 3.9d shows the scanning transmission electron microscopy coupled with energy-dispersive X-ray spectroscopy (STEM-EDS) image, in which the Mn element is localized exclusively at the nanoparticles' location, confirming the existence of Mn inside the nanoparticles. We use the same STEM-EDS analysis to demonstrate that Co and Ni element were also existence inside the nanoparticles (Figure 3.10 and Figure 3.11).

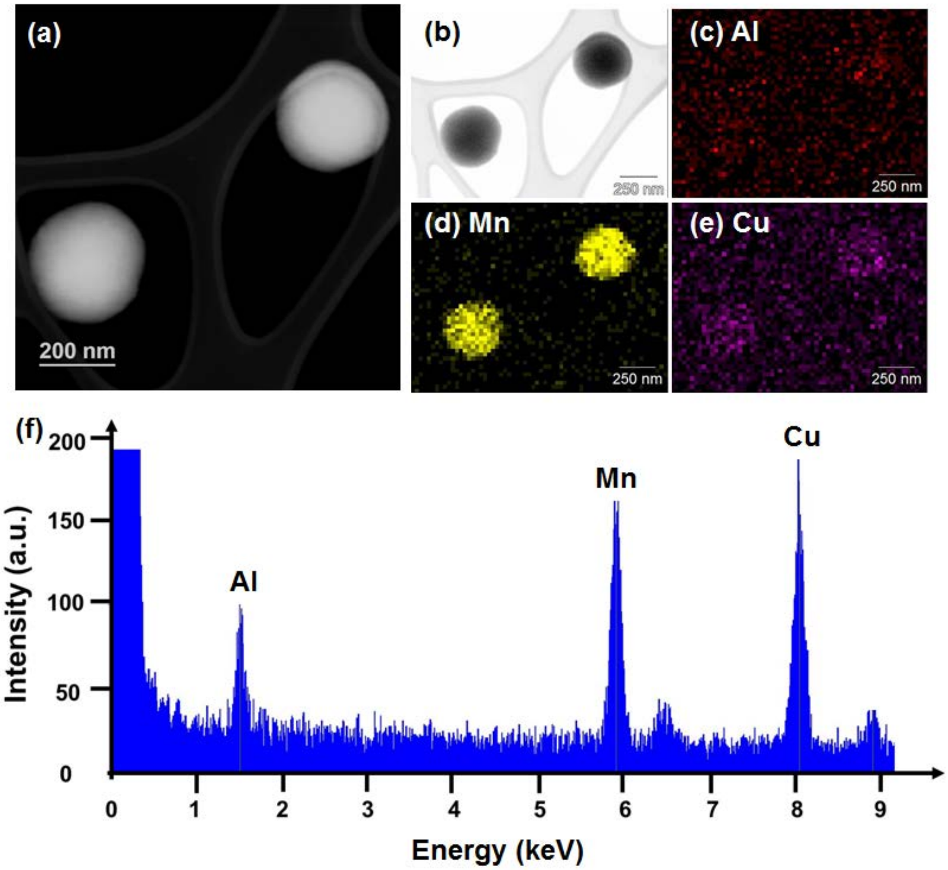

Figure 3.9. STEM-EDS analysis of Mn(III)-loaded PDA -NPs. (a) Dark Field STEM image of particles prior to EDS elemental mapping. (b) Bright field STEM image of the region of interest used for mapping. (c-e) EDS elemental maps of the ROI for the characteristic X-ray emission peaks for (c) Al, (d) Mn, and (e) Cu. Al and Cu signal is background from the microscope column or sample holder/grid. Mn signal location overlays exclusively on the particles' locations. (f) Raw EDS spectrum (summed over ROI), showing the clear Mn signal generated from the particles. Copyright 2017 American Chemical Society.[17]

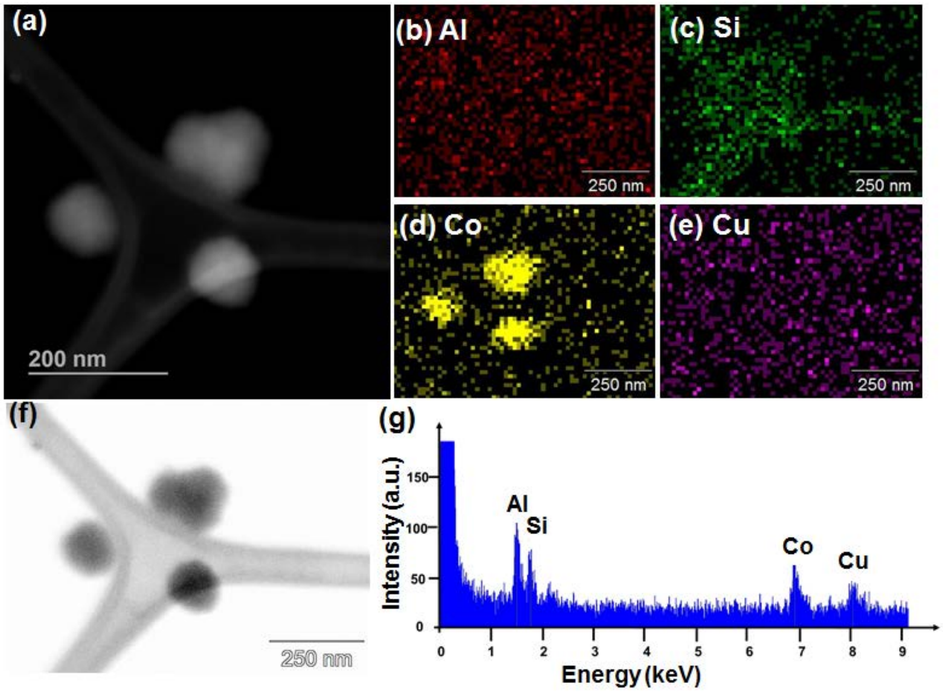

Figure 3.10. STEM -EDS analysis of Co(II)-loaded PDA NPs. (a) Dark Field STEM image of particles prior to EDS elemental mapping. (b-e) EDS elemental maps of the region of interest (as indicated in f) for the characteristic X-ray emission peaks for (b) Aluminum, (c) Silicon, (d) Cobalt, and (e) Copper. Al, Si, and Cu signal is background signal from the microscope column or sample holder/grid. (f) Bright field STEM image of the ROI used for mapping. Co signal location overlays exclusively on the particles' locations. (g) Raw EDS spectrum (summed over ROI), showing the clear Co peak generated from the particles. Copyright 2017 American Chemical Society.[17]

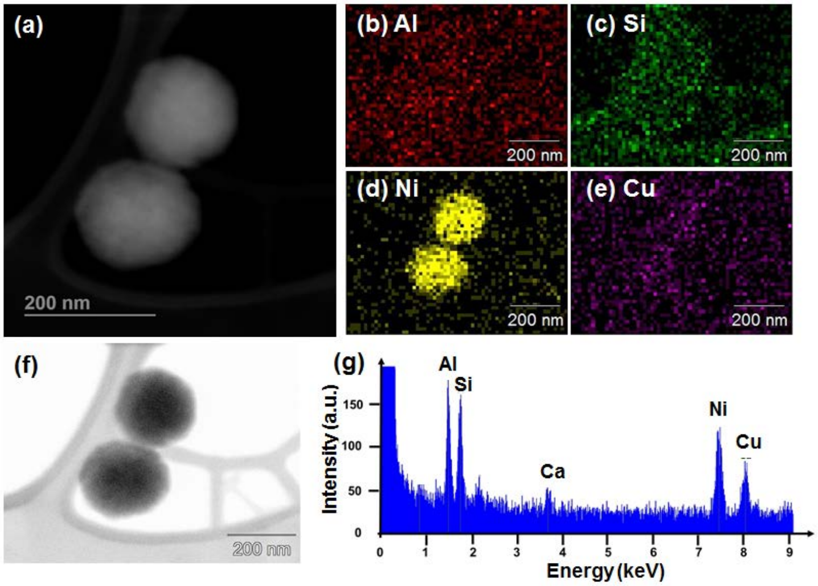

Figure 3.11. STEM-EDS analysis of Ni(II)-loaded PDA NPs. (a) Dark Field STEM image of particles prior to EDS elemental mapping. (b-e) EDS elemental maps of the region of interest (as indicated in f) for the characteristic X-ray emission peaks for (b) Al, (c) Si, (d) Ni, and (e) Cu. Al, Si, and Cu signal is background signal from the microscope column or sample holder/grid. (f) Bright field STEM image of the ROI used for mapping. Ni signal location overlays exclusively on the particles' locations. (g) Raw EDS spectrum (summed over ROI), showing the clear Ni signal generated from the particles. Very low Ca signal is detected, which is also localized over the particles. Copyright 2017 American Chemical Society.[17]

3.3.2 Magnetochemical Analysis & MR Imaging Analysis

The pre-doping strategy provides access to a series of metal-loaded synthetic melanin nanoparticles with a much higher metal content than is possible for the post-doping strategy. The magnetometry analysis of Ni(II), Co(II) and Mn(III)-loaded synthetic melanin nanoparticles were characterized using a Quantum Design MPMS3 SQUID with a maximum field of 7 T to access the spin-state and inter-ion interactions. 10mg of solid samples were packed into standard Quantum Design plastic sample holders. Magnetization data were collected in DC mode and corrected for diamagnetic contributions using Pascal's constants. We use the same synthetic method to access different Ni(II), Co(II) and Mn(III) content. The formulation and metal content in the resulting nanoparticles are included in Table 3.6. We analyzed three Ni(II)-loaded samples, including 4.0, 5.4, 7.4, and 13.4% Ni(II) loading ones which are shown in Figure 3.12a. All the three examples show a largely constant $\chi_M T$ value along the temperature. Additionally, the deviations are presented only at low temperatures (below 25K), which may be attributed to the weak zero-field splitting effects. We exclude the possibility of antiferromagnetic coupling effect since this fact don't increase with the increase of Ni(II) loading. It is noted that the $\chi_M T$ values vary erratically at different Ni(II) loadings, possibly because of the small spin (S = 1) and hygroscopic nature of the Ni(II)-loaded synthetic melanin particles.[22] Although the variation in $\chi_M T$ values prevents quantitative analysis of the magnetic interactions, we can still speculate that antiferromagnetic coupling between Ni(II) centers are very weak.

Table 3.6. Reactants and their formulations for the preparation of metal-loaded synthetic nanoparticle.

Sample	Dopamine Hydrochloride (mM)	Metal Salt (µM)	Tris (mM)	pH	Metal %
Ni(II)-2	2.2	210	25	9.7	7.4
Ni(II)-3	2.2	104	16	9.2	5.4
Ni(II)-4	2.2	64	13	9.1	4.0
Co(II)-2	2.2	210	25	9.6	5.5
Co(II)-3	2.2	21	2.5	8.9	2.0
Mn(III)-2	2.2	210	25	9.3	4.3
Mn(III)-3	2.2	42	5	8.5	1.6
Mn(III)-4	2.2	21	2.5	8.5	1.1

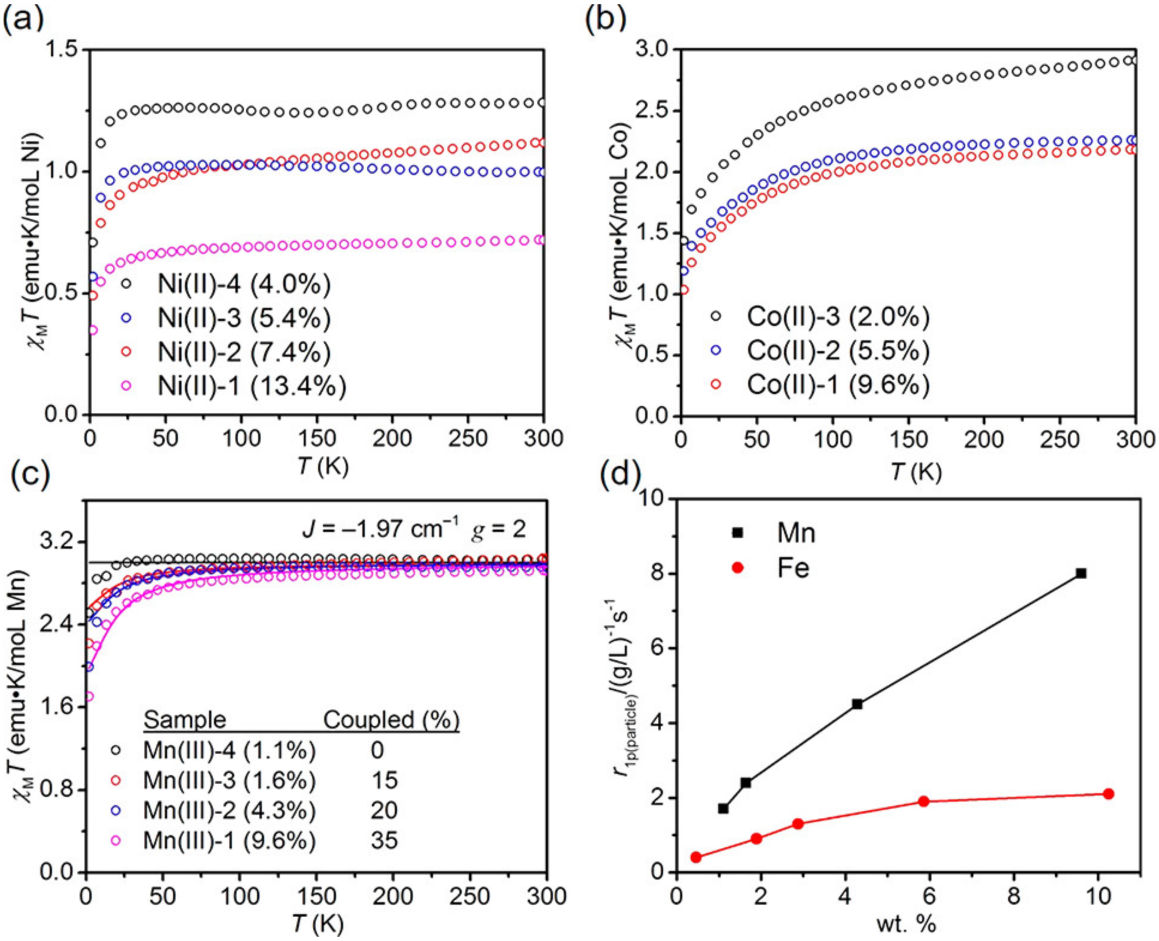

Figure 3.12. Temperature dependence of the product of magnetic susceptibility and temperature (χMT) for (a) Ni(II)-, (b) Co(II)-, and (c) Mn(III)-loaded synthetic melanin nanoparticles. Susceptibility data for Mn(III)-loaded particles are globally fit using eq 1 (J = −1.97 cm–1; g = 2). (d) Dependence of per-particle relaxivity on the wt % of Mn(III) or Fe(III) demonstrating the effect of reduced antiferromagnetic coupling strength on MRI contrast ability. Copyright 2017 American Chemical Society.[17]

Figure 3.12 b shows the $\chi_M T$ value over temperature. Both of two high Co(II) loading (5.5 and 9.6 %) samples show a gradually decay of $\chi_M T$ value from 2 emu•K/cm^{-3} to 1 emu•K/cm^{-3}. This result is consistent with the high spin (S = 3/2) of Co(II) ion with the considerable unquenched orbital moment. Although antiferromagnetic coupling effect would result in a similar decay in $\chi_M T$ value, this is not the case in Co(II)-loaded nanoparticles since the decay isn't affected by Co(II) loading. By contrast Co(II)-3 (2.0%) exhibited higher $\chi_M T$ value over the whole temperature range. We speculate this is due to the existence of some population of oxidized (S = 2) Co(III) ions.

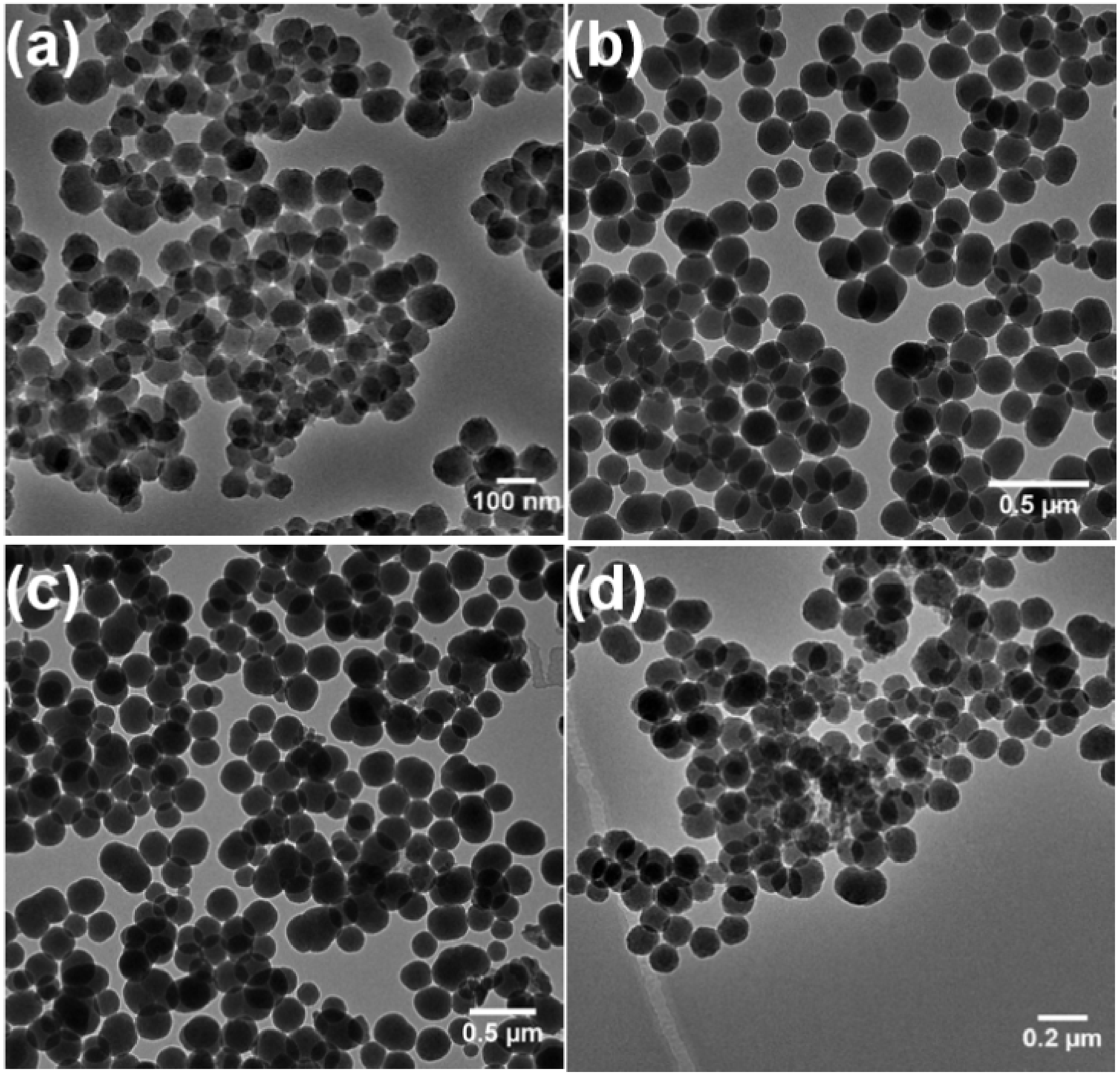

Figure 3.13. Representative TEM images of (a) Mn(III)-1, (b) Mn(III)-2, (c) Mn(III)-3, (d) Mn(III)-4. Copyright 2017 American Chemical Society.[17]

In the previous chapter, we demonstrate that magnetometry is an effective tool for analyzing the parameters that control MRI performance in Fe(III)-loaded synthetic melanin system.[23] Manganese shares many properties that make Fe(III) a good T_1 MR imaging probe. Therefore, we think Mn(III)-loaded synthetic melanin nanoparticles is a good example to compare with the Fe(III)-loaded system, due to the difference in coupling pathway. A series of Mn(III)-doped synthetic melanin nanoparticle with different Mn(III) loading were prepared via pre-doping strategy. Figure.3.13 shows the TEM image of Mn(III)-1, 2, 3 and 4. Figure 3.12c is the temperature dependence of the product of magnetic susceptibility and temperature ($\chi_M T$) for Mn(III)-loaded synthetic melanin nanoparticles under a 5000 Oe magnetic field. Importantly, we found that all the four Mn(III)-loaded samples show much less deviation of $\chi_M T$ compared with the Fe(III)-loaded ones, suggesting that antiferromagnetic coupling between Mn(III) centers are much weaker. We think this is because Jahn-Teller distortion in Mn(III) complex diminish the coupling effect. Like the modeling interactions in Fe(III)-loaded system, we also incorporate an isotropic g value and magnetic coupling constant J in the Mn(III)-loaded synthetic melanin nanoparticles. Magnetically isolated and magnetically coupled Mn(III) cation are all discussed in this model. We perform a global fitting of susceptibility data through an HDVV Hamiltonian (Eq. 1)

$$\hat{\boldsymbol{H}} = -2\boldsymbol{J}_{\boldsymbol{Mn-Mn}}\hat{\boldsymbol{S}}_{\boldsymbol{1}} \cdot \hat{\boldsymbol{S}}_{\boldsymbol{2}} \qquad (\boldsymbol{1})$$

where $\hat{S}_1$ and $\hat{S}_2$ are spin operators for equivalent interacting spins. It was found that the coupling constant J (-1.1 cm^{-1}) was significantly lower than the one of Fe(III)-catecholate (-24.8 cm^{-1}), [14,24-26] suggesting that Mn(III)-loaded system has small antiferromagnetic coupling effect.

The MR relaxivity of Mn(III) and Fe(III)-loaded synthetic melanin nanoparticle was obtained by Bruker 7.0 T magnet. Figure 3.4 shows the T_1-weighted MR images of Mn(III)-loaded synthetic melanin nanoparticle at different particle concentrations. The test tubes containing a higher concentration of nanoparticles appeared brighter on T_1 weighted images. It is noted that the T_1 signal starts to saturate at the highest loading sample and T_2-effects dominate the signal behavior.[27, 28] The $1/T_1$ value (obtained from Figure 3.14) versus Mn(III) concentration were plotted in Figure 3.15. Table 3.7 summarized the r_1 relaxivity values of Mn(III)-1, 2, 3 and 4. Compared with other nanoparticle T_1-weighted contrast agents, such as Fe(III)-loaded synthetic melanin nanoparticles, this Mn(III)-loaded nanoparticles show very high relaxivity value.[13, 14, 29, 30] The r_2/r_1 ratios were calculated and listed in Table 3.7. We also consider the "per particle-relaxivity" ($r_{1p(particle)}$) [23] as we discussed in the last chapter. We compared the $r_{1p(particle)}$ value of Mn(III) and Fe(III) loaded synthetic melanin nanoparticles in Figure 3.12d and $r_{1p(ion)}$ as well as $r_{1p(spin)}$ in Figure

3.16. Importantly, Mn(III)-loaded sample show significantly higher relaxivity values ($r_{1p(particle)}$, $r_{1p(ion)}$ and $r_{1p(spin)}$) than Fe(III) samples, even though Fe(III) has higher spin compared with Mn(III). We conclude that this is because Mn(III)-loaded sample presents much weaker antiferromagnetic coupling effect. Therefore, this analysis suggests that Mn(III)-loaded synthetic melanin nanoparticles has better MRI performance compared with Fe(III)-loaded ones. Additionally, we demonstrate the facile way of using magnetometry to guide the design and optimization of nanoparticle-based MRI contrast agents.

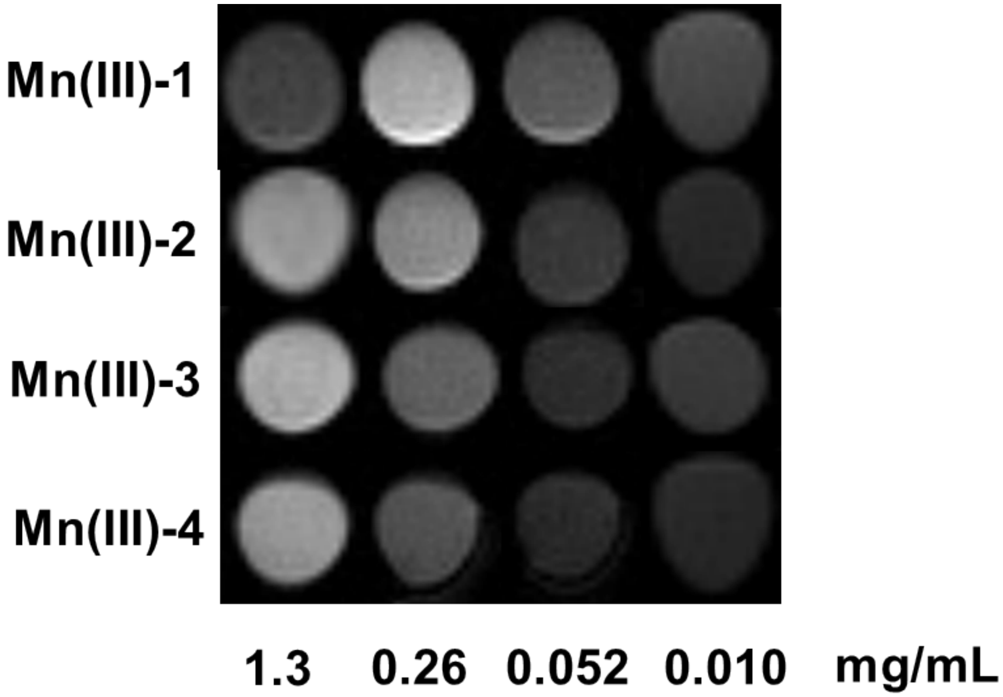

Figure 3.14. T1-weighted MR images of (a) Mn(III)-1, (b) Mn(III)-2, (c) Mn(III)-3, (4) Mn(III)-4 in aqueous solution at different particle concentrations. Copyright 2017 American Chemical Society.[17]

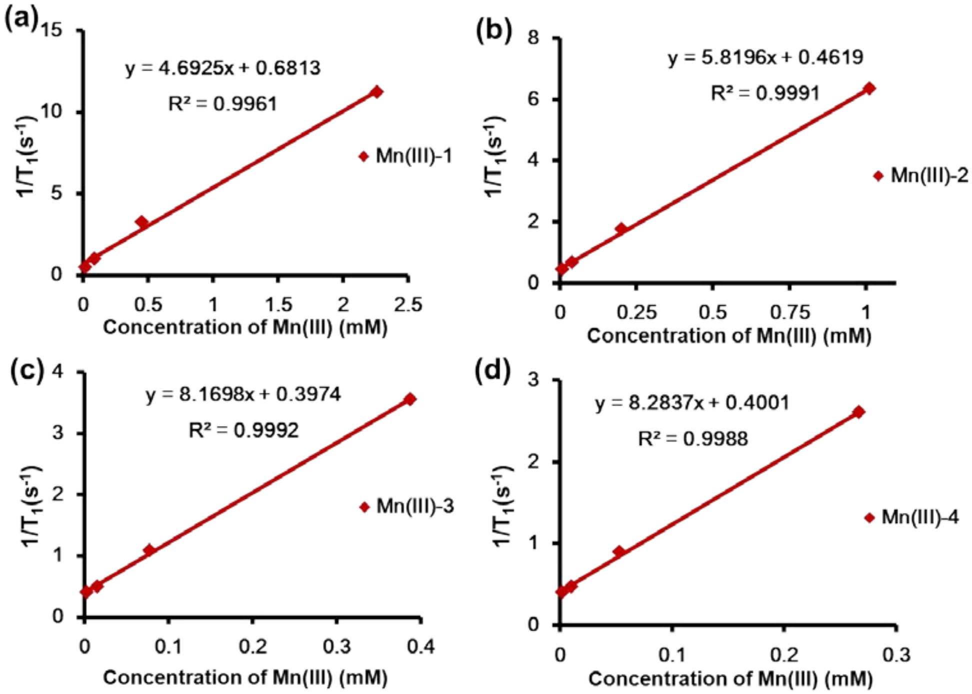

Figure 3.15. T1 MRI relaxivity plots of (a) Mn(III)-1, (b) Mn(III)-2, (c) Mn(III)-3, (4) Mn(III)-4 at at 7 T to determine r1. Copyright 2017 American Chemical Society.[17]

Table 3.7. MR relaxivity results for Mn(III)-loaded synthetic melanin nanoparticles**.**

Sample	$r_{1p(Mn(III))}$(mM^{-1}s^{-1})	$r_{2p(Mn(III))}$(mM^{-1}s^{-1})	$r_{1p\ (particle)}$((g/L)$^{-1}$s^{-1})	r_2/r_1
Mn(III)-1	4.7	38.4	8.2	8.2
Mn(III)-2	5.8	61.5	4.5	10.6
Mn(III)-3	8.2	113.5	2.4	13.8
Mn(III)-4	8.3	112.69	1.7	13.5

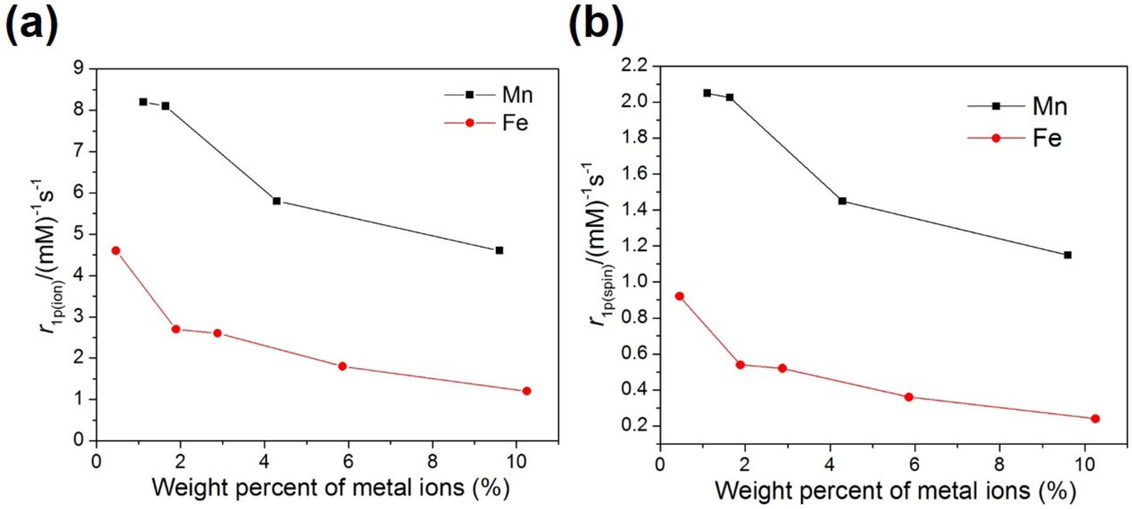

Figure 3.16. The r1 relaxation rates (a) per metal ion, (b) per spin as a function of weight percent of metal ion (%). Copyright 2017 American Chemical Society.[17]

3.4 Conclusion

In conclusion, a facile pre-doping strategy was developed to synthesize various metal-loaded synthetic melanin nanoparticles in a single step process. We find the Fe(III) ion can accelerate the polymerization speed via complexation with dopamine. Compared with the post-doping strategy, the pre-doping approach can achieve much higher metal loading, allowing the structural study of synthetic melanin nanoparticles. Magnetometry analysis of Ni(II)- and Co(II)-loaded synthetic melanin nanoparticles reveals the magnetic structural information in these disordered magnetic systems. We anticipate that higher metal loadings and enhanced synthetic techniques will allow us to quantify our analysis of the more complex and low moment systems, thus allowing even more structural information to be extracted. These techniques may prove vital to the study of high anisotropy metal-chelates where standard electron paramagnetic resonance (EPR) techniques are not feasible. The magnetochemical and MRI analysis of Fe(III) and Mn(III)-loaded synthetic melanin nanoparticles revealed that the weak antiferromagnetic coupling between Mn(III) centers enhances their MRI performance. This method also provides means to optimize the complicated biomaterial system for future applications from MRI contrast agents to electronic devices.

3.5 Acknowledge

Chapter 3 is adapted in full print from Zhao Wang,[a] Yijun Xie,[a] Yiwen Li, Huang Y., Lucas R Parent, Treffly B. Ditri, Nanzhi Zang., Jeffery D. Rinehart,* and Nathan C. Gianneschi,* Tunable, Metal-Loaded Polydopamine Nanoparticles Analyzed by Magnetometry, Chemistry of Materials 2017, 29, 8195-8201. Copyright 2017 American Chemical Society. The dissertation author is the first author of this paper. For Chapter 3, I would like to thank our collaborators Yijun Xie and Prof. Jeffrey D. Rinehart for analysis of magnetic properties of the nanoparticles. I really appreciate my colleague Dr. Lucas R Parent and Yuran Huang for helping to character the nanoparticles. I also thank the helpful discussion from Dr. Treffly B. Ditri Dr. Yiwen Li and Nanzhi Zang.

3.6 References

1. Miao, Z.-H.; Wang, H.; Yang, H.; Li, Z.-L.; Zhen, L.; Xu, C.-Y., Intrinsically Mn2+-Chelated Polydopamine Nanoparticles for Simultaneous Magnetic Resonance Imaging and Photothermal Ablation of Cancer Cells. *ACS Applied Materials & Interfaces* **2015,** *7* (31), 16946-16952.

2. Liu, F.; He, X.; Zhang, J.; Chen, H.; Zhang, H.; Wang, Z., Controllable synthesis of polydopamine nanoparticles in microemulsions with pH-activatable properties for cancer detection and treatment. *Journal of Materials Chemistry B* **2015,** *3* (33), 6731-6739.

3. Fan, Q.; Cheng, K.; Hu, X.; Ma, X.; Zhang, R.; Yang, M.; Lu, X.; Xing, L.; Huang, W.; Gambhir, S. S.; Cheng, Z., Transferring Biomarker into Molecular Probe: Melanin Nanoparticle as a Naturally Active Platform for Multimodality Imaging. *Journal of the American Chemical Society* **2014,** *136* (43), 15185-15194.

4. Chen, Y.; Ai, K.; Liu, J.; Ren, X.; Jiang, C.; Lu, L., Polydopamine-based coordination nanocomplex for T1/T2 dual mode magnetic resonance imaging-guided chemo-photothermal synergistic therapy. *Biomaterials* **2016,** *77*, 198-206.

5. Ju, K.-Y.; Lee, S.; Pyo, J.; Choo, J.; Lee, J.-K., Bio-inspired Development of a Dual-Mode Nanoprobe for MRI and Raman Imaging. *Small* **2015,** *11* (1), 84-89.

6. Yoon, Y. I.; Ju, K. Y.; Cho, H.-S.; Yu, K. N.; Lee, J. J.; Ahn, G. J.; Lee, S.-H.; Cho, M. H.; Lee, H. J.; Lee, J.-K.; Yoon, T.-J., Enhancement of cancer specific delivery using ultrasound active bio-originated particles. *Chemical Communications* **2015,** *51* (46), 9455-9458.

7. Ju, K.-Y.; Lee, J. W.; Im, G. H.; Lee, S.; Pyo, J.; Park, S. B.; Lee, J. H.; Lee, J.-K., Bio-Inspired, Melanin-Like Nanoparticles as a Highly Efficient Contrast Agent for T1-Weighted Magnetic Resonance Imaging. *Biomacromolecules* **2013,** *14* (10), 3491-3497.

8. Hong, L.; Simon, J. D., Current Understanding of the Binding Sites, Capacity, Affinity, and Biological Significance of Metals in Melanin. *The Journal of Physical Chemistry B* **2007,** *111* (28), 7938-7947.

9. Simpson, M. J.; Wilson, J. W.; Robles, F. E.; Dall, C. P.; Glass, K.; Simon, J. D.; Warren, W. S., Near-Infrared Excited State Dynamics of Melanins: The Effects of Iron Content, Photo-Damage, Chemical Oxidation, and Aggregate Size. *The Journal of Physical Chemistry A* **2014,** *118* (6), 993-1003.

10. Ju, K.-Y.; Lee, Y.; Lee, S.; Park, S. B.; Lee, J.-K., Bioinspired Polymerization of Dopamine to Generate Melanin-Like Nanoparticles Having an Excellent Free-Radical-Scavenging Property. *Biomacromolecules* **2011,** *12* (3), 625-632.

11. Sever, M. J.; Wilker, J. J., Visible absorption spectra of metal-catecholate and metal-tironate complexes. *Dalton Transactions* **2004,** (7), 1061-1072.

12. Holten-Andersen, N.; Harrington, M. J.; Birkedal, H.; Lee, B. P.; Messersmith, P. B.; Lee, K. Y. C.; Waite, J. H., pH-induced metal-ligand cross-links inspired by mussel yield self-healing polymer networks with near-covalent elastic moduli. *Proceedings of the National Academy of Sciences* **2011,** *108* (7), 2651-2655.

13. Srivastava, T. N.; Mohan, G., Complex Compounds of Ga(III) and In(III) with Catechol. *Zeitschrift für anorganische und allgemeine Chemie* **1970,** *379* (1), 82-87.

14. Freeman, G. E.; Raymond, K. N., Specific sequestering agents for the actinides. 12. Synthetic and structural chemistry of gadolinium and holmium catecholates. *Inorganic Chemistry* **1985,** *24* (9), 1410-1417.

15. Charkoudian, L. K.; Franz, K. J., Fe(III)-Coordination Properties of Neuromelanin Components: 5,6-Dihydroxyindole and 5,6-Dihydroxyindole-2-carboxylic Acid. *Inorganic Chemistry* **2006,** *45* (9), 3657-3664.

16. Paris, I.; Martinez-Alvarado, P.; Perez-Pastene, C.; Vieira, M. N. N.; Olea-Azar, C.; Raisman-Vozari, R.; Cardenas, S.; Graumann, R.; Caviedes, P.; Segura-Aguilar, J., Monoamine transporter inhibitors and norepinephrine reduce dopamine-dependent iron toxicity in cells derived from the substantia nigra. *Journal of Neurochemistry* **2005,** *92* (5), 1021-1032.

17. Wang, Z.; Xie, Y.; Li, Y.; Huang, Y.; Parent, L. R.; Ditri, T.; Zang, N.; Rinehart, J. D.; Gianneschi, N. C., Tunable, Metal-Loaded Polydopamine Nanoparticles Analyzed by Magnetometry. *Chemistry of Materials* **2017,** *29* (19), 8195-8201.

18. Hong, L.; Liu, Y.; Simon, J. D., Binding of Metal Ions to Melanin and Their Effects on the Aerobic Reactivity¶. *Photochemistry and Photobiology* **2004,** *80* (3), 477-481.

19. Ho, C.-C.; Ding, S.-J., The pH-controlled nanoparticles size of polydopamine for anti-cancer drug delivery. *Journal of Materials Science: Materials in Medicine* **2013,** *24* (10), 2381-2390.

20. Estelrich, J.; Sánchez-Martín, M. J.; Busquets, M. A., Nanoparticles in magnetic resonance imaging: from simple to dual contrast agents. *International journal of nanomedicine* **2015,** *10*, 1727.

21. Hider, R. C.; Kong, X., Chemistry and biology of siderophores. *Natural Product Reports* **2010,** *27* (5), 637-657.

22. Brückner, C.; Caulder, D. L.; Raymond, K. N., Preparation and Structural Characterization of Nickel(II) Catecholates. *Inorganic Chemistry* **1998,** *37* (26), 6759-6764.

23. Li, Y.; Xie, Y.; Wang, Z.; Zang, N.; Carniato, F.; Huang, Y.; Andolina, C. M.; Parent, L. R.; Ditri, T. B.; Walter, E. D.; Botta, M.; Rinehart, J. D.; Gianneschi, N. C., Structure and Function of Iron-Loaded Synthetic Melanin. *ACS Nano* **2016,** *10*, 10186-10194.

24. Grillo, V. A.; Hanson, G. R.; Wang, D.; Hambley, T. W.; Gahan, L. R.; Murray, K. S.; Moubaraki, B.; Hawkins, C. J., Synthesis, X-ray Structural Determination, and Magnetic Susceptibility, Mössbauer, and EPR Studies of (Ph4P)2[Fe2(Cat)4(H2O)2]·6H2O, a Catecholato-Bridged Dimer of Iron(III). *Inorganic Chemistry* **1996,** *35* (12), 3568-3576.

25. Gorun, S. M.; Lippard, S. J., Magnetostructural correlations in magnetically coupled (.mu.-oxo)diiron(III) complexes. *Inorganic Chemistry* **1991,** *30* (7), 1625-1630.

26. Taylor, S. W.; Chase, D. B.; Emptage, M. H.; Nelson, M. J.; Waite, J. H., Ferric Ion Complexes of a DOPA-Containing Adhesive Protein from Mytilus edulis. *Inorganic Chemistry* **1996,** *35* (26), 7572-7577.

27. Bjørnerud, A., The Physics of Magnetic Resonance Imaging. *The Physics of Magnetic Resonance Imaging* **2016**, FYS-KJM 4740 Lecture Notes.

28. Kim, B. H.; Lee, N.; Kim, H.; An, K.; Park, Y. I.; Choi, Y.; Shin, K.; Lee, Y.; Kwon, S. G.; Na, H. B.; Park, J.-G.; Ahn, T.-Y.; Kim, Y.-W.; Moon, W. K.; Choi, S. H.; Hyeon, T., Large-Scale Synthesis of Uniform and Extremely Small-Sized Iron Oxide Nanoparticles for High-Resolution T1 Magnetic Resonance Imaging Contrast Agents. *Journal of the American Chemical Society* **2011,** *133* (32), 12624-12631.

29. Huang, J.; Xie, J.; Chen, K.; Bu, L.; Lee, S.; Cheng, Z.; Li, X.; Chen, X., HSA coated MnO nanoparticles with prominent MRI contrast for tumor imaging. *Chemical Communications* **2010,** *46* (36), 6684-6686.

30. Kim, T.; Momin, E.; Choi, J.; Yuan, K.; Zaidi, H.; Kim, J.; Park, M.; Lee, N.; McMahon, M. T.; Quinones-Hinojosa, A.; Bulte, J. W. M.; Hyeon, T.; Gilad, A. A., Mesoporous Silica-Coated Hollow Manganese Oxide Nanoparticles as Positive T1 Contrast Agents for Labeling and MRI Tracking of Adipose-Derived Mesenchymal Stem Cells. *Journal of the American Chemical Society* **2011,** *133* (9), 2955-2961.

Chapter 4

High Relaxivity Gadolinium-Polydopamine Nanoparticles

4.1Introduction

In the past decade, magnetic resonance imaging (MRI) technology became progressively crucial in clinical diagnosis.[1] One of the key targets is to generate a high-resolution, noninvasive and versatile 3D imaging modality without ionizing radiation that can be widely employed to obtain internal anatomical and functional information of soft tissues.[2] Typical contrast agents used in MRI diagnosis include ferromagnetic inorganic nanoparticles[3-4] and stable paramagnetic chelates.[5] Among them, Gadolinium (Gd)-based chelates are of particular interest in clinical use due to the high magnetic moment, asymmetric electronic ground state, offering excellent performance in efficiently enhancing signal contrast by increasing the relaxation rates of surrounding water protons.[6-7] The relaxivity (r_1) is a measure of how sensitivity a contrast agent would be. It is important to increase the relaxivity of the contrast agent because: (1) high relaxivity contrast agent gives better signal-to-noise ratio and (2) reduce the contrast agent dose, therefore lowering the release and accumulation of Gd ions in bone tissue, which has been reported to induce a severe disease called the nephrogenic systemic fibrosis (NSF). [8-9]

To date, commercial contrast agents use linear or macrocyclic Gd chelating ligands, such as DPTA (diethylene triamine pentaacetic acid), DOTA (1,4,7,10-tetraazacyclododecane-1,4,7,10-tetraacetic acid) and their derivatives. However, these small molecular Gd chelators have low relaxivity (<10 $mM^{-1}s^{-1}$) due to their fast rotational correlation (τ_R=100 ps) and a low coordinate water molecule (q=1).[7] Moreover, these small molecular contrast agents have short blood half-life and tissue retention time that limit its application to long-time imaging collection.

The relaxivity of contrast agent can be affected by a few parameters: (1) the electronic properties of the gadolinium, (2) water exchange rate, (3) the ion to water proton distance, (4) the number of coordinated water molecules (q), (5) rotational correlation time (τ_R). Since the electronic properties of the gadolinium are hard to change, researchers have been dedicated to optimizing other four parameters to get higher relaxivity. For example, the correlation time, τ_R, of small molecular contrast agents can be significantly increased by covalently or non- covalently bound to macromolecules, such as polymers,[10-12] nanoparticles,[13-15] proteins[16-18] and liposomes.[19-20] The non-covalently bounded MRI contrast agents often suffer from their weak Gd binding affinity, limiting its application in vivo.[21] The development of protein engineering enables the design of Gd-specific binding proteins that showed excellent metal selectivity and stability. However, the large-scale synthesis is still difficult, and immunogenicity risk is a concern. On the other hand, the covalently bounded MRI contrast agents are made via conjugation of small molecule chelators. The relaxivity enhancement is not as good as Gd-specific binding proteins due to the free rotation of chelates on the surface. In addition, the nanoparticles or micelles preparation need extra effort besides the chelates synthesis. The conjugation efficiency is also a limit. The number of coordinated water molecules can also be increased via design new class of chelate ligands other than polyamino carboxylate. Raymond group developed hexadentate oxygen donor chelators with higher relaxivity due to the increased coordinated water molecules.[22-23]

As mentioned in the previous sections, self-oxidation polymerization of dopamine monomer under alkaline conditions has enabled the synthesis of natural melanin mimics with the similar chemical structure as well as physical and biological properties.[24] It has been demonstrated that catechol-based functional groups are able to chelate various metal ions, including Fe^{3+}, Mn^{2+} and Cu^{2+}.[25] Due to the strong metal binding ability of catechol-based functional groups, synthetic melanin nanoparticles have been employed in a growing number of studies, such as bioimaging,[26] batteries,[27-28] catalysts,[29] and environmental remediation.[30] I have discussed about our efforts on developing synthetic method for achieving controllable metal loading of synthetic melanin nanoparticles, including a variety of metal ions: Mn(III), Fe(III), Co(II), Ni(II), Cu (II), Zn(II) and Ga(III).[31] However, this pre-doping strategy isn't compatible with Gd ion. To overcome this issue, we introduce a simple displacement method to synthesize a series of Gd(III)-loaded synthetic melanin nanoparticles with different Gd loading, allowing investigating the optimized Gd loading for MRI contrast enhancement. There are several advantages of using Gd(III)-loaded synthetic melanin nanoparticles as contrast agents: (1) the relatively large size nanoparticle substantially slow down the rotational diffusion; (2) free rotation of chelates on the surface was restricted due to the crosslinked polydopamine 3D network; (3) the rotation and movement of catechols in the 3D crosslinked network would be constrained, leading to the formation of unsaturated Gd-catecholate, allowing more water molecule to coordinate.

4.2Preparation of Gd(III)-Loaded Synthetic Melanin Nanoparticles

All chemicals were obtained from Sigma-Aldrich and used without further purification. We first examine the compatibility of pre-doping strategy with the synthesis of Gd(III)-loaded synthetic melanin nanoparticles. Figure 4.1 showed the TEM of the amorphous aggregate generated by direct incorporation of Gd (III) during the polymerization. Considering the application of this kind of material, where the morphology plays an important role in determining their behavior, we decide to use an alternative approach, that is, use the Mn(III)-loaded nanoparticles as the template with Mn(III) binding sites primed for displacement when treated with $GdCl_3$. The synthetic strategy is illustrated in Figure 4.2.

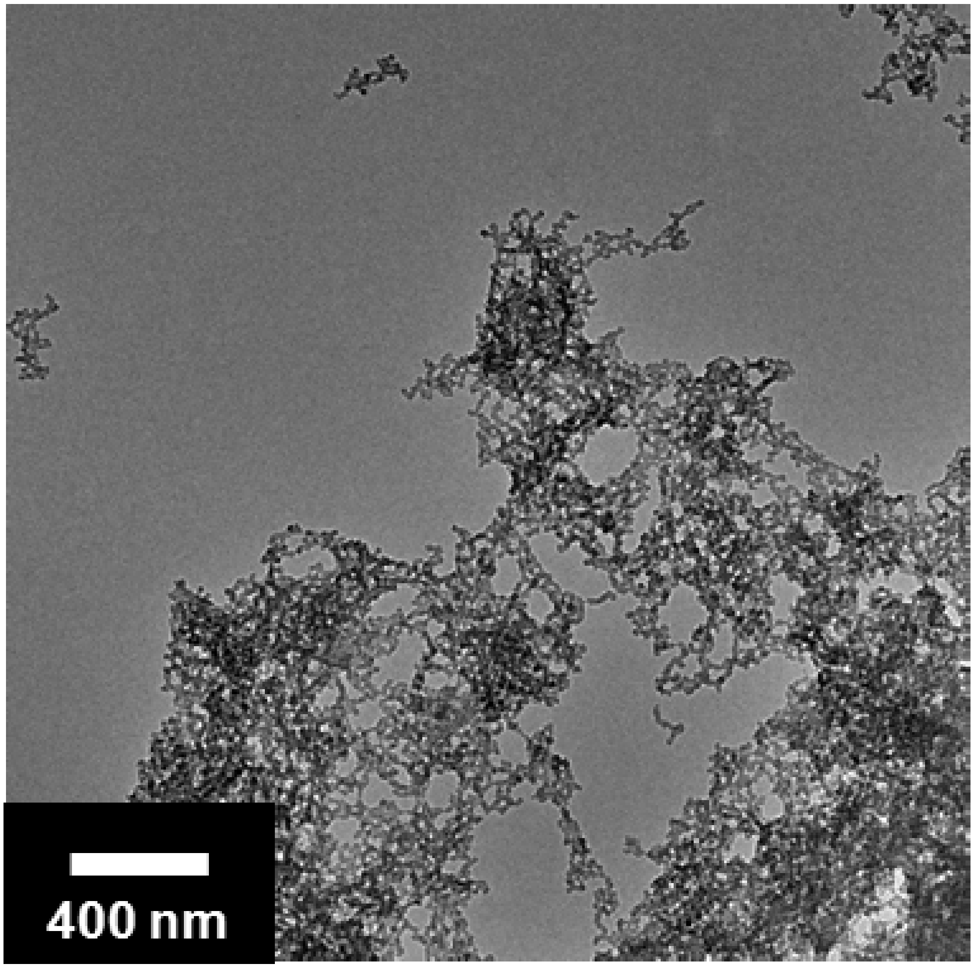

Figure 4.1. TEM image of Gd-polydopamine nano-aggregates synthesized via pre-doping strategy. Copyright 2017 John Wiley & Sons, Inc.[32]

Sample of Mn(III)-2, 3, 4 and 5 are synthesized via pre-doing strategy using the method described in chapter 3 and served as a template for exchanging with Gd(III) ion (Figure 4.2b). In a typical reaction to synthesize Mn(III)-2, dopamine hydrochloride(2.2mM) and of $Mn(Ac)_3 \cdot 2H_2O$ (2.1μM) were fully dissolved in 130 mL deionized water under stirring at room temperature for 1 h. We saw a red solution, indicating the formation of a Mn(III)-dopamine species. Subsequently, 20 mL Tris solution (2.5mM) was quickly injected into the reaction solution. After another 2 h reaction, the nanoparticles were separated by centrifugation and washed three times with deionized water. Finally, an excess of $GdCl_3$ salt was added to the Mn(III)-loaded sample solution and stirred overnight. The resulting samples (Gd-2, 3, 4 and 5) were separated by centrifugation and washed three times with deionized water.

In addition, samples using post-doping strategy, including Mn(III)-1 and Gd(III)-1, were prepared by the same method as described in chapter 3 (Figure 4.2a). The first step is to synthesize polydopamine nanoparticles through a typical oxidation polymerization in basic pH. In the second step, 20mL of polydopamine nanoparticle solution was incubated with a large excess $Mn(Ac)_3{\bullet}2H_2O$, or $GdCl_3$, respectively. The precipitate was removed by filtration. Excess of soluble metal salts can be removed via repeated wash with water and centrifuge.

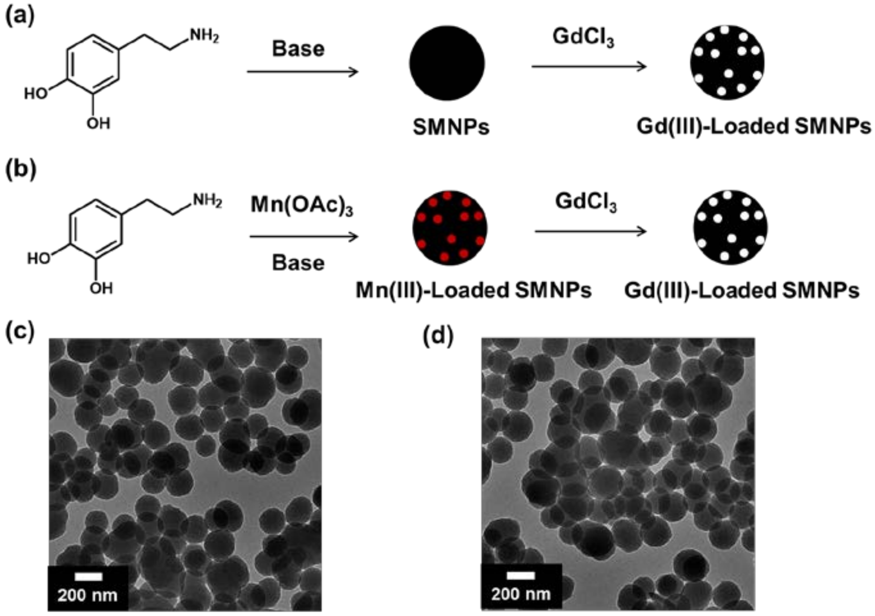

Figure 4.2 Synthesis of Gd(III)-loaded synthetic melanin nanoparticle (SMNP) via pre-doping strategy generate particles. White and red dots represent Gd(III) and Mn(III) ions respectively (c) TEM micrograph of Mn-4 and (d) corresponding Gd-4. Copyright 2017 John Wiley & Sons, Inc.[32]

4.3 Characterization of Metal-Loaded Synthetic Melanin Nanoparticles

4.3.1 Analysis the Metal Loading via ICP-OES and XPS

The advance of pre-doping strategy is to control the metal loading in the nanoparticle via adding different amounts of metal salt during the polymerization. tris-Mn(III)-dopamine complexes are formed in basic solution. Thus, the highest achievable feed ratio for the Mn(III) versus dopamine is 1:3. We can easily prepare lower loading nanoparticle via add less of the Mn(III) salts. Therefore, we can synthesize a series of Gd(III)-loaded synthetic melanin nanoparticles via metal displacement method to achieve variable Gd loadings. The incorporation of Mn can be confirmed by X-ray Photoelectron Spectroscopy (XPS). XPS spectra (Thermo Scientific ESCALAB 250Xi) were collected at the Keck II facility of NUANCE at Northwestern University using monochromated Al Ka X-rays. A low-energy electron flood gun was used to compensate for XPS induced surface charging. The carbon 1s line (284.8 eV) was used as a reference to calibrate the XPS spectra. As shown in Figure 4.3, the XPS spectrum of Mn(III)-loaded synthetic melanin nanoparticles showed a characteristic peak of Mn($2p_{3/2}$) at 641.7eV, which can be assigned to Mn(III). The magnetometry studies of these Mn(III)-loaded nanoparticles in chapter 3 have corroborated the trivalent oxidation state of Manganese, possibility attribute to the highly oxidative conditions during the synthesis. The complete exchanging from Mn(III) to Gd(III) was confirmed by analysis of XPS and ICP-OES data. Figure 4.3b showed the characteristic peaks of C(1s), O(1s), N(1s), and Gd(4d). Importantly, the characteristic peaks of Mn2p have disappeared after the displacement reaction. The procedure of ICP-OES experiment is described in chapter 2. The metal loading in Table 4.1 was calculated based on the ICP results. Note that Gd(III)-loaded nanoparticles also showed a negligible amount of Mn (0.006 wt.%) by ICP-OES measurement, consistent with the XPS data. Based on these data, we speculated that Mn(III) exhibits a much weaker binding towards polydopamine compared with Gd(III).[33]

Table 4.1. Metal loading of Mn(III) and Gd(III)-loaded synthetic melanin nanoparticles.

Sample	Mn(III)%	Radius(nm)[a]	Sample	Gd(III)%	Radius(nm)[a]	Method[b]
Mn-1	0	87 ± 3	Gd-1	2	92 ± 6	a
Mn-2	1	112 ± 9	Gd-2	3	109 ± 8	b
Mn-3	2	103 ± 7	Gd-3	5	98 ± 6	b
Mn-4	4	87 ± 9	Gd-4	11	98 ± 9	b
Mn-5	10	116 ± 6	Gd-5	17	118 ± 4	b

[a]Determined by dynamic light scattering (DLS) [b] Method a is the post-particle formation doping strategy. Method **b** is the Mn(III) displacement method shown in Figure 4.2.

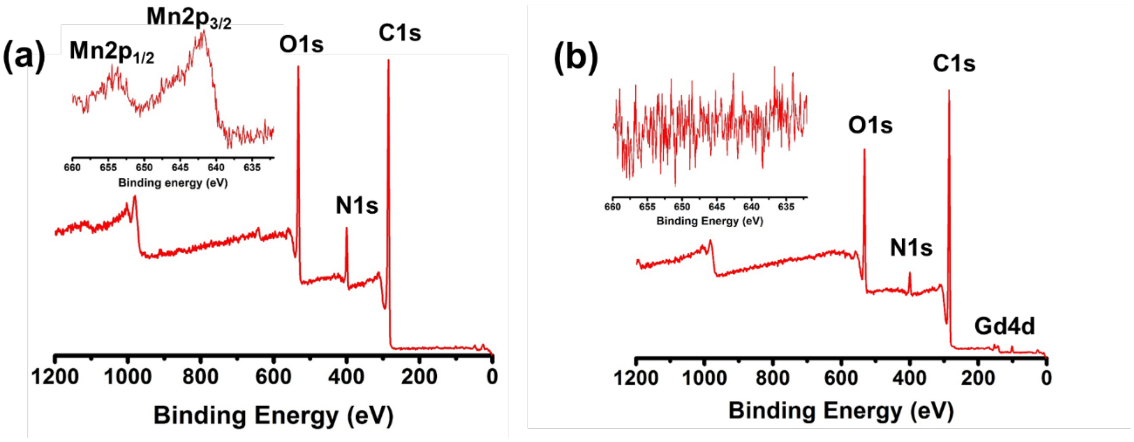

Figure 4.3. XPS spectrum of (a) Mn(III)-loaded synthetic melanin nanoparticles and (b) Gd(III)-loaded synthetic melanin nanoparticles. Copyright 2017 John Wiley & Sons, Inc.[32]

The size and morphology of Mn(III) and Gd(III)-loaded synthetic melanin nanoparticles were characterized by TEM and DLS. Figure 4.2 c and d shows the TEM image of Mn-4 and Gd-4. The additional TEM images of sample Mn-1, 2, 3, 5 and Gd-1, 2, 3 and 5 were shown in Figure 4.4. Although the sizes of different Gd(III)-loaded samples are different due to the size difference from Mn(III) template, we didn't observe any change in morphology in the corresponding samples. (i.e. Mn-1 versus Gd-1, Mn-2 versus Gd-2). Coupled with the TEM date, we also measure the hydrodynamic radius via DLS experiments. Figure 4.5 shows the DLS results, with each figure contains the one Gd(III)-loaded sample and its corresponding Mn(III) template. We summary the size information from DLS experiments in Table 4.1. When considering the size distribution, the size remains the same during the displacement reaction, indicating that spherical structure is mainly dependent on the crosslinking of dopamine unit other than the dopamine-metal coordination. To consider the application as MRI contrast agent, we expect them to have good colloid stability. Therefore, we also measure zeta potential of these samples. The result showed that they have highly negative zeta potential value (**Gd-1**: −17.8 V; **Gd-2**: −31.3 V; **Gd-3**; −50.6 V; **Gd-4**: −20.7 V; **Gd-5**; −24.7 V), demonstrating their high stability in solution.

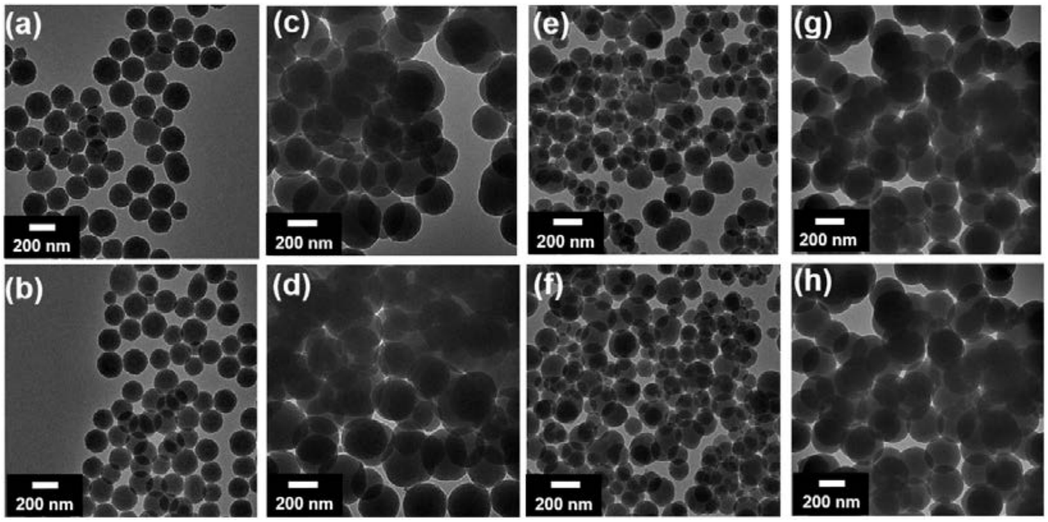

Figure 4.4. Representative TEM images: (a) Mn-1; (b) Gd-1; (c) Mn-2 ; (d) Gd-2; (e) Mn-3; (f) Gd-3; (g) Mn-5 and (h)Gd-5. Copyright 2017 John Wiley & Sons, Inc.[32]

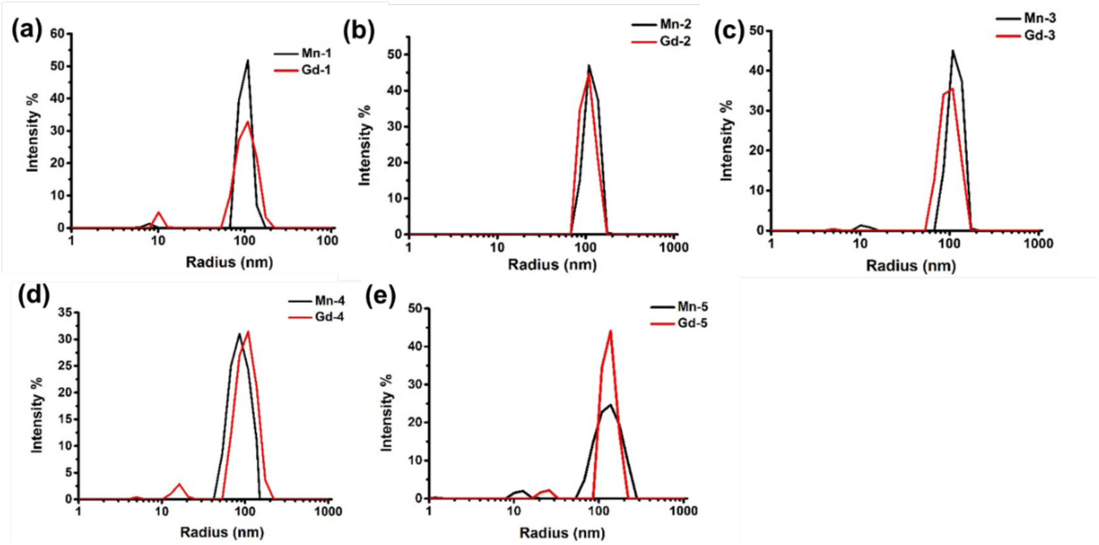

Figure 4.5. Dynamic light scattering of: (a) Mn-1 and Gd-1; (b) Mn-2 and Gd-2; (c) Mn-3; and Gd-3; (d) Mn-4 and Gd-4; (e) Mn-5 and Gd-5. Copyright 2017 John Wiley & Sons, Inc.[32]

4.3.2 Characterization via NMRD and MR Imaging Analysis

In chapter 2 and 3, we described the effort on investigating the magnetic interaction between Fe(III) and Mn(III) centers and their influence on the relaxivity value. [34] We hypothesized that the higher relaxivity value of Mn(III)-loaded nanoparticles compared Fe(III)-loaded sample is due to the weaker antiferromagnetic coupling. To further confirm this assumption, we choose the Gd(III)-loaded synthetic melanin nanoparticle as the model to evaluate their MRI performance. It is known that the Gd(III) would exhibit much less antiferromagnetic coupling compared with Fe(III) and Mn(III) centers. Therefore, if our hypothesis is correct, the increase of the Gd loading shouldn't lead to the relaxivity loss, but the rather significant increase in "per-particle relaxivity". In another context, increase the Gd concentration inside the nanoparticles would also lead to the Gd centers less exposed to water. In this case, we think the relaxivity would also decrease on a Gd-center basis. Herein, to rationalize the synthesis and optimize the MRI performance, we aimed to find the best synthetic conditions that can provide the highest relaxivities in a wide Gd loading range.

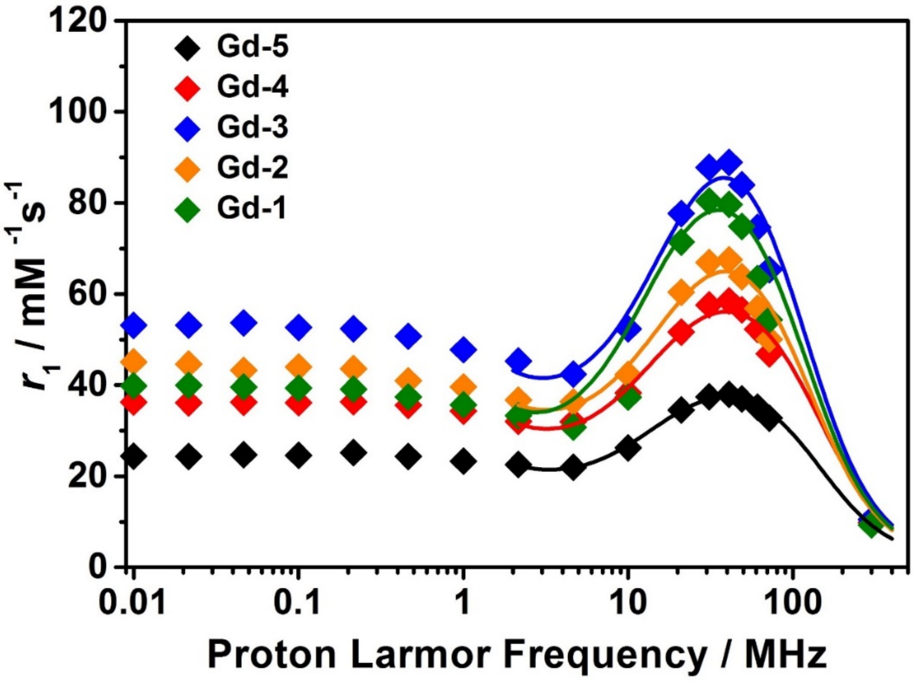

Figure 4.6. 1H NMRD profiles for Gd-i (i=1-5). The x-axis is proton Larmor frequency, y-axis is r1 value per Gd(III) ion for each sample. Copyright 2017 John Wiley & Sons, Inc.[32]

We first perform the NMRD experiments to determine the field dependence relaxivity values (Figure 4.6).[35-36] In contrast to the NMRD profiles of Fe(III)-loaded synthetic melanin nanoparticles, Figure 4.6 showed a decrease of relaxivity before 5 MHz and a broad peak at around 40 MHz, which is a characteristic sign of slow rotation systems. It is noted that NMRD profiles of five samples exhibited the same characteristics shape but offset by a scaling factor, indicating that the parameter that affects the relaxivity value isn't dependent on the field strength. Therefore, two possible parameters: hydration number q and the distance between the coordinated water proton and electron spin (r_{GdH}) can cause this non-field-dependent relaxivity change. However, the r_{GdH} value is almost fixed in the range of 3.0-3.2 Å, even with the shift in coordination chemistry from the Gd(III) and its ligand.[37] In this context, we attribute the effect of relaxivity value in the change in hydration number q. To give a quantitive analysis of the hydration state of the Gd(III) ion of five samples, we first assume Gd-5 sample has an average hydration number q equals to 1. This assumption is based on the fact that other Gd-based macromolecular contrast agents with similar r_1 value have q value equals to 1.[38-40] Since Bloembergen-Morgan (SBM) theory isn't working well at low magnetic fields for slow rotation systems, we only consider to analyze data above 3 MHz. Coordinated water residence time (τ_M) is used to describe the water exchange rate from inner sphere to bulk. We fixed τ_M at 30 ns since the water exchange does not limit r_1. Then we performed the fit through three variables parameters, namely the overall rotational correlation time (τ_R), the correlation time for the transient zero-field splitting (ZFS; τ_V) and the amplitude of the transient ZFS (Δ^2). Table 4.2 listed the best fitting result of three variables parameters obtained from NMRD data. The overall rotational correlation time, the correlation time for the transient zero-field splitting and the amplitude of the transient ZFS of Gd-5 is then calculated to be 1.2 ns, 17ps and $8.1*10^{18}$ s^{-2} respectively. We believe that the highly crosslinked structure results in a rotationally limited system at the Gd centers. Therefore, the internal rotation of Gd complex is restricted, leading to a perfect fit across the entire range. By contrast to the Gd-5, Gd-3 has the highest relaxivity value. Thus, we use the similar fitting process of NMRD profile, but a higher hydration number (q=2), suggesting more Gd ions are accessible to water molecules. The overall rotational correlation time, the correlation time for the transient zero-field splitting and the amplitude of the transient ZFS of Gd-3 is then calculated to be 1.5 ns, 16ps and 8.4*1018 s^{-2} respectively. Since transient zero-field splitting and the magnitude of the transient ZFS are almost the same in this two samples, we decided to fit the NMRD data of Gd-1, 2 and 4 with only variable q and τ_R. The results were also shown in Table 4.2, where the τ_R is almost unchanged and the hydration number decrease from 1.8 to 1.4.

Table 4.2. Selected relaxation parameters obtained from the analysis of NMRD profiles (298 K).[a]

Gd-i	r_1 (mM^{-1} s^{-1})[b]	$\mathit{\Delta}^2$ (10^{18} s^{-2})[c]	τ_V (ps)[c]	τ_R (ns)	r (Å)[d]	q	τ_M (ns)[d]
Gd-1	63.4	8.1[d]	17[d]	1.5 ± 0.2	3.0	1.8± 0.1	30
Gd-2	56.9	8.1[d]	17[d]	1.4 ± 0.1	3.0	1.6± 0.1	30
Gd-3	74.6	8.4±1.1	16 ±1	1.5 ± 0.3	3.0	2[d]	30
Gd-4	52.3	8.1[d]	17[d]	1.4 ± 0.1	3.0	1.4± 0.1	30
Gd-5	35.1	8.1±0.9	17±1	1.2 ± 0.3	3.0	1[d]	30

[a] The outer-sphere component of the relaxivity was estimated using standard values for the distance of closest approach *a* (4 Å) and the relative diffusion coefficient of solute and solvent *D* (2.2×10^{-5} cm^2 s^{-1}); [b] 60 MHz; [c] the parameters for electronic relaxation are used as empirical fitting parameters and do not have a real physical meaning for slowly tumbling nanosized systems. Low-field data, those most affected by electronic relaxation, were not included in data analysis; [d] fixed during the fit.

The longitudinal and transverse relaxation time (T_1 and T_2) at 60 MHz were acquired with a contrast agent analyzer (a Time Domain-NMR instrument, Bruker, Minispec mq60, 1.41 T/60 MHz, 37 °C). Table 4.3 showed the r_1 values at 60MHz. Among them, Gd-3 has the highest r_1 value (75 mM^{-1}s^{-1}). It is more than 20-fold of commercially available Gd contrast agents (i.e. Gd-DOTA) and even many macromolecules (such as liposome and dendrimer).[41] By contrast, Gd-5 has the highest Gd loading but with the lowest r_1 value (35 mM^{-1}s^{-1}). Considering the fitting result, the significant drop of r_1 can attribute to the less overall hydration number, resulting from a less accessible Gd to water environment within the core of the particle. Figure 4.7 summarized the r_2 / r_1 ratios obtained from the NMRD data at various field strengths (20-70MHz). Although the r_2 / r_1 ratio increase with the frequency increase, the highest one is still under 3. These data prove that these Gd(III)-loaded synthetic melanin nanoparticles can be used as effective T_1-weighted contrast agents with low interference from T_2 effects.

Table 4.3. r_1 and r_2 values at 1.4T (60 MHz).

Sample	**Gd-1**	**Gd-2**	**Gd-3**	**Gd-4**	**Gd-5**
r_1($mM^{-1}s^{-1}$)	67	57	75	52	35
r_2/r_1	1.9	1.8	1.9	2.3	1.8

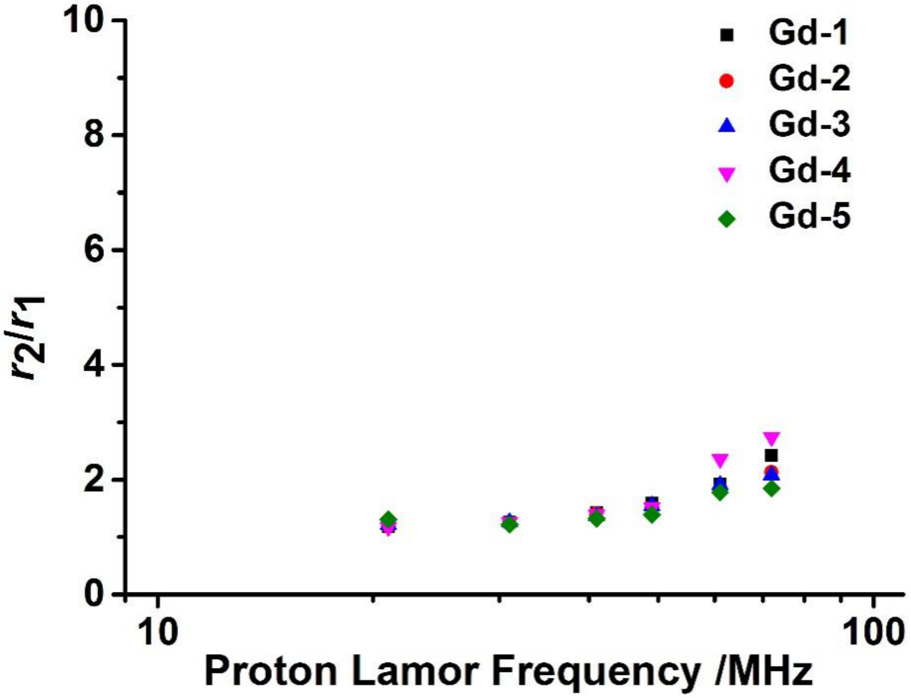

Figure 4.7. The r2/ r1 value at various field strengths (20-70MHz) of Gd-i (i=1-5). Copyright 2017 John Wiley & Sons, Inc.[32]

In the past chapters, we have used the "per particle-relaxivity" ($r_{1p(particle)}$) to describe the local concentration necessary to achieve the desirable T_1 MR imaging contrast under different magnetic fields.[42] It was found that the "per particle-relaxivity" of Fe(III)-loaded nanoparticles isn't increased linearly with the increase of Fe concentration due to the antiferromagnetic coupling. Herein, we perform the analysis of "per particle-relaxivity" for the Gd(III)-loaded synthetic melanin nanoparticles to further examination of our theory on the antiferromagnetic coupling effect on the relaxivity value. Figure 4.8 showed the calculated "per particle-relaxivity" ($r_{1p(particle)}$) value of five samples. Not surprisingly, the plots of $r_{1p(particle)}$ showed that relaxivity increases monotonically with concentration of Gd. So Gd-5 that has the highest Gd loading present the highest per particle relaxivity among five samples. This is consistent with our assumption that Gd(III) exhibits a much less antiferromagnetic coupling compared with Fe(III) and Mn(III) centers.

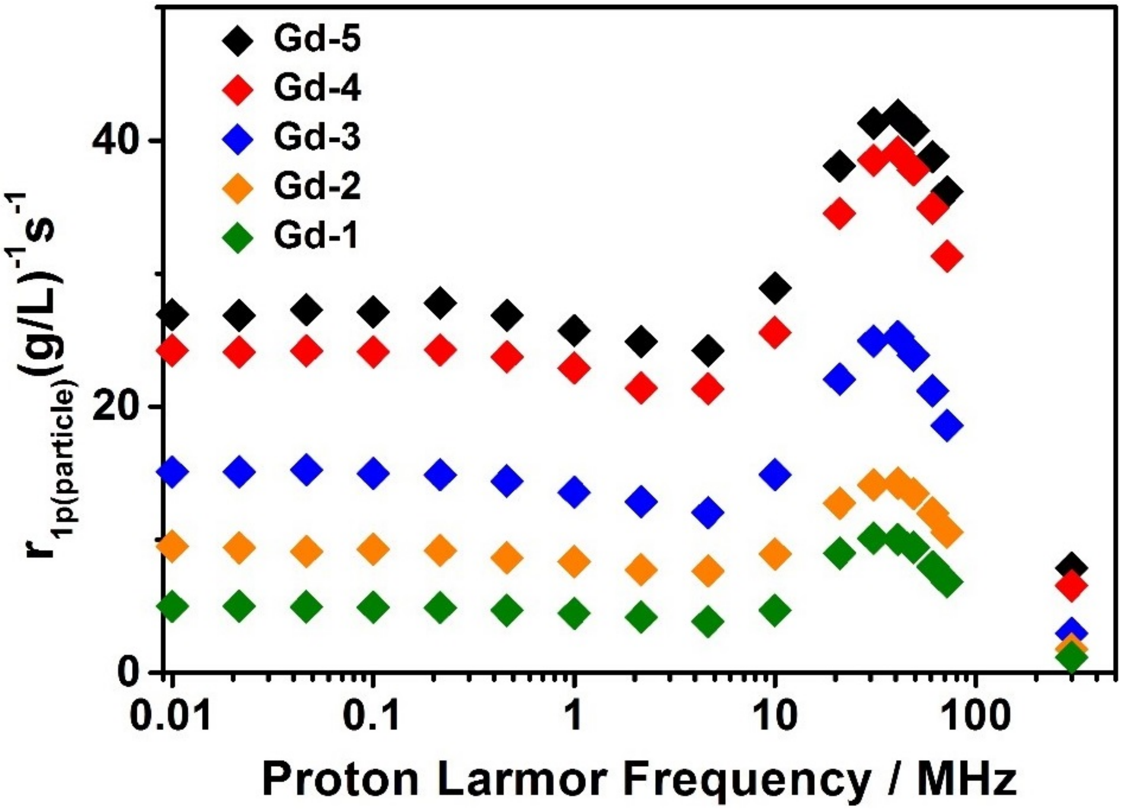

Figure 4.8. ^{1}H NMRD profiles for Gd-i (i=1-5). The x-axis is proton Larmor frequency, y-axis is r1 value per nanoparticle for each sample. Copyright 2017 John Wiley & Sons, Inc.[32]

The above discussions focus on the evaluation of these samples at the relatively low magnetic field. In this paragraph, we evaluate the potential application of these nanoparticles at high magnetic fields. The MR images were acquired on a Bruker 7.0T magnet with Avance II hardware equipped with a 72 mm quadrature transmit/receive coil. T_1 contrast was determined by selecting regions of interest (ROI) using Software ParaVision Version 5.1. The parameters for 7T MRI are: TR=750.0ms, TE=12.6ms, echo=1/1, FOV= 6.91/3.12 cm, slice thickness=2mm, nex=2mm, matrix=256*116. Figure 4.9 showed a phantom image of each nanoparticle at a concentration gradient. We observed a brighter phantom image as the Gd(III) concentration increased and r_1 value was calculated after the curve fitting of $1/T_1$ versus Gd (III) ions concentrations. Like the r_1 value at 60 MHz, Gd-3 has the highest r_1 value (10.5 $mM^{-1}s^{-1}$), while Gd-2 has lowest values at 7T. Nevertheless, these values are still much higher than commercial contrast agents that shows an r_1 value around 3 mM^{-1} s^{-1}.[43] More importantly, the r_1 value of Gd-5 is very close to that of Gd-3, indicating that we can significantly lower the dosage without sacrificing the contrast enhancement ability. We also calculated the r_2/r_1 values and summarized in Table 4.4. Not surprisingly, these values are much higher than the ones at lower magnetic field due to the enhanced T_2 effects. To evaluate the performance of these nanoparticles as contrast agents, HeLa cells were seeded in 15 cm round tissue culture dishes and allowed to attach overnight. After washing twice with sterile PBS, the cells were incubated with Gd-3 and polydopamine nanoparticles (PD-NP) for 24 hours at normal cell culture condition. The cells were washed with PBS three times to remove excess nanoparticles, and then treated with 0.05% trypsin to remove them from the dishes. The cells were gathered by centrifuge at 300 g for 3 min and washed with PBS buffer twice. The MR images were acquired on a Bruker 7.0T magnet with Avance II hardware equipped with a 72 mm quadrature transmit/receive coil. Figure 4.9f showed the MR images of Gd-3 at different particle concentration, polydopamine nanoparticle and control. Control image showed barely any bright contrast since it contains only HeLa cells. Polydopamine nanoparticles showed some brightness due to its ability to sequester Fe(III) from the biological fluid. HeLa cells internalized with Gd-3 provide enhanced positive contrast in the T_1-weighted MR images measurement than the others, demonstrating that our nanoparticles could be used as effective Gd-based T_1 MRI contrast agents.

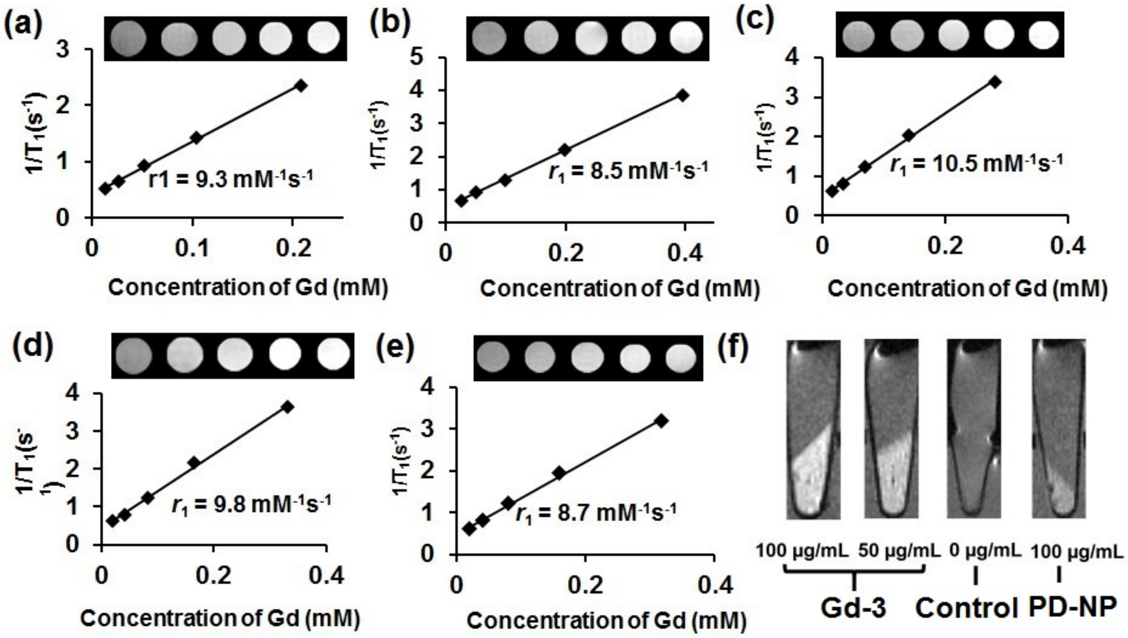

Figure 4.9. MRI characterization of Gd-i (i=1-5) on a Bruker 7T magnet. Plots of 1/T1 versus Gd(III) concentration and its corresponding image of (a) Gd-1; (b) Gd-2; (c) Gd-3; (d) Gd-4; (e) Gd-5.(f) In vitro T1-weighted MR images of HeLa cells incubated with Gd-3 and PD- NP at diffferent concentrations for 24h. Copyright 2017 John Wiley & Sons, Inc.[32]

Table 4.4. r_1 result for each sample shown in Figure 4.9.

Sample	Gd-1	Gd-2	Gd-3	Gd-4	Gd-5
r_1(mM^{-1}s^{-1})	9.3	8.5	10.5	9.8	9.8
r_2/r_1	18.1	12.8	16.3	14.7	14.7

4.3.3 Cell Viability Assay and Stability of Nanoparticles in Different Mediums

In vitro cytotoxicity of Gd-1, Gd-3, Gd-4, Gd-5 and PD-NP was determined in HeLa cells by the CCK-8 (cell counting kit-8) assay. HeLa cells were incubated on 96-well plates with 1*10^4 cells per well in High-glucose DMEM medium containing 10% fetal bovine serum and 1% antibiotics at 37 °C in 5% CO_2 humidified atmosphere for 24 h and 48 hours. Addition of 10 μL of

CCK-8 solution to each well and incubation for another 4 hours at 37 °C resulted in the formation of formazan crystals. Then the absorbance value at 460 nm was recorded using a microplate reader. The absorbance value of the untreated cells was used as the reference value of 100% cellular viability. Figure 4.10 showed the cell viability data at 24 and 48 hours, without apparent cytotoxicity observed at levels up to 125 µg mL^{-1} for Gd-1, 2, 3, and 4. However, Gd-5 showed higher cytotoxicity due to the high content of Gd(III). Transmetallation of a gadolinium complex would result in a release of free Gd ion. Thus, it is important to examine the selectivity of these nanoparticles for Gd^{3+} over physiological metal ions, such as Ca^{2+} and Zn^{2+}. We dispersed Gd-3 that showed high relaxivity as an example in the maximum human blood concentration (2.5mM for Ca^{2+} and 0.15mM Zn^{2+}) solution respectively for 7days. The nanoparticles were separated by centrifugation and washed three times with deionized water before sending for ICP-OES analysis. Figure 4.11 showed more than 90% of Gd ions was still bound to the particle, indicating no significant release of Gd ion occurs. To determine the stability of Gd-3 in different media, we dispersed these nanoparticles in water, 10mM HEPES and 1x PBS buffer. 100ul of Gd-3 solution (three replicates) were added in 500ul dialysis tubes with Mw=10000 respectively, and dialyzed to 500mL medium under room temperature with magnetic stirring. Gd-3 aliquots were taken at time points as 24h, 48h, 72h, 5day and 7days for ICP-OES analysis. Figure 4.12 showed the amount of Gd ion chelated to the nanoparticles does not change significantly over time in water, 4-(2-hydroxyethyl)-1-piperazineethanesulfonic acid (HEPES) and Phosphate Buffered Saline (PBS) buffer, indicating its promise for in vivo applications.

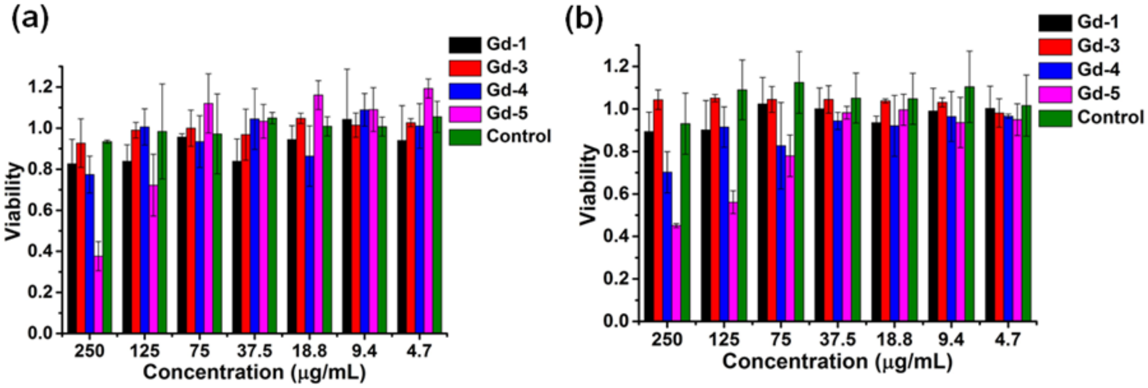

Figure 4.10. Cell viability of HeLa cells exposed to different concentrations of Gd-1, Gd-3, Gd-4, Gd-5 and control (PD-NP) at 24 and 48 hours. Copyright 2017 John Wiley & Sons, Inc.[32]

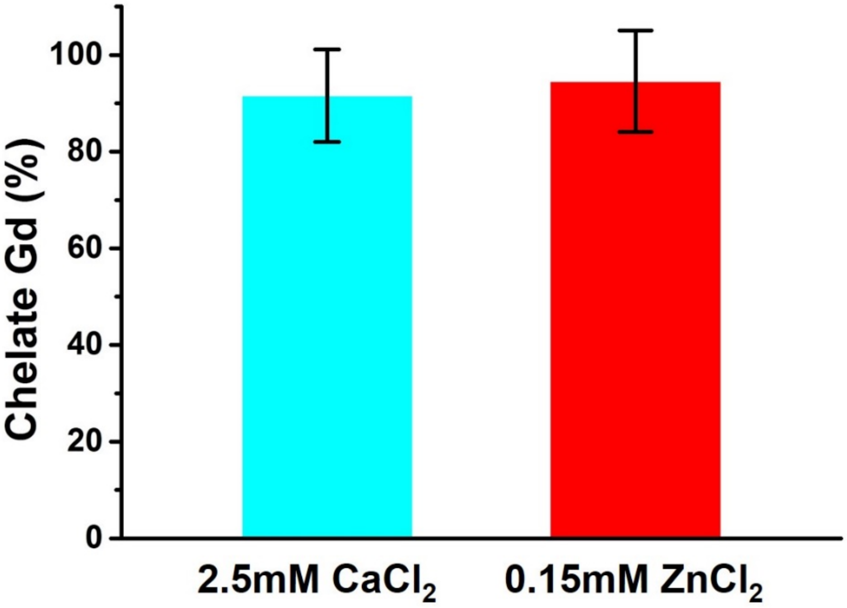

Figure 4.11. Gd-polydopamine complex stability over Ca2+ and Zn2+ cations. Copyright 2017 John Wiley & Sons, Inc.[32]

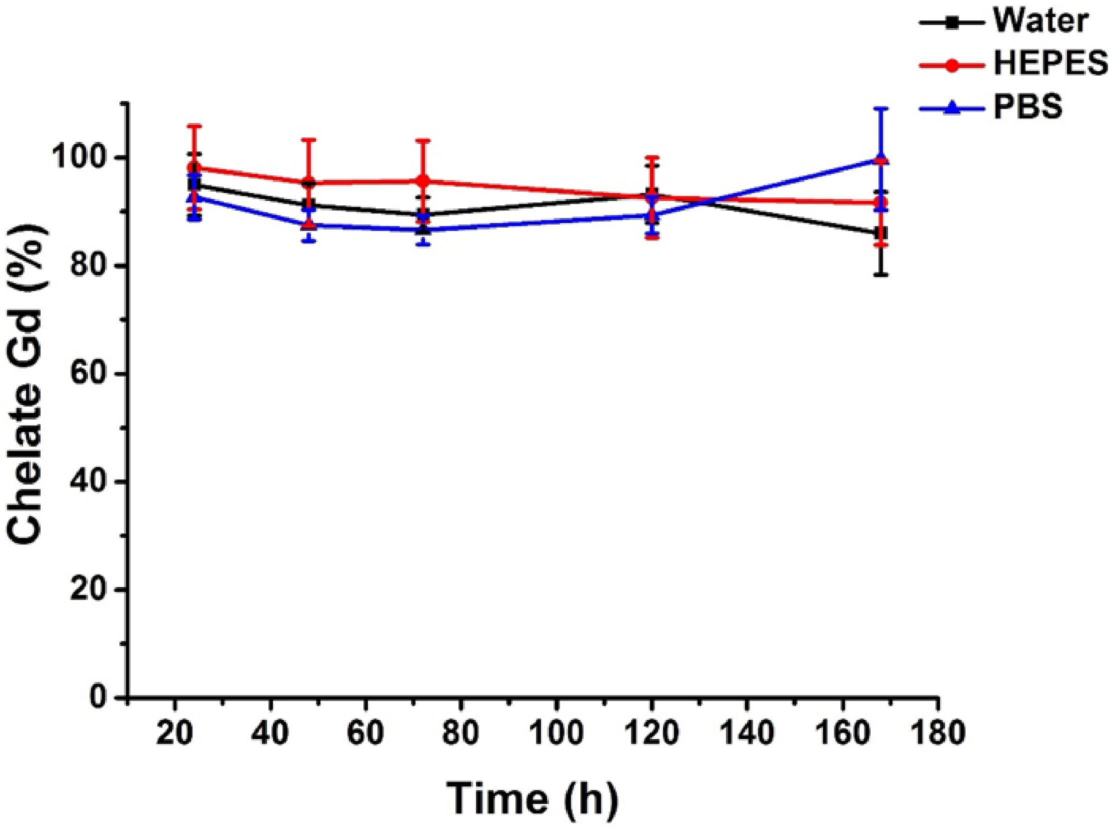

Figure 4.12. Stability of Gd-3 sample over different media. Copyright 2017 John Wiley & Sons, Inc.[32]

4.3.4 Magnetochemical Analysis

In chapter 2 and 3, we described the effort on investigating the magnetic interaction between Fe(III) and Mn(III) centers and their influence on the relaxivity value. We hypothesized that the higher relaxivity value of Mn(III)-loaded nanoparticles compared Fe(III)-loaded sample is due to the weaker antiferromagnetic coupling. At the previous section, we found that Gd(III)-loaded synthetic melanin nanoparticles has even better MRI performance compared with Mn(III)-loaded ones. We assumed this is due to the negligible antiferromagnetic coupling between Gd centers. To prove this, the magnetic properties of Gd(III)-loaded nanoparticles with different Gd concentrations were investigated by variable-temperature magnetic susceptibility measurements from 2 to 300 K under a 5000 Oe magnetic field (Figure 4.13). In contrast to Fe(III) and Mn(III)-loaded system, we did not observe significant deviation for three Gd(III)-loaded sample. The single-ion, spin-only behavior with the $\chi_M T$ equal to 7.88 emu K cm^{-3} mol^{-1} indicates a negligible antiferromagnetic coupling between Gd(III) centers that prove our assumption. Since antiferromagnetic coupling isn't a parameter in this system, we believe that the low relaxivity in high Gd concentration sample is attributed to the larger size particles that prevent the water access to the core.

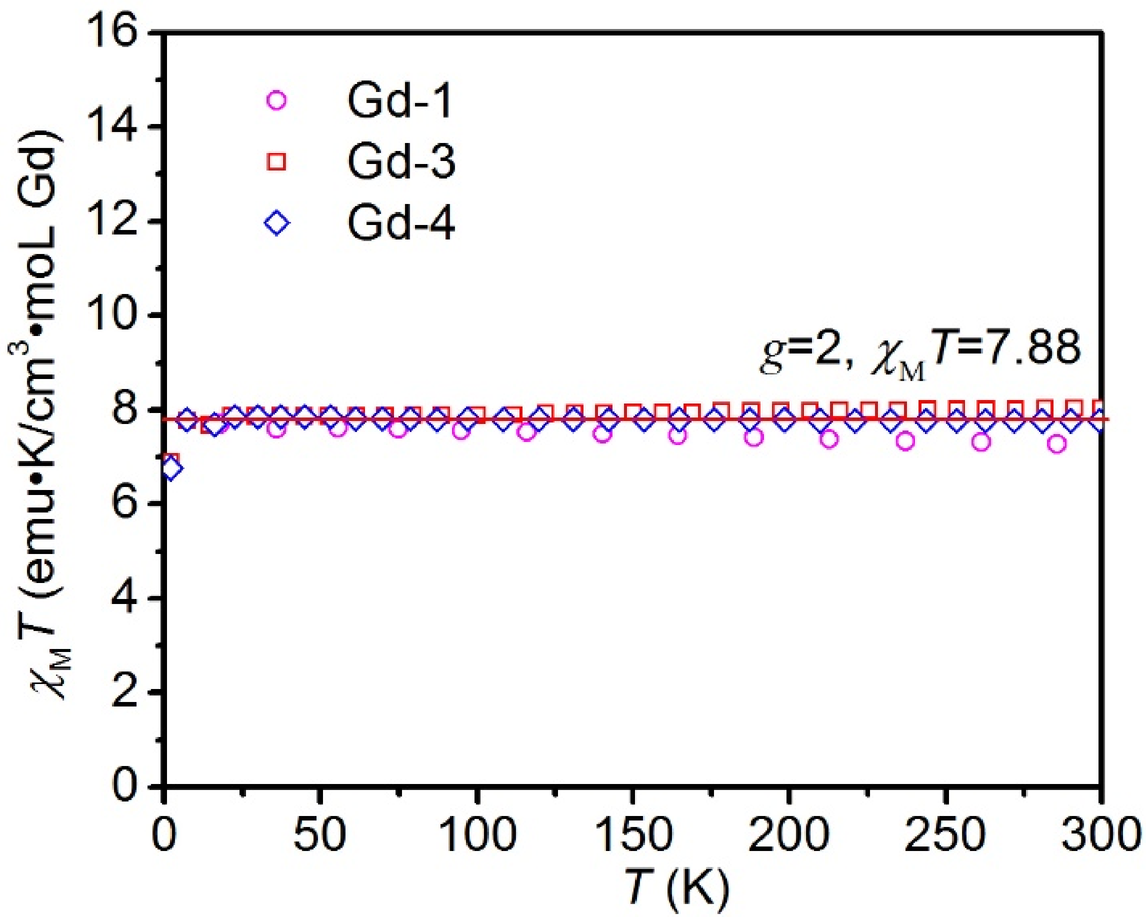

Figure 4.13. Temperature dependence of the product of magnetic susceptibility and temperature (χMT) for Gd-1, Gd-3 and Gd-4 samples. The solid line describes the behavior of an isolated, isotropic Gd (III) ion. Copyright 2017 John Wiley & Sons, Inc.[32]

4.4 Conclusion

In conclusion, we reported a facial and scalable synthetic approach for generating Gd(III)-loaded synthetic melanin nanoparticles that shows much higher relaxivities than traditional nanoparticle-based contrast agent. This is because, compared with the surface conjugation of small molecule chelator, the free rotation of crosslinked catechol groups is sharply restricted. In addition, we did not observe appreciable deviation for three Gd(III)-loaded sample, indicates a negligible antiferromagnetic coupling between Gd(III) centers that prove our assumption. The as-prepared nanoparticles show significant MRI signal enhancement for in vitro imaging and the value of longitudinal relaxivity is as high as 75 mM^{-1} s^{-1} at 1.41 T and 10.5 mM^{-1} s^{-1} at 7 T for Gd-3. The further increase of Gd loading wouldn't significantly lower the r_1 value, providing a promising way of decreasing the dosage of contrast agent. The high stability of Gd-chelates over physiological metal ions such Ca^{2+} and Zn^{2+} and low cytotoxicity show its promising application for in vivo MR imaging. Moreover, another study in our group shows that these nanoparticles have strong optical absorption in the near-infrared region that could be used as photothermal and photoacoustic (PA) contrast agent. Taking advantage of these features, it is possible to produce an MRI and PA dual imaging system as well as a photothermal therapy platform shortly.

4.5 Acknowledge

Chapter 4 is adapted in full print from Zhao Wang, Fabio Carniato, Yijun Xie, Yuran Huang, Yiwen Li, Sha He, Nanzhi Zang., Jeffery D. Rinehart, * Mauro Botta,* and Nathan C. Gianneschi,* High Relaxivity Gadolinium-Polydopamine Nanoparticles, Small 2017, DOI: 10.1002/smll.201701830. Copyright 2017 Wiley-VCH. The dissertation author is the first author of this paper. For Chapter 4, I would like to thank our collaborators: Fabio Carniato, Prof. Mauro Botta, Yijun Xie, Prof. Jeffery D. Rinehart. I also appreciate the help from my colleague Yuran

Huang, Yiwen Li and Nanzhi Zang. In addition, I want to thank Dr. Sha He for support with the measurement of relaxivities.

4.6 References

1. Fox, M. D.; Raichle, M. E., Spontaneous fluctuations in brain activity observed with functional magnetic resonance imaging. *Nature Reviews Neuroscience* **2007,** *8* (9), 700-711.

2. Terreno, E.; Castelli, D. D.; Viale, A.; Aime, S., Challenges for molecular magnetic resonance imaging. *Chemical Reviews* **2010,** *110* (5), 3019-3042.

3. Na, H. B.; Song, I. C.; Hyeon, T., Inorganic nanoparticles for MRI contrast agents. *Advanced Materials* **2009,** *21* (21), 2133-2148.

4. Laurent, S.; Forge, D.; Port, M.; Roch, A.; Robic, C.; Vander Elst, L.; Muller, R. N., Magnetic iron oxide nanoparticles: Synthesis, stabilization, vectorization, physicochemical characterizations and biological applications. *Chemical Reviews* **2008,** *108* (6), 2064-2110.

5. Lauffer, R. B., Paramagnetic metal complexes as water proton relaxation agents for NMR imaging: Theory and design. *Chemical Reviews* **1987,** *87* (5), 901-927.

6. Caravan, P.; Ellison, J. J.; McMurry, T. J.; Lauffer, R. B., Gadolinium(III) chelates as MRI contrast agents: Structure, dynamics, and applications. *Chemical Reviews* **1999,** *99* (9), 2293-2352.

7. Caravan, P., Strategies for increasing the sensitivity of gadolinium based MRI contrast agents. *Chemical Society Reviews* **2006,** *35* (6), 512-523.

8. Aime, S.; Caravan, P., Biodistribution of gadolinium-based contrast agents, including gadolinium deposition. *Journal of Magnetic Resonance Imaging* **2009,** *30* (6), 1259-1267.

9. Kribben, A.; Witzke, O.; Hillen, U.; Barkhausen, J.; Daul, A. E.; Erbel, R., Nephrogenic Systemic Fibrosis. Pathogenesis, Diagnosis, and Therapy. *Journal of the American College of Cardiology* **2009,** *53* (18), 1621-1628.

10. Wen, X.; Jackson, E. F.; Price, R. E.; Kim, E. E.; Wu, Q.; Wallace, S.; Charnsangavej, C.; Gelovani, J. G.; Li, C., Synthesis and Characterization of Poly(l-glutamic acid) Gadolinium Chelate: A New Biodegradable MRI Contrast Agent. *Bioconjugate Chemistry* **2004,** *15* (6), 1408-1415.

11. Huang, C.-H.; Tsourkas, A., Gd-based macromolecules and nanoparticles as magnetic resonance contrast agents for molecular imaging. *Current topics in medicinal chemistry* **2013,** *13* (4), 411-421.

12. Bogdanov, A. A.; Weissleder, R.; Frank, H. W.; Bogdanova, A. V.; Nossif, N.; Schaffer, B. K.; Tsai, E.; Papisov, M. I.; Brady, T. J., A new macromolecule as a contrast agent for MR angiography: preparation, properties, and animal studies. *Radiology* **1993,** *187* (3), 701-706.

13. Randolph, L. M.; LeGuyader, C. L. M.; Hahn, M. E.; Andolina, C. M.; Patterson, J. P.; Mattrey, R. F.; Millstone, J. E.; Botta, M.; Scadeng, M.; Gianneschi, N. C., Polymeric Gd-DOTA amphiphiles form spherical and fibril-shaped nanoparticle MRI contrast agents. *Chemical Science* **2016**.

14. Taylor, K. M. L.; Kim, J. S.; Rieter, W. J.; An, H.; Lin, W.; Lin, W., Mesoporous Silica Nanospheres as Highly Efficient MRI Contrast Agents. *Journal of the American Chemical Society* **2008,** *130* (7), 2154-2155.

15. Chen, K.-J.; Wolahan, S. M.; Wang, H.; Hsu, C.-H.; Chang, H.-W.; Durazo, A.; Hwang, L.-P.; Garcia, M. A.; Jiang, Z. K.; Wu, L.; Lin, Y.-Y.; Tseng, H.-R., A small MRI contrast agent library of gadolinium(III)-encapsulated supramolecular nanoparticles for improved relaxivity and sensitivity. *Biomaterials* **2011,** *32* (8), 2160-2165.

16. Yang, J. J.; Yang, J.; Wei, L.; Zurkiya, O.; Yang, W.; Li, S.; Zou, J.; Zhou, Y.; Maniccia, A. L. W.; Mao, H.; Zhao, F.; Malchow, R.; Zhao, S.; Johnson, J.; Hu, X.; Krogstad, E.; Liu, Z.-R., Rational Design of Protein-Based MRI Contrast Agents. *Journal of the American Chemical Society* **2008,** *130* (29), 9260-9267.

17. Song, Y.; Kang, Y. J.; Jung, H.; Kim, H.; Kang, S.; Cho, H., Lumazine Synthase Protein Nanoparticle-Gd(III)-DOTA Conjugate as a T1 contrast agent for high-field MRI. *Scientific Reports* **2015,** *5*, 15656.

18. Caravan, P., Protein-Targeted Gadolinium-Based Magnetic Resonance Imaging (MRI) Contrast Agents: Design and Mechanism of Action. *Accounts of Chemical Research* **2009,** *42* (7), 851-862.

19. Kabalka, G. W.; Buonocore, E.; Hubner, K.; Davis, M.; Huang, L., Gadolinium-labeled liposomes containing paramagnetic amphipathic agents: Targeted MRI contrast agents for the liver. *Magnetic Resonance in Medicine* **1988,** *8* (1), 89-95.

20. Cheng, Z.; Thorek, D. L. J.; Tsourkas, A., Porous Polymersomes with Encapsulated Gd-Labeled Dendrimers as Highly Efficient MRI Contrast Agents. *Advanced Functional Materials* **2009,** *19* (23), 3753-3759.

21. Caravan, P.; Greenwood, J. M.; Welch, J. T.; Franklin, S. J., Gadolinium-binding helix-turn-helix peptides: DNA-dependent MRI contrast agents. *Chemical Communications* **2003,** (20), 2574-2575.

22. Werner, E. J.; Datta, A.; Jocher, C. J.; Raymond, K. N., High-Relaxivity MRI Contrast Agents: Where Coordination Chemistry Meets Medical Imaging. *Angewandte Chemie International Edition* **2008,** *47* (45), 8568-8580.

23. Thompson, M. K.; Misselwitz, B.; Tso, L. S.; Doble, D. M. J.; Schmitt-Willich, H.; Raymond, K. N., In Vivo Evaluation of Gadolinium Hydroxypyridonate Chelates: Initial Experience as Contrast Media in Magnetic Resonance Imaging. *Journal of Medicinal Chemistry* **2005,** *48* (11), 3874-3877.

24. Ju, K.-Y.; Lee, Y.; Lee, S.; Park, S. B.; Lee, J.-K., Bioinspired Polymerization of Dopamine to Generate Melanin-Like Nanoparticles Having an Excellent Free-Radical-Scavenging Property. *Biomacromolecules* **2011,** *12* (3), 625-632.

25. Liu, Y.; Ai, K.; Lu, L., Polydopamine and Its Derivative Materials: Synthesis and Promising Applications in Energy, Environmental, and Biomedical Fields. *Chemical Reviews* **2014,** *114* (9), 5057-5115.

26. Zhang, X.; Wang, S.; Xu, L.; Feng, L.; Ji, Y.; Tao, L.; Li, S.; Wei, Y., Biocompatible polydopamine fluorescent organic nanoparticles: facile preparation and cell imaging. *Nanoscale* **2012,** *4* (18), 5581-5584.

27. Jiang, H.; Yang, L.; Li, C.; Yan, C.; Lee, P. S.; Ma, J., High-rate electrochemical capacitors from highly graphitic carbon-tipped manganese oxide/mesoporous carbon/manganese oxide hybrid nanowires. *Energy & Environmental Science* **2011,** *4* (5), 1813-1819.

28. Jiang, H.; Sun, T.; Li, C.; Ma, J., Peapod-like nickel@mesoporous carbon core-shell nanowires: a novel electrode material for supercapacitors. *RSC Advances* **2011,** *1* (6), 954-957.

29. Ai, K.; Liu, Y.; Ruan, C.; Lu, L.; Lu, G. M., Sp2 C-Dominant N-Doped Carbon Sub-micrometer Spheres with a Tunable Size: A Versatile Platform for Highly Efficient Oxygen-Reduction Catalysts. *Advanced Materials* **2013,** *25* (7), 998-1003.

30. Fu, J.; Chen, Z.; Wang, M.; Liu, S.; Zhang, J.; Zhang, J.; Han, R.; Xu, Q., Adsorption of methylene blue by a high-efficiency adsorbent (polydopamine microspheres): kinetics, isotherm, thermodynamics and mechanism analysis. *Chemical Engineering Journal* **2015,** *259*, 53-61.

31. Wang, Z.; Xie, Y.; Li, Y.; Huang, Y.; Parent, L. R.; Ditri, T.; Zang, N.; Rinehart, J. D.; Gianneschi, N. C., Tunable, Metal-Loaded Polydopamine Nanoparticles Analyzed by Magnetometry. *Chemistry of Materials* **2017,** *29* (19), 8195-8201.

32. Wang, Z.; Carniato, F.; Xie, Y.; Huang, Y.; Li, Y.; He, S.; Zang, N.; Rinehart, J. D.; Botta, M.; Gianneschi, N. C., High Relaxivity Gadolinium-Polydopamine Nanoparticles. *Small* **2017,** *13* (43), n/a-n/a.

33. Larsson, B.; Tjälve, H., Studies on the melanin-affinity of metal ions. *Acta Physiologica Scandinavica* **1978,** *104* (4), 479-484.

34. Li, Y.; Xie, Y.; Wang, Z.; Zang, N.; Carniato, F.; Huang, Y.; Andolina, C. M.; Parent, L. R.; Ditri, T. B.; Walter, E. D.; Botta, M.; Rinehart, J. D.; Gianneschi, N. C., Structure and Function of Iron-Loaded Synthetic Melanin. *ACS Nano* **2016,** *10* (11), 10186-10194.

35. Koenig, S. H.; Brown, R. D., Field-cycling relaxometry of protein solutions and tissue: Implications for MRI. *Progress in Nuclear Magnetic Resonance Spectroscopy* **1990,** *22* (6), 487-567.

36. Aime, S.; Botta, M.; Terreno, E., Gd(III)-BASED CONTRAST AGENTS FOR MRI. In *Advances in Inorganic Chemistry*, Academic Press: 2005; Vol. Volume 57, pp 173-237.

37. Caravan, P.; Astashkin, A. V.; Raitsimring, A. M., The Gadolinium(III)−Water Hydrogen Distance in MRI Contrast Agents. *Inorganic Chemistry* **2003,** *42* (13), 3972-3974.

38. Botta, M.; Tei, L., Relaxivity Enhancement in Macromolecular and Nanosized GdIII-Based MRI Contrast Agents. *European Journal of Inorganic Chemistry* **2012,** *2012* (12), 1945-1960.

39. Caravan, P.; Ellison, J. J.; McMurry, T. J.; Lauffer, R. B., Gadolinium(III) Chelates as MRI Contrast Agents: Structure, Dynamics, and Applications. *Chemical Reviews* **1999,** *99* (9), 2293-2352.

40. Accardo, A.; Tesauro, D.; Aloj, L.; Pedone, C.; Morelli, G., Supramolecular aggregates containing lipophilic Gd(III) complexes as contrast agents in MRI. *Coordination Chemistry Reviews* **2009,** *253* (17–18), 2193-2213.

41. Tang, J.; Sheng, Y.; Hu, H.; Shen, Y., Macromolecular MRI contrast agents: Structures, properties and applications. *Progress in Polymer Science* **2013,** *38* (3–4), 462-502.

42. Sitbon, G.; Bouccara, S.; Tasso, M.; Francois, A.; Bezdetnaya, L.; Marchal, F.; Beaumont, M.; Pons, T., Multimodal Mn-doped I-III-VI quantum dots for near infrared fluorescence and magnetic resonance imaging: from synthesis to in vivo application. *Nanoscale* **2014,** *6* (15), 9264-9272.

43. Noebauer-Huhmann, I. M.; Szomolanyi, P.; Juras, V.; Kraff, O.; Ladd, M. E.; Trattnig, S., Gadolinium-Based Magnetic Resonance Contrast Agents at 7 Tesla: In Vitro T1 Relaxivities in Human Blood Plasma. *Investigative Radiology* **2010,** *45* (9), 554-558.

Chapter 5

Enzyme-Regulated Topology of a Cyclic Peptide Brush Polymer for Tuning Assembly

5.1 Introduction

Over the past decade, “smart” polymers that can undergo substantial changes in properties triggered by different stimuli, such as temperature, pH, light, magnetic fields and enzymatic activity represent a growing class of materials that are finding an increasingly important role in various applications, such as drug delivery, tissue engineering biosensor and so on.[1-5] Although single-stimuli-responsive polymers have been intensively studied, polymers that are responsive to two or more stimuli (dual/multi-responsive polymers) are gaining increased attention due to their ability to form more sophisticated systems.[6-9] The incorporation of enzyme activity into polymers is especially intriguing as enzymes show high selectivity, substrate specificity, operate under mild condition and are applicable both in vitro and in vivo.[10-11] To date, most of peptide decorated polymer systems use graft-onto,[12] graft-from polymerization[13] or graft-through strategies to get brush polymers structure with linear peptides as pendant groups. By contrast, we are more interested in developing tools to incorporate cyclic peptides into the brush polymer system. This is because, cyclic structures exhibit distinctive physical and chemical properties that are different from the linear analogous, such as self-assembly behavior,[14-16] rheology,[17-18] biodistribution[19-20] and biological activity,[21-22] that may be attributed to the release of physical constraints imposed by the cyclic structure. However, most studies on the effects of topology rely on the synthesis of both the linear and cyclic polymers. Using external stimuli to trigger a topology change has yet to be thoroughly explored. To this end, we aim to integrate enzyme stimulus that could trigger the topology change of the thermo-responsive ELPs and investigate the topological effects on self-assembly behavior of ELPs.

Elastin-like polypeptides (ELPs) are a class of bio-inspired thermo-responsive polymers that have been garnering increased attention in recent years. The most commonly used ELPs are composed of multiple repeat unit of $(VPGXG)_n$ where X can be any amino acid except proline.[23] Control of molecular topology has long been a challenge in macromolecules. Though the synthesis of linear ELPs has been successfully achieved either by recombinant methods or polymerize pendant short elastin sequence monomers over the past decade,[24-27] the nonlinear topologies gained less attention. One pioneering work of constructing ELPs with alternative nonlinear topologies was reported by David A. Tirrell and coworkers, in which a series of ELPs of circular, tadpole, star, and H-shape were prepared by genetically encoded SpyTag−SpyCatcher chemistry.[28]

5.2 Synthetic Route for Preparation of Cyclic ELP-Based Brush Polymer

5.2.1 Synthesis of Cyclic ELP-Based Norbornene Monomer

Amino acids were purchased from AAPPTEC and NovaBiochem. N-(Glycine)-cis-5-norbornene-exo dicarboximide(Nor-Gly).[29-30] Figure 5.1 showed a linear version of peptide monomer (L1). The elastin-based sequence VPGGGVPGLG was coupled with one Fmoc-Lys(Boc)-OH for further cyclization reaction and 5-norbornene-exo-carboxylic acid for ring-opening metathesis polymerization (ROMP). It was synthesized by a standard Fluorenylmethyloxycarbonyl (Fmoc)-based solid phase peptide synthesis (SPPS) using Wang resin (AAPPTEC) via an AAPPTEC Focus XC automated synthesizer. Fmoc deprotection step was processed in DMF containing 20% 4-methylpiperidine. Amino acid couplings reaction was carried out in N, N, N’, N’-Tetramethyl-O-(1H-benzotriazol-1-yl)uronium hexafluorophosphate (HBTU) and N, N-Diisopropylethylamine (DIPEA) system with resin: amino: acid: HBTU: DIPEA ratio of 1:3.5:3.4:4. Finally, the peptide was cleaved from the resin using a mixture of Trifluoroacetic acid (TFA): H_2O: Triisopropylsilane (TIPS) equals to 95:2.5:2.5 for 45 minutes. The resulting peptides were precipitated and washed with cold ether three times, followed by preparative HPLC purification. The cyclization reaction was performed in the same condition as solid phase peptide synthesis (SPPS) method except with longer reaction time and lower concentration to avoid intermolecular coupling (Figure 5.1). It was performed by dissolving 200 mg L1 in 200 mL Dimethylformamide (DMF), followed by the addition of 200mg HBTU and 92µL DIPEA in 40 mL DMF. The reaction mixture was left to stir for three days. An additional 200mg of HBTU and 92µL DIPEA in 40 mL DMF were added to the reaction and left stirring for two more days. After the reaction, the solvent was removed by vacuum distillation at 55 °C. The product was precipitated and washed with cold ether. After purification by preparative HPLC, the lyophilized sample is a white solid (yield 75%). Figure 5.2 showed ^{1} H (400 MHz) NMR spectrum of the monomer with the presence of norbornene olefin (peak a). Figure 5.3 showed electrospray ionization mass spectrometry (ESI-MS) data and reversed-phase high-performance liquid chromatography (RP-HPLC) profile monitoring at λ_{abs} = 214 nm, that confirmed the identities and purities of the product.

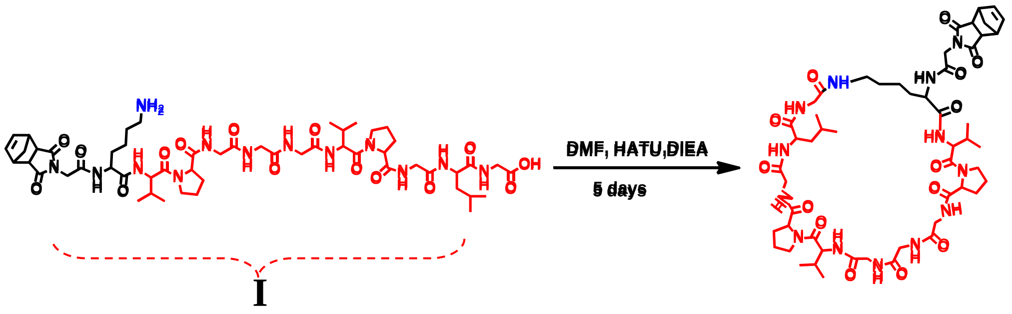

Figure 5.1. Cyclization reaction of linear peptide monomer (L1). Range I is the elastin-based sequence VPGGGVPGLG (red color). Copyright 2015 Royal Society of Chemistry.[31]

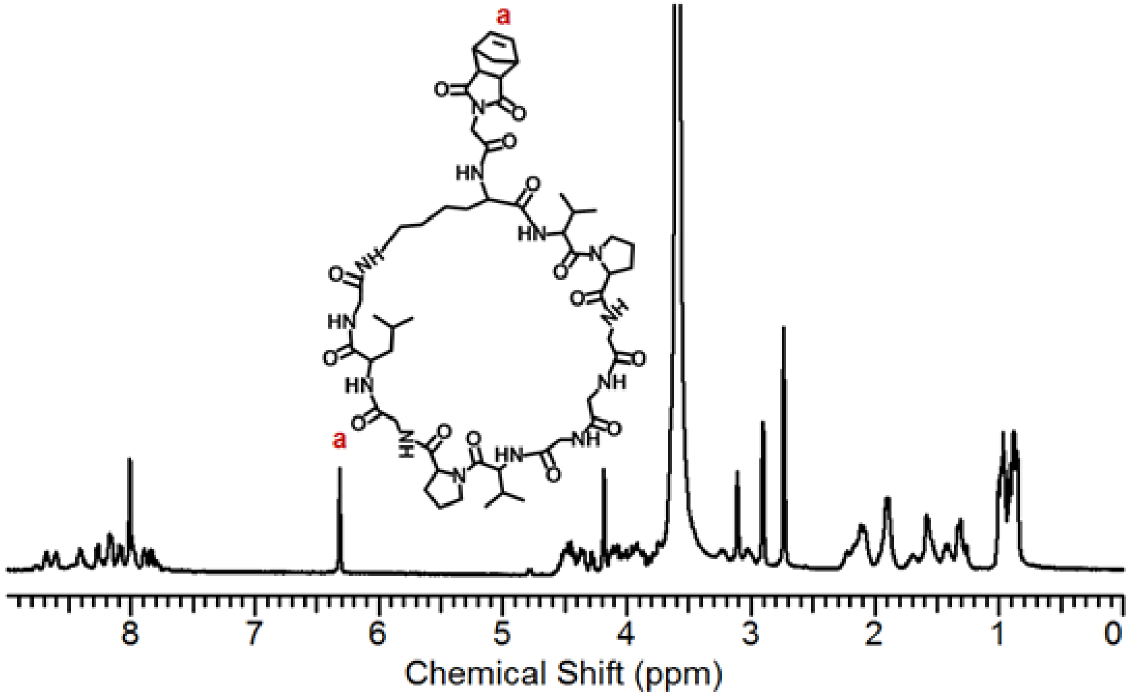

Figure 5.2. ^{1}H NMR spectrum of 1 in DMF-d7. Copyright 2015 Royal Society of Chemistry.[31]

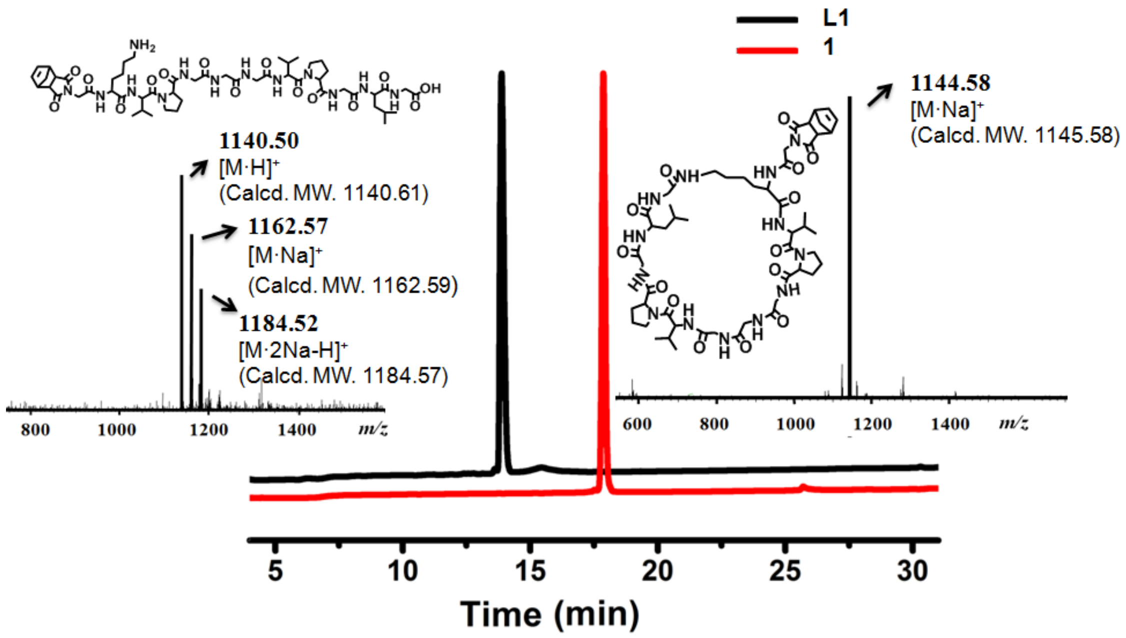

Figure 5.3. ESI-MS data and HPLC traces of linear peptide monomer (L1) and cyclic peptide monomer (1). HPLC gradient: 20%-60% ACN over 30mins. Copyright 2015 Royal Society of Chemistry.[31]

5.2.2 Synthesis of Gd-Based Termination Agent

The addition of a novel, functional gadolinium- 1,4,7,10-tetraazacyclododecane-1,4,7,10-tetraacetic acid (DOTA) based termination agent (Gd-TA), to provide a tag for magnetic resonance imaging (MRI) in future applications of these materials as *in vivo* imaging agents.[32] To synthesize Gd-TA, a stirred solution of DOTA -tris (tert - butyl ester) (172 mg, 0.30 mmol) in dry DMF (0.6 mL) was added DIPEA (242 µL, 1.40 mmol) and 1-[Bis(dimethylamino)methylene]-1H-1,2,3-triazolo[4,5-b]pyridinium 3-oxid hexafluorophosphate (HATU) (132 mg, 0.35 mmol) followed by a solution of the diamine (80 mg, 0.145 mmol) and DIPEA (242 µL, 1.40 mmol) in dry DMF (1 mL). The reaction was stirred under a nitrogen atmosphere for 48 hrs and dried under vacuum. The compound was dissolved in a 1:1 TFA: CH_2Cl_2 solution (20 mL) and stirred at room temperature for 6 hrs. The reaction was concentrated to dryness and purified by Prep-HPLC (40%-60%B) followed by lyophilization to give 111mg (69%) of **2** as a white solid. ^{1}H NMR (DMF-d_7): δ (ppm) 7.2 (m, 4H), 6.95 (m, 4H), 5.92 (m, 2H), 4.78 (d, 4H), 4.02-3.23 (m, 44H). ^{13}C NMR (DMF-d_7): δ (ppm) 172.97, 160.12, 158.17, 132.76, 130.86, 129.62, 122.05, 119.68, 117.31, 115.62, 114.95 65.13, 56.51, 55.60, 54.91, 52.36, 50.65, 41.85. ESI, 1097.55 $[M-H]^-$, found: 1097.87). Figure 5.6 showed electrospray ionization mass spectrometry (ESI-MS) data and reversed-phase high-performance liquid chromatography (RP-HPLC) profile monitoring at λ_{abs} = 214 nm, that confirmed the identity and purity of the product.

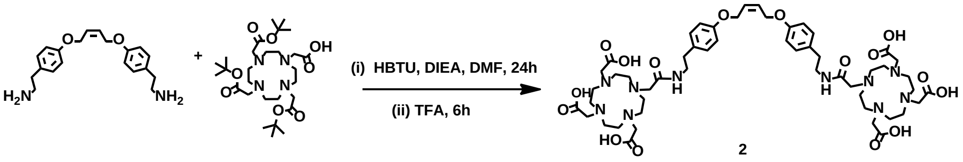

Figure 5.4. Synthesis of 2. Copyright 2015 Royal Society of Chemistry.[31]

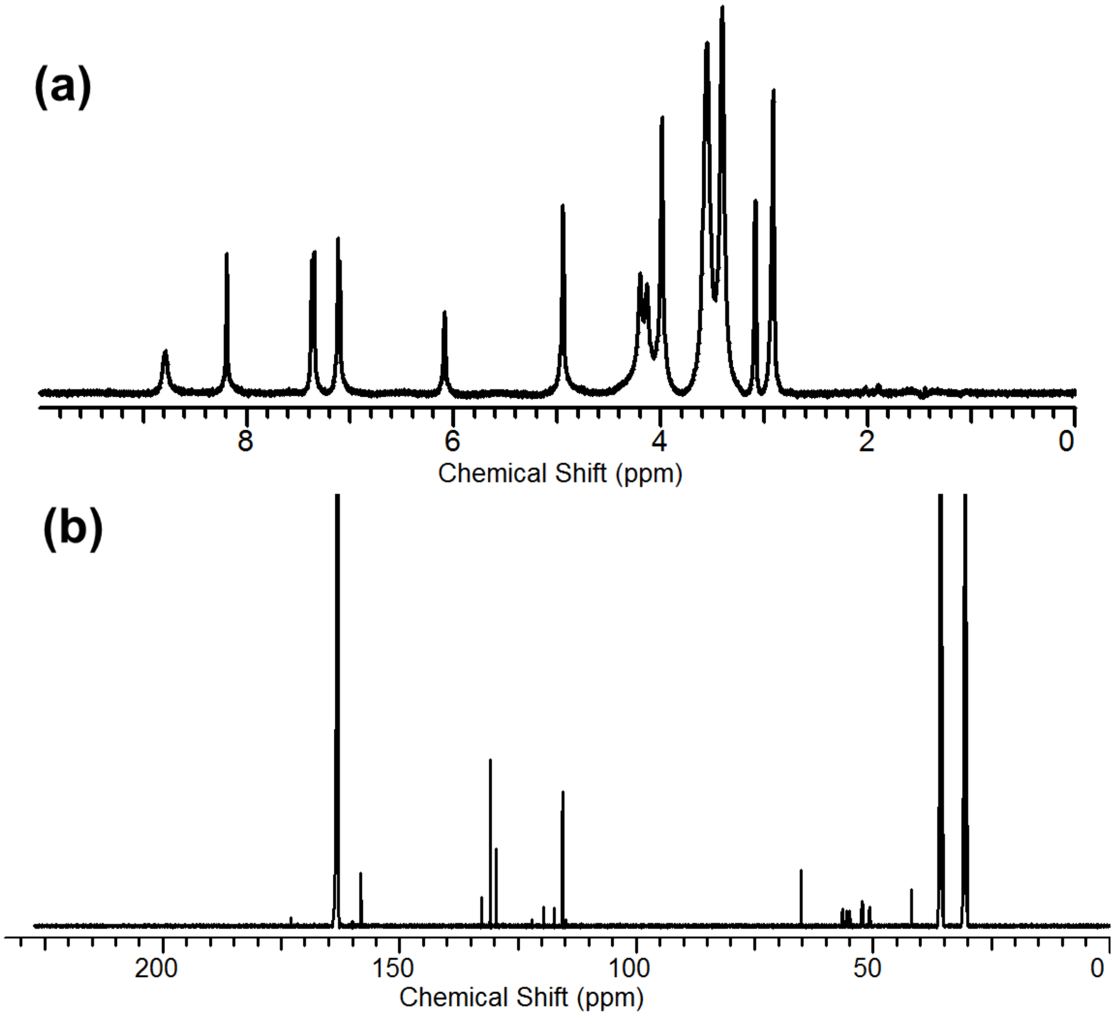

Figure 5.5. ^{1}H NMR and ^{13}C NMR of 2 in DMF-d7. Copyright 2015 Royal Society of Chemistry.[31]

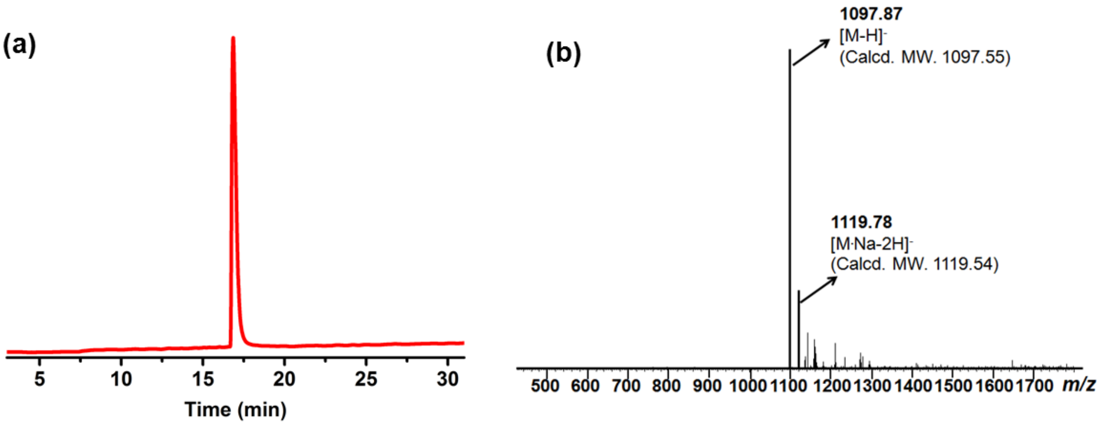

Figure 5.6. (a) HPLC trace of 2 (10%-50% ACN over 30 mins) and (b) ESI-MS of 2. Copyright 2015 Royal Society of Chemistry.[31]

Gd-TA was prepared by dissolving 2 (111mg) and an excess of $GdCl_3$ (100 mg, 0.37 mmol) in 5mL water. The pH was adjusted to 6 with 1M NaOH and stirred at r.t. for 24 hrs. The final product was purified by Prep-HPLC (10%-50% B) followed by lyophilization to give Gd-TA as a white powder (67%). ESI, 1407.45 $[M-H]^-$, found: 1407.36. Figure 5.6 showed electrospray ionization mass spectrometry (ESI-MS) data and reversed-phase high-performance liquid chromatography (RP-HPLC) profile monitoring at λ_{abs} = 214 nm, that confirmed the identity and purity of the product.

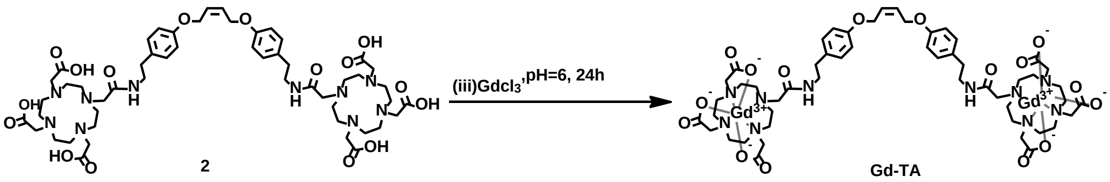

Figure 5.7. Synthesis of Gd-TA. Copyright 2015 Royal Society of Chemistry.[31]

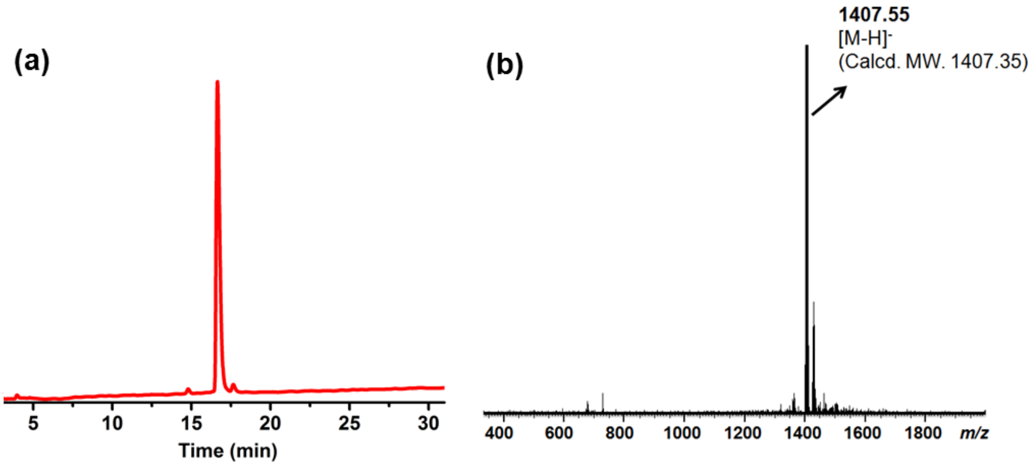

Figure 5.8. (a) HPLC trace of Gd-TA (10%-50% ACN over 30 mins) and (b) ESI-MS of GD-TA. Copyright 2015 Royal Society of Chemistry.[31]

5.2.3 Synthesis ELP-Based Homopolymer

ELP-based homopolymer was directly synthesized via ROMP[33] using modified 2nd generation Grubb's catalyst (Figure 5.9) and terminated by Gd modified termination agent. The detailed synthesis is described as follows: 1 equivalent catalyst and five equivalents of monomer one were dissolved in DMF to a final volume of 500 µL under an inert atmosphere. The resulting mixture was left to stir under N_2 for 3 hours followed by quenching with 1.2 equivalent Gd-TA. ^{1} H (400 MHz) NMR spectra of the polymer (P0) (before quenching with Gd-TA) confirmed the absence of monomer (no olefin peak at 6.30 ppm) and the presence of broad trans and cis olefin peaks of the polymer backbone at 5.80 and 5.55 ppm, respectively (Figure S4). Excess of termination agent was removed via dialysis from DMF into the water as evidenced by HPLC trace in Figure 5.10. The purified polymer P1 was characterized by matrix-assisted laser desorption ionization-time of flight mass spectrometry (MALDI-TOF MS) and size exclusion chromatography using a multiangle light scattering detector (SEC-MALS). The molecular weight of P1 was determined by MALDI-TOF MS (Figure 5.11a) the average molecular weight of the peak at 6409.8 Da match well with the calculated values (6402.9 Da). Figure 5.11b showed SEC trace of a single and narrow distribution as an indication of well-defined polymer with molecular weight 7000 Da consistent with MALDI data and polydispersity index (PDI) equals 1.03). ^{1} H (400 MHz) NMR spectra of the polymer (**P0**) (before quenching with Gd-TA) confirmed the absence of monomer 1 (no olefin peak at 6.30 ppm) and the presence of broad trans and cis olefin peaks of the polymer backbone at 5.80 and 5.55 ppm, respectively (Figure 5.12).

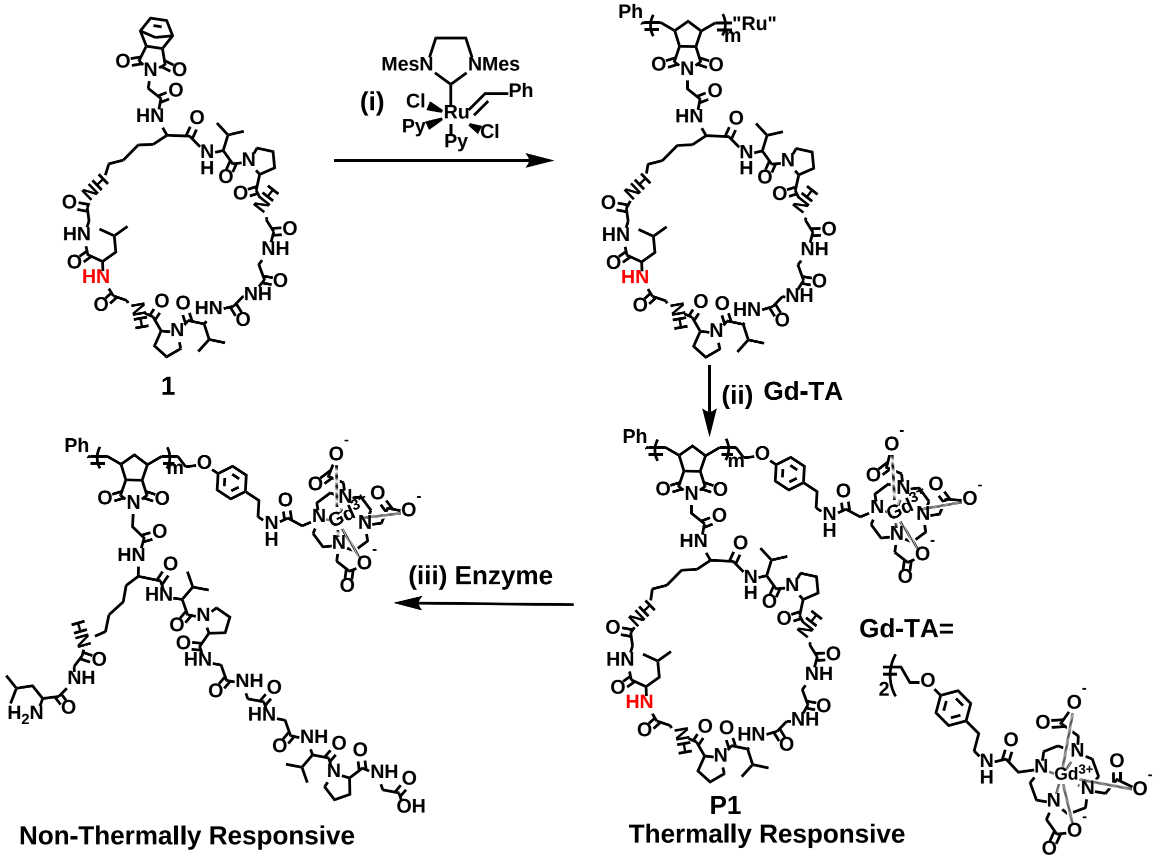

Figure 5.9. Synthetic scheme of homopolymer P1 using ROMP initiator (IMesH2)(C5H5N)2(Cl)2Ru=CHPh (“Ru”) and Gd-containing termination agent (Gd-TA). For P1, m = 5. The structure post-enzyme treatment is drawn to represent the ideal result of 100% peptide cleavage. Enzyme cleavage site is shown in red color. Copyright 2015 Royal Society of Chemistry.[31]

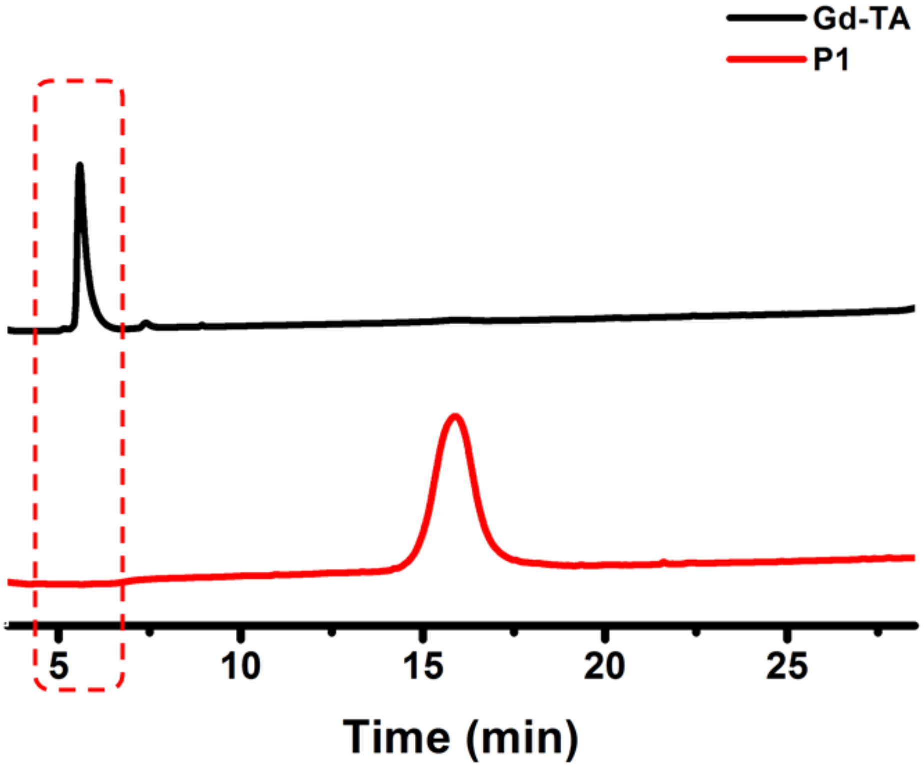

Figure 5.10. HPLC trace of (a) Gd-TA and (b) P1 after dialysis. HPLC gradient: 20%-100% ACN over 30 min. Copyright 2015 Royal Society of Chemistry.[31]

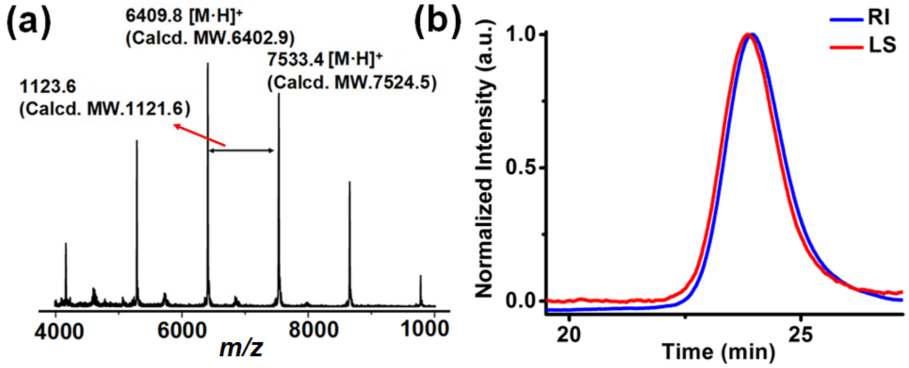

Figure 5.11. (a): MALDI-TOF mass spectrum, and (b) SEC trace of P1. Copyright 2015 Royal Society of Chemistry.[31]

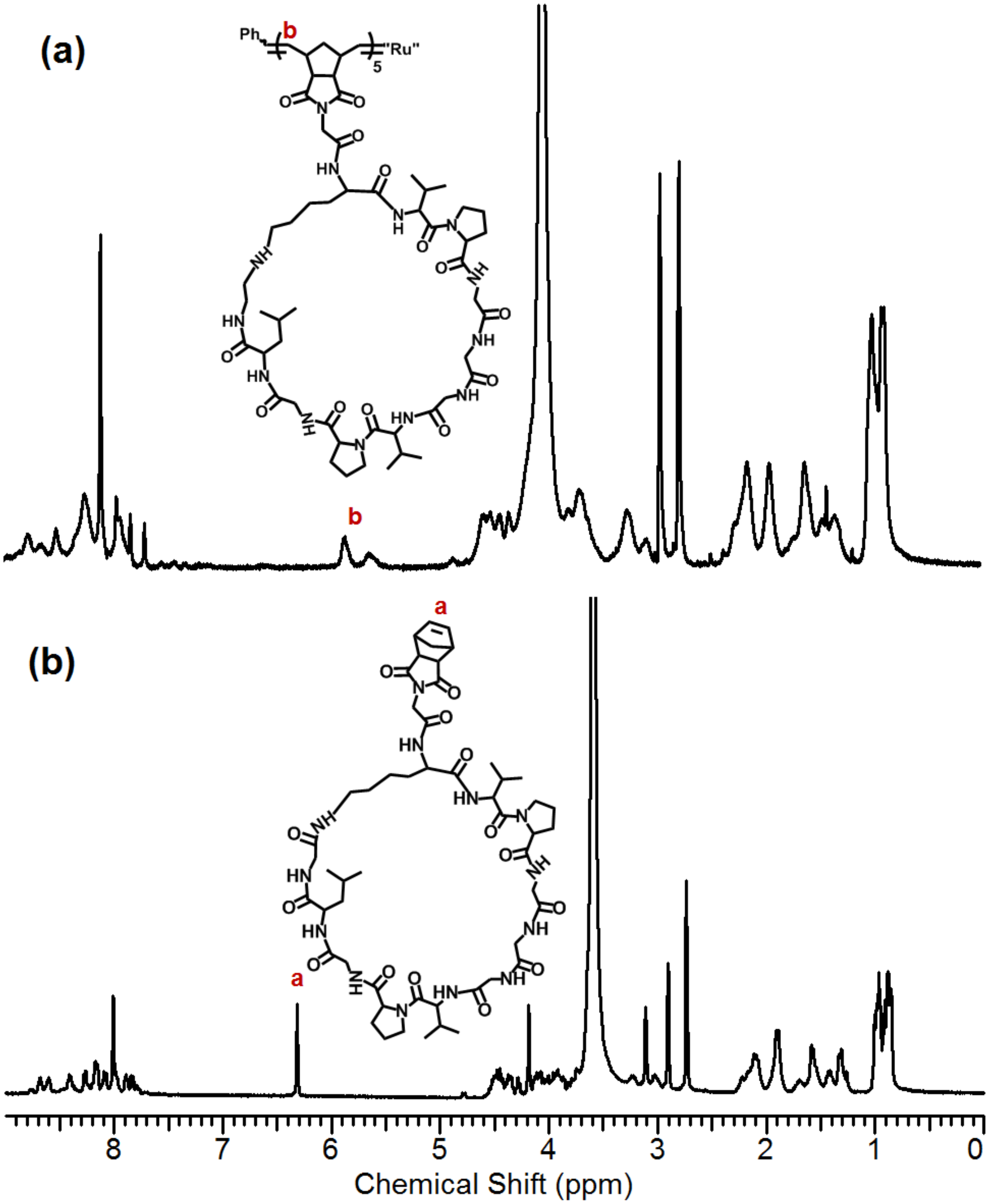

Figure 5.12 ^{1}H NMR spectra of (a) P0 and (b) 1 in DMF-d7. Copyright 2015 Royal Society of Chemistry.[31]

5.2.4 Synthesis ELP-Based Copolymer

The elp-based copolymer was synthesized via feeding norbornenyl-phenyl monomer and monomer 1 sequentially (Figure 5.13). The resulted in block copolymer shown narrow and monomodal molecular-weight distribution (PDI=1.03) (Figure 5.14). The number average molecular obtained from SEC is 9000 Da agreed with the expected molecular weight. The detailed synthesis is described as follows: 1 equivalent catalyst and ten equivalent norbornenyl-phenyl monomers 2 in was dissolved 200 µL DMF under an inert atmosphere. The resulting mixture was left to stir under N_2 for ten mins followed by adding five equivalent 1 in 500 µl DMF. The resulting mixture was left to stir under N_2 for 3 hours followed by quenching with 1.2 equivalent Gd-TA.

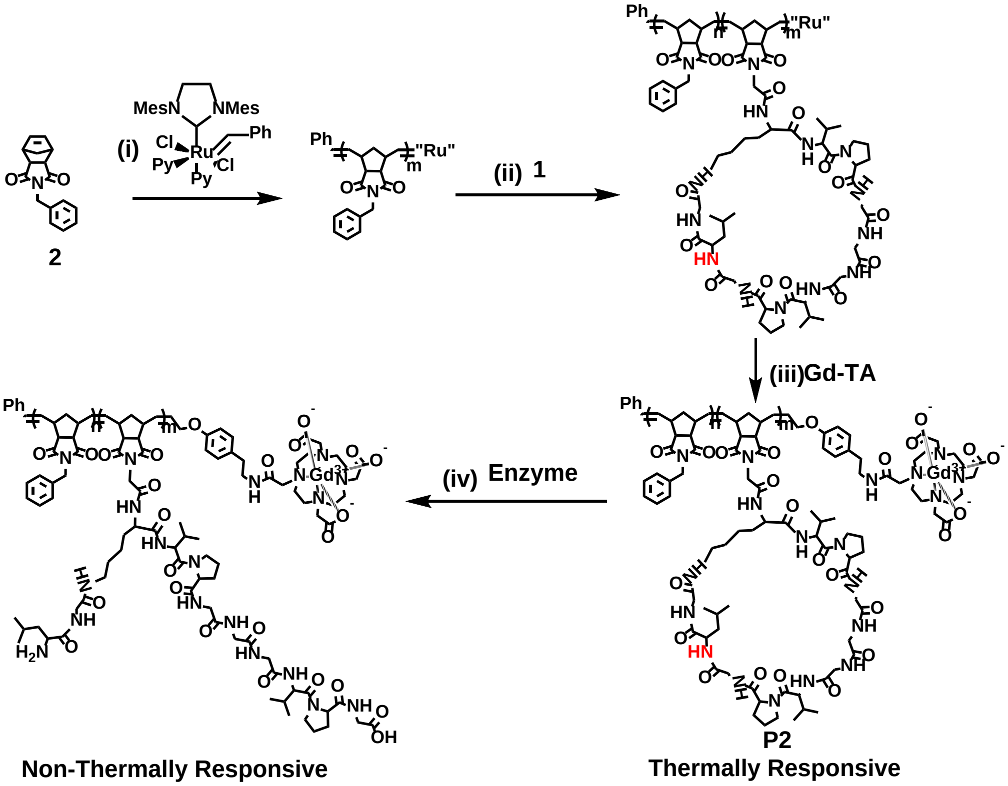

Figure 5.13 General synthetic scheme of copolymer P2 using ROMP initiator “Ru”, and Gd-TA. For P2, m = 5, n = 10. The structure post enzyme treatment is drawn to represent an ideal 100% peptide cleavage. Enzyme cleavage site is shown in red color. Copyright 2015 Royal Society of Chemistry.[31]

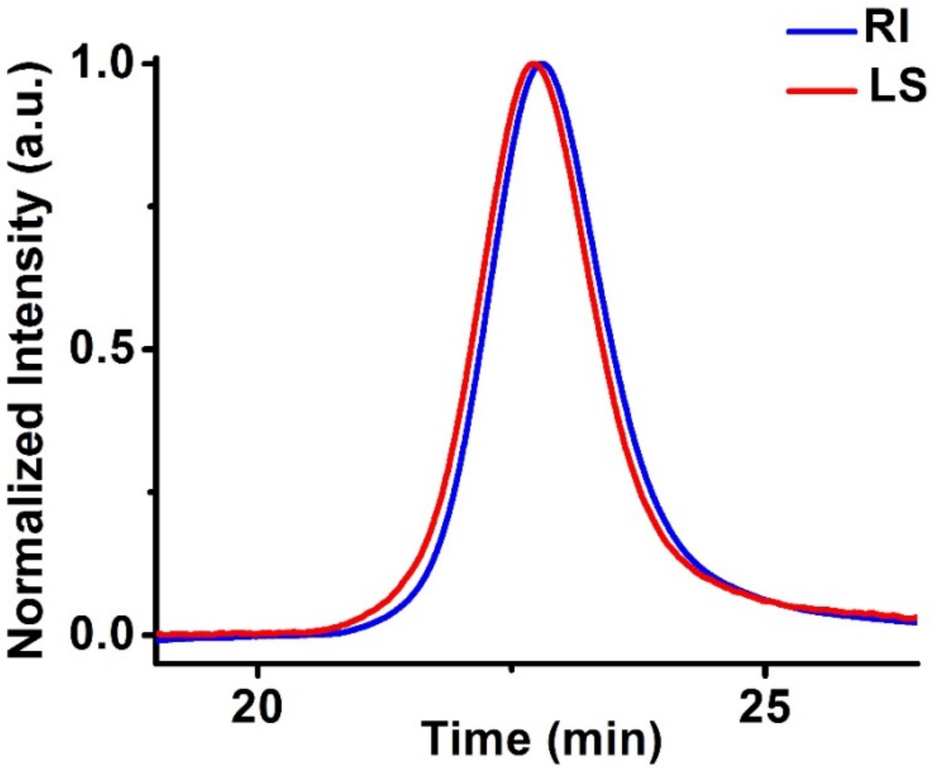

Figure 5.14. SEC trace of P2. Copyright 2015 Royal Society of Chemistry.[31]

5.3 Self-assembly of ELP-Based Homopolymer and Copolymer

Thermolysin is a thermostable metalloproteinase, that cleaves at the N-terminus of hydrophobic residues (IIe, Leu, Val, Ala, Met, Phe) but blocks by the Pro next to it (along with the C-terminus direction).[34] In this section, we use this enzyme as an example to explore the self-assembly behavior of ELP-based homopolymer and copolymer under enzyme stimulus. Figure 5.15 showed the designed sequence with a single cleavage site at position 1, while the cleavage of position 2 and 3 is hindered by the presence of proline. Therefore, the sequence after cleavage is still linked to the polymer, forming a Y shape linear counterpart without truncated by-product. This can be confirmed by incubating 1 with thermolysin and denatured thermolysin as a control. HPLC analysis showed a 100% cleavage in less than 1h with the treatment of thermolysin whiles the control suggested no cleavage of the substrate (Figure 5.16). The identity of each HPLC peak was confirmed by ESI-MS analysis (Figure 5.17). Moreover, the heat stability of thermolysin allows substrate cleavage performed at a high temperature that compatible with the condition of thermo-responsive study.[35]

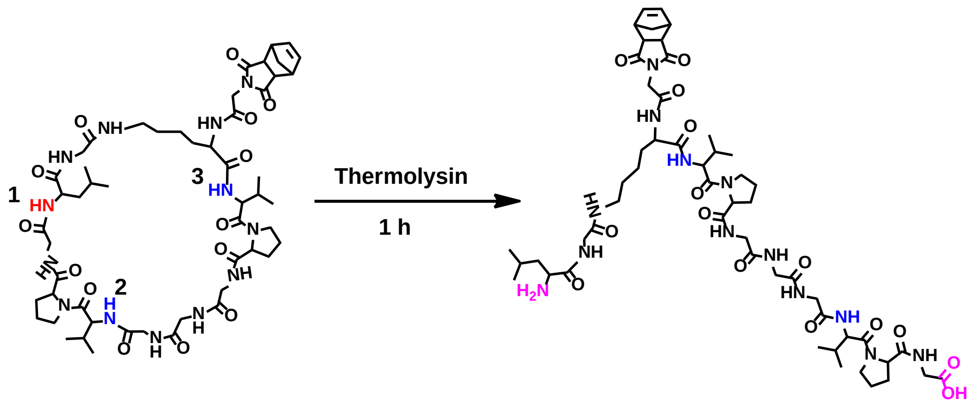

Figure 5.15. Thermolysin cleavage of 1 at position 1 (red color). Position 2 and 3 (blue color) are not the cleavage sites as Proline residues besides the cleavage sites block the thermolysin cleavage. After the cleavage, one carboxylic acid and amine group were released (pink color). Copyright 2015 Royal Society of Chemistry.[31]

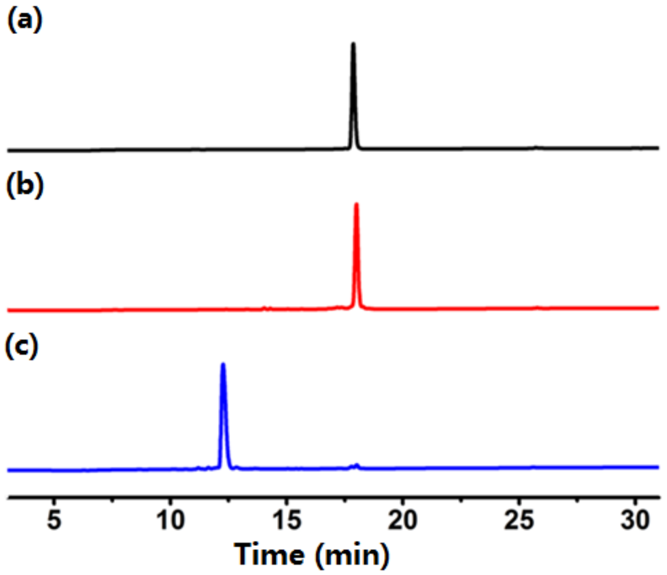

Figure 5.16. HPLC trace of (a) 1; (b) 1 treated with denatured thermolysin at 55 °C for 1 h; (c) 1 treated with thermolysin at 55 °C for 1 h. HPLC gradient: 20%-60% ACN over 30mins. Copyright 2015 Royal Society of Chemistry.[31]

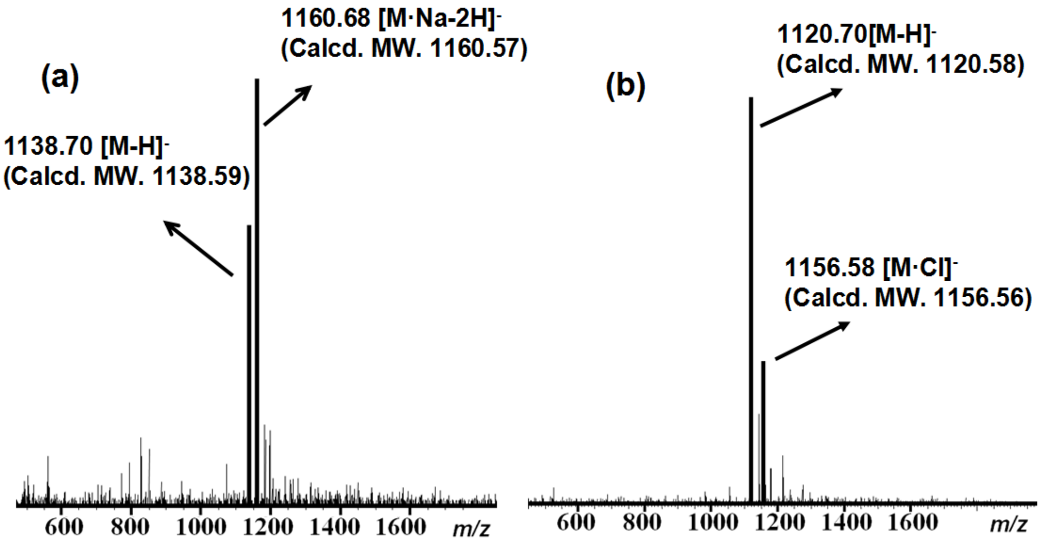

Figure 5.17. ESI-MS of (a) 1 treated with thermolysin for 1 h, and (b) 1 treated with denatured thermolysin for 1 h. Copyright 2015 Royal Society of Chemistry.[31]

The homopolymer (P1) exhibited a temperature-responsive phase behavior similar to the linear elastin-based oligomers, that is significantly affected by molecular weight, concentration and pH.[26] To obtain a lower critical solution temperature (LCST) near body temperature without sacrificing the enzyme activity, we synthesized the polymer with degree of polymerization equals to 5 and dissolve in phosphate buffered saline (PBS) at pH 6. The lower critical solution temperature transitions were measured by UV/Vis spectroscopy. In Figure 5.18, the LCST behavior of P1 was strongly correlated to the polymer concentration. As shown Figure 5.19, LCST increased from 34 °C to 55 °C, while polymer concentration decreased from 0.6 to 0.1mg/ml. Over this concentration range, the data fit well as a logarithmic function of concentration. A similar dependence on concentration was also observed with both ELPs synthesized by recombinant protein expression and synthetic polymers with short ELPs sequences as side chains and could be explained by the facilitated transition from random coils to β sheets at high concentration.[27, 36-37] It is known that, above the LCST, the thermo-responsive polymer (for example, PNIPAM) start to dehydrate and self-organize into large amorphous aggregates or precipitate in aqueous solution.

Surprisingly, P1 exhibited a strong tendency to form ordered cylindrical structure upon heating the aqueous solution as characterized by TEM (Figure 5.18b). Although the detailed mechanism is unknown, we expect that a certain number of cyclic elastin-based side chains become hydrophobic above LCST which provides suitable driving force for the fiber formation. Additionally, the cloudy solution could return to clear in less than 5 minutes, as indicated by the disappear of fiber structures via TEM.

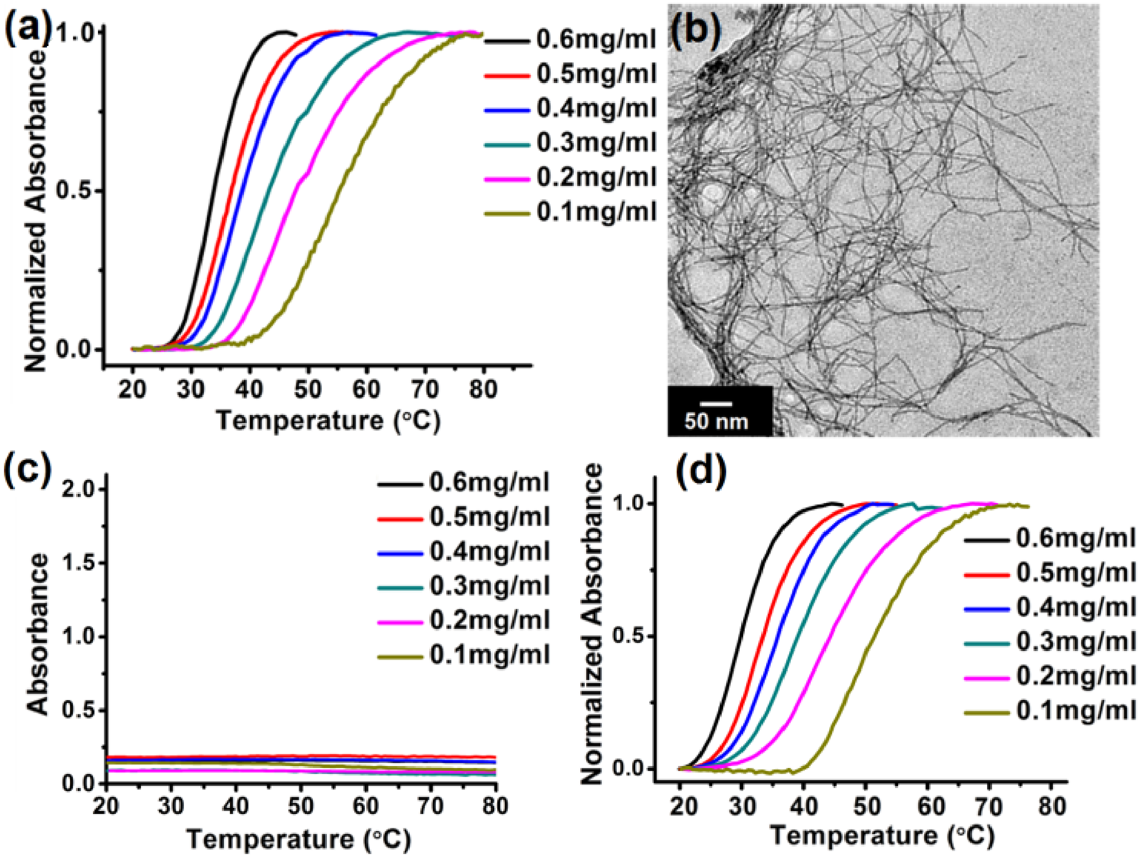

Figure. 5.18. (a) LCST behavior of P1 measured by UV-Vis spectroscopy at 550 nm; (b) TEM image of cylindrical structure formed by P1 (0.6mg/ml) at 40°C. (c) LCST behavior of P1 treated with thermolysin at 55 °C for 1 h. (d) LCST behavior of P1 treated with denatured thermolysin at 55 °C for 1 h. Copyright 2015 Royal Society of Chemistry.[31]

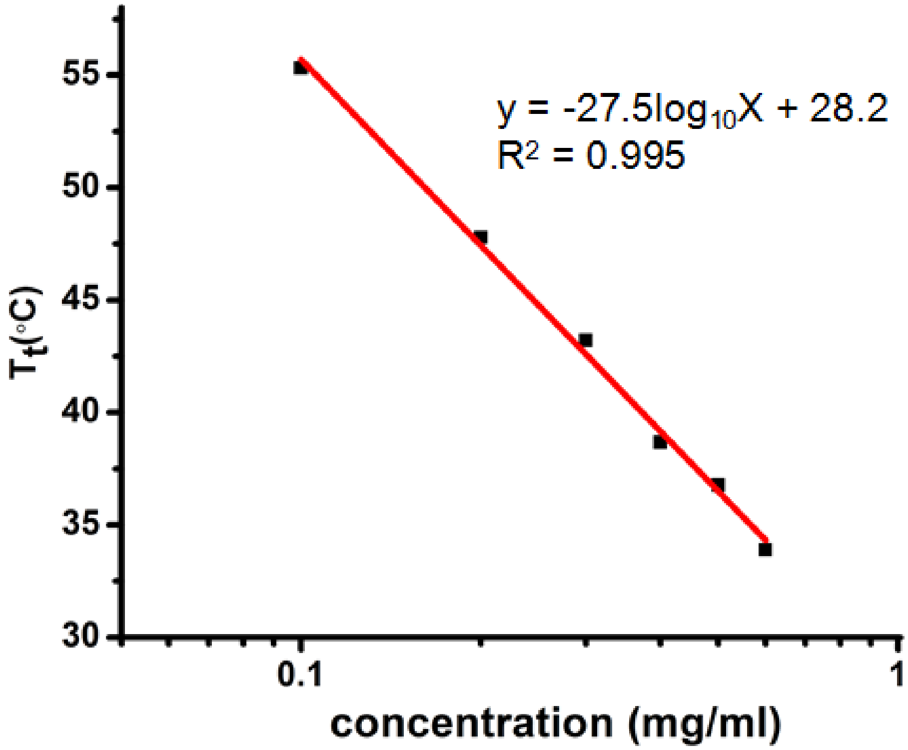

Figure 5.19. LCST versus concentrations of P1 in PBS at pH = 6. LCST was taken as the midpoint on the UV-Vis spectrum. Copyright 2015 Royal Society of Chemistry.[31]

The enzyme sensitivity of P1 was investigated by incubating the P1 solution with thermolysin at 55 °C for 1h. Since the enzyme treatment didn't release the truncated sequences, the traditional way of quantitative analysis of the released fragment is difficult. But it is still able to say that more than one side chain was activated by the enzyme per polymer, indicated by the total shift of HPLC trace of P1 compared with P1 treated by thermolysin, whereas the control experiment remained its retention time (Figure 5.20). Figure 5.18c showed a significant increase of LCST (above 100 Celsius) as a consequence of breaking up ring structure. By contrast, samples treated with denatured thermolysin showed no significant change in LCST (Figure 5.18d). Visually, upon adding the enzyme to the P1 solution at 55 °C, the cloudy solution gradually become clear, suggesting an enzyme-driven disassembly of cylindrical structure (Figure 5.21).

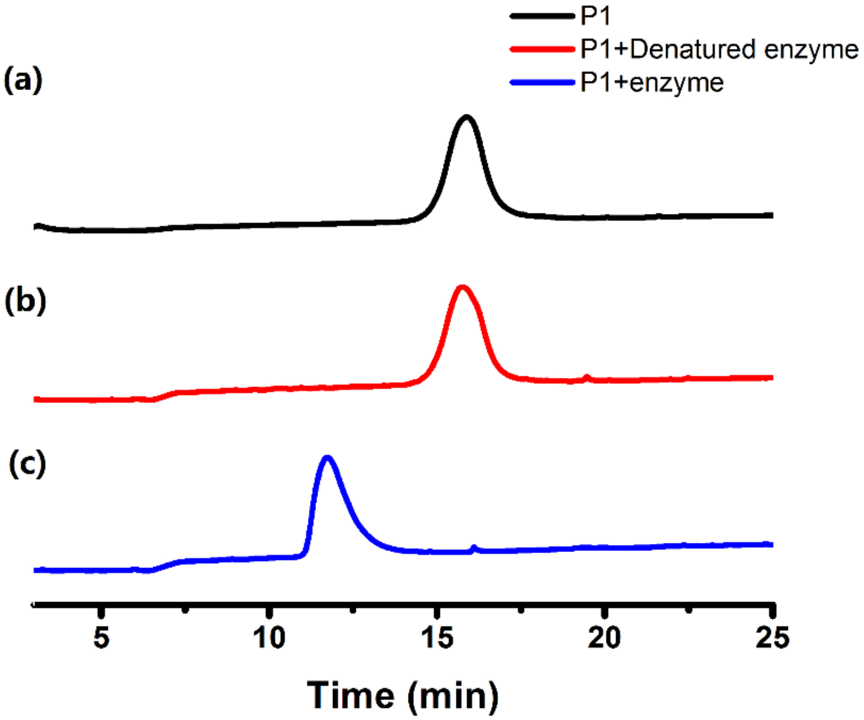

Figure 5.20. HPLC trace of (a) P1, (b) P1 with denatured enzyme at 55 °C for 1 h, (c) P1 treated with thermolysin at 55 °C for 1h. HPLC gradient: 20%-100% ACN over 30 min. Copyright 2015 Royal Society of Chemistry.[31]

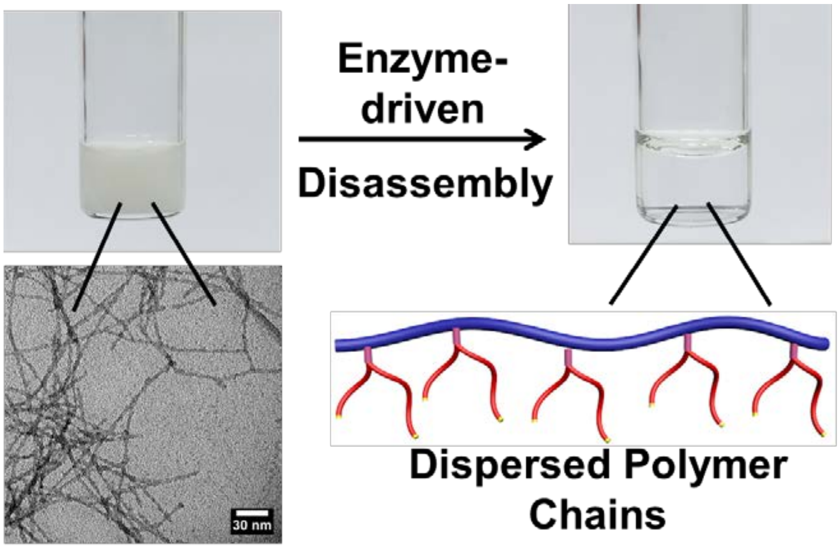

Figure 5.21. Digital photographs showing the cloudy solution become clear after enzyme treatment. Copyright 2015 Royal Society of Chemistry.[31]

To establish the kinetics of the micelle disassembly, this enzymatic reaction was monitored by UV-Vis spectroscopy and DLS. Figure 5.22 indicated the fast disassembly process by strongly decreased turbidity upon adding an enzyme to the hot solution while the P1 and control showed only slightly decrease in absorbance for 1 h, indicating the remained aggregation. Meanwhile, the cloudy solution went back to clear after incubating enzyme for 1h as the absorbance reached its minimum. A similar result was obtained by DLS. The scattering intensity significantly dropped upon adding an enzyme (Figure 5.22b). In addition, we didn't observe morphology change in solutions treated with denatured enzyme (Figure 5.23). This enzyme-driven phase transition could be explained by the resulted linear architecture that contributes additional enthalpy from the released two chain end groups as well as decrease the length of ELP sequence- contains only one run of the VPGXG unit.[38]

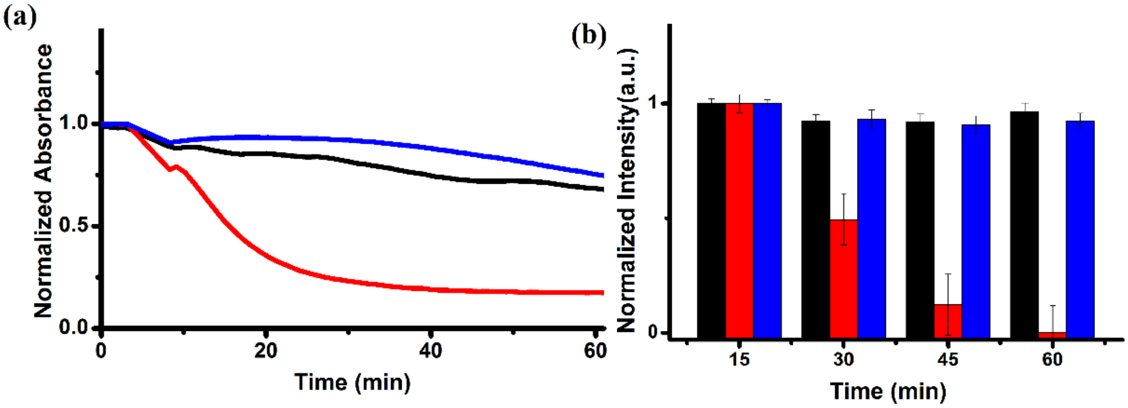

Figure 5.22. (a) UV-Vis spectroscopy of the enzyme-driven disassembly process at 550 nm and (b) Scattering intensity of the polymers during the enzyme-driven disassembly process as measured by DLS. All solutions were pre-heat to 55 °C and equilibrant for 5 min before starting. P1 (black), P1 with an enzyme (red) and P1 with a denatured enzyme (blue). Copyright 2015 Royal Society of Chemistry.[31]

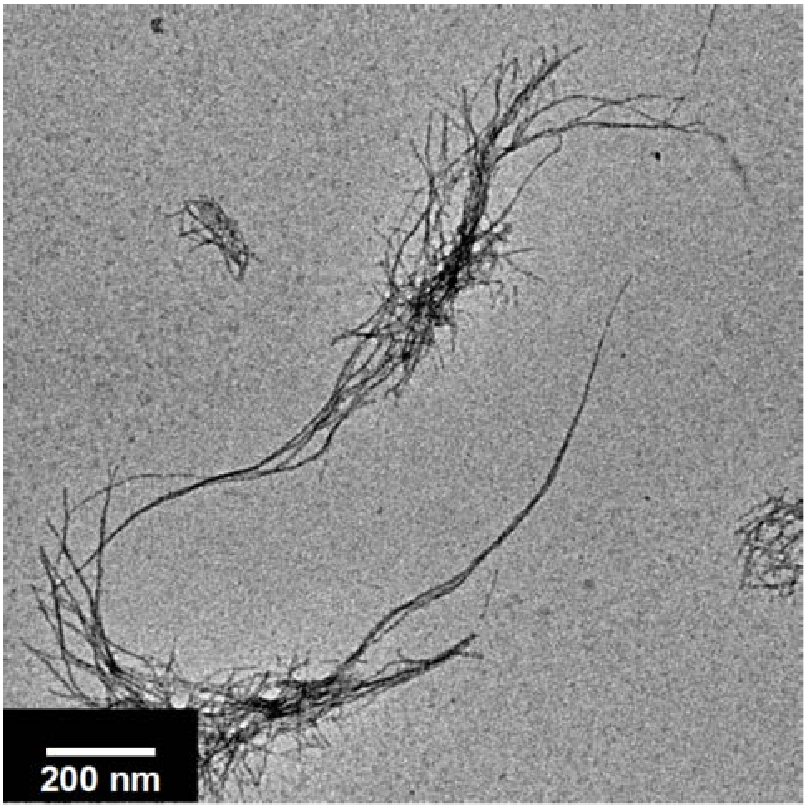

Figure 5.23. TEM image of the cylindrical structure formed by P1 with denatured enzyme above the LCST. Copyright 2015 Royal Society of Chemistry.[31]

The ability of amphiphilic macromolecules to self-assemble in selective solvents has been intensively investigated and widely used in many applications.[39-41] The morphology of these self-assembled amphiphilic macromolecules could be controlled by changing hydrophilic -hydrophobic ratio. Responsive micelles was then obtained by introduce triggers such as temperature, pH, light and enzyme, to either increase or decrease this hydrophilic -hydrophobic ratio.[42-44] Taking advantage of the active natural of ELP, the ELP-based copolymer was synthesized by copolymerizing hydrophobic norbornenyl −phenyl monomer with monomer 1 (Figure 5.13).

The self-assembly of the copolymer was induced by adding water to the DMF solution (1mg/ml) followed by dialysis into water. At room temperature, it assembled into spherical micelles (Figure 5.24a) with the size to be approximately 10 nm in diameter, as characterized by TEM and DLS, where the sized estimated by TEM is always smaller than the sized measured by DLS (Figure

5.24d). It is suggested that the hydrophilic ELP corona that stabilizes the micelle would become more hydrophobic by the elevated temperature and resulted in the partial aggregation of micelles consequently because of the strengthened hydrophobic interaction. The LCST of micelle was also determined by Uv-Vis spectrum (Figure 5.25). The morphology of the block copolymer above LCST was characterized by TEM. Small spherical micelles underwent intermolecular micellization to form larger spherical micelles (around 20 nm in diameter) (Figure 5.24b). The reversed morphology transition was then achieved by increasing the hydrophilicity of the block polymer. As discussed before, the linear shape architecture after enzyme treatment raises the total hydrophilicity by two free hydrophilic groups (-COOH and $–NH_2$). Thus, the hydrophilic interaction induced the morphology shift back to small spherical micelles with diameter around 10 nm, like the initially formed micelles (Figure 5.24c). A control experiment was conducted by applying the same condition except using a denatured enzyme, showing the formation of large micelles (Figure 5.26). More interestingly, the morphology of large micelles couldn't undergo transition back to small spherical micelles without the aids of the enzyme (Figure 5.27). We hypothesized that the high glass transition temperatures of the polymer would result in a slow kinetics of chain reorganization.[45] Therefore, the enzyme is an essential requirement for driving the morphology transition to the smaller size. The stability of these micelles was evaluated by measuring the zeta potentials. Figure 5.28 showed the zeta potential decrease from -20.6 to -26.1 mV for untreated micelles upon heating. The denatured enzyme treated micelles showed the same trend- zeta potential decrease from -9.6 to -17.5 mV upon heating. These data indicate a micellar structural rearrangement happened upon heating.[46] In contrast, after thermolysin treatment, zeta potential that remains constant due to the high micellar structure stability when heated.

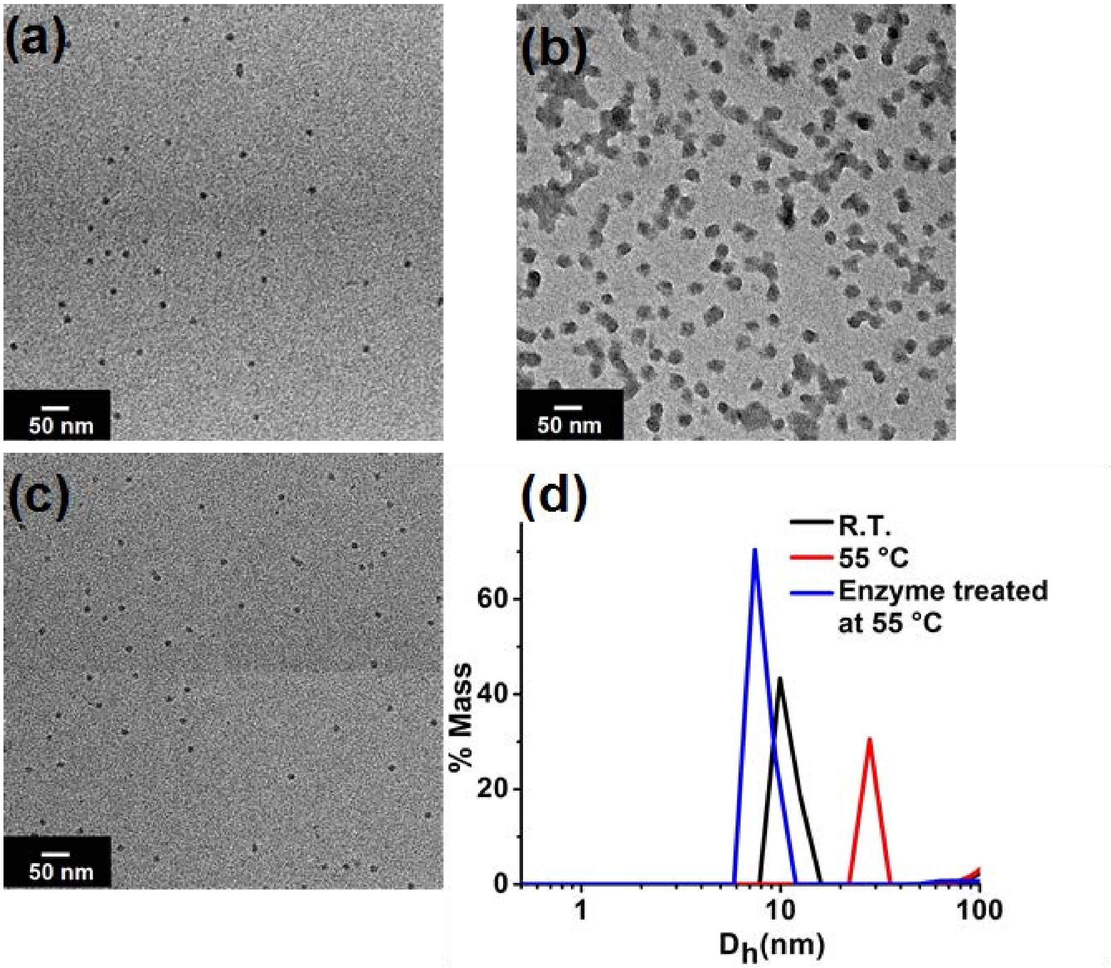

Figure 5.24. TEM images of P2 micelles (a) at room temperature, (b) at 55 °C for 6 h, and (c) with enzyme at 55 °C for 6 h. (d) DLS data of P2 micelles: at room temperature (black curve), at 55 °C for 6 h (red curve), with enzyme at 55 °C for 6 h (blue curve). Copyright 2015 Royal Society of Chemistry.[31]

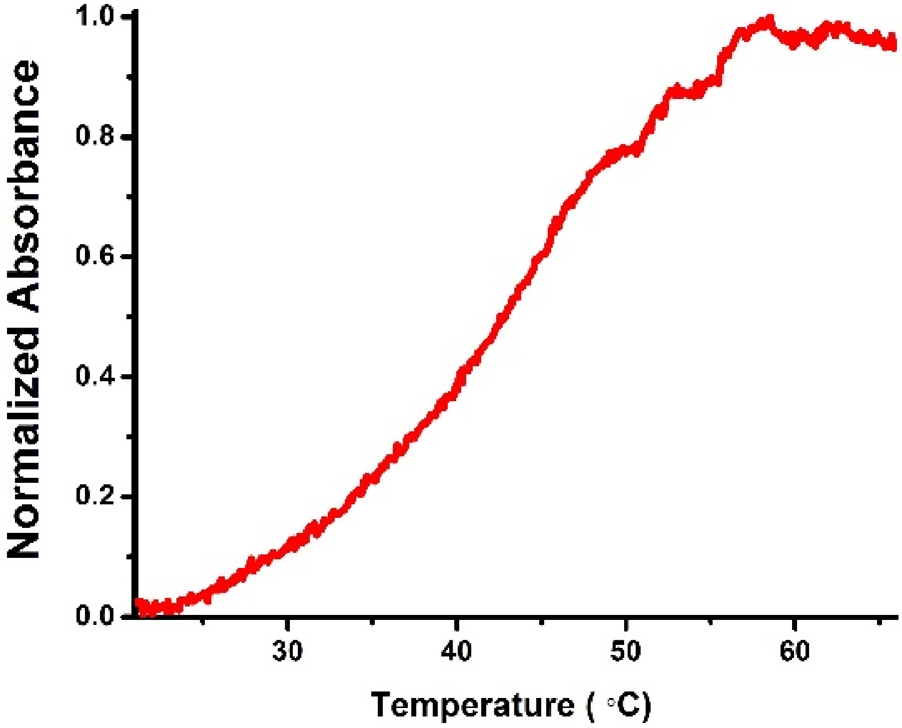

Figure 5.25. LCST behavior of P2 micelle solution (0.6 mg/mL) at 550 nm. Copyright 2015 Royal Society of Chemistry.[31]

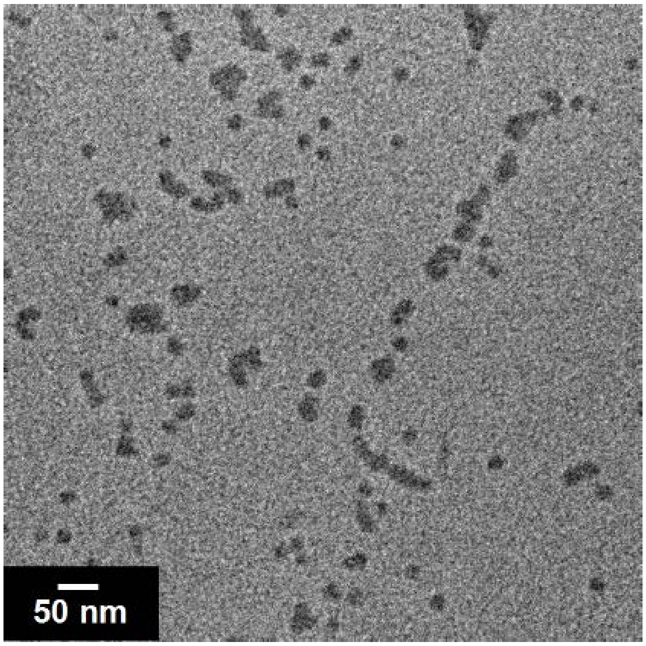

Figure 5.26. TEM image of P2 micelles treated with denatured enzyme. Copyright 2015 Royal Society of Chemistry.[31]

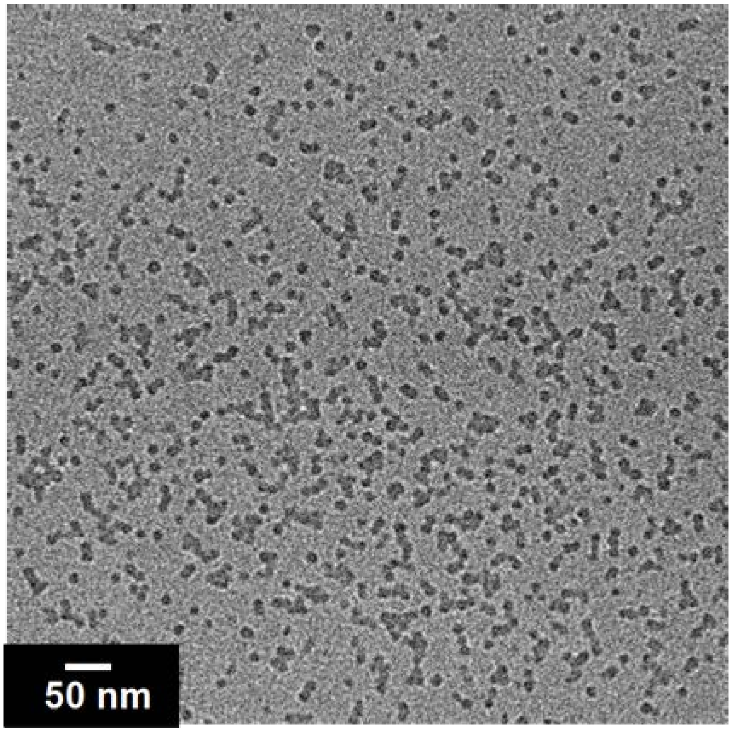

Figure 5.27. TEM image of P2 micelles treated at 55°C for 6 h followed by cooling at room temperature for 3days. Copyright 2015 Royal Society of Chemistry.[31]

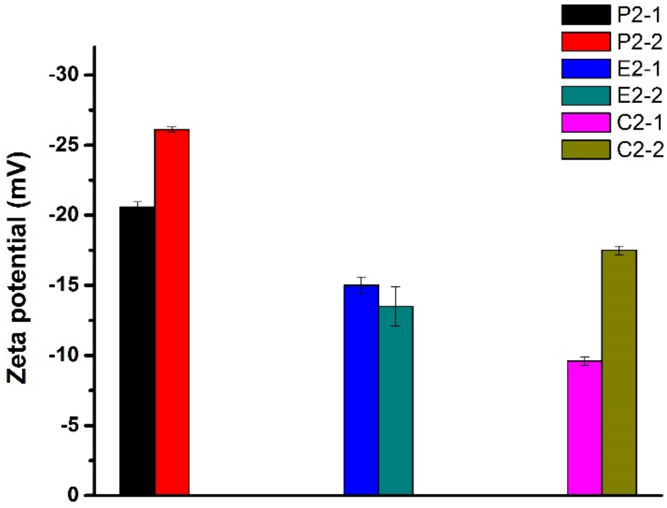

Figure 5.28. Zeta potential of P2-1: P2 micelle at r.t., P2-2: P2 micelle at 55 °C, E2-1: Enzyme treated P2 micelle at rt, E2-2: Enzyme treated P1 at 55 °C, C2-1: Denatured enzyme treated P2 micelle at rt, C2-2: Denatured enzyme treated P2 micelle above 55 °C. Copyright 2015 Royal Society of Chemistry.[31]

The longitudinal relaxation time (T_1) measurements were acquired with a Bruker 7.0 T magnet with Avance II hardware equipped with a 72 mm quadrature transmit/receive coil. T_1 contrast was determined by selecting regions of interest (ROI) using Software ParaVision Version 5.1. The parameters for 7 T MRI of P1: TR = 500.0 ms, TE = 12.6 ms, Echo length = 1, FOV = 8.31 x 3.99 cm^2, slice thickness = 1 mm, NEX = 1 mm, matrix = 256*123. The parameters for 7 T MRI of P2 micelles: TR = 500.0 ms, TE = 12.6 ms, Echo length = 1, FOV = 7.31 x 3.12 cm^2, slice thickness = 1 mm, NEX = 1 mm, matrix = 272*116. r_1 value was calculated after the curve fitting of 1/ T_1 (s^{-1}) *versus* Gd(III) ion concentration (μM). The Gd(III) ion concentration was calibrated by ICP-OES. Figure 5.29 showed the relaxivities of untreated P1 ((3.0 ± 0.2) mM^{-1}s^{-1}) and thermolysin treated P1 (3.7 ± 0.4) mM^{-1}s^{-1}). P2 micellar nanoparticles have similar relaxivities before and after enzyme treatment ((4.2 ± 0.2) mM^{-1}s^{-1} to (3.4 ± 0.1) mM^{-1}s^{-1}). These values are consistent with other reported Gd-based contrast agents at 7T field.[47] Copyright 2015 Royal Society of Chemistry.[31]

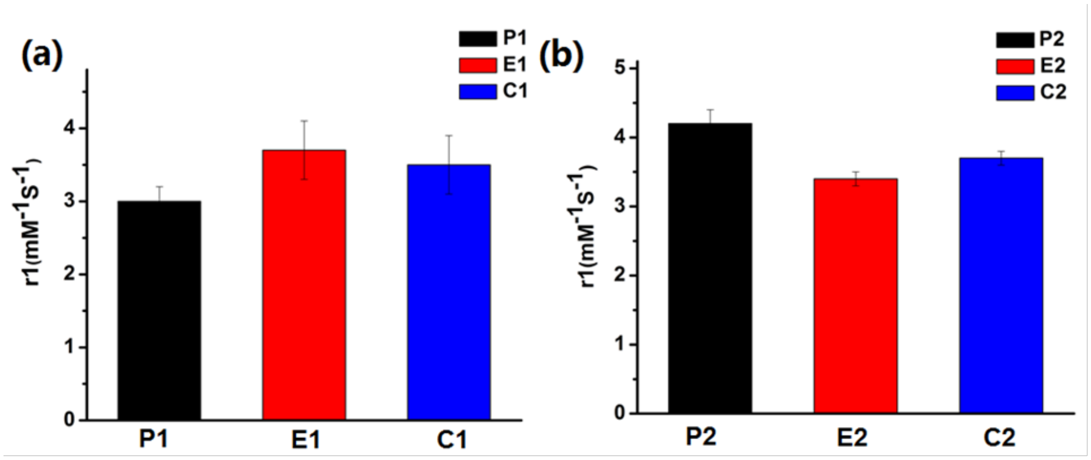

Figure 5.29. Relaxivity of P1 and P2 micelles: (a) P1: untreated P1, E1: enzyme treated P1, C1: denatured enzyme treated P1. (b) P2: untreated P2 micelle, E2: enzyme treated P2 micelle, C2: denatured enzyme treated P2 micelle. Copyright 2015 Royal Society of Chemistry.[31]

5.4 Conclusion

In summary, we have developed a novel strategy to integrate an enzymatic trigger into a cyclic peptide material. The idea of applying enzymes to control the microscopic topology and macroscopic material property gives a new way to design a dual-responsive system. This design is based on the fact that cyclic peptides have different physical properties compared with their linear analogs due to the topological differences. The homopolymer exhibits an LCST behavior at near body temperature. The block copolymer forms spherical micelles due to the amphiphilic nature. Both two polymers could self-assemble/disassemble upon thermo and enzyme stimuli. Additionally, Gd-DOTA at the polymer chain end will provide an MRI tag to allow monitoring the materials behavior *in vivo*.

5.5 Acknowledge

Chapter 5 is adapted in full print from Zhao Wang, [a] Yiwen Li, [a] Yuran Huang, Matthew P. Thompson, Clare L. M. LeGuyader, Swaget Sahu, Nathan Gianneschi, “Enzyme-regulated Topology of a Cyclic Peptide Brush Polymer for Tuning Assembly” Chemical Communications, 2015, 51, 17108-17111. Copyright 2015 Royal Society of Chemistry. The dissertation author is the first author of this paper. For Chapter 5, I would like to thank Dr. Yiwen Li and Prof. Nathan C. Gianneschi for designing this project. I also appreciate Yuran Huang and Dr. Matthew P. Thompson for helping with synthesis and characterization of the materials. Dr. Clare L. M. LeGuyader and Dr. Swaget Sahu give valuable suggestions and discussion.

5.6 References

1. Roy, D.; Cambre, J. N.; Sumerlin, B. S., Future perspectives and recent advances in stimuli-responsive materials. *Progress in Polymer Science* **2010,** *35* (1–2), 278-301.

2. Alarcon, C. d. l. H.; Pennadam, S.; Alexander, C., Stimuli responsive polymers for biomedical applications. *Chemical Society Reviews* **2005,** *34* (3), 276-285.

3. Stuart, M. A. C.; Huck, W. T. S.; Genzer, J.; Muller, M.; Ober, C.; Stamm, M.; Sukhorukov, G. B.; Szleifer, I.; Tsukruk, V. V.; Urban, M.; Winnik, F.; Zauscher, S.; Luzinov, I.; Minko, S., Emerging applications of stimuli-responsive polymer materials. *Nat Mater* **2010,** *9* (2), 101-113.

4. Theato, P.; Sumerlin, B. S.; O'Reilly, R. K.; Epps, I. I. I. T. H., Stimuli responsive materials. *Chemical Society Reviews* **2013,** *42* (17), 7055-7056.

5. Blum, A. P.; Kammeyer, J. K.; Rush, A. M.; Callmann, C. E.; Hahn, M. E.; Gianneschi, N. C., Stimuli-Responsive Nanomaterials for Biomedical Applications. *Journal of the American Chemical Society* **2015,** *137* (6), 2140-2154.

6. Schattling, P.; Jochum, F. D.; Theato, P., Multi-stimuli responsive polymers - the all-in-one talents. *Polymer Chemistry* **2014,** *5* (1), 25-36.

7. Cheng, R.; Meng, F.; Deng, C.; Klok, H.-A.; Zhong, Z., Dual and multi-stimuli responsive polymeric nanoparticles for programmed site-specific drug delivery. *Biomaterials* **2013,** *34* (14), 3647-3657.

8. Zhuang, J.; Gordon, M. R.; Ventura, J.; Li, L.; Thayumanavan, S., Multi-stimuli responsive macromolecules and their assemblies. *Chemical Society Reviews* **2013,** *42* (17), 7421-7435.

9. Callahan, D. J.; Liu, W.; Li, X.; Dreher, M. R.; Hassouneh, W.; Kim, M.; Marszalek, P.; Chilkoti, A., Triple Stimulus-Responsive Polypeptide Nanoparticles That Enhance Intratumoral Spatial Distribution. *Nano Letters* **2012,** *12* (4), 2165-2170.

10. Randolph, L. M.; Chien, M.-P.; Gianneschi, N. C., Biological stimuli and biomolecules in the assembly and manipulation of nanoscale polymeric particles. *Chemical Science* **2012,** *3* (5), 1363-1380.

11. Zelzer, M.; Todd, S. J.; Hirst, A. R.; McDonald, T. O.; Ulijn, R. V., Enzyme responsive materials: design strategies and future developments. *Biomaterials Science* **2013,** *1* (1), 11-39.

12. Wiss, K. T.; Krishna, O. D.; Roth, P. J.; Kiick, K. L.; Theato, P., A versatile grafting-to approach for the bioconjugation of polymers to collagen-like peptides using an activated ester chain transfer agent. *Macromolecules* **2009,** *42* (12), 3860-3863.

13. Sumerlin, B. S., Proteins as Initiators of Controlled Radical Polymerization: Grafting-from via ATRP and RAFT. *ACS Macro Lett.* **2012,** *1* (1), 141-145.

14. Choi, S.-j.; Jeong, W.-j.; Kang, S.-K.; Lee, M.; Kim, E.; Ryu, D. Y.; Lim, Y.-b., Differential Self-Assembly Behaviors of Cyclic and Linear Peptides. *Biomacromolecules* **2012,** *13* (7), 1991-1995.

15. Zhang, B.; Zhang, H.; Li, Y.; Hoskins, J. N.; Grayson, S. M., Exploring the Effect of Amphiphilic Polymer Architecture: Synthesis, Characterization, and Self-Assembly of Both Cyclic and Linear Poly(ethylene gylcol)-b-polycaprolactone. *ACS Macro Letters* **2013,** *2* (10), 845-848.

16. Williams, R. J.; Dove, A. P.; O'Reilly, R. K., Self-assembly of cyclic polymers. *Polymer Chemistry* **2015**.

17. Kricheldorf, H. R., Cyclic polymers: Synthetic strategies and physical properties. *Journal of Polymer Science Part A: Polymer Chemistry* **2010,** *48* (2), 251-284.

18. Yamamoto, T.; Tezuka, Y., Topological polymer chemistry: a cyclic approach toward novel polymer properties and functions. *Polymer Chemistry* **2011,** *2* (9), 1930-1941.

19. Nasongkla, N.; Chen, B.; Macaraeg, N.; Fox, M. E.; Fréchet, J. M. J.; Szoka, F. C., Dependence of Pharmacokinetics and Biodistribution on Polymer Architecture: Effect of Cyclic versus Linear Polymers. *Journal of the American Chemical Society* **2009,** *131* (11), 3842-3843.

20. Fani, M.; Psimadas, D.; Zikos, C.; Xanthopoulos, S.; Loudos, G. K.; Bouziotis, P.; Varvarigou, A. D., Comparative evaluation of linear and cyclic 99mTc-RGD peptides for targeting of integrins in tumor angiogenesis. *Anticancer Research* **2006,** *26* (1 A), 431-434.

21. Craik, D. J., Seamless Proteins Tie Up Their Loose Ends. *Science* **2006,** *311* (5767), 1563-1564.

22. White, C. J.; Yudin, A. K., Contemporary strategies for peptide macrocyclization. *Nat Chem* **2011,** *3* (7), 509-524.

23. MacEwan, S. R.; Chilkoti, A., Elastin-like polypeptides: Biomedical applications of tunable biopolymers. *Peptide Science* **2010,** *94* (1), 60-77.

24. Meyer, D. E.; Chilkoti, A., Genetically Encoded Synthesis of Protein-Based Polymers with Precisely Specified Molecular Weight and Sequence by Recursive Directional Ligation: Examples from the Elastin-like Polypeptide System. *Biomacromolecules* **2002,** *3* (2), 357-367.

25. Ayres, L.; Vos, M. R. J.; Adams, P. J. H. M.; Shklyarevskiy, I. O.; van Hest, J. C. M., Elastin-Based Side-Chain Polymers Synthesized by ATRP. *Macromolecules* **2003,** *36* (16), 5967-5973.

26. Roberts, S. K.; Chilkoti, A.; Setton, L. A., Multifunctional Thermally Transitioning Oligopeptides Prepared by Ring-Opening Metathesis Polymerization. *Biomacromolecules* **2007,** *8* (8), 2618-2621.

27. Conrad, R. M.; Grubbs, R. H., Tunable, Temperature-Responsive Polynorbornenes with Side Chains Based on an Elastin Peptide Sequence. *Angewandte Chemie International Edition* **2009,** *48* (44), 8328-8330.

28. Zhang, W.-B.; Sun, F.; Tirrell, D. A.; Arnold, F. H., Controlling Macromolecular Topology with Genetically Encoded SpyTag–SpyCatcher Chemistry. *Journal of the American Chemical Society* **2013,** *135* (37), 13988-13997.

29. Chien, M.-P.; Rush, A. M.; Thompson, M. P.; Gianneschi, N. C., Programmable Shape-Shifting Micelles. *Angew. Chem. Int. Ed.* **2010,** *49* (30), 5076-5080.

30. Sanford, M. S.; Love, J. A.; Grubbs, R. H., A Versatile Precursor for the Synthesis of New Ruthenium Olefin Metathesis Catalysts. *Organometallics* **2001,** *20* (25), 5314-5318.

31. Wang, Z.; Li, Y.; Huang, Y.; Thompson, M. P.; LeGuyader, C. L. M.; Sahu, S.; Gianneschi, N. C., Enzyme-regulated topology of a cyclic peptide brush polymer for tuning assembly. *Chemical Communications* **2015,** *51* (96), 17108-17111.

32. Bogdanov Jr, A. A.; Weissleder, R.; Frank, H. W.; Bogdanova, A. V.; Nossif, N.; Schaffer, B. K.; Tsai, E.; Papisov, M. I.; Brady, T. J., A new macromolecule as a contrast agent for MR angiography: Preparation, properties, and animal studies. *Radiology* **1993,** *187* (3), 701-706.

33. Bielawski, C. W.; Grubbs, R. H., Living ring-opening metathesis polymerization. *Progress in Polymer Science* **2007,** *32* (1), 1-29.

34. Keil, B., *Specificity of Proteolysis*. Springer-Verlag: 1992.
35. Habraken, G. J. M.; Peeters, M.; Thornton, P. D.; Koning, C. E.; Heise, A., Selective Enzymatic Degradation of Self-Assembled Particles from Amphiphilic Block Copolymers Obtained by the Combination of N-Carboxyanhydride and Nitroxide-Mediated Polymerization. *Biomacromolecules* **2011,** *12* (10), 3761-3769.

36. Fernández-Trillo, F.; Duréault, A.; Bayley, J. P. M.; van Hest, J. C. M.; Thies, J. C.; Michon, T.; Weberskirch, R.; Cameron, N. R., Elastin-Based Side-Chain Polymers: Improved Synthesis via RAFT and Stimulus Responsive Behavior. *Macromolecules* **2007,** *40* (17), 6094-6099.

37. Meyer, D. E.; Chilkoti, A., Quantification of the Effects of Chain Length and Concentration on the Thermal Behavior of Elastin-like Polypeptides. *Biomacromolecules* **2004,** *5* (3), 846-851.

38. Nuhn, H.; Klok, H.-A., Secondary Structure Formation and LCST Behavior of Short Elastin-Like Peptides. *Biomacromolecules* **2008,** *9* (10), 2755-2763.

39. Mai, Y.; Eisenberg, A., Self-assembly of block copolymers. *Chemical Society Reviews* **2012,** *41* (18), 5969-5985.

40. Wang, Z.; Li, Y.; Dong, X.-H.; Yu, X.; Guo, K.; Su, H.; Yue, K.; Wesdemiotis, C.; Cheng, S. Z. D.; Zhang, W.-B., Giant gemini surfactants based on polystyrene-hydrophilic polyhedral oligomeric silsesquioxane shape amphiphiles: sequential "click" chemistry and solution self-assembly. *Chemical Science* **2013,** *4* (3), 1345-1352.

41. Blanazs, A.; Armes, S. P.; Ryan, A. J., Self-Assembled Block Copolymer Aggregates: From Micelles to Vesicles and their Biological Applications. *Macromolecular Rapid Communications* **2009,** *30* (4-5), 267-277.

42. Amir, R. J.; Zhong, S.; Pochan, D. J.; Hawker, C. J., Enzymatically Triggered Self-Assembly of Block Copolymers. *Journal of the American Chemical Society* **2009,** *131* (39), 13949-13951.

43. Chien, M.-P.; Rush, A. M.; Thompson, M. P.; Gianneschi, N. C., Programmable Shape-Shifting Micelles. *Angewandte Chemie International Edition* **2010,** *49* (30), 5076-5080.

44. André, X.; Zhang, M.; Müller, A. H. E., Thermo- and pH-Responsive Micelles of Poly(acrylic acid)-block-Poly(N,N-diethylacrylamide). *Macromolecular Rapid Communications* **2005,** *26* (7), 558-563.

45. Moughton, A. O.; O'Reilly, R. K., Thermally induced micelle to vesicle morphology transition for a charged chain end diblock copolymer. *Chem. Commun.* **2010,** *46* (7), 1091-1093.

46. Shahidan, N. N.; Liu, R.; Cellesi, F.; Alexander, C.; Shakesheff, K. M.; Saunders, B. R., Thermally Triggered Assembly of Cationic Graft Copolymers Containing 2-(2-Methoxyethoxy)ethyl Methacrylate Side Chains. *Langmuir* **2011,** *27* (22), 13868-13878.

47. Noebauer-Huhmann, I. M.; Szomolanyi, P.; Juras, V.; Kraff, O.; Ladd, M. E.; Trattnig, S., Gadolinium-Based Magnetic Resonance Contrast Agents at 7 Tesla: In Vitro T1 Relaxivities in Human Blood Plasma. *Invest. Radiol.* **2010,** *45* (9), 554-558.